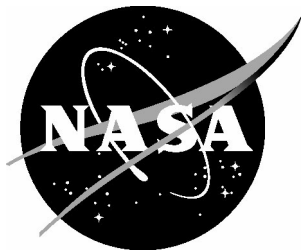


NASA/TP-2005-213533



# Aeroelastic Sizing for High-Speed Research (HSR) Longitudinal Control Alternatives Project (LCAP)

*Joanne L. Walsh, H. J. Dunn, W. Jefferson Stroud, J.-F. Barthelemy,  
Robert P. Weston, Carl J. Martin, and Robert M. Bennett  
Langley Research Center, Hampton, Virginia*

---

July 2005

## The NASA STI Program Office . . . in Profile

Since its founding, NASA has been dedicated to the advancement of aeronautics and space science. The NASA Scientific and Technical Information (STI) Program Office plays a key part in helping NASA maintain this important role.

The NASA STI Program Office is operated by Langley Research Center, the lead center for NASA's scientific and technical information. The NASA STI Program Office provides access to the NASA STI Database, the largest collection of aeronautical and space science STI in the world. The Program Office is also NASA's institutional mechanism for disseminating the results of its research and development activities. These results are published by NASA in the NASA STI Report Series, which includes the following report types:

- **TECHNICAL PUBLICATION.** Reports of completed research or a major significant phase of research that present the results of NASA programs and include extensive data or theoretical analysis. Includes compilations of significant scientific and technical data and information deemed to be of continuing reference value. NASA counterpart of peer-reviewed formal professional papers, but having less stringent limitations on manuscript length and extent of graphic presentations.
- **TECHNICAL MEMORANDUM.** Scientific and technical findings that are preliminary or of specialized interest, e.g., quick release reports, working papers, and bibliographies that contain minimal annotation. Does not contain extensive analysis.
- **CONTRACTOR REPORT.** Scientific and technical findings by NASA-sponsored contractors and grantees.

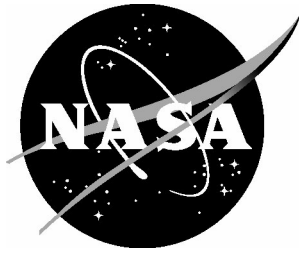
- **CONFERENCE PUBLICATION.** Collected papers from scientific and technical conferences, symposia, seminars, or other meetings sponsored or co-sponsored by NASA.
- **SPECIAL PUBLICATION.** Scientific, technical, or historical information from NASA programs, projects, and missions, often concerned with subjects having substantial public interest.
- **TECHNICAL TRANSLATION.** English-language translations of foreign scientific and technical material pertinent to NASA's mission.

Specialized services that complement the STI Program Office's diverse offerings include creating custom thesauri, building customized databases, organizing and publishing research results ... even providing videos.

For more information about the NASA STI Program Office, see the following:

- Access the NASA STI Program Home Page at <http://www.sti.nasa.gov>
- E-mail your question via the Internet to [help@sti.nasa.gov](mailto:help@sti.nasa.gov)
- Fax your question to the NASA STI Help Desk at (301) 621-0134
- Phone the NASA STI Help Desk at (301) 621-0390
- Write to:  
NASA STI Help Desk  
NASA Center for AeroSpace Information  
7121 Standard Drive  
Hanover, MD 21076-1320

NASA/TP-2005-213533



# Aeroelastic Sizing for High-Speed Research (HSR) Longitudinal Control Alternatives Project (LCAP)

*Joanne L. Walsh, H. J. Dunn, W. Jefferson Stroud, J.-F. Barthelemy,  
Robert P. Weston, Carl J. Martin, and Robert M. Bennett  
Langley Research Center, Hampton, Virginia*

National Aeronautics and  
Space Administration

Langley Research Center  
Hampton, Virginia 23681-2199

---

July 2005

The use of trademarks or names of manufacturers in the report is for accurate reporting and does not constitute an official endorsement, either expressed or implied, of such products or manufacturers by the National Aeronautics and Space Administration.

Available from:

NASA Center for AeroSpace Information (CASI)  
7121 Standard Drive  
Hanover, MD 21076-1320  
(301) 621-0390

National Technical Information Service (NTIS)  
5285 Port Royal Road  
Springfield, VA 22161-2171  
(703) 605-6000

# **Aeroelastic Sizing for High Speed Research (HSR) Longitudinal Control Alternatives Project (LCAP)**

## **Contributors**

Jean-François Barthelemy	NASA LaRC, MDOB/ASCAC
Robert Bennett	NASA LaRC, AB/SMC, retired, DRA
Kwan Chang	LMES, now BCAG
Peter Coen	NASA LaRC, SAB/ASCAC
Augustine Dovi	LMES, now Raytheon Technical Services Co.
H. J. Dunn	NASA LaRC, MDOB/ASCAC
Winifred Feldhaus	NASA LaRC, STAB/SEC
James Fenbert	NASA LaRC, now Symantec, Inc.
Neal Frink	NASA LaRC, CAB/AAAC
Mike Fox	ViGYAN, Inc, now Lockheed Martin Aeronautics Co.
Javier Garriz	CSC, now Symantec, Inc.
Clyde Gumbert	NASA LaRC, MDOB/ASCAC
Carl Martin	LMES, NASA LaRC, MTSB/SMC, now University of Wisconsin, Madison
Patrick Mitchell	BCAG
Paresh Parikh	ViGYAN, Inc., now CAB/AAAC
Edward Parlette	ViGYAN, Inc.
Anthony Pototzky	LMES, now NASA LaRC, AB/SMC
Jamshid Samareh	CSC, now NASA LaRC, MDOB/ASCAC
Vic Spain	LMES, now NASA LaRC, AB/SMC
Jeff Stroud	NASA LaRC, ACMB/SMC
Joanne Walsh	NASA LaRC, MDOB/ASCAC
Joseph Walz	NASA LaRC, ACMB/SMC, now retired
Robert Weston	NASA LaRC, MDOB/ASCAC
Gregory Wrenn	LMES, now SWALES
Thomas Zeiler	LMES, now University of Alabama

## **Consultants**

Chris Borland	BCAG
Bruce Kimoto	MD, now BCAG
Steve Scotti	NASA LaRC, MTSB/SMC
Ross Sheckler	Dynaacs Corporation
Martin Waszak	NASA LaRC, DCB/AirSC
Richard Wood	NASA LaRC, CAB/AAAC

## Abbreviations

AAAC	Aerodynamics, Aerothermodynamics, & Acoustics Competency
AB	Aeroelasticity Branch
ACMB	Analytical & Computational Methods Branch
AirSC	Airborne Systems Competency
ASCAC	Aerospace Systems, Concepts & Analysis Competency
BCAG	Boeing Commercial Airplane Group
CAB	Configuration Aerodynamics Branch
CSC	Computer Sciences Corporation
DCB	Dynamics and Control Branch
DRA	Distinguished Research Associate
Dynacs	Dynacs Corporation
LaRC	Langley Research Center
LMES	Lockheed Martin Engineering Services
MD	McDonnell Douglas
MDOB	Multidisciplinary Optimization Branch
MTSB	Metals and Thermal Structures Branch
SAB	Systems Analysis Branch
SMC	Structures and Materials Competency
SEC	Systems Engineering Competency
SWALES	Swales Aerospace
STAB	Structures and Thermal Analysis Branch
ViGYAN	ViGYAN, Inc.

This report is the product of collaboration between several organizations at NASA Langley Research Center and several contractor organizations. Written credit cannot possibly account for every contribution to the successful completion of the LCAP study; indeed, most interactions occurred in informal one-on-one exchanges or open discussions among ad hoc subteams. Nevertheless, the following write-up attempts to acknowledge as many individual contributions as possible.

The modeling effort for this study was considerable because the models provided by the HSR partners had to be modified to represent the unique configurations considered here. The structural modeling efforts began with an *EAL* FEM model that was initially developed by C. Martin and S. Scotti. This *EAL* FEM model was based on a Boeing-provided FEM. Modifications for the baseline and alternate configurations were done by W. Feldhaus and P. Mitchell. C. Martin, J. Stroud, and R. Bennett provided input. The aerodynamic modeling effort entailed the derivation of both proper paneling for linear methods and surface and field grids for nonlinear methods. In addition, care was taken to model control surfaces and flap and slat deflections. R. Weston led the model derivation efforts and developed the linear model; P. Parikh developed the nonlinear model. J. Garriz developed the volume grids. R. Sheckler and N. Frink provided expertise.

Structural and sensitivity analyses were carried out by using an *EAL*-based procedure assembled by C. Martin and S. Scotti; this procedure is discussed in the report, and appropriate references are provided. J. Walsh performed the analyses; H. J. Dunn derived graphic results. J. Walz carried out a number of special assignments to validate selected results. J. Stroud provided expert consultation, problem

formulation, and results analysis. The weights model and weights estimations were handled at Boeing to maintain the proprietary nature of the information. P. Mitchell provided fast turnaround and constant guidance.

Linear aerodynamic analyses were carried out with the *USSAERO* computer program; R. Weston set up the analyses and correlated the results with existing wind tunnel and nonlinear aerodynamic models. J. Fenbert provided alternate linear aerodynamic analyses. Nonlinear analyses were handled with *USM3D*; E. Parlette set up and ran these nonlinear cases. M. Fox collected experimental data for validation of aerodynamic analysis computer programs. N. Frink, the author of *USM3D*, provided extensions to his computer program to handle details of the geometry. Static aeroelastic analyses were provided in a trim procedure that was developed and run by G. Wrenn. R. Weston and G. Wrenn developed the procedure for implementing corrections to the pressure distributions to account for nonlinear aerodynamics.

Procedures that built on the *ISAC* computer program were used for the flutter calculations. T. Zeiler authored the procedures and was largely responsible for the flutter and flutter sensitivity analyses of the Aft-Tail configuration and for a portion of the analyses of the Three-Surface configuration. K. Chang then took over and completed the analyses of the Three-Surface and Canard configurations. H. J. Dunn provided alternate *MSC/NASTRAN*-based analyses; R. Bennett provided input throughout the study.

As discussed in the report, the entire sizing process was integrated around a procedure that was initially put together by S. Scotti and C. Martin. As the procedure was enhanced to include flutter calculations, external weights calculations, and aeroelastic trim calculations, C. Martin continued both as a consultant on the implementations and as a hands-on participant in the interfacing of the various components. He trained the team on use of the computer program and ran the first few cycles for the first configuration. J. Walsh then took over and ran the remaining design cycles.

The written documentation of the effort was largely the work of J. Walsh, with contributions from J. Stroud, R. Weston, R. Bennett, and J. Barthelemy. J. Stroud helped substantially in editing the work. The electronic (CD-ROM) documentation was the brainchild and realization of H. J. Dunn; C. Gumbert generated some of the graphic results as did R. Weston.

Finally, the entire LCAP study went quite beyond this work to include additional efforts in performance sizing, aerodynamics, and dynamics and control. P. Coen led the entire activity, together with a team of leads for the various disciplines. J. Barthelemy was the lead for aeroelastic sizing; M. Waszak, for dynamics and control; R. Weston, for linear aerodynamics; and R. Wood, for nonlinear aerodynamics. C. Borland led the Boeing team; B. Kimoto led the McDonnell Douglas team. A. Dovi and V. Spain led the LMES team.

## Contents

Summary .....	6
Nomenclature .....	7
1. Introduction and Background .....	8
2. Assumptions and Ground Rules .....	9
3. Modeling .....	9
3.1 Model History .....	10
3.2 Model Modifications .....	10
3.2.1 Aft-Tail Configuration .....	11
3.2.2 Canard Configuration.....	11
3.2.3 Three-Surface Configuration .....	12
3.3 Weights Model.....	12
3.4 Finite-Element Model (FEM) .....	12
3.4.1 Boundary Conditions for Trimmed Loads Analysis.....	13
3.4.2 Boundary Conditions for Dynamics Analysis.....	13
3.4.3 Boundary Conditions for Optimization.....	13
3.5 Aeroloads Model.....	13
3.5.1 Linear Model ( <i>USSAERO</i> ) .....	13
3.5.2 Nonlinear Model ( <i>USM3D</i> ).....	14
3.6 Flutter Model.....	14
3.7 Optimization Model.....	14
4. Aeroelastic Sizing Process .....	14
4.1 Analyses.....	15
4.1.1 Weights Analysis .....	15
4.1.2 Mass and Center of Gravity (cg) Analysis .....	15
4.1.3 Dynamic Analysis.....	15
4.1.4 Flutter Analysis.....	16
4.1.5 Trimmed Loads Analysis .....	16
4.1.5.1 Linear Aerodynamic Analysis ( <i>USSAERO</i> ).....	17
4.1.5.2 Nonlinear Aerodynamic Analysis ( <i>USM3D</i> ) .....	17
4.1.5.3 Nonlinear Loads Correction.....	17
4.1.5.4 Aeroelastic Trim Loop.....	18
4.1.6 Assembly of Loads for Buckling and Strain Analyses .....	19
4.1.7 Strain Analysis.....	19
4.1.8 Buckling Analysis.....	19
4.2 Optimization Formulation.....	20
4.2.1 Objective Function.....	20
4.2.2 Design Variables.....	20
4.2.3 Constraints .....	21
4.2.3.1 Kresselmeier-Steinhauser (KS) Constraint Function .....	21
4.2.3.2 Strain Constraints .....	21
4.2.3.3 Buckling Constraints .....	21
4.2.3.4 Ply-Mixture Constraints.....	22
4.2.3.5 Flutter Constraints .....	22
4.2.4 Sensitivity Analyses.....	22
4.2.4.1 Strain and Buckling Constraint Derivatives.....	22

4.2.4.2 Ply-Mixture Constraint Derivatives.....	23
4.2.4.3 Flutter Constraint Derivatives .....	23
4.3 Optimization Strategy.....	23
4.3.1 Outer Loop (Cycle) .....	23
4.3.2 Inner Loop (Iteration).....	24
4.3.3 Aeroelastic Sizing Process Timings.....	24
5. Optimization Results.....	25
5.1 Convergence.....	25
5.2 Weight.....	25
5.2.1 FEM Weight .....	25
5.2.2 Operational Empty Weight .....	26
5.2.2.1 Aft-Tail Configuration.....	26
5.2.2.2 Three-Surface Configuration.....	26
5.2.2.3 Canard Configuration .....	27
5.3 Aeroelastic Trim Results .....	27
5.4 Variation of Modal Frequencies.....	28
5.5 Design Variable Results .....	28
5.5.1 Design Variable Values.....	28
5.5.1.1 Comparisons Between Designs for Three-Surface and Aft-Tail Configurations.....	29
5.5.1.2 Comparisons Between Designs for Canard and Aft-Tail Configurations	29
5.5.2 Design Variable Bounds.....	30
5.5.2.1 Fuselage .....	30
5.5.2.2 Wing .....	30
5.6 Constraints .....	31
5.6.1 Strain Constraints.....	31
5.6.1.1 Strain Constraints for Linear Designs.....	32
5.6.1.2 Strain Constraints for Nonlinear Designs .....	32
5.6.2 Buckling Constraints.....	33
5.6.2.1 Buckling Constraints for Linear Designs.....	33
5.6.2.2 Buckling Constraints for Nonlinear Designs .....	33
5.6.3 Ply-Mixture Constraints .....	34
5.6.4 Flutter Constraints.....	34
5.6.4.1 Aft-Tail Configuration.....	35
5.6.4.2 Three-Surface Configuration.....	35
5.6.4.3 Canard Configuration .....	35
6. Concluding Remarks.....	35
References .....	37
Tables.....	39
Figures.....	59

## Summary

The Longitudinal Control Alternatives Project (LCAP) compared three high-speed civil transport configurations to determine potential advantages of the three associated longitudinal control concepts. The three aircraft configurations included a conventional configuration with a layout having a horizontal aft tail (denoted the Aft-Tail configuration), a configuration with a forward canard in addition to a horizontal aft tail (denoted the Three-Surface configuration), and a configuration with only a forward canard (denoted the Canard configuration). The three configurations were aeroelastically sized and were compared on the basis of operational empty weight (OEW) and longitudinal control characteristics. One of the ground rules of the study was that wings for the Three-Surface and Canard configurations were required to be the same size and at the same location as the wing for the Aft-Tail configuration. This requirement could penalize the Three-Surface and Canard configurations since normally the wing size and location would change for a different control concept. This report describes the methods that were used and the results that were generated for the aeroelastic sizing of the three configurations.

The sized structure consisted of composite honeycomb sandwich panels on both the wing and the fuselage. Design variables were the core depth of the sandwich and the thicknesses of the composite material which made up the face sheets of the sandwich.

Each configuration was sized for minimum structural weight under linear and nonlinear aeroelastic loads. Design requirements used in the optimization included strain, buckling, and subsonic and supersonic flutter constraints. In addition, for the composite face sheets of the sandwich panels that were sized, constraints were placed on the ratios of ply thickness to total laminate thickness for each ply orientation. These constraints were denoted ply-mixture constraints. All types of constraints affected the design. A greater number of buckling and ply-mixture constraints were active compared with the number of strain constraints. Several flutter constraints were active for each configuration.

Sizing under linear aerodynamic loads required between 5 and 10 design cycles for each configuration. The final designs for the three configurations differed by less than 9 percent in sized theoretical finite-element weight and 1 percent in OEW. Three additional design cycles under nonlinear aerodynamic loads resulted in a slight reduction (less than 0.5 percent) in OEW and caused some redistribution of material.

The overall conclusion of this report was that the final OEWs for the three configurations were too similar to differentiate between the three configurations; thus, further comparison is required on the basis of longitudinal control characteristics, including ride and handling qualities. Differences between the three configurations may have been more pronounced if adjustments to the overall configurations, such as shifts in wing location, had been allowed.

## Nomenclature

CFD	computational fluid dynamics
cg	center of gravity
$\square$	strain
<i>FEM</i>	finite element model
g	constraint
HSCT	high-speed civil transport
HSR	high-speed research
IGES	Initial Graphics Exchange Specification
<i>K</i>	curvature
KEAS	knots equivalent airspeed
<i>KS</i>	Kresselmeier-Steinhauser function
LCAP	Longitudinal Control Alternatives Project
<i>M</i>	Mach number
OEW	operational empty weight
OML	outer mold line
<i>p-k</i>	flutter analysis method
$t_{ply}$	total ply thickness
$t_0$	0 <sup>0</sup> ply thickness
$t_{45}$	+45 <sup>0</sup> ply thickness
$t_{90}$	90 <sup>0</sup> ply thickness
$V_D$	dive velocity
<i>X, Y, Z</i>	coordinate axes

### Computer Programs

<i>AM-FM</i>	calculates realistic or as-built weights (ref. 4)
<i>CDC ICEM</i>	wetted surface definition (ref. 9)
<i>EAL</i>	finite element analysis (ref. 3)
<i>EALWTS</i>	translates design variable data into input for <i>AM-FM</i>
<i>ELFINI</i>	finite element analysis (ref. 1)
<i>ELFMAS</i>	translates <i>AM-FM</i> output into nodal masses
<i>MINOS</i>	optimizer (ref. 25)
<i>MSC/NASTRAN</i>	finite element analysis (ref. 2)
<i>OVERFLOW</i>	Navier-Stokes CFD computer program (ref. 17)
<i>USM3D</i>	unstructured Euler-equation flow solver (refs. 11-13)
<i>USSAERO</i>	linear aerodynamic analysis computer program (refs. 6 and 7)
<i>VGRID3D</i>	generates 3-D flow-field grid (ref. 10)
<i>ZONA51</i>	supersonic flutter analysis (ref. 16)

## **1. Introduction and Background**

In discussions between Boeing, McDonnell Douglas, and NASA in 1994, concern was expressed in regard to the ride quality and handling qualities of the long, slender configurations that were under consideration for the High-Speed Research (HSR) program in development of future supersonic transport aircraft. Of particular concern was the arrangement of the longitudinal control surfaces and their influence on the overall weight, ride quality, and handling qualities of the aircraft. This area of consideration was suggested as an appropriate application of multidisciplinary optimization (MDO) techniques at NASA Langley Research Center (LaRC). A consistent evaluation of three aircraft configurations was recommended to examine potential advantages of three different longitudinal control concepts. The three high-speed civil transport (HSCT) configurations were: a conventional layout with a horizontal aft tail (denoted the Aft-Tail configuration), a layout having a forward canard in addition to the horizontal aft tail (denoted the Three-Surface configuration), and a layout having only a forward canard (denoted the Canard configuration). Aeroelastic behavior was considered; operational empty weight (OEW) was used as a metric, along with ride quality and handling qualities. This study was called the Longitudinal Control Alternatives Project (LCAP).

The objective of the study was to compare three configuration concepts for high speed civil transport aircraft. It was felt that being long, slender and, therefore flexible, typical supersonic transports would present special challenges. It was decided to identify major differences among the candidate configuration concepts from the standpoint of longitudinal stability and control and ride and handling qualities. To obtain reasonably representative results, realistic weights needed to be developed that reflected a fully sized structure and factored in typical strength, stability and flutter requirements.

The present paper describes the approach used to produce sized structural designs for the three configurations. Other studies (not reported elsewhere) included i) CFD calculations of pressure distributions at selected load cases, ii) estimate of longitudinal stability derivatives, derived from CFD results and existing experimental information, iii) calculation of handling quality metrics, iv) calculation of ride quality metrics, v) evaluation of control requirements, and vi) performance resizing of the vehicle based on structural design.

To ensure relevance to the HSR project, Boeing provided the LCAP team with detailed data on one of their current designs of an aft-tail supersonic aircraft (see Section 3.1 for additional information). The Boeing input included for the baseline aircraft i) a detailed geometry (IGES format) with various flap deflections, ii) a complete finite element model, iii) eight selected load conditions (Mach number, altitude, gross weight) that were felt to be critical in the design, and iv) complete consistent mass matrices for the selected load cases and that reflected the appropriate fuel states.

Boeing also supplied the modified configurations for the canard and three surface aircrafts, along with new geometries, updated mass matrices and 4 additional load conditions that were felt critical to designs with canard surfaces.

In the course of the study, as described later in this report, Boeing re-evaluated the weight and weight distributions for each intermediate design and sent NASA LaRC the updated weight matrices to pursue the design effort.

The study was made up of two studies: one conducted by LaRC with Boeing support, based on a Boeing aft tail configuration, and one conducted by McDonnell Douglas, based on their arrow-wing

configuration. At LaRC, a team of both LaRC and contractor personnel was assembled to perform the analysis and design. Boeing provided support to this team, and both McDonnell Douglas and Boeing personnel provided guidance and input. This report describes the aeroelastic sizing work that was performed at LaRC for this project. Additional results are available on a CD-ROM supplement to this report.

## **2. Assumptions and Ground Rules**

The planform views of the three HSCT configurations are shown in figure 1; all three configurations were based on a Boeing design with a horizontal aft tail. The sizes of the horizontal aft tail and canard surfaces were provided by Boeing. No adjustments to the overall configuration, such as shifts in wing location, were made to the Canard or to the Three-Surface configuration. Minimal changes in the finite-element model (FEM) were made to accommodate the canard structure. The structural concept and FEM for both the canard and the canard support were developed by LaRC with guidance from Boeing. (See section 3.2.) No recambering, control-surface sizing, or area ruling was performed to aerodynamically integrate the revised control surfaces. However, the fuselage fillet at the root of the canard, which was lofted by Boeing for subsonic wind-tunnel tests, was relofted by LaRC to provide a fillet that was more appropriate for supersonic flight. It was realized that these ground rules could possibly penalize the Three-Surface and Canard configurations. An overview of the LCAP process is shown in figure 2. The steps for the aeroelastic sizing portion of the project are shown in figure 3.

Boeing provided the five mass cases listed in table 1. The masses were practical construction (i.e., realistic or “as-built”) weights that represented variations in payload and fuel ranging from the OEW to maximum gross takeoff weight. These masses were updated during the aeroelastic sizing. Boeing also provided a limited number of load conditions that they considered to be critical design load conditions; the associated flap deflections were also provided. These load conditions and flap deflections are given in table 2. Eight load conditions were used for the Aft-Tail configuration; 12 load conditions were used for the Three-Surface and Canard configurations. The mass cases that were used for each load condition are given in table 3.

After the aeroelastic sizing (fig. 3) was complete, the design was given to the controls investigators for an assessment of the rigid and flexible stability and control derivatives, the control requirements, and the ride quality and handling qualities. Experimental data were used for the stability and control work where possible. The controls study considered only the longitudinal characteristics. No detailed control system was designed for these configurations; only simple control laws were applied to facilitate the analyses, such as for ride quality.

Factors such as the interaction between propulsion and aerodynamics and other operational considerations were not included in the LCAP study. However, vehicle performance and sizing were evaluated at the end of optimization under both linear and nonlinear loads.

## **3. Modeling**

The LCAP aeroelastic sizing process required several models because each type of analysis required its own model. In this section of the report, the modeling effort and the evolution of the Aft-Tail FEM that was used by LaRC in the LCAP activity are discussed. A discussion of how this FEM was modified to

obtain the FEMs for the Three-Surface and Canard configurations follows. Finally, the models required for each analysis used in the LCAP aeroelastic sizing process are discussed.

### 3.1 Model History

In December 1992, prior to LCAP, Boeing made a structural FEM for a Boeing HSCT available to LaRC under a loan agreement that was signed earlier. The transmittal letter is shown in figure 4. The structural model was for a conventional aft-tail configuration of an HSCT with no canard. As noted in the transmittal letter, the model had already undergone one sizing cycle for loads (strength) and flutter. The structural model was compatible with the computer program *ELFINI* (ref. 1). LaRC engineers converted the model to be compatible with the *MSC/NASTRAN* (ref. 2) and *EAL* (ref. 3) finite-element computer programs. The primary reason for requesting the structural model from Boeing was so that LaRC engineers could use the structural model to calculate loads for design studies of HSCT components.

The structural model transmitted to LaRC was given the designation 1080-892 STR Model E by Boeing. Later, when the LCAP activity was initiated, this model was selected even though Boeing had already upgraded their structural model to the designation 1080-892 STR Model F. Model F was not used for LCAP because the model would have required conversion from an *ELFINI* to an *EAL* model; for Model E, that conversion had already been made. Model F differed from Model E in many small ways; for example, Model F was stiffer in various regions. Later, the LCAP model was also stiffened in some of the same regions.

In addition to the structural model described above, which was used to calculate elastic response, Boeing also provided the LCAP team with the Initial Graphics Exchange Specification (IGES) files that described the outer mold line (OML) for each of the three configurations. These OML descriptions, which describe the external wetted surfaces, were based on the Boeing 1080-892 Reference H configuration. The aerodynamic models were derived from the OMLs. The LCAP structures team worked primarily with the structural model. However, because of shape differences between the aerodynamic model and the structural model, both models had to be considered. The structural model and the OML of the Aft-Tail configuration are shown in figures 5 and 6, respectively. In figure 7, the structural model and the OML are superimposed on one another. (In figs. 5, 6, 7(a), and 7(b), the view is from the nose toward the tail.) In figure 5(a), the structural model is shaded. In figure 5(b), the structural model is a wire-frame view. During the aeroelastic trim loop, the structural and aerodynamic shapes prescribed in the FEM and OML, respectively, are considered to be the shapes at the Mach 2.4 cruise load condition.

In figure 7, the structural and OML surfaces are superimposed to highlight the differences. The surfaces that are shown are those that are visible after the models have been superimposed. The major differences between the structural and OML surfaces are the location and the dihedral of the wing and the location and the incidence angle of the horizontal tail. Small differences can also be seen in the shape of the fuselage.

### 3.2 Model Modifications

The structural models for each of the three LCAP configurations were obtained by modifying the Boeing model denoted 1080-892 STR Model E. The FEMs for all three configurations are shown in figure 8.

For each configuration, the size of the horizontal aft tail and the size of the canard were prescribed by Boeing. For each configuration, the external shape of the aerodynamic model differed from that of the structural model. Whereas each aerodynamic model was based on the 1080-892 Reference-H

configuration (denoted “OML” in figs. 6 and 7), each structural model was based on the 1080-892 STR Model E (denoted “FEM” in figs. 5, 7, and 8). Because aerodynamic loads calculated on the aerodynamic model had to be transferred to the structural model (and, conversely, because deflections calculated on the structural model had to be transferred to the aerodynamic model), the differences in shape had to be taken into account. Since the planforms of the OML and FEM were nearly identical, z-direction projection methods were used to transfer forces and displacements between the models (section 4.1.5.4). The OMLs were available for the three configurations. The goal was to create appropriate structural models of the Canard configuration and the Three-Surface configuration. This goal was accomplished by creating and placing the structural model of the canard on the Aft-Tail structural model. Engineering judgment and the OMLs were used as guides. These modifications are explained in the following sections.

**3.2.1 Aft-Tail Configuration.** The initial structural model (Model E) was modified as follows: the design variables (section 4.2.2) were increased by 10 percent, the engine struts were stiffened, the internal fuselage structure that supported the horizontal aft tail was stiffened, and the floor structure was stiffened. The resulting structural model was the initial structural design for all three configurations. The rationale for these four modifications was as follows. The Aft-Tail FEM that was delivered to LaRC had previously undergone one cycle of sizing by Boeing. The LaRC team felt that this sizing cycle might give the Aft-Tail configuration an advantage in the LCAP study. Thus, the design variables were increased by 10 percent for all three configurations in an effort to eliminate any bias in the results. Animation of the vibration modes for the Aft-Tail configuration indicated motion of the engine struts in the range of frequencies of interest. Because no design variables controlled the stiffness of the struts, the engine struts were stiffened to raise the frequencies out of the range of interest. The internal fuselage structure that supported the horizontal aft tail was stiffened to raise the tail vibration frequency above 5 Hz. Spurious floor modes were also noted. Again, because no design variables controlled the stiffness of the floor area, rigid links were added and the floor beams were stiffened to remove these spurious modes.

**3.2.2 Canard Configuration.** The finite-element model of the canard was created with the assistance of Boeing personnel. In the vicinity of the canard, the fuselage of the structural model was lower than the OML of the fuselage. Therefore, to position the canard on the structural model, the canard was moved down to a location that corresponded approximately to the position of the canard on the OML. The final location of the canard on the structural model was guided by two considerations. The planform view of the canard on the structural model had to be the same as the planform view of the canard OML. This consideration defined the longitudinal location. In addition, the canard shaft and support structure could not intrude into the cabin; this structure had to remain below the floor. This consideration helped to define the canard pivot point and the anhedral angle.

In figure 9, the canard and support structure for the structural model (or FEM) and the canard OML are shown with the FEM of a portion of the fuselage. The support structure for the structural model of the canard and the floor of the fuselage are also shown. Because of the anhedral angle of the canard, the canard support structure could not have a carry-through structure as was used in the horizontal aft tail. Note that the two canards are not at the same vertical location and that the canard of the structural model is below the canard OML, as explained above.

The vibration modes of the structural model were calculated and animated. For the Canard and Three-Surface configurations, the backup structure (the canard support and shaft) was stiffened to raise the canard modes above the lower wing-fuselage modal frequencies. As a result of this stiffening, the canard mode moved into the range of 5–6 Hz.

**3.2.3 Three-Surface Configuration.** As shown in table 4, to obtain the Three-Surface configuration the canard for the Canard configuration was reduced to 50 percent of its original planform area, and the horizontal aft tail on the Aft-Tail configuration was reduced to 50 percent of its original planform area. The location of the pivot point and the orientation on the fuselage of both the canard and the aft tail remained the same. The canard and tail support structures within the fuselage were not reduced in size.

In figure 10, two horizontal aft tails are shown with a portion of the FEM for the fuselage. One is the tail OML and the other (denoted “FEM”) is the tail for the structural model. Note that in figures 7 and 10, the incidence angles of the horizontal tails differ by  $10^\circ$ . The support structure for the tail of the structural model is also shown.

### 3.3 Weights Model

Boeing’s proprietary computer program, *AM-FM* (ref. 4), was used to obtain realistic or as-built weights for the trimmed loads and flutter analyses. In order to obtain as-built weights, a weights model for each configuration was required to transfer the latest sizing information to the *AM-FM* program. The same weights model that was described in reference 4 was used in the LCAP activity. The Aft-Tail FEM was divided into 14 meshes, as shown in figure 11. These 14 meshes were also used for both the Three-Surface and Canard configurations. Initially for each configuration, Boeing provided a set of 42 mass files in the *ELFINI* format that defined the as-built weight distributions. Twenty-one files described the structure, and 12 files described the systems and equipment. In addition, three files described the payload, and six files described the fuel for various load conditions. Each of these files corresponded to 1 of the 14 meshes. Some meshes had more than one associated file. For example, four files were associated with mesh 1: one file represented the weight distribution for the structural part of the inboard wing, the second file represented the weight distribution of the nonstructural part of the inboard wing, the third file represented the weight distribution of the systems and equipment of the inboard wing, and the fourth file represented the weight distribution of the wing main landing gear. During the sizing process, only 5 of the 42 files changed. The part of the structure that changed was contained in meshes 1 through 5, indicated by the color areas. Note that no mesh was associated with the canard surface for either the Three-Surface or the Canard configuration because no *ELFINI* FEM existed for the canard structure. Realistic weights were generated by Boeing and LaRC for the canard structure by evenly distributing the canard weight on the FEM nodes of the canard surface.

### 3.4 Finite-Element Model (FEM)

The three LCAP configurations shared essentially the same FEM. The only differences occurred in the horizontal tail, the canard, and the support structures for the horizontal tail and canard. The basic FEM used in these studies was a refined, symmetric half-model. The FEM included the floors, rings, frames, control surfaces, and a stick model of the engines with supports. Each model had approximately 40,000 degrees of freedom. The FEMs for the three configurations are shown in figure 8.

The material properties used in the LCAP study were provided by Boeing (ref. 5). The skins, webs, and rods were graphite/bismaleimide. The sandwich panels on the wing and the fuselage had a titanium honeycomb core. The material properties for the resized structure used in the analyses are given in table 5.

A separate FEM was used for each of the three configurations. For each configuration, the various analyses required various boundary conditions; however, the FEM for each configuration remained the same. The boundary conditions that were used are as follows.

**3.4.1 Boundary Conditions for Trimmed Loads Analysis.** Boundary conditions were provided by Boeing. In addition to symmetry constraints, the model was restrained at one point on the front spar and at one point on the rear spar. This model (i.e., the FEM with these boundary conditions) was used in the mass and center of gravity (cg) analysis (section 4.1.2) and in the trimmed loads analysis (section 4.1.5).

**3.4.2 Boundary Conditions for Dynamic Analysis.** The boundary conditions were free-free (i.e., no degrees of freedom were eliminated) for the symmetric model. This model (i.e., the FEM with these boundary conditions) was used in the dynamic analysis (section 4.1.3) to calculate the vibration modes and frequencies that were used in both the flutter (section 4.1.4) and flutter sensitivity analyses (section 4.2.4.3).

**3.4.3 Boundary Conditions for Optimization.** Boeing provided two sets of boundary conditions for the symmetric response of the model. One set was for all flight load cases; the other set was for the taxi load case. For the optimization analysis performed at LaRC, these two sets of boundary conditions were combined into a single, functionally equivalent set. The combination of the two sets of boundary conditions into a single set greatly reduced the computational effort required during optimization. Using only one set of boundary conditions required that the stiffness matrix needed to be factored only once and the stiffness matrix sensitivities needed only be calculated once. This model (i.e., the FEM and these boundary conditions) was used in the strain (section 4.1.7), buckling (section 4.1.8), and strain and buckling constraint derivatives analyses (section 4.2.4.1).

### **3.5 Aeroloads Model**

For the three configurations, the IGES OMLs provided by Boeing were used as the basis for the aerodynamic models for both the linear and nonlinear aerodynamic analyses. No vertical tail or engine nacelles were included in the aerodynamic models.

**3.5.1 Linear Model (USSAERO).** The surface grid that is used in the *USSAERO* aerodynamic analysis computer program (refs. 6 and 7) is described in a wavedrag format (ref. 8), which imposes some restrictions on the manner in which the surface geometry can be represented. The fuselage is described by a longitudinal series of up to 30 constant-*X* cross sections; each lifting surface is described by a contiguous lateral series of up to 20 constant-*Y* airfoil sections. One set of percent chord locations is used for the node locations of all airfoil sections of a lifting surface. Each airfoil section is defined by specifying at each chordwise location the airfoil half-thickness and the *Z*-offset of the airfoil midpoint relative to the airfoil leading edge. Separate surface grids are generated for each of the seven flap settings. The size limitations of the computer program allow the configuration surface to be divided into a maximum of 600 panels on the body and 600 panels on the lifting surfaces.

The surface grid in wave-drag format was extracted from the IGES OML, which was provided by Boeing, by first generating a high-density point definition (30,000 points) for the fuselage and lifting surfaces. For the fuselage, constant-*X* sections were interpolated at the 30 fuselage stations chosen for the linear model. For the *Y* and *Z* coordinates of the wavedrag format, a cubic-spline fit of each section was then used to calculate 20 equally spaced points azimuthally. A similar process was used with the constant-*Y* sections through the wing and horizontal tail surfaces to calculate the airfoil thickness and camber specifications for the lifting-surface wave-drag definition. The spanwise locations of 16 airfoil sections were chosen to best satisfy several requirements: nearly uniform spanwise spacing, location of planform breaks in the leading and trailing edges, and locations of the inboard and outboard edges of the main wing flaps. The remaining 4 of the 20 airfoil sections allowed in the *USSAERO* input file are evenly distributed

across the span of the horizontal tail. Figure 12 illustrates the resulting surface definition for load condition LX26 on the Aft-Tail configuration, which had the largest flap deflections.

**3.5.2 Nonlinear Model (*USM3D*).** The IGES OML was used as the basis for the surface definition, with the leading- and trailing-edge wing flaps deflected according to the schedule in table 2. A wetted-surface definition for each configuration setting, including appropriate gaps for the deflected wing flaps and control surfaces, was obtained using the *CDC ICEM* (ref. 9) package. After the control surfaces were deflected according to the requirements of each load condition, the tetrahedral unstructured-grid-generation package *VGRID3D* (ref. 10) was used to generate the three-dimensional flow-field grid that was used as input to *USM3D* (refs. 11–13). Several iterations were performed with *USM3D* for some grids to achieve reasonable grid densities and flow computations. A typical volume grid contained on the order of 600,000 tetrahedral cells. Figure 13 illustrates typical surface grid distributions for use in the *USM3D* and *USSAERO* analyses.

### 3.6 Flutter Model

To remain consistent with the aims of the LCAP study, only symmetric flutter analyses were performed. Therefore, for the flutter modeling, symmetric vibration modes were used. For each of the 5 mass cases given in table 1, 30 elastic vibration modes and 3 rigid-body modes were calculated with the *EAL* dynamic analysis. The flutter modeling included only aerodynamics that were calculated with linear theory. The use of computational fluid dynamics (CFD) methods (i.e., methods based on numerical solution of the nonlinear aerodynamic Euler or Navier-Stokes equations (such as *USM3D*)) was impractical within the time and framework of this study. The nonlinear corrections from CFD methods used for the aerodynamic loads were developed late in the study such that the timely application and validation of similar procedures for flutter were not feasible. Approximately 279 panels, or boxes, were used on the wing, fuselage, tail, and canard of the half-aircraft. (See fig. 14.) The same box layout was used for both subsonic and supersonic cases, but the layout had to be revised slightly for the Canard and Three-Surface configurations. The same models were used for other flight conditions to calculate rigid and flexible dynamic stability derivatives for the stability and control portion of the LCAP effort.

### 3.7 Optimization Model

To limit the number of independent design variables and to place the design variables where they were most effective, the optimization model for each configuration was divided into zones in which the design variables were uniform. Thirty-nine zones were located on the fuselage, and 22 zones were located on the wing (11 on the upper surface and 11 on the lower surface), for a total of 61 zones. (See fig. 15.) Each zone consisted of several finite elements.

## 4. Aeroelastic Sizing Process

The objective of the aeroelastic sizing (fig. 3) was to design composite sandwich panels on both the wing and fuselage so that the resulting design was a minimum-weight design that satisfied a set of inequality constraints on material strength, buckling, subsonic and supersonic flutter, and the proportion of composite material at specified ply orientations. Trimmed aerodynamic loads were calculated on the flexible aircraft for several flight conditions. Structural response was calculated by using a finite-element analysis. Each optimization cycle consisted of complete analyses of both aerodynamic loads and flutter, followed by a series of design variable moves based on approximate analyses. A complete analysis was carried out at the end of each cycle. The aerodynamic loads were first calculated by using a linear

aerodynamic analysis. After the aeroelastic sizing was reasonably converged, the linear loads were corrected by using a nonlinear aerodynamic analysis.

As shown in figure 3, the aeroelastic sizing process consisted of several aeroelastic sizing "cycles" within which one or more sizing optimization "iterations" were accomplished. The weights analysis, mass and cg analysis, dynamic analysis, flutter and flutter sensitivity analyses, and aeroelastic loads analysis were done in the outer loop. The buckling analysis, strain analysis, ply-mixture analysis, associated sensitivity analyses, and optimization were done in the inner loop. The analyses are discussed first, then the optimization formulation is discussed, and finally a detailed discussion of the optimization strategy is presented.

## 4.1 Analyses

**4.1.1 Weights Analysis.** The weights model that was discussed earlier was used for the weights analysis to provide the as-built weights. The weights analysis consisted of three computer programs: *AM-FM*, *EALWTS*, and *ELFMASS*. The *AM-FM* computer program is a Boeing proprietary code that calculates as-built weights based on the FEM topology and structural element thickness information. The *AM-FM* computer program uses Boeing proprietary algorithms that provide weight increments based on geometry, design criteria, and manufacturing requirements and practices (ref. 4). The *EALWTS* and *ELFMASS* computer programs, which are data interfaces between *EAL* and *AM/FM*, were developed for the LCAP activity and were run at LaRC. The *EALWTS* computer program is a FORTRAN computer program that translates the design variable information that is obtained from the resizing into input (total skin thickness and core thickness) for the *AM-FM* computer program. The *EALWTS* computer program was executed five times (i.e., once for each mesh shown in color in fig. 11). The *AM-FM* computer program was run at Boeing to generate the as-built weights. The *ELFMASS* computer program is a FORTRAN computer program that translates these as-built weights from the *AM-FM* computer program into nodal point masses for use with the LaRC computer programs in the mass and cg, dynamic, and trimmed loads analyses. Initially, the *ELFMASS* computer program was executed for each of the 42 files described in section 3.3. Subsequently, this computer program was executed only for the files that corresponded to the five meshes shown in color in figure 11.

**4.1.2 Mass and Center of Gravity (cg) Analysis.** The mass and cg analysis was performed in *EAL*. The mass and cg information was generated by using the as-built weights, based on the current set of design variables. For the mass and cg analysis, the model described in section 3.4.1 was used; the appropriate *EAL* mass files, which were generated by the weights analysis, were assembled into the five mass cases shown in table 1. The total mass and cg locations for all mass cases were also calculated. This mass information was used subsequently in the dynamic and trimmed loads analyses.

**4.1.3 Dynamic Analysis.** Vibration modes that were needed for the flutter analysis were calculated in the dynamic analysis. The dynamic analysis, like the mass and cg analysis, was performed in *EAL*. For the dynamic analysis, the current set of design variable values and the 5 mass files that were generated in the mass and cg analysis were used to calculate 33 vibration modes (3 rigid-body and 30 elastic modes) for each of the 5 mass cases. With the selection of 33 modes, the highest vibration frequencies were approximately 15 Hz (nearly 3 times higher than the highest expected flutter frequency). For that reason, 33 modes appeared to be a reasonable limit on the number of vibration modes used for flutter. Vibration modal information for selected grid points was supplied for the flutter analysis.

**4.1.4 Flutter Analysis.** The flutter envelope for the aircraft used in this study was the same as that used for the Boeing model 1080-892 STR Model E (refs. 5 and 14). Below the dive velocity  $V_D$ , the aircraft was required to be flutter free with no structural damping, and at  $1.15V_D$  the aircraft was required to be flutter free with a structural damping of 3 percent.

The flutter analyses used the  $p-k$  analysis in the computer program *ISAC* (ref. 15); the *ISAC* computer program performed a determinant iteration to determine reasonable approximations to the damping of the minimally damped aeroelastic modes. Altitude was varied from 80,000 to 10,000 ft by using standard atmospheric subroutines. The resulting modal dampings and frequencies were plotted versus velocity in knots equivalent airspeed (KEAS). The velocity for each flutter instability point or crossing was calculated and listed. The list included crossings for rigid-body modes, both crossings of the hump modes (points A and B, fig. 16), and spurious crossings. A manual selection was required to eliminate crossings for the rigid-body modes (this type of flutter would be eliminated by a control system), the end-of-flutter points from the hump modes (point B, fig. 16), any crossings greater than 20 percent above  $1.15V_D$ , and spurious crossings caused by the loss of root tracking in the *ISAC* system. To facilitate automatic calculation of the flutter points, each case was run both with no structural damping and with structural damping of 3 percent.

Linear unsteady aerodynamic methods were used for both subsonic and supersonic flow. For subsonic flow, the doublet lattice method (included in the *ISAC* system) was used. For supersonic flow, the *ZONA51* computer program (ref. 16) was used. Because the complex aerodynamic influence matrices are a function of only the configuration geometry, Mach number, and reduced frequency, the matrices were calculated once for each configuration. A common box, or panel layout, was used for both the subsonic doublet lattice and the supersonic *ZONA51* analyses. The interpolation for the vibration modal information from the *EAL* FEM grid to the unsteady aerodynamic grid was set up for each configuration with common wing points; however, some differences were necessary to account for the different tail and canard surfaces. This grid interpolation setup applied to all mass cases for the design cycles for each configuration and to both subsonic and supersonic cases. The interpolated modal information and aerodynamic influence matrices were used to calculate the generalized forces for the flutter analysis.

Flutter was evaluated for zero and 3-percent structural damping at three subsonic Mach numbers ( $M = 0.65, 0.80, \text{ and } 0.95$ ) and four supersonic Mach numbers ( $M = 1.20, 1.50, 2.00, \text{ and } 2.60$ ). Rather than selecting critical mass cases, flutter was evaluated for all five mass cases. Initially, flutter calculations were also made for  $M = 1.05$  for the Aft-Tail configuration. This condition was later omitted because the value of  $M$  was too close to  $M = 1.0$  for linear theory.

#### **4.1.5 Trimmed Loads Analysis**

An initial objective of the LCAP activity specified the use of a nonlinear aerodynamic analysis computer program to determine loads. However, a prohibitively large amount of computer time would have been needed to perform the multiple nonlinear analyses for all load cases during the aeroelastic trim loop. Computer and calendar time limitations led to the choice of a nonlinear corrections process. This process relied on a one-time calculation of the nonlinear aerodynamics at each load condition. The differences in pressure between the nonlinear analyses and the corresponding linear analyses at matching conditions were applied as corrections to subsequent linear analyses during the aeroelastic trim loop described below.

**4.1.5.1 Linear Aerodynamic Analysis (*USSAERO*).** The *USSAERO* computer program (refs. 6 and 7) was chosen as the linear aerodynamic analysis for calculating the pressure distribution and aerodynamic characteristics of wing-body-tail combinations in both subsonic and supersonic potential flow. The *USSAERO* computer program provides a unified approach to the aerodynamic analysis of wing-body-tail configurations in subsonic and supersonic flow. This computer program permits the analysis of noncircular bodies, provides a more accurate representation of the rounded wing leading edges, and allows the determination of wing interference effects in the presence of the body.

In *USSAERO*, a constant source distribution is used on the body panels. A constant source and a linearly varying vortex distribution are used on the wing and horizontal tail panels. The strength of the wing source distribution is set to the slope of the wing thickness distribution, and linearly varying vortex distributions are used to simulate the effects of camber, twist, and incidence angle. For the LCAP activity, the planar boundary condition option was used for both the subsonic and supersonic speed conditions.

**4.1.5.2 Nonlinear Aerodynamic Analysis (*USM3D*).** The *USM3D* computer program is an unstructured Euler-equation flow solver (refs. 11–13) based on a cell-centered finite-volume approach that is implemented for tetrahedral cells. The fluxes across the cell faces are computed with Roe's flux-difference-splitting scheme. Higher order accuracy is achieved by a fast multidimensional linear reconstruction algorithm that takes advantage of the geometrically invariant features of tetrahedra. Solutions are advanced in time by a three-stage Runge-Kutta time-stepping scheme with convergence accelerated to steady state by local time stepping and implicit residual smoothing. The computer program requires 45 words/cell of memory. The first-order scheme, used throughout the LCAP activity, used 12  $\mu\text{sec}/\text{cell}/\text{cycle}$  on a single processor of the Cray Y-MP. A special wake boundary condition was developed for the LCAP activity and was applied to the sharp-edged lateral face at the wing break and at faces that resulted when flap and control-surface deflections opened up a flow gap. This boundary condition was used to prevent negative pressures as the flow accelerated around the sharp edges.

Figures 17 and 18 present comparisons of the wing pressure distributions for a 2.2-percent scale wind-tunnel model and for three CFD computer programs at  $M = 0.90$  and 2.4 (cruise) for the Aft-Tail configuration. The predicted wing pressure distributions for the *USSAERO* (linear) computer program, the *USM3D* (Euler) computer program, and the *OVERFLOW* (Navier-Stokes; ref. 17) computer program were compared with one another and with available wind-tunnel data. The constant- $X$  and constant- $Y$  cross sections shown correspond to rows of pressure ports on the wind-tunnel model. In figures 17 and 18, the locations are given in scale inches for the full-scale aircraft. Although viscous-dominated flow characteristics such as a leading-edge vortex (seen in fig. 17 for the experimental and Navier-Stokes analysis pressures) were not captured by *USSAERO* or *USM3D*, the remainder of the pressure distribution characteristics were represented fairly well.

**4.1.5.3 Nonlinear Loads Correction.** To keep the grid-generation requirements and the computational time for the nonlinear aerodynamics calculations within reason, a nonlinear loads correction process was employed; this correction process relied on a one-time calculation of the nonlinear aerodynamics at each load condition. An unstructured grid was generated for each load condition by using the appropriate wing flap settings for that load condition and by using estimated horizontal control surface settings that were expected to result in a zero pitching moment. For each grid, the *USM3D* computer program was run in a mode in which the angle of attack was determined as part of the solution process for the prescribed lift coefficient.

For each *USM3D* calculation, a corresponding *USSAERO* run was made for which the same total-configuration *Z*-force coefficient and the same horizontal control surface *Z*-force coefficient were obtained by choosing the appropriate angle of attack and horizontal control surface deflection. After the *USM3D* aerodynamic forces were mapped to the *USSAERO* grid, the difference in the *Z* force (i.e., the *USM3D* minus the *USSAERO* calculation) at each panel was computed. Because the forces for the total configuration matched, the integration of the force difference over the total configuration yielded a zero net force but a nonzero pitching moment. Two assumptions have been made; this difference (denoted the nonlinear correction) represents the load redistribution that is attributable to nonlinear effects and the pressure changes during aeroelastic deformation can be primarily accounted for by changes in the linear aerodynamic analysis (i.e., changes in the nonlinear corrections will be secondary). These assumptions were tested by using *USM3D* directly in the aeroelastic trim loop (see section 4.1.5.4) for one load case (LX43) on the Aft-Tail configuration. Figure 19 shows the nondimensionalized nonlinear corrections for the rigid configuration (Mach 2.4 cruise shape); figure 20 shows the nonlinear corrections on the deformed shape when *USM3D* is used throughout the aeroelastic calculations. For illustrative purposes, the nonlinear corrections have been nondimensionalized by using the free-stream dynamic pressure and the panel area. A comparison of these figures reveals that the distribution of the nonlinear corrections is nearly the same, except in a small region at the wing tip.

**4.1.5.4 Aeroelastic Trim Loop.** Figure 21 illustrates the aeroelastic trim loop process, which produced the converged aeroelastic trimmed loads for each load condition in table 2 except for the cruise and taxi conditions. The process required approximately five iterations to converge for each load condition. The boxes on the left (labeled A-F) designate computer programs (solid arrows indicate the control sequence); the rounded boxes on the right designate interface files that were used to transfer data from one computer program to the next computer program (dashed arrows indicate data flow).

A wavedrag deck description of the initial configuration was used to start the process. A *USSAERO* input file (program A, fig. 21) was generated by appending the *USSAERO* directives that specified flight conditions (Mach numbers and angles of attack), horizontal control surface deflection angles, and other fixed geometric conditions. The *USSAERO* computer program (program B, fig. 21) was then run for each load condition at a combination of angles of attack and horizontal control surface deflection angles that spanned the range of interest. The assembled pressure output files from these runs were then used as input to program C to determine the angles of attack and horizontal control surface deflection angles that produced the required lift for each load condition, with no net pitching moment. In addition, for the Three-Surface configuration the normal force for the horizontal tail had to be of equal magnitude and opposite direction to the normal force for the canard. The resulting forces at the center of each aerodynamic panel were output for each load condition. Program D distributed the force of each aerodynamic panel to the three closest FEM nodes such that the force and its moments about the *X* and *Y* axes were conserved. This process conserved the total configuration force but may have resulted in a small net moment that was deemed negligible. These distributed forces were combined with load-condition inertia forces to produce the applied forces. The FEM deflections (program E) calculated by *EAL* at selected nodes were used to recalculate (program F) the wing camber definition in the wavedrag deck, which provided the starting point for the next iteration of the aeroelastic trim loop. The conventional linear superposition assumption was used for the structural deflections. The prescribed shape at the Mach 2.4 cruise condition was taken as the basis for the deflected shape at other load conditions. Figure 22 shows the wing deflections in the wavedrag definition for the Aft-Tail configuration at  $M = 0.95$ . These deflections are typical of all three configurations.

To include the nonlinear aerodynamic effects, the only change that was made in the aeroelastic trim loop process occurred in the interface between programs B and C. This change involved the addition of the corresponding nonlinear corrections for each load condition to the linear panel forces calculated by *USSAERO*.

**4.1.6 Assembly of Loads for Buckling and Strain Analyses.** To account for an internal cabin pressure of 10.78 psi, additional internal forces at selected fuselage nodes (provided by Boeing) were added to the converged aeroelastic trimmed loads for each load condition. The forces for the taxi condition were obtained by multiplying the inertia forces (nodal masses multiplied by  $-1.0$ ) by the load factor from table 2 and adding reaction forces at 2 nodes – the locations of the forward and aft landing gears. The resulting forces for all the load conditions were then multiplied by a factor of safety (1.5) and used in the strain and buckling analyses during optimization.

**4.1.7 Strain Analysis.** For each optimization load case, internal loads were calculated by using *EAL*. Then, these internal loads were used to calculate the inplane strains in each finite element that made up the skin panels on the wing and fuselage. To provide a conservative design, strains were calculated at the outermost layer. In short, the following conventional approach was used in these calculations (ref. 18).

The strain distribution  $\epsilon$  through the thickness was assumed to have the form

$$\epsilon = \epsilon^o + zK \quad (1)$$

where  $\epsilon^o$  are the mid-plane strains,  $K$  are the curvatures, and  $z$  is the distance from the mid-plane. For a balanced, symmetric laminate (which was the case for the panels used in the LCAP activity), the mid-plane strains and curvatures are related to the internal forces  $N$  and moments  $M$  by

$$N = [A]\epsilon^o \quad (2)$$

and

$$M = [D]K \quad (3)$$

where  $[A]$  and  $[D]$  are the orthotropic inplane and bending stiffness matrices. The strain at the outer fiber was then calculated by using the element forces produced by *EAL* with

$$\epsilon = [A]^{-1} N \pm \frac{t}{2} [D]^{-1} M \quad (4)$$

where  $t$  is the total sandwich thickness (core height plus twice the face sheet thickness). The maximum and minimum strains were compared with the tension and compression strain limits in the  $0^\circ$ ,  $\pm 45^\circ$ , and  $90^\circ$  ply orientations to compute the values of the strain constraints. (See section 4.2.3.2.)

**4.1.8 Buckling Analysis.** Skin panels on the wing and fuselage were analyzed for buckling. The buckling analysis was based on a biaxial inplane loading ( $N_x$  and  $N_y$ ) of an orthotropic plate with shear ( $N_{xy}$ ) interaction. The plate was assumed to be square with an edge length of either 30 or 35 in., based on the local frame spacing. Generally, wing panels were assumed to have an edge length of 30 in., and fuselage panels were assumed to have an edge length of 35 in. Simple-support boundary conditions were assumed for all four edges.

The interaction equation that defines buckling was assumed to have the form

$$\frac{N_x}{N_{xcr}} + \left( \frac{N_{xy}}{N_{xycr}} \right)^2 = 1 \quad (5)$$

The first term on the left side corresponds to buckling under loads  $N_x$  and  $N_y$  only, and the second term corresponds to buckling under load  $N_{xy}$  only. Buckling under loads  $N_x$  and  $N_y$  assumes that the ratio  $N_x/N_y$  is maintained. The loads  $N_x$  and  $N_y$  are scaled by the same factor up to failure. Thus,  $N_x/N_{xcr} = N_y/N_{ycr}$ . The following equation was used for the buckling load  $N_{xcr}$  (ref. 19, eq. 11.2.33):

$$N_{xcr} = \frac{\left[ D_{11} \left( \frac{m}{a} \right)^4 + 2(D_{12} + 2D_{66}) \left( \frac{m}{a} \right)^2 \left( \frac{n}{b} \right)^2 + D_{22} \left( \frac{n}{b} \right)^4 \right]}{\left( \frac{m}{a} \right)^2 + \frac{N_y}{N_x} \left( \frac{n}{b} \right)^2} \quad (6)$$

where  $N_x$  and  $N_y$  are the applied inplane loads;  $D_{ij}$  are orthotropic bending stiffnesses;  $m$  and  $n$  are the numbers of buckling half-waves in the  $x$  and  $y$  directions, respectively;  $a$  and  $b$  are lengths of edges parallel to the  $x$  and  $y$  directions, respectively (here,  $a = b$ ). To calculate the minimum values of  $N_{xcr}$ ,  $m$  and  $n$  were varied from 1 to 5.

Shear buckling was defined by the following equation (ref. 20):

$$N_{xycr} = \left( \frac{2}{b} \right)^2 \left( D_{11} D_{22}^3 \right)^{\frac{1}{4}} 8.125 + \frac{5.05}{\square} \quad (7)$$

where

$$\square = \frac{\sqrt{D_{11} D_{22}}}{D_{12} + 2D_{66}} \quad (8)$$

## 4.2 Optimization Formulation

The theoretical FEM weight was minimized subject to inequality constraints to prevent excessive strain, to prevent buckling and flutter, and to maintain a practical laminate for the composite face sheets of sandwich panels on the surface of the wing and fuselage. Many loading conditions were considered, including both subsonic and supersonic flutter. A more detailed discussion of the optimization is presented in the sections below.

**4.2.1 Objective Function.** The objective function that was minimized was the FEM weight of the sized structure.

**4.2.2 Design Variables.** The sized structure consisted of composite honeycomb sandwich panels on both the wing and fuselage. Figure 23 shows a section of a composite honeycomb sandwich panel and lists the design variables used in the optimization. The composite honeycomb sandwich section was assumed to

be balanced and symmetric, and the core height was assumed to be sufficiently large such that the location of the individual plies in the face sheets would not affect the overall bending stiffness. These assumptions, along with limitations on the ply angles, reduced the number of design variables to four per zone. These four design variables were the total thickness of the  $0^\circ$  plies in one face, the total thickness of the  $90^\circ$  plies in one face, the total thickness of the  $+45^\circ$  plies in one face, and the honeycomb core height.

The 4 design variables in each of 61 design variable zones (fig. 15) yielded a total of 244 design variables per configuration. Figure 24 shows the orientation of the composite plies. On the fuselage,  $0^\circ$  plies were aligned longitudinally. On the inboard wing,  $0^\circ$  plies were aligned streamwise. On the outboard wing,  $0^\circ$  plies were normal to (approximately) the 50-percent-chord line.

### 4.2.3 Constraints

**4.2.3.1 Kresselmeier-Steinhauser (KS) Constraint Function.** To reduce the total number of strain, buckling, and flutter constraints, a cumulative constraint known as the Kresselmeier-Steinhauser function (KS, ref. 21) was used. Note that the KS function was not used for the ply-mixture constraints. The KS function is an envelope function that approximates the active constraint boundary and is given by

$$g = KS = \frac{1}{\beta} \prod_{i=1}^{nc} e^{\beta g_i} \quad (9)$$

where  $nc$  is the number of individual constraints,  $g_i$  is the  $i$ th individual constraint (e.g., individual strain, buckling, or flutter constraint), and  $\beta$  is a user-specified pull-down factor. The larger the value of  $\beta$ , the closer the envelope remains to the boundary of the feasible region. The KS function is a single measure of constraint satisfaction or violation. The KS function is a single-valued function that is continuous and differentiable. For the strain and buckling constraints,  $\beta$  had a value of 50. For the flutter constraints,  $\beta$  had a value between 10 and 35.

**4.2.3.2 Strain Constraints.** For each optimization load case, strains were calculated for each finite element that made up the wing and fuselage skin panels (see section 4.1.7). These strains were then compared with allowable strains (table 5) to obtain the individual strain constraints. The most critical strain constraint was selected in each finite element and was given by

$$g_{strain} = \frac{strain}{allowable\ strain} \quad (10)$$

These critical constraints were then combined by using a KS function to produce both a single strain constraint for the quadrilateral elements within a given design variable zone and a single strain constraint for the triangular elements within a given design variable zone. A total of 96 strain constraints were used (61 for the quadrilateral elements and 35 for the triangular elements).

**4.2.3.3 Buckling Constraints.** Buckling constraints were handled in the same manner as the strain constraints. For each optimization load case, buckling constraints were calculated for each finite element that made up the wing and fuselage skin panels, as discussed in section 4.1.8. Each individual buckling constraint was given by

$$g_{buckling} = \frac{N_x}{N_{xcr}} + \frac{N_{xy}}{N_{xycr}} + \frac{N_{xy}}{N_{xycr}}^2 \quad (11)$$

The individual buckling constraints were then combined by using a KS function to produce a single buckling constraint for the quadrilateral elements within a given design variable zone and a single buckling constraint for the triangular elements within a given design variable zone. A total of 96 buckling constraints were used (61 for the quadrilateral elements and 35 for the triangular elements).

**4.2.3.4 Ply-Mixture Constraints.** For the composite face sheets of the sandwich panels, constraints were imposed on the ratios of ply thickness to total laminate thickness for each ply orientation. These ratios were specified by Boeing (ref. 5). The constraints were as follows:  $0^\circ$  plies were to make up at least 10 percent of the face sheet laminate,  $90^\circ$  plies were to make up at least 10 percent of the face sheet laminate,  $\pm 45^\circ$  plies were to make up at least 40 percent of the face sheet laminate but no more than 60 percent of the face sheet laminate. Therefore, 4 ply-mixture constraints were used for each design variable zone, for a total of 244 ply-mixture constraints. The four ply-mixture constraints described above were defined by the following equations:

$$g = \left[ \frac{0.1}{T \square 0.1} \right] (t_{90} + 2t_{45}) \square t_0 \square 0 \quad (12)$$

$$g = \left[ \frac{0.1}{T \square 0.1} \right] (t_0 + 2t_{45}) \square t_{90} \square 0 \quad (13)$$

$$g = \left[ \frac{0.4}{T \square 0.4} \right] (t_0 + t_{90}) \square 2t_{45} \square 0 \quad (14)$$

$$g = \left[ \frac{\square 0.6}{T \square 0.6} \right] (t_0 + t_{90}) + 2t_{45} \square 0 \quad (15)$$

**4.2.3.5 Flutter Constraints.** The KS function was also used to reduce the number of flutter constraints. For a given combination of Mach number, mass condition, and damping, several flutter conditions (crossings) may exist. A single constraint was written for the flutter speed at each crossing. Then, all constraints for one combination of Mach number, mass condition, and damping were combined into one KS function. If no crossing existed for a given combination, then the KS function was set to  $\square 1.0$ , and the corresponding flutter constraint derivatives were set to 0. A total of 70 flutter KS functions were used. (During the first two cycles for the Aft-Tail configuration, 80 flutter KS functions were used because  $M = 1.05$  was included.) Because the constraints were defined in terms of flutter speed, convergence may have been affected because crossings sometimes disappeared from one cycle to the next.

## 4.2.4 Sensitivity Analyses

**4.2.4.1 Strain and Buckling Constraint Derivatives.** The derivatives of the strain and buckling constraints were calculated by using the *EAL* procedures described in reference 22. These procedures were based on the semianalytical approach described in reference 23. That semianalytical approach used analytical expressions for the derivatives of the displacements with respect to design variables and used finite-difference techniques to calculate the derivatives of the stiffness matrix with respect to the design variables. The displacements and displacement derivatives were then used in linear Taylor's series

approximations to obtain new displacements. These new displacements were used to calculate new strain and buckling constraints. Finite-difference techniques were then used to calculate the strain and buckling constraint derivatives.

**4.2.4.2 Ply-Mixture Constraint Derivatives.** The derivatives of the ply-mixture constraints were obtained analytically.

**4.2.4.3 Flutter Constraint Derivatives.** The flutter constraint derivatives were calculated by using the process described in reference 24. This process used the generalized aerodynamic forces at the flutter conditions and calculated the derivatives of the flutter speed with respect to the modal frequencies and generalized masses. The derivatives of the generalized mass and generalized stiffness matrices with respect to the design variables were obtained in a separate *EAL* procedure. Derivatives of the stiffness matrix and the theoretical mass matrix with respect to the design variable were computed with finite-difference methods. (The theoretical mass matrix is made up of the masses represented in the finite-element model.) These matrices of mass and stiffness derivatives were then pre- and post-multiplied by the vibration mode shapes for each mass case to produce the matrices of generalized mass and stiffness derivatives. The derivatives of the theoretical mass matrix with respect to the design variables were used as an approximation. Implementing and interfacing the sensitivity calculations with the *AM-FM* computer program would have been time-consuming and beyond the scope of the LCAP study.

### 4.3 Optimization Strategy

This section describes the aeroelastic sizing process (fig. 3) and gives the timings for the various steps. As mentioned earlier, the aeroelastic sizing process consisted of an outer loop (fig. 3(a)) and an inner loop (fig. 3(b)). Only the inner loop was completely automated.

**4.3.1 Outer Loop (Cycle).** The outer loop (fig. 3(a)) began with the weights analysis, which produced the as-built weights for the individual files described in section 3.3. Initially, all 42 files were run through the weights analysis. On subsequent cycles, only the five files that represented the structural components indicated by the colored meshes in figure 11 needed to be updated by the weights analysis. Then, these 42 individual mass files were assembled into the five mass cases described in table 1. The cg locations and total masses for the five mass cases were calculated and verified with Boeing. These five mass cases represented the as-built weight distribution on a nodal point basis.

Next, *EAL* vibration modes were calculated in a dynamics analysis for use in the flutter analysis for the five mass cases. The flutter constraints and the flutter sensitivities were calculated in program A. The flutter results were examined manually to determine the amount of constraint violation (if any) and the type of flutter mode (e.g., hump mode) involved. A decision was made to proceed with the current design, go back to a previous design iteration (i.e., a set of design variable values from an earlier iteration), or in some instances modify the FEM and repeat the analyses. If the decision was made to proceed, then the aeroelastic trimmed loads (program B) were calculated. These converged loads were then assembled into the optimization load cases (program C) which were used for the buckling and strain analyses.

Next, cycle convergence was checked manually by examining the objective function and constraint histories over several cycles. If the aeroelastic sizing process was considered to be sufficiently converged, then the process was stopped after a final analysis consisting of strain and buckling analyses, objective function (FEM weight) and constraint evaluations was performed. Otherwise, the move limits

and maximum number of iterations for the inner loop were manually selected based on a qualitative assessment of the accuracy of the constraint approximation in the previous cycle. Then, the inner loop, which involved several iterations, was performed with the aeroelastic trimmed loads held constant. The optimization was performed in the inner loop. After the inner loop was completed, the optimization results were examined to determine which iteration would be considered the end of the current aeroelastic sizing cycle (i.e., the appropriate design variable set was chosen). After this design variable set was chosen, the outer loop (cycle) was completed.

**4.3.2 Inner Loop (Iteration).** The inner loop (fig. 3(b)) was based on the process described in reference 22. The only differences were the additions of the ply-mixture constraints and the flutter constraints present in the LCAP aeroelastic sizing process. The linear programming option of *MINOS* (based on the simplex method, ref. 25) was used. An iteration consisted of *EAL* and *MINOS* execution for a given move limit on the design variables. The *EAL* computer program calculated the strain, buckling, and ply-mixture constraints (programs D and E, fig. 3(b)). The FEM weight was also calculated. The strain, buckling, and ply-mixture constraint sensitivities (program F, fig. 3(b)) were calculated. The buckling, strain, ply-mixture, and flutter constraints and their associated sensitivities were assembled (program G, fig. 3(b)) into the constraint matrix and the sensitivity matrix for the optimizer. Note that the buckling, strain, and ply-mixture constraints and their associated sensitivities were obtained from programs E and G (fig. 3(b)). In contrast, the flutter constraints and flutter constraint sensitivities were obtained from program A (fig. 3(a)). The *MINOS* computer program then used this information to find the set of design variable values that minimized the objective function (FEM theoretical weight) and satisfied the constraints. The design variable values were saved for each iteration. At the end of the specified number of iterations, the inner loop was complete.

**4.3.3 Aeroelastic Sizing Process Timings.** Because the aeroelastic sizing process involved several different computers and because some of the steps in the process could not be automated, only an approximate turnaround time can be given for the entire process. After the process was in place, an entire aeroelastic cycle averaged 1 week to complete. Note that this 1-week turnaround time included scheduling the work so that the optimization (an automated but time-consuming process) could take place over a weekend and scheduling other time-consuming, automated analyses to run at night. The approximate timings for each major step of the aeroelastic sizing process are given in table 6. As indicated in the column labeled “Comments,” some of the steps are largely automated, for example, the aeroelastic trimmed airloads. Other steps are not automated, for example, the flutter analysis (i.e., choosing the flutter crossings).

The flutter calculations were performed on workstations. Even with storage of the unsteady aerodynamic matrices, which eliminated the large amount of time required for regeneration, the number of calculations required as a result of two values of structural damping, 7 Mach numbers, 5 mass cases, 33 modes, and up to 29 altitudes led to a huge number of flutter calculations. These calculations were done en masse by a shell script for the subsonic cases and a shell script for the supersonic cases. Initially, 24–36 hours turnaround time was required for calculations on two machines simultaneously. In the latter part of the study, when faster workstations were available, the turnaround time was reduced to 12–14 hours (overnight). With the large number of calculations required, computer speed critically affected design cycle turnaround time for the optimization.

## 5. Optimization Results

In this section, results of the study are first discussed in terms of convergence. Then the weight, aeroelastic trim results, variation of modal frequencies, design variable results, and constraints are considered.

All three configurations started from the same initial design. (See section 3.2.1.) The term “linear design” refers to the final design that was obtained by using linear aerodynamic loads; the term “nonlinear design” refers to the final design that was obtained by using nonlinear aerodynamic loads.

### 5.1 Convergence

Convergence was declared when all constraints were satisfied and when weight changes were minimal. After the designs converged for linear aerodynamic loads, three additional optimization cycles were performed with nonlinear aerodynamic loads. If more optimization cycles had been allowed, significant changes in the OEW would not have been likely.

Table 7 summarizes the number of active or violated constraints and the number of design variables at the upper or lower bounds. The number of active constraints and the number of design variables at the upper or lower bounds can be used as a qualitative assessment of convergence. Recall that in this paper a constraint or design variable bound was considered active if its value was in the range of  $\pm 0.02$ . Table 7a summarizes the number of active constraints and active design variable bounds for each configuration for the initial, linear, and nonlinear designs. Table 7b provides the corresponding information for violated constraints and violated design variable bounds. (As can be seen in table 7b, there are no violated design variable bounds.) The linear design of the Aft-Tail configuration was the most converged, and the linear design of the Three-Surface configuration was the least converged. Remember, however, that these observations are strictly qualitative. In addition, as discussed in section 5.6.3, the formulation of the ply-mixture constraints causes a large number of these constraints to be in the range of  $\pm 0.02$ , which is the range that defines an active constraint. If a ply-mixture constraint is formulated in such a way that it is consistent with formulations for the strain and buckling constraints and if data from the initial, linear, and nonlinear designs are inserted into that formulation, then the result is a much smaller number of active ply-mixture constraints. However, table 7 gives an accurate listing of the number of active constraints, based on the constraint formulations used in this study.

### 5.2 Weight

#### 5.2.1 FEM Weight

The FEM weight includes only the weight governed by the design variables. Figure 25 shows the FEM weight as a function of the cumulative maximum allowable percent “move” of the design variables for all three configurations. The numerals along each curve indicate the beginning of the cycle. The “nl” associated with a numeral refers to the use of trimmed aeroelastic loads with nonlinear corrections. The intermediate symbols indicate iterations within the cycle. For example, in the fourth Aft-Tail design cycle, eight iterations were run. During each iteration, the maximum change in each design variable was 5 percent of the value at the beginning of the cycle. Therefore, design cycle 4 allowed up to a 40-percent change (move) in each design variable.

Each optimization was divided into two parts — a linear loads optimization and a nonlinear loads optimization. First, each configuration was optimized with linear loads until all constraints were either satisfied or active and the weight change was minimal. The Aft-Tail configuration required 5 optimization cycles, the Three-Surface configuration required 7 cycles, and the Canard configuration

required 10 cycles. Then in the second part, only three optimization cycles were performed with nonlinear loads.

Table 8 compares the three configurations on the basis of the FEM weights for the initial, linear, and nonlinear designs. As can be seen in table 8, the effect of using nonlinear aerodynamic loads was modest; a decrease was noted in the weight for all three configurations when compared with the corresponding designs based on linear loads. A comparison of the nonlinear design FEM weights shows the Three-Surface design to be 1.6 percent heavier than the Aft-Tail design and the Canard design to be 6.8 percent heavier than the Aft-Tail design.

**5.2.2 Operational Empty Weight.** Recall from sections 3.3, 4.1.1, and 4.1.2 that the operational empty weight (OEW) is an as-built weight obtained from Boeing's *AM/FM* computer program. Table 9 compares the three configurations on the basis of OEW for the initial, linear, and nonlinear designs. All three designs obtained with linear loads have nearly the same OEW (within approximately 1 percent). The effect of including nonlinear loads is minimal as well.

The changes in OEW can be broken down further into components on the aircraft. (See section 3.3.) These components (i.e., inboard wing, outboard wing, forward body, mid body, and aft body) correspond to meshes 1–5 in figure 11, respectively. The histories of these five components, as well as the total OEW, are plotted in figures 26–28 for the Aft-Tail, Three-Surface, and Canard configurations, respectively. The component weight changes between the linear and initial designs, the nonlinear and linear designs, and the nonlinear and initial designs are summarized in tables 10–12 for the Aft-Tail, Three-Surface, and Canard configurations, respectively. Note that although the total resized component weight does not equal the total OEW weight, the total change in resized component weight is equal to the total change in OEW.

**5.2.2.1 Aft-Tail Configuration.** The resized component weights and the OEW of the Aft-Tail configuration obtained from the *AM/FM* computer program are plotted as a function of cycle number in figure 26. Total and resized component weight differences between the initial, linear, and nonlinear designs are given in table 10. Most of this weight change occurred during optimization with linear loads.

When nonlinear loads were applied to the linear design, constraint violations were noted. The optimizer was able to satisfy the violated constraints in three cycles with little change in OEW (0.1 percent) from that of the linear design. (As shown in table 10, the change in weight was 386 lb; as noted in table 9, the OEW of the linear design was 285,758 lb.) Overall, little change was realized in the resized component weights (less than 2.5 percent). As shown in table 10 and figure 26, the optimizer eliminated weight from the Inboard Wing and added weight to the Aft Body. The weights of the remaining three components changed by less than 1 percent.

During the overall optimization process (denoted Nonlinear—Initial in table 10), most of the weight decrease occurred in the inboard wing, outboard wing, and aft body components; weight increase was noted in the Forward Body component. Very little weight change was noted in the Mid Body component.

**5.2.2.2 Three-Surface Configuration.** The resized component weights and the OEW for the Three-Surface configuration obtained from the *AM/FM* computer program are plotted as a function of cycle in figure 27. For linear loads, the weight change patterns for the Three-Surface configuration are different from those of the Aft-Tail configuration. For the Three-Surface configuration, the weight increased in the

Mid Body component, and the weight decreased in that component for the Aft-Tail configuration. As shown in table 11, approximately half of the total weight change occurred during the optimization with linear loads.

The introduction of nonlinear loads had more effect on the resized component weights for the Three-Surface configuration than for the Aft-Tail configuration. The nonlinear loads caused a weight increase in the Outboard Wing component, and the weight decreased in the Forward Body and Mid Body components. The weights remained the same in the Inboard Wing and Aft Body components.

**5.2.2.3 Canard Configuration.** The resized component weights and the OEW of the Canard configuration obtained from the *AM/FM* computer program are plotted as a function of cycle in figure 28. At the start of optimization with linear loads, the buckling constraints were violated by a much greater amount than in the case of either the Aft-Tail or the Three-Surface configuration, and the optimizer required more cycles (i.e., 10) to satisfy the constraints (see fig. 25) with a slight increase in weight. The changes in the resized component weights followed the same trend as for the Three-Surface and Aft-Tail configurations, although the magnitudes of the percentage changes were much larger. Weight increases were noted in the Forward Body and Mid Body components, and weight decreases were noted in the Aft Body, Outboard Wing, and Inboard Wing components.

In comparing the nonlinear and linear designs, the trends in weight change were similar to those for the other two configurations, although the magnitudes were different. The exception was the Aft Body component, which had a decrease in weight for the nonlinear design. Weight decreases were noted for the Inboard Wing, Aft Body, and Forward Body components. Weight increases were noted for the Outboard Wing component. A small increase was noted in the weight for the Mid Body component.

For the overall optimization, the change in OEW (i.e., a decrease of 0.35 percent) was nearly the same as for the other two configurations. As shown in figure 28 and table 12, the optimizer added weight to the Forward Body and Mid Body components and removed weight from the Inboard Wing, Outboard Wing, and Aft Body components. These trends were the same as those noted for the other two configurations, except for the Mid Body component, which increased significantly in weight. For the other two configurations, the weight for this component decreased slightly.

### 5.3 Aeroelastic Trim Results

The aircraft angles of attack and horizontal control surface deflection angles that resulted from the aeroelastic trim calculations at each load condition are shown for each configuration in tables 13-15. Each table presents results for three points in the design: the initial design with linear aerodynamic loads and no nonlinear corrections, the end of linear design both with and without nonlinear corrections, and the end of nonlinear design. The angles are those for which the following two conditions were satisfied: the total configuration lift equaled the weight times the load factor, and the total pitching moment was zero. For the Three-Surface configuration, the additional condition was imposed that the normal force for the canard had to be equal and opposite to the normal force for the tail.

The horizontal control surface deflection angles were measured relative to the aircraft; therefore, the horizontal control surface angles of attack could be obtained by adding the aircraft angles of attack to the horizontal control surface angles of attack. Large horizontal control surface angles of attack (well above 20°) were needed in order to trim several of the load conditions for which  $M = 0.5$ . The horizontal control surface would be stalled at these conditions and could not provide sufficient control moment; therefore, a

change to the wing leading-edge flap deflections would be needed in order to trim the aircraft. Furthermore, it is unlikely that the aircraft would be able to achieve a negative 1-g condition with such large leading-edge flap deflections (table 2). The leading-edge flap deflections would need to be reduced considerably.

#### 5.4 Variation of Modal Frequencies

The frequencies of the first four modes at the beginning of each design cycle are shown in figure 29 for each configuration for mass case 1. Mode 1 was primarily free-free fuselage bending. For each configuration, the initial value of mode 1 was near 1.5 Hz, and the final value was somewhat higher. Changes during a design cycle were on the order of a few tenths of 1 Hz. The frequencies for the Aft-Tail and Three-Surface configurations were nearly the same and were slightly higher at the end of the design than at the beginning. However, the final value of the first modal frequency for the Canard configuration was significantly higher than the value of the first modal frequency for the other two configurations. This increase resulted from the strengthening of the forward fuselage between the wing and canard that was necessary to carry the canard loads for trim. The other modes displayed similar but smaller frequency increases.

The results shown are for the OEW case (mass case 1). Similar but smaller changes in frequency were obtained for the other mass cases. Plots for each of the five mass cases and for the first 30 elastic modes, which generally include all vibration modes with frequencies below 20 Hz, are available on the CD-ROM attached to this report.

#### 5.5 Design Variable Results

As described in detail in section 4.2.2, the wing and fuselage structure that was sized consisted of sandwich panels with filamentary composite face sheets. The panels were on the surface of the wing and fuselage. The sized structure was divided into design variable zones (fig. 15) in which the design variables were uniform. Four design variables were used in each design variable zone. The design variables were the total thickness of the 0° plies in one face, the total thickness of the 90° plies in one face, the total thickness of the +45° plies in one face, and the honeycomb core thickness (fig. 23). Four design variables in each of 61 design variable zones yielded a total of 244 design variables per configuration.

This section of the report presents the values of the design variables for the initial design, the design obtained with linear loads, and the design obtained with nonlinear loads for each configuration. The discussion includes comparisons that demonstrate how the designs for the Three-Surface and Canard configurations differ from the designs for the Aft-Tail configuration. The upper and lower bounds placed on the design variables and on the regions in which the bounds are active are also discussed. These bounds are the absolute bounds (i.e., not the temporary move limits).

**5.5.1 Design Variable Values.** The values of the design variables for the initial design, the designs obtained with linear loads, and the designs obtained with nonlinear loads are presented in tables 16-18. The design variable values are given for each of 61 design variable zones. The zones are shown in figure 15.

Values of the design variables for the designs obtained with nonlinear loads are indicated graphically in figures 30-31. Instead of showing the thickness of composite material at each ply orientation, the total ply thickness is shown in figure 30. The total ply thickness  $t_{ply}$  is the thickness of two face sheets of a sandwich panel and is given by

$$t_{ply} = 2(t_0 + t_{90} + 2t_{45}) \quad (16)$$

where  $t_0$  is the thickness of the  $0^\circ$  plies in one face sheet,  $t_{90}$  is the thickness of the  $90^\circ$  plies in one face sheet, and  $t_{45}$  is the thickness of the  $+45^\circ$  plies in one face sheet. The honeycomb core thickness is shown in figure 31. Colors are used to indicate the numerical values.

**5.5.1.1 Comparisons Between Designs for Three-Surface and Aft-Tail Configurations.** Differences between designs are shown first in terms of total ply thickness (fig. 32) and then in terms of core thickness (fig. 33). The differences are obtained by subtracting the values for the Aft-Tail configuration from the values for the Three-Surface configuration. Note that the differences can be positive or negative. The differences are then displayed on the Three-Surface configuration. In figures 32-33, the largest positive difference is denoted “Max”; the largest negative difference is denoted “Min.” Designs obtained with linear loads (denoted linear designs) are compared first, then those obtained with nonlinear loads (denoted nonlinear designs) are compared; differences are shown in inches.

The differences in the total ply thickness between the Three-Surface and the Aft-Tail linear designs are shown in figure 32(a). Little difference was noted between the two designs. As shown in figure 32(b), the difference was larger for the nonlinear designs than for the linear designs. Little difference was noted on the fuselage. The difference was greater on the wing, particularly on the upper surface of the wing box.

The differences in core thickness between the Three-Surface and Aft-Tail linear designs are shown in figure 33(a). The largest positive difference occurred on the lower fuselage at the center of the aircraft. Large positive differences also occurred along the wing box and on the fuselage at the canard. The largest negative differences occurred on the fuselage between the trailing edge of the wing and the horizontal tail.

The differences in core thickness between the Three-Surface and the Aft-Tail nonlinear designs are shown in figure 33(b). The differences are similar to, but less than, the differences that were obtained for the linear designs.

**5.5.1.2 Comparisons Between Designs for Canard and Aft-Tail Configurations.** Differences between designs for the Canard and Aft-Tail configurations are shown first in terms of total ply thickness (fig. 34) and then in terms of core thickness (fig. 35). The differences are obtained by subtracting the values for the Aft-Tail configuration from the values for the Canard configuration. Note that the differences can be positive or negative. The differences are then displayed on the Canard configuration. In figures 34-35, the largest positive difference is denoted “Max”; the largest negative difference is denoted “Min.” Designs obtained with linear loads (denoted linear designs) are compared first, then those obtained with nonlinear loads (denoted nonlinear designs) are compared; differences are shown in inches.

The differences in total ply thickness between the Canard and the Aft-Tail linear designs are shown in figure 34(a). The largest positive difference was on the fuselage in the area of the wing box, indicated by the red color in figure 34(a). The largest negative difference occurred at the horizontal tail attachment position, along the upper wing box, and in the lower inboard wing box.

The differences in total ply thickness between the Canard and the Aft-Tail nonlinear designs are shown in figure 34(b). The differences were similar to those seen for linear loads (fig. 34(a)), except in the vicinity of the upper, outer wing box.

The differences in the core thickness between the Canard and Aft-Tail linear designs are shown in figure 35(a). There were positive differences in the forward fuselage (indicated by the red color), and there were negative differences in the aft fuselage (indicated by the blue color).

The differences in core thickness between the Canard and Aft-Tail nonlinear designs are shown in figure 35(b). The differences were similar to those obtained for the linear designs.

**5.5.2 Design Variable Bounds.** During aeroelastic sizing, practical limits (called design variable bounds) were placed on the values of the design variables. The upper and lower bounds on the design variables are given in table 19. The regions on the aircraft where these bounds are active are discussed here. These regions are designated in the same manner as in figure 11. Only the nonlinear designs are discussed in this report. The CD-ROM supplement contains complete information for all three configurations for both linear and nonlinear designs.

**5.5.2.1 Fuselage.** The ply thickness design variables were not at upper bounds in any region on the fuselage. The sandwich panels on the sides of the fuselage have relatively thin face sheets; many of the ply thickness design variables are at or near their lower bounds. These face sheets are thin because symmetric loads were used in the optimization. For all configurations, the  $90^\circ$  plies, which are in the circumferential direction, and the  $+45^\circ$  plies are at or near their lower bounds, except in the mid-fuselage region. For the Aft-Tail and Three-Surface configurations, the  $0^\circ$  plies are at their lower bounds on the sides of the forward and aft fuselage. For the Canard configuration, the  $0^\circ$  plies are at their lower bounds only on the side of the aft fuselage.

No regions exist on the fuselage where the core thickness design variables are at the upper bounds. For the Canard configuration, the core thickness is at a lower bound just ahead of the canard. For the Three-Surface configuration, the core thickness is at a lower bound just ahead of and behind the canard. For the Aft-Tail configuration, the core thickness is at a lower bound over most of the forward fuselage and for a portion of the mid fuselage.

**5.5.2.2 Wing.** No ply thickness design variable is at a lower bound for (1) the wing box of any configuration and (2) the lower surface of the wing for the Canard configuration. The Three-Surface configuration is the only configuration for which the ply thickness design variables are at their upper bounds. The locations and ply orientations for these upper bounds are as follows: for the upper surface outboard wing box,  $90^\circ$  plies; for the upper surface inboard wing box at the wing break,  $0^\circ$  and  $+45^\circ$  plies. For all configurations, several regions exist on the inboard wing where a ply thickness design variable is at a lower bound; of these, more regions exist for which the  $90^\circ$  plies are at a lower bound than for which the  $0^\circ$  or  $+45^\circ$  plies are at a lower bound. (See the CD-ROM supplement for illustration.)

The core thickness does not reach an upper bound in any region on the wing. The core is at a lower bound only on the lower surface of the wing for the Aft-Tail and Three-Surface configurations. For the Aft-Tail configuration, the wing tip and wing box at the wing break are at a lower bound. For the Three-Surface configuration, the wing tip is at a lower bound.

## 5.6 Constraints

This section describes the active constraints and describes the location of these constraints on the three configurations. Note that there are the four types of constraints—strain, buckling, ply-mixture, and flutter. A cumulative constraint approach (the KS constraint function) was used to reduce the number of constraints. As explained earlier, each configuration had a total of 494 constraints—96 KS strain constraints, 96 KS buckling constraints, 244 ply-mixture constraints, and 70 KS flutter constraints.

The linear designs for the Aft-Tail, Three-Surface, and Canard configurations were the designs obtained at the end of design cycles 5, 7, and 10, respectively. At the beginning of the next design cycle for each configuration (cycles 6, 8, and 11, respectively), these three designs were analyzed by using newly calculated linear airloads and as-built weights. The results of these analyses are presented in the sections of this report that deal with strain, buckling, and flutter constraints for linear designs.

Likewise, the nonlinear designs for the Aft-Tail, Three-Surface, and Canard configurations were the designs obtained at the end of design cycles 8, 10, and 13, respectively. These design cycles were followed by an additional analysis with newly calculated airloads (with nonlinear corrections) and as-built weights. The final analyses are denoted 9nl, 11nl, and 14nl, respectively, in figure 25. The results of these analyses are presented in the sections of this report that deal with strain, buckling, and flutter constraints for nonlinear designs.

Constraint histories are given in figure 36 for the Aft-Tail configuration, figure 37 for the Three-Surface configuration, and figure 38 for the Canard configuration. Table 7 summarizes the constraint status for the initial, linear, and nonlinear designs for all three configurations. The results show that strain, buckling, and flutter constraints were violated for the initial design.

One can get a qualitative sense of the degree of convergence in this optimization problem. In the absence of redundant constraints, the maximum of number of active constraint in a nonlinear programming problem is less than or equal to the number of design variables. So, given a feasible design, if the number of active constraints is high relative to the number of design variables, one can infer that the design is fairly well converged (note that the opposite is NOT true, if the number of active constraints is low relative to the number of design variables, the design might or might not be converged).

In the LCAP study, for the three feasible final designs with linear loads for the Aft-Tail, Three-Surface, and Canard configurations, the number of active constraints are respectively 118, 85, and 93 percent of the number of design variables, a sign that optimization has progressed fairly well in all three designs, and to comparable degrees of convergence. (The fact that some designs exceed 100 percent active constraints is due to the fact that we do not use a strict criterion to identify active constraints ( $g=0$ ), but a somewhat relaxed one ( $-0.02 \leq g \leq 0.02$ )). After introduction of the nonlinear loads and re-optimization, the numbers of active constraints are 105, 118, and 107 percent for the Aft-Tail, Three-Surface, and Canard configurations, respectively, indicating a similar degree of convergence. (See table 7)

**5.6.1 Strain Constraints.** Information regarding the strain constraints is presented in figures 39–44. Figures 39–41 show the results for the linear designs for each configuration. Figures 42–44 show the results for the nonlinear designs.

Each figure is divided into two parts. In the (a) portion of each figure, the colors indicate the values of the strain constraints in each design variable zone. Recall that a design variable zone can contain both

quadrilateral and triangular finite elements. Recall also that during the optimization the KS constraint functions for the quadrilateral and triangular finite elements were formulated separately (This is done for each load case). To reduce the number of figures, the results are shown together. In the (a) figures, each design variable zone was assigned a color based on the maximum of the KS constraint for the quadrilateral elements and the triangular elements within that design variable zone. In other words, in the optimization the strain constraints for the quadrilateral and triangular elements were separate; in the figures, the strain constraints for the quadrilateral and triangular elements were compared, and the larger number is shown. Red indicates that a constraint was violated. An orange color indicates that the constraint was active (within  $\pm 2$  percent). Yellow, green, and blue colors mean that the constraint was satisfied.

In the (b) portion of each figure, the design variable zones were color coded by the load case that produced the largest KS constraint function for that zone. The load cases are defined in tables 1-3. As shown in the figures, 7 load cases were used to design the Aft-Tail configuration and 11 load cases were used for the other two configurations.

**5.6.1.1 Strain Constraints for Linear Designs.** As shown in figures 39(a)-41(a), relatively few strain constraints were active (orange). For the Aft-Tail configuration (figure 39(a)), the areas that had an active strain constraint were the outer section of the inboard wing, the inner section of the outboard wing, and the upper and lower fuselage sections aft of the trailing edge of the wing. The results for the Three-Surface (fig. 40(a)) and Canard (fig. 41(a)) configurations were similar to those for the Aft-Tail configuration, except for the sections of the fuselage aft of the wing trailing edge. In that area, the Three-Surface configuration had only a small region in which the strain constraint was near active (indicated by the yellow color on the fuselage crown in fig. 40(a)). For the Canard configuration, the strain constraint in that area was well satisfied (indicated by the blue color on the fuselage crown in fig. 41(a)). Figures 39(b)-41(b) show which of the load cases produced the largest strain constraints for the Aft-Tail, Three-Surface, and Canard configurations, respectively. For example, as shown in figure 39(b) for the Aft-Tail configuration, load case LX55 produced the active strain constraint on that portion of the wing box just inboard of the wing break. At the same location, for the Three-Surface configuration (fig. 40(b)), load case LZ2X produced the active strain constraints, while for the Canard configuration (fig. 41(b)), load case LY25 produced the active strain constraints. Note that the load cases that produced the largest values of the strain constraint for the Three-Surface and Canard configurations were not considered during the linear design of the Aft-Tail configuration.

**5.6.1.2 Strain Constraints for Nonlinear Designs.** The effect of introducing nonlinear loads can be seen by comparing the color plots of the strain constraints shown in figures 42(a)-44(a) with the corresponding plots in figures 39(a)-41(a). For the Aft-Tail configuration (fig. 42(a)), the number of regions with active strain constraints was reduced substantially (compare with fig. 39(a)). The only region with active strain constraints on the nonlinear design was the upper inboard wing box at the wing break. For the Three-Surface configuration (fig. 43(a)), the trend was reversed: the number of regions with active or nearly active strain constraints increased substantially (compare with fig. 40(a)). The trend was the same for the Canard configuration (fig. 44(a)) as for the Three-Surface configuration: the addition of nonlinear loads increased the number of the regions with active strain constraints substantially (compare with fig. 41(a)). The nonlinear design for the Canard configuration (fig. 44(a)) had more regions with active strain constraints than did the nonlinear designs for the remaining two configurations (figs. 42(a) and 43(a)).

The load cases that produced the largest strain constraints for the nonlinear designs are shown in figures 42(b)-44(b). For all three configurations, load case L#43 produced the largest strain constraints in the wing box. In addition, for the Aft-Tail and Three-Surface configurations, load case L#55 produced the largest strain constraints on the fuselage at the horizontal tail. Note that load cases L#43 and L#55 were considered in the design of all three configurations.

**5.6.2 Buckling Constraints.** The discussion in the introduction to section 5.6 applies to buckling constraints as well as to strain constraints. Furthermore, the approach used to present the buckling constraint results is the same that used in section 5.6.1 for strain constraints.

**5.6.2.1 Buckling Constraints for Linear Designs.** The buckling constraints for the linear designs are presented in figures 45-47. Figures 45(a), 46(a), and 47(a) indicate the values of the buckling constraints for the Aft-Tail, Three-Surface, and Canard configurations, respectively. As shown in figures 45(a)-47(a), large areas of all three aircraft had buckling constraints that were active or near active. For the Aft-Tail configuration, buckling was an active constraint for nearly the entire aircraft. For the Three-Surface configuration, the pattern was similar, except that buckling constraints were not active on the inboard wing box. For the Canard configuration, buckling constraints were active on the upper inboard wing, the outer wing, and the central fuselage.

Figures 45(b)-47(b) show those load cases that produced the largest buckling constraints. As indicated by the variety of colors, a large number of load cases produced active buckling constraints. The taxi load cases (LX03, LZ03, and LY03) produced the largest buckling constraint in the areas ahead of the main wheel well and around the nose wheel. The largest buckling constraint was produced by load case LX55 over a substantial portion of the Aft-Tail configuration. Patterns of load case activity were similar for all three configurations. Several load cases that produced the largest buckling constraint values for the Three-Surface and Canard configurations were not considered during the linear design of the Aft-Tail configuration.

**5.6.2.2 Buckling Constraints for Nonlinear Designs.** The effect of introducing nonlinear loads can be seen by comparing the color plots of the buckling constraint shown in figures 48(a)-50(a) with the corresponding plots in figures 45(a)-47(a). For the Aft-Tail configuration (fig. 48(a)), the number of regions with active buckling constraints was reduced slightly (compare with fig. 45(a)). Still, buckling constraints were active on nearly the entire aircraft. For the Three-Surface configuration (fig. 49(a)), the number of regions that had active buckling constraints increased substantially (compare with fig. 46(a)). In addition, one buckling constraint was violated on the upper crown of the aft fuselage, as indicated by the red color in the figure. This 5.5-percent violation occurred when the final trimmed aeroelastic loads were calculated and the final analysis was performed. This violation was not expected and occurred only for this design. For the Canard configuration (fig. 50(a)), the number of regions with active buckling constraints increased substantially (compare with fig. 47(a)).

As in the case of the linear designs, a large number of load cases produced active buckling constraints for the nonlinear designs. (See figs. 48(b)-50(b).) Load case L#43 was more active for the nonlinear designs than for linear designs. In some regions, load case L#26 produced the largest buckling constraint for the Three-Surface and Canard configurations; that load case was not considered for the nonlinear design of the Aft-Tail configuration.

**5.6.3 Ply-Mixture Constraints.** Ply-mixture constraints were introduced to ensure proper distribution of plies in the various layers (section 4.2.3.4). They made up a large portion of the active constraints for intermediate and final designs, this was an artifact of the constraint’s algebraic formulation. For example, consider the ply-mixture constraint for the 0° plies, it states that those plies must make up at least 10 percent of the laminates

$$g = \left[ \frac{0.1}{1 - 0.1} \right] (t_{90} + 2t_{45}) - t_0 \leq 0 \quad (12)$$

Given typical values for the variables in the problem, the constraint value was often within the bounds marking active constraints ( $-0.02 \leq g \leq 0.02$ ). As a result, using equation 12 for the ply-mixture constraint many have caused premature convergence.

If, instead, that ply-mixture constraint had been formulated slightly differently

$$g = 1 - \frac{t_0}{0.1(t_0 + t_{90} + 2t_{45})} \leq 0 \quad (17)$$

the same problem would not have occurred and the designs might have progressed further and shown lower weight and more stress, buckling or flutter constraints active. For example, the values of the 0° ply-mixture constraint as defined in equations (12) and (17) are given in figures 51 and 52, respectively, for the nonlinear design of the Aft-Tail configuration. A significant difference between the two figures is evident. In figure 51, the constraint is active or near active for the entire aircraft. In figure 52, the constraint is active for only a small portion of the aircraft.

In this study, all ply-mixture constraints were defined similar to equation (12) rather than equation (17). Therefore, a count of the number of active (within  $\pm 0.02$ ) ply-mixture constraints probably overstates the importance of ply-mixture requirements as drivers in the designs.

**5.6.4 Flutter Constraints.** The initial designs for all three configurations had violated flutter constraints. Table 20 summarizes these violated flutter constraints. At the end of optimization, no flutter constraints were violated for any configuration. Table 21 summarizes the active flutter constraints for all three configurations for the initial, linear, and nonlinear designs.

Sample flutter results for each configuration, for mass cases 1 and 5, and for no damping are shown in figures 53-61. Similar results are available on the CD-ROM supplement for all mass cases. The figures give flutter conditions in the space defined by Mach number ( $M$ ) and equivalent airspeed  $V_{eq}$ , where constant altitude curves are straight lines that radiate from the origin. The  $V_D$  envelope is also shown. Flutter points with zero damping should be outside (above) the  $V_D$  envelope. Vertical lines indicate the Mach numbers at which flutter was calculated; each dot represents a flutter condition, and the corresponding flutter frequency is given, if available. When clearly identifiable, flutter boundaries are drawn.

Although the number of active flutter constraints was small compared with the total number of constraints, the flutter constraints were significant drivers in the optimization. Because of nonlinearities and discontinuities, the flutter constraints were the most unpredictable constraints used in this optimization.

**5.6.4.1 Aft-Tail Configuration.** Flutter results for zero damping for the initial design of the Aft-Tail configuration are shown for mass cases 1 and 5 in figure 53. Significant violations of the flutter envelope are apparent for each mass case. For the OEW (mass case 1), shown in figure 53(a), the hatched region is a hump mode with a frequency near 4 Hz that involves fuselage and engine motions and is particularly prominent at supersonic speeds. These regions change significantly with mass configuration, and only a low supersonic region of violation is apparent for mass case 5 (fig. 53(b)). Considerable interpolation or interpretation was made in the transonic speed range. These results might be modified if nonlinear aerodynamics methods were used in the flutter analysis.

Boundaries for the Aft-Tail configuration at the end of the linear design with zero damping are shown in figure 54 for mass cases 1 and 5. This configuration was essentially flutter-free within the operating envelopes, as required. For mass case 1 (fig. 54(a)), the boundary was outside the envelope, but for mass case 5 (fig. 54(b)) flutter was critical (and may even have had slight violations between Mach 1.2 and Mach 1.5). In this case, the aeroelastic sizing yielded flutter boundaries that were essentially tangent to the required envelopes, with no additional margin.

Boundaries for the end of the nonlinear design with zero damping are shown in figure 55 for mass cases 1 and 5. The results are similar to those for the linear design. Because these results started from the linear design, some of the mass cases were already close to the operating envelope, and difficulties with flutter constraint violations were frequently encountered during subsequent design cycles with nonlinear loads.

**5.6.4.2 Three-Surface Configuration.** Flutter results for zero damping for the initial design of the Three-Surface configuration are shown in figure 56 for mass cases 1 and 5. Qualitatively, the results are similar to those of the Aft-Tail configuration. The boundaries for zero damping for mass cases 1 and 5 for the linear design are shown in figure 57. Sample results for the nonlinear design with zero damping are also shown in figure 58. An isolated region of flutter near the operating envelope was evident for mass case 5 (fig. 58(b)).

**5.6.4.3 Canard Configuration.** Flutter results for the initial design of the Canard configuration with zero damping are shown for mass cases 1 and 5 in figure 59. Qualitatively, the results are similar to those of the other configurations. The boundaries for the linear design for zero damping are shown in figure 60. Sample results for the nonlinear design for zero damping are shown in figure 61. Again, an isolated region of flutter near the operating envelope was evident for mass case 5 (fig. 61(b)).

## **6. Concluding Remarks**

The Longitudinal Control Alternatives Project (LCAP) was conducted to compare Aft-Tail, Three-Surface, and Canard alternatives for a high-speed civil transport configuration on the basis of operational empty weight (OEW) and longitudinal control characteristics. The Aft-Tail configuration was an early baseline model for Boeing's high-speed civil transport work, and the other two configurations were simple modifications of the Aft-Tail layout. This report describes the methods used and the results generated for the aeroelastic sizing of each of the three configurations.

Each configuration was sized for minimum structural weight under linear and nonlinear aeroelastic loads. Several symmetric load cases were considered, in addition to one taxi condition. Constraints used in the optimization included strain, buckling, subsonic flutter, and supersonic flutter. In addition, for the

composite face sheets of the sandwich panels that were being sized, practical constraints were placed on the ratios of ply thickness to total laminate thickness for each ply orientation.

Sizing under linear aerodynamic loads required 5–10 design cycles for each configuration, yielding in designs that differed by, at most, 9 percent in sized theoretical finite-element weight and 1 percent in OEW. Three additional design cycles under nonlinear aerodynamic loads yielded slightly (less than 0.5-percent OEW) reduced weights and caused some redistribution of material. Most load cases were active at least once for each configuration, including those that were used for the Three-Surface and Canard configurations but not for the Aft-Tail configuration.

Many (up to 55 percent) of the buckling constraints were active; these active constraints affected most of the resized areas. Relatively few (less than 10 percent) of the strain constraints were active and affected mostly areas along the wing box, carry through, and, occasionally, areas of the fuselage aft of the wing or around the horizontal tail support. A few (up to 6) flutter constraints were generally active for each design; these included both subsonic and supersonic conditions.

With differences in OEW of less than 1 percent for the three configurations, none had a significant advantage. However, distinct differences were noted in the structural stiffness distributions in the fuselage of the three configurations because of the changing locations of the control surfaces. Because weight did not appear to be a discriminating factor, the longitudinal control and ride quality characteristics of each configuration should be examined as a possible basis for comparison. These factors were evaluated in the LCAP study but are not discussed in this report. Also, differences between the three configurations may have been more pronounced if adjustments to the overall configurations, such as shifts in wing location, were allowed.

## References

1. ELFINI Base User Guide, Version 6.4, Avions Marcel Dassault-Bréguet Aviation, June, 1990.
2. Lahey, R. S.; Miller, M. P.; and Reymond, M.: MSC/NASTRAN Reference Manual, Version 68, The MacNeal-Schwendler Corporation, 1994.
3. Whetstone, W. D.: EISI-EAL Engineering Analysis Reference Manual. Engineering Information Systems, Inc. July 1983.
4. Mitchell, Patrick M.: Advanced Finite Element Weight Estimation Process on the High Speed Civil Transport. SAWE Paper No. 2169, 52nd Annual Conference of the Society of Allied Weight Engineers, Inc., Biloxi, MS, May 24-25, 1993.
5. "ELFINI Finite-Element Model of HSCT 1080-892STR "E" Configuration - Model, Loads, Sizing, Optimization, Flutter, Weights, and Gust", Structures B-Y87B-JW-C93-069, September 29, 1993.
6. Woodward, F.A., "An Improved Method for the Aerodynamic Analysis of Wing-Body-Tail Configurations in Subsonic and Supersonic Flow, Part I - Theory and Application", NASA CR-2228, Part I, May 1973.
7. Woodward, F.A., "USSAERO Computer Program Development, Versions B and C", NASA CR-3228, April 1980.
8. Craidon, Charlotte B., "User's Guide for a Computer Program for Calculating the Zero-Lift Wave Drag of Complex Aircraft Configurations", NASA TM-85670, 1983.
9. ICEM Introduction and System Controls Reference," Control Data Publication No. 60000201, Revision C, August, 1991
10. Pirzadeh, S., "Viscous Unstructured Three-Dimensional Grids by the Advancing-Layers Method," AIAA 94-0417, 1994.
11. Frink, N.T., Parikh, P., and Pirzadeh, S., "A Fast Upwind Solver for the Euler Equations on Three-Dimensional Unstructured Meshes", AIAA 91-0102, Jan. 1991.
12. Frink, N.T., "Recent Progress Toward a Three-Dimensional Unstructured Navier-Stokes Flow Solver", AIAA 94-0061, January 1994.
13. Frink, N.T., Parikh, P., and Pirzadeh, S., "Aerodynamic Analysis of Complex Configurations using Unstructured Grids", AIAA 91-3292, September 1991.
14. Bhatia, K. G.; and Wertheimer, J.: Aeroelastic Challenges for a High Speed Civil Transport. 34th AIAA/ASME/ASCE/AHS/ASC Structures, Structural Dynamics, and Materials Conference, La Jolla, CA. AIAA Paper 93-1478. April 1993.

15. Adams, William M., Jr.; and Hoadley, Sherwood T.: "ISAC: A Tool for Aeroservoelastic Modeling and Analysis." NASA TM 109031, Dec. 1993.
16. Liu, D. D.; James, D. K.; Chen, P. C.; and Pototzky, A. S.: "Further Studies of Harmonic Gradient Method for Supersonic Aeroelastic Applications." *Journal of Aircraft*, vol. 28, no. 9, pp 598-605, Sept. 1991.
17. Jespersen, D., Pulliam, T., Buning, P., "Recent Enhancements to OVERFLOW", AIAA-97-0644, 35th Aerospace Sciences Meeting, Reno, NV, January 1997.
18. Jones, R. M.: *Mechanics of Composite Materials*, McGraw-Hill Book Co., New York, pp. 45-57, 1975.
19. Haftka, Raphael T.; and Gurdal, Zafer: *Elements of Structural Optimization*. Kluwer Academic Publ., 1992.
20. Stroud, W. Jefferson; and Agranoff, Nancy: *Minimum-Mass Design of Filamentary Composite Panels Under Combined Loads: Design Procedure Based on Simplified Buckling Equations*, NASA TN D-8257, 1976, Table III.
21. Kresselmeier, G; and Steinhauser, R.: *Systematic Control Design by Optimizing a Vector Performance Index*. *Computer Aided Design on Control Systems*, W. A. Cuenod, ed., Pergamon Press, 1980, pp. 113-117.
22. Martin, Carl.: *Documentation for a Structural Optimization Procedure Developed Using the Engineering analysis Language (EAL)*. NASA CR 201632, October 1996.
23. Camarda, C. J. and Adelman, H. M.: *Static and Dynamic Structural-Sensitivity Derivatives Calculations in the Finite-Element-Based Engineering Analysis Language (EAL) System*. NASA TM 85743, March 1984.
24. Zeiler, Thomas A.: "Aeroservoelasticity in HiSAIR." 4th AIAA/USAF/NASA/OAI Symposium on Multidisciplinary Analysis and Optimization, AIAA Paper 92-4719, Cleveland, OH. September 21-23, 1992.
25. Murtagh, Bruce A. and Saunder, Michael A.: *MINOS 5.4 User's Guide (preliminary)*. Technical Report SOL 83-20R, Systems Optimization Laboratory, Stanford University, Stanford, CA, 1983 (revised 1993).

Table 1. Mass Cases

Mass Case	Description
@M01	Operational empty weight (OEW)
@M02	Maximum zero-fuel weight + aft tank fueled to aft cg limit
@M03	Medium weight, aft cg limit
@M04	Maximum take-off gross weight, aft cg limit
@M05	Maximum take-off gross weight, forward cg limit

Note that @ = 1 for Aft-Tail configuration, @ = 2 for Canard configuration, and @ = 3 for Three-Surface configuration.

Table 2. Load Conditions and Flap Deflections

Condition ID	$V_E$ ID	Load factor (g's limit)	$V_E$ (KEAS)	MACH number	Altitude ( $10^3$ ft)	Wing flap deflections, deg			
						Outboard		Inboard	
						L.E.	T.E.	L.E.	T.E.
L#79	Cruise	1.0	413.0	2.40	60.9	0	0	0	0
L#42	$V_C$	□1.0	350.0	0.95	29.0	10	3	0	0
L#43	$V_D$	2.5	419.4	0.95	20.7	10	3	0	0
L#45	+HAA	2.5	286.9	0.95	37.5	10	3	0	0
L#52	$V_C$	□1.0	389.3	1.20	34.5	10	0	0	0
L#55	+HAA	2.5	337.1	1.20	40.5	10	0	0	0
L#56	□HAA	□1.0	255.7	1.20	52.0	10	0	0	0
L&25	+HAA	2.5	253.3	0.50	14.0	25	7	25	7
L&26	□HAA	□1.0	192.5	0.50	27.0	38	13	38	13
L&2X	+HAA	2.5	253.3	0.50	14.0	28	4	28	4
L&2Y	□HAA	□1.0	192.6	0.50	27.0	42	8	42	8
L#03	Taxi	1.5	□	□	□	□	□	□	□

Note that # = X for Aft-Tail, Y for Canard, or Z for Three-Surface configuration, and & = Y for Canard, or Z for Three-Surface configuration,

$V_E$  = equivalent airspeed,  $V_C$  = cruise speed,  $V_D$  = dive speed, HAA = high angle of attack, KEAS = knots equivalent airspeed, L.E. = leading edge, and T.E. = trailing edge.

Table 3. Load Conditions and Corresponding Mass Cases

Condition ID	Configuration mass case	
	Aft-Tail	Three-Surface/Canard
L#79	1M03	@M03
L#42	1M05	@M04
L#43	1M05	@M04
L#45	1M05	@M04
L#52	1M05	@M04
L#55	1M05	@M04
L#56	1M05	@M04
L#25	Not used	@M04
L#26	Not used	@M04
L#2X	Not used	@M05
L#2Y	Not used	@M05
L#03	1M05	@M04

Note that @ = 2 for Canard or = 3 for Three-Surface configuration and # = X for Aft-Tail, Y for Canard, or Z for Three-Surface configuration.

Table 4. Planform Areas (ft<sup>2</sup>)

Configuration	Horizontal tail	Canard
Aft-Tail	700	□
Three-Surface	350	300
Canard	□	600

Table 5. Material Properties and Allowables

Composite face sheets properties (Ply makeup is of high-modulus carbon fibers in toughened Bismaleimide resin matrix)	
Young's modulus in fiber direction	$E_{11} = 36.2 \square 10^6$ psi
Young's modulus in transverse direction	$E_{22} = 1.4 \square 10^6$ psi
Shear modulus	$G_{12} = 0.66 \square 10^6$ psi
Poisson's ratio	$\square_{12} = 0.38$
Density	$\square = 0.057$ lb/in <sup>3</sup>
Strain allowables (Applied to strains in the fiber direction, transverse to fiber direction, and in shear direction of each layer of composite face sheets)	
Tension	0.008
Compression	0.006
Shear	0.012
Honeycomb sandwich core properties (Titanium hexagonal-cell material)	
Density	$\square = 3.6$ lb/ft <sup>3</sup>

Table 6. Representative Timings

Process	Turnaround time			Comments	Computer type
	Aft-Tail	Three-Surface	Canard		
Weight	3 hr	3 hr	3 hr	Largely automated	Majority of time spent on Cray® 2 <sup>1</sup> at Boeing
Assemble mass cases and calculate cg's	1 hr	1 hr	1 hr	Manual process	DEC™ Alpha™ 3000 <sup>2</sup>
Dynamics	5 hr	5 hr	5 hr	Automated	DEC™ Alpha™ 3000
Flutter	3 days	3 days	3 days	Largely automated, includes 1 day to manually select flutter crossings	Sun® Sparc 20 <sup>3</sup>
Flutter sensitivity	12 hr	12 hr	12 hr	Largely automated	DEC™ Alpha™ 3000
Trimmed airloads	7-8 hr	20-30 hr	20 hr	Largely automated	IBM® SP2 <sup>4</sup> and DEC™ Alpha™ 3000
Assemble loads cases	1 hr	1 hr	1 hr	Manual process	DEC™ Alpha™ 3000
Iteration loop*	4.25 hr per iteration	6.5 hr per iteration	6.5 hr per iteration	Largely automated	DEC™ Alpha™ 3000
Total, 1 cycle	7 days				

\*Typical cycle required 8-10 iterations.

<sup>1</sup>Cray is a registered trademark of Cray Research, Inc.

<sup>2</sup>DEC and Alpha are trademarks of Digital Equipment Corp.

<sup>3</sup>Sun is a registered trademark of Sun Microsystems, Inc.

<sup>4</sup>IBM and SP2 are registered trademarks of International Business Machines Corporation.

Table 7a. Active Constraints and Design Variable Bounds

Constraint type			Aft-Tail			Three-Surface			Canard		
			Initial	Linear	Nonlinear	Initial	Linear	Nonlinear	Initial	Linear	Nonlinear
Strain		Subtotal	5/96	12/96	1/96	1/96	1/96	7/96	1/96	5/96	10/96
Buckling		Subtotal	0/96	54/96	40/96	0/96	20/96	48/96	0/96	36/96	44/96
Ply mix	$0^0 \geq 0.1$		55/61	45/61	42/61	55/61	45/61	50/61	55/61	36/61	44/61
	$90^0 \geq 0.1$		47/61	48/61	47/61	47/61	47/61	47/61	47/61	47/61	48/61
	$+45^0 \geq 0.4$		56/61	50/61	50/61	56/61	53/61	55/61	56/61	48/61	51/61
	$+45^0 \leq 0.6$		45/61	33/61	31/61	45/61	34/61	35/61	45/61	31/61	34/61
	Subtotal		203/244	176/244	170/244	202/244	179/244	187/244	203/244	162/244	177/244
Flutter	Subsonic zero damping		0/15	0/15	0/15	1/15	0/15	0/15	0/15	0/15	0/15
	Subsonic 3-percent damping		0/15	2/15	0/15	2/15	1/15	0/15	0/15	2/15	0/15
	Supersonic zero damping		2/25*	2/20	2/20	1/20	3/20	0/20	1/20	2/20	1/20
	Supersonic 3-percent damping		0/25*	2/20	1/20	0/20	0/20	0/20	0/20	0/15	0/20
	Subtotal		2/80*	6/70	3/70	4/70	4/70	0/70	1/70	4/70	1/70
DV bound	Lower		0/244	44/244	43/244	0/244	4/244	44/244	0/244	22/244	29/244
	Upper		0/244	0/244	0/244	0/244	0/244	3/244	0/244	0/244	0/244
	Subtotal		0/488	44/488	43/488	0/488	4/488	47/488	0/488	22/488	29/488
All		Total	210/1004*	292/994	257/994	207/994	207/994	286/994	203/994	228/994	261/994

Note that in the notation acc/T used in the table, acc is the number of active quantities and T is the number of possible quantities.

\*Initially for Aft-Tail configuration, flutter was also evaluated at  $M = 1.05$  for all five mass cases.

Table 7b. Violated Constraints and Design Variable Bounds

Constraint type			Aft-Tail			Three-Surface			Canard		
			Initial	Linear	Nonlinear	Initial	Linear	Nonlinear	Initial	Linear	Nonlinear
Strain		Subtotal	0/96	0/96	0/96	1/96	0/96	0/96	4/96	0/96	0/96
Buckling		Subtotal	9/96	0/96	0/96	11/96	0/96	1/96	13/96	0/96	0/96
Ply mix	$0^0 \geq 0.1$		0/61	0/61	0/61	0/61	0/61	0/61	0/61	0/61	0/61
	$90^0 \geq 0.1$		0/61	0/61	0/61	0/61	0/61	0/61	0/61	0/61	0/61
	$+45^0 \geq 0.4$		0/61	0/61	0/61	0/61	0/61	0/61	0/61	0/61	0/61
	$+45^0 \leq 0.6$		0/61	0/61	0/61	0/61	0/61	0/61	0/61	0/61	0/61
		Subtotal	0/244	0/244	0/244	0/244	0/244	0/244	0/244	0/244	0/244
Flutter	Subsonic zero damping		0/15	0/15	0/15	4/15	0/15	0/15	0/15	0/15	0/15
	Subsonic 3-percent damping		0/15	0/15	0/15	1/15	0/15	0/15	1/15	0/15	0/15
	Supersonic zero damping		19/25*	0/20	0/20	8/20	0/20	0/20	7/20	0/20	0/20
	Supersonic 3-percent damping		5/25*	0/20	0/20	0/20	0/20	0/20	0/20	0/15	0/20
		Subtotal	24/80*	0/70	0/70	13/70	0/70	0/70	8/70	0/70	0/70
DV bound	Lower		0/244	0/244	0/244	0/244	0/244	0/244	0/244	0/244	0/244
	Upper		0/244	0/244	0/244	0/244	0/244	0/244	0/244	0/244	0/244
		Subtotal	0/488	0/488	0/488	0/488	0/488	0/488	0/488	0/488	0/488
All		Total	33/1004*	0/994	0/994	25/994	0/994	1/994	8/994	0/994	0/994

Note that in the notation acc/T used in the table, acc is the number of active quantities and T is the number of possible quantities.

\*Initially for Aft-Tail configuration, flutter was also evaluated at  $M = 1.05$  for all five mass cases.

Table 8. Comparison of Resized FEM Weight for Full Aircraft (lb)

	Initial design	Linear design	Nonlinear design
Aft-Tail	26820	24244	23920
Three-Surface	26818	24896	24292
Canard	26820	26364	25554

Table 9. Comparison of OEW Weight for Full Aircraft (lb)

	Initial design	Linear design	Nonlinear design
Aft-Tail	288764	285758	285374
Three-Surface	288764	287462	286392
Canard	288756	288778	287748

Table 10. Comparison of Resized Component Weights for Aft-Tail Configuration (lb)

Resized component	Initial component weight	Weight change		
		(Linear $\square$ Initial)	(Nonlinear $\square$ Linear)	(Nonlinear $\square$ Initial)
Inboard Wing	26070	$\square$ 1522	$\square$ 582	$\square$ 2104
Outboard Wing	6638	$\square$ 432	+40	$\square$ 392
Forward Body	5858	+652	$\square$ 4	+648
Mid Body	12004	$\square$ 122	$\square$ 10	$\square$ 132
Aft Body	8938	$\square$ 1582	+172	$\square$ 1410
Total	59505	$\square$ 3006	$\square$ 386	$\square$ 3392

Table 11. Comparison of Resized Component Weights for Three-Surface Configuration (lb)

Resized component	Initial component weight	Weight change		
		(Linear $\square$ Initial)	(Nonlinear $\square$ Linear)	(Nonlinear $\square$ Initial)
Inboard Wing	26072	$\square$ 814	$\square$ 52	$\square$ 866
Outboard Wing	6638	$\square$ 504	+576	+72
Forward Body	5858	+1000	$\square$ 536	+464
Mid Body	12004	+794	$\square$ 1096	$\square$ 302
Aft Body	8936	$\square$ 1780	+38	$\square$ 1742
Total	59505	$\square$ 1304	$\square$ 1070	$\square$ 2374

Table 12. Comparison of Resized Component Weights for Canard Configuration (lb)

Resized component	Initial component weight	Weight change		
		(Linear $\square$ Initial)	(Nonlinear $\square$ Linear)	(Nonlinear $\square$ Initial)
Inboard Wing	26068	$\square$ 1376	$\square$ 756	$\square$ 2132
Outboard Wing	6634	$\square$ 554	+200	$\square$ 354
Forward Body	5856	+1498	$\square$ 140	+1358
Mid Body	12004	+2038	+96	+2134
Aft Body	8936	$\square$ 1582	$\square$ 432	$\square$ 2041
Total	59498	+24	$\square$ 1032	$\square$ 1008

Table 13. Aeroelastic Trim Results for Aft-Tail Configuration (deg)

Load condition	Initial linear design		Linear design				Nonlinear design	
	No nonlinear corrections		No nonlinear corrections		With nonlinear corrections		With nonlinear corrections	
	$\alpha$	$\alpha_f$	$\alpha$	$\alpha_f$	$\alpha$	$\alpha_f$	$\alpha$	$\alpha_f$
LX79	3.89	0.1	3.85	0.1	3.85	0.1	3.85	0.2
LX42	3.54	0.4	3.55	0.5	3.43	0.6	3.42	0.5
LX43	7.32	3.9	7.37	3.6	8.49	1.4	8.46	1.2
LX45	14.87	15.4	14.92	14.3	14.62	16.5	14.60	16.8
LX52	3.32	2.5	-3.37	2.4	3.08	2.7	3.08	2.7
LX55	12.71	11.1	12.80	9.9	12.51	10.1	12.50	10.2
LX56	7.99	4.6	8.04	4.4	7.69	5.2	7.86	5.3

Table 14. Aeroelastic Trim Results for Three-Surface Configuration (deg)

Load condition	Initial linear design			Linear design						Nonlinear design		
	No nonlinear corrections			No nonlinear corrections			With nonlinear corrections			With nonlinear corrections		
	$\alpha$	$\alpha_c$	$\alpha_f$	$\alpha$	$\alpha_c$	$\alpha_f$	$\alpha$	$\alpha_c$	$\alpha_f$	$\alpha$	$\alpha_c$	$\alpha_f$
LZ79	4.18	5.0	0.0	4.16	4.8	0.0	4.17	5.2	0.33	4.16	5.3	0.4
LZ42	3.56	4.1	0.2	3.66	4.3	0.3	3.58	1.2	1.61	3.57	1.1	1.7
LZ43	7.38	9.7	1.0	7.38	9.5	1.2	9.25	13.4	1.22	9.10	12.7	0.0
LZ45	17.44	32.9	13.6	16.80	29.8	11.8	17.18	29.0	9.64	17.25	29.8	11.6
LZ52	3.18	3.3	1.4	3.22	3.5	1.5	3.50	3.5	1.55	3.48	3.3	1.6
LZ55	15.35	8.3	4.9	15.59	8.0	3.3	15.22	8.3	4.93	15.16	8.2	4.8
LZ56	7.79	9.0	2.1	7.81	8.9	2.2	8.02	8.4	2.36	7.98	8.1	2.5
*LZ25	17.76	18.8	4.9	20.99	25.1	6.0	22.19	18.6	9.72	22.08	18.2	9.6
LZ26	35.43	42.0	23.0	33.03	40.6	19.3	34.48	46.3	16.2	34.03	41.3	20.8
LZ2X	21.15	10.1	23.5	21.42	8.4	34.9	19.66	13.7	19.88	19.47	14.4	17.5
LZ2Y	26.72	31.9	6.6	26.10	31.4	6.3	26.10	31.4	6.34	26.18	31.3	6.5

\*Relaxed moment requirement.

Table 15. Aeroelastic Trim Results for Canard Configuration (deg)

Load condition	Initial linear design		Linear design				Nonlinear design	
	No nonlinear corrections		No nonlinear corrections		With nonlinear corrections		With nonlinear corrections	
	$\alpha$	$\alpha_c$	$\alpha$	$\alpha_c$	$\alpha$	$\alpha_c$	$\alpha$	$\alpha_c$
LY79	4.16	-4.7	4.15	-4.5	4.18	-5.4	4.17	-5.4
LY42	-3.77	5.4	-3.85	5.5	-4.07	3.2	-4.04	3.1
LY43	7.22	-8.5	7.24	-8.4	8.58	-12.6	8.52	-12.3
LY45	15.32	-19.8	15.11	-18.1	15.64	-18.9	15.55	-18.7
LY52	-3.32	1.8	-3.38	1.8	-3.35	1.1	-3.35	1.0
LY55	11.82	-11.5	11.88	-11.0	12.22	-17.9	12.17	-17.7
LY56	-8.78	6.5	-8.91	6.4	-8.84	6.7	-8.82	6.5
LY25	23.10	-29.9	22.88	-29.6	19.03	-39.0	18.97	-38.1
LY26	-15.49	40.3	-15.75	40.9	-20.51	73.6	-19.29	62.7
LY2X	20.18	-17.5	20.11	-16.2	19.63	-28.0	19.56	-27.8
LY2Y	-16.27	28.9	-16.14	27.0	-19.71	46.4	-19.55	45.4

Table 16. Design Variable Values for Aft-Tail Configuration (in)

Forward fuselage												
Zone	Initial design				Linear design				Nonlinear design			
	0° ply	90° ply	+45° ply	Core	0° ply	90° ply	+45° ply	Core	0° ply	90° ply	+45° ply	Core
1	0.00814	0.00407	0.00814	0.22000	0.0074	0.0037	0.0074	0.21887	0.00836	0.0037	0.0074	0.21245
2	0.00814	0.00407	0.00814	0.22000	0.02210	0.00442	0.00884	0.2	0.02284	0.00457	0.00913	0.2
3	0.00814	0.00407	0.00814	0.88000	0.03972	0.00794	0.01589	0.30135	0.03720	0.00744	0.01488	0.27114
4	0.00814	0.00407	0.00814	0.22000	0.03972	0.00794	0.01589	0.2	0.03950	0.00790	0.01580	0.2
5	0.00814	0.00407	0.00814	0.22000	0.00904	0.0037	0.00740	0.2	0.0074	0.0037	0.0074	0.2
6	0.00814	0.00407	0.00814	0.22000	0.00889	0.0037	0.00776	0.29281	0.0074	0.0037	0.0074	0.29849
7	0.00814	0.00407	0.00814	0.88000	0.01008	0.0037	0.00850	0.54406	0.00781	0.0037	0.00849	0.54058
8	0.00814	0.00407	0.00814	0.22000	0.01850	0.0037	0.0074	0.24106	0.01850	0.0037	0.0074	0.24901
9	0.00814	0.00407	0.00814	0.88000	0.02390	0.00478	0.00956	0.30007	0.02499	0.00500	0.01000	0.29060
10	0.00814	0.00407	0.00814	0.88000	0.03440	0.00706	0.01459	0.41399	0.03974	0.00795	0.01590	0.39087

Mid fuselage												
Zone	Initial design				Linear design				Nonlinear design			
	0° ply	90° ply	+45° ply	Core	0° ply	90° ply	+45° ply	Core	0° ply	90° ply	+45° ply	Core
11	0.00814	0.00407	0.00814	0.22000	0.03381	0.00676	0.01352	0.2	0.03414	0.00683	0.01366	0.2
12	0.00814	0.00407	0.00814	1.10000	0.02499	0.00500	0.00999	0.30228	0.02909	0.00582	0.01164	0.30288
13	0.00814	0.00407	0.00814	0.22000	0.00957	0.00370	0.0074	0.26666	0.00741	0.0037	0.00820	0.23890
14	0.00814	0.00407	0.00814	0.88000	0.01333	0.00445	0.01333	0.22672	0.01206	0.00402	0.01206	0.2
15	0.00814	0.00407	0.00814	0.44000	0.02289	0.00763	0.02289	0.20500	0.02165	0.00722	0.02165	0.2
16	0.00814	0.00407	0.00814	0.66000	0.01279	0.00407	0.01194	0.48317	0.01312	0.00437	0.01312	0.43473
17	0.02442	0.00814	0.01628	0.66000	0.01882	0.00665	0.01910	0.48399	0.01780	0.00629	0.01807	0.47244
18	0.02442	0.00814	0.01628	0.44000	0.02798	0.00560	0.01119	0.49383	0.03075	0.00615	0.01230	0.55210
19	0.02442	0.00814	0.01628	0.52800	0.06570	0.01314	0.02628	0.33068	0.05686	0.01137	0.02275	0.41067
20	0.04884	0.01221	0.02442	0.88000	0.03855	0.00771	0.01542	0.53682	0.04237	0.00847	0.01695	0.60045
21	0.06512	0.01221	0.02442	1.10000	0.05115	0.01023	0.02046	0.7037	0.04838	0.00968	0.01935	0.66561
22	0.00814	0.00407	0.00814	1.10000	0.02648	0.00530	0.01059	0.34347	0.03059	0.00612	0.01224	0.30992
23	0.00814	0.00407	0.00814	0.22000	0.01738	0.00370	0.00776	0.47201	0.02111	0.00422	0.00844	0.38427
24	0.00814	0.00407	0.00814	0.50600	0.01017	0.00846	0.01398	0.41257	0.01118	0.00761	0.01410	0.37121
25	0.01628	0.00814	0.01628	4.07000	0.00753	0.00545	0.00974	0.93413	0.00776	0.00466	0.00931	0.59223

Table 16. Continued

Aft fuselage												
Zone	Initial design				Linear design				Nonlinear design			
	0° ply	90° ply	+45° ply	Core	0° ply	90° ply	+45° ply	Core	0° ply	90° ply	+45° ply	Core
26	0.03256	0.00814	0.01628	0.88000	0.02076	0.00415	0.00830	0.84316	0.02170	0.00443	0.00907	0.97928
27	0.03256	0.00814	0.01628	0.88000	0.01624	0.0037	0.0074	0.83465	0.01668	0.0037	0.00776	0.88713
28	0.01628	0.00814	0.01628	0.88000	0.01325	0.0037	0.0074	0.67807	0.01610	0.00427	0.0074	0.70884
29	0.01628	0.00814	0.01628	0.88000	0.01569	0.0037	0.00792	0.56383	0.01813	0.00415	0.00962	0.68483
30	0.00814	0.00407	0.00814	0.88000	0.0074	0.0037	0.00758	0.73007	0.0074	0.0037	0.00791	0.56536
31	0.00814	0.00407	0.00814	0.88000	0.0074	0.0037	0.0074	0.50025	0.0074	0.0037	0.0074	0.36849
32	0.00814	0.00407	0.00814	0.88000	0.0074	0.0037	0.0074	0.75709	0.00814	0.0037	0.0074	0.60370
33	0.00814	0.00407	0.00814	0.88000	0.0074	0.0037	0.0074	0.62592	0.0074	0.0037	0.0074	0.77755
34	0.04884	0.01221	0.02442	1.10000	0.02977	0.00595	0.01191	0.96715	0.03112	0.00622	0.01245	0.74558
35	0.04884	0.01221	0.02442	1.10000	0.02418	0.00484	0.00967	1.05850	0.02528	0.00506	0.01011	0.84342
36	0.02442	0.00814	0.01628	1.10000	0.01669	0.0037	0.0074	0.96821	0.01774	0.00370	0.0074	0.82864
37	0.01628	0.00814	0.01628	1.10000	0.01979	0.00396	0.00792	0.84157	0.02527	0.00505	0.01011	0.75720
38	0.02442	0.00814	0.01628	0.88000	0.02388	0.00627	0.01527	0.54912	0.02755	0.00885	0.02155	0.78004
39	0.01628	0.00814	0.01628	0.88000	0.0074	0.0037	0.0074	0.24875	0.00945	0.00472	0.00945	0.37274

Inboard wing upper surface												
Zone	Initial design				Linear design				Nonlinear design			
	0° ply	90° ply	+45° ply	Core	0° ply	90° ply	+45° ply	Core	0° ply	90° ply	+45° ply	Core
40	0.02849	0.08954	0.07326	1.14400	0.07328	0.07349	0.08494	0.43605	0.06474	0.06667	0.07025	0.51471
42	0.01221	0.06512	0.02442	1.01200	0.02100	0.05606	0.05779	0.37732	0.02088	0.05574	0.04976	0.34739
45	0.02035	0.08954	0.0407	0.96800	0.00771	0.03856	0.01542	0.90176	0.00729	0.03647	0.01459	0.72857
46	0.00407	0.00814	0.00814	1.12200	0.01625	0.00815	0.01320	0.67505	0.02158	0.0074	0.01450	0.62501
47	0.00407	0.00814	0.00814	1.12200	0.01329	0.0074	0.00902	0.50758	0.01390	0.0074	0.0074	0.45094
50	0.00407	0.00814	0.00814	0.92400	0.00571	0.00921	0.01119	0.4441	0.00488	0.00916	0.01053	0.39636
52	0.00407	0.00814	0.00814	0.72600	0.00370	0.0074	0.00833	0.41656	0.0037	0.0074	0.00787	0.34980

Table 16. Concluded

Inboard wing lower surface												
Zone	Initial design				Linear design				Nonlinear design			
	0° ply	90° ply	+45° ply	Core	0° ply	90° ply	+45° ply	Core	0° ply	90° ply	+45° ply	Core
41	0.02849	0.06512	0.06512	0.77000	0.06726	0.04340	0.07198	0.25114	0.07145	0.04285	0.06363	0.2
43	0.02035	0.06512	0.03256	0.96800	0.01740	0.05220	0.05220	0.22217	0.01930	0.05507	0.05238	0.21015
44	0.02035	0.06512	0.03256	0.96800	0.02264	0.05540	0.02846	0.30803	0.02141	0.05792	0.02692	0.29764
48	0.01221	0.01628	0.01628	1.25400	0.03279	0.0074	0.01340	0.42127	0.03195	0.00742	0.01485	0.41344
49	0.00407	0.00814	0.00814	0.90200	0.01986	0.01046	0.02132	0.43788	0.02236	0.01040	0.02120	0.43491
51	0.01628	0.01628	0.01628	1.43000	0.01514	0.01089	0.00868	0.41865	0.01749	0.01139	0.00962	0.41438
53	0.00407	0.00814	0.00814	1.18800	0.00489	0.0074	0.0074	0.47030	0.00565	0.0074	0.0074	0.42162

Outboard wing upper surface												
Zone	Initial design				Linear design				Nonlinear design			
	0° ply	90° ply	+45° ply	Core	0° ply	90° ply	+45° ply	Core	0° ply	90° ply	+45° ply	Core
54	0.02035	0.09768	0.0407	0.94600	0.01815	0.09077	0.03631	0.73778	0.01717	0.08586	0.03434	0.73600
55	0.02035	0.08954	0.0407	0.99000	0.01622	0.08107	0.03243	0.71631	0.01622	0.08108	0.03243	0.69117
56	0.01628	0.05698	0.03256	0.90200	0.01360	0.05378	0.03431	0.65338	0.01625	0.06294	0.04168	0.62048
57	0.01221	0.03256	0.03256	0.66000	0.01799	0.05220	0.04058	0.39991	0.01702	0.05581	0.03880	0.49644

Outboard wing lower surface												
Zone	Initial design				Linear design				Nonlinear design			
	0° ply	90° ply	+45° ply	Core	0° ply	90° ply	+45° ply	Core	0° ply	90° ply	+45° ply	Core
58	0.01628	0.07326	0.03256	0.59400	0.01248	0.06242	0.02497	0.47142	0.01373	0.06867	0.02747	0.39196
59	0.01628	0.06512	0.03256	0.81400	0.01151	0.05598	0.02381	0.45858	0.01259	0.05852	0.02597	0.38911
60	0.01221	0.04070	0.03256	0.48400	0.01100	0.03500	0.03200	0.33159	0.01348	0.04305	0.03912	0.27148
61	0.01221	0.03256	0.03256	0.35200	0.01799	0.06415	0.04273	0.2	0.01572	0.06068	0.03845	0.2

Table 17. Design Variable Values for Three-Surface Configuration (in)

Forward fuselage												
Zone	Initial design				Linear design				Nonlinear design			
	0° ply	90° ply	+45° ply	Core	0° ply	90° ply	+45° ply	Core	0° ply	90° ply	+45° ply	Core
1	0.00814	0.00407	0.00814	0.22000	0.00927	0.00379	0.00758	0.21737	0.00775	0.0037	0.0074	0.25650
2	0.00814	0.00407	0.00814	0.22000	0.02693	0.00539	0.01077	0.20487	0.02036	0.00407	0.00814	0.2
3	0.00814	0.00407	0.00814	0.88000	0.04159	0.00832	0.01664	0.67175	0.03144	0.00629	0.01258	0.45949
4	0.00814	0.00407	0.00814	0.22000	0.04159	0.00832	0.01664	0.20487	0.03475	0.00695	0.01390	0.2
5	0.00814	0.00407	0.00814	0.22000	0.00839	0.00379	0.00797	0.20487	0.0074	0.0037	0.0074	0.2
6	0.00814	0.00407	0.00814	0.22000	0.00798	0.00379	0.00839	0.29576	0.0074	0.0037	0.0074	0.29925
7	0.00814	0.00407	0.00814	0.88000	0.00906	0.00398	0.00978	0.47039	0.0074	0.0037	0.00772	0.48010
8	0.00814	0.00407	0.00814	0.22000	0.01992	0.00398	0.00797	0.27090	0.01715	0.0037	0.0074	0.22083
9	0.00814	0.00407	0.00814	0.88000	0.02830	0.00566	0.01132	0.60777	0.02140	0.00428	0.00856	0.41573
10	0.00814	0.00407	0.00814	0.88000	0.04159	0.00832	0.01664	0.57812	0.03515	0.00703	0.01406	0.44149

Mid fuselage												
Zone	Initial design				Linear design				Nonlinear design			
	0° ply	90° ply	+45° ply	Core	0° ply	90° ply	+45° ply	Core	0° ply	90° ply	+45° ply	Core
11	0.00814	0.00407	0.00814	0.22000	0.03956	0.00791	0.01582	0.24336	0.03467	0.00697	0.01388	0.27682
12	0.00814	0.00407	0.00814	1.10000	0.03579	0.00716	0.01432	0.49161	0.02986	0.00597	0.01194	0.55674
13	0.00814	0.00407	0.00814	0.22000	0.00874	0.00379	0.00797	0.34043	0.0074	0.0037	0.00740	0.33210
14	0.00814	0.00407	0.00814	0.88000	0.01202	0.00454	0.01242	0.54989	0.00909	0.0037	0.00952	0.37613
15	0.00814	0.00407	0.00814	0.44000	0.02442	0.01062	0.02628	0.35310	0.01670	0.00726	0.01797	0.30603
16	0.00814	0.00407	0.00814	0.66000	0.01453	0.00484	0.01453	0.46268	0.01045	0.0037	0.00994	0.47845
17	0.02442	0.00814	0.01628	0.66000	0.01946	0.00653	0.01950	0.48937	0.01889	0.00630	0.01889	0.53154
18	0.02442	0.00814	0.01628	0.44000	0.03396	0.00683	0.01373	0.64682	0.02737	0.00547	0.01095	0.69110
19	0.02442	0.00814	0.01628	0.52800	0.06871	0.01374	0.02748	0.33072	0.04982	0.00998	0.02001	0.45240
20	0.04884	0.01221	0.02442	0.88000	0.04118	0.00824	0.01647	0.54961	0.02817	0.00563	0.01127	0.62689
21	0.06512	0.01221	0.02442	1.10000	0.01651	0.00802	0.01773	0.73684	0.01742	0.01105	0.01340	0.85747
22	0.00814	0.00407	0.00814	1.10000	0.02342	0.00507	0.01112	0.56267	0.02163	0.00433	0.00865	0.43525
23	0.00814	0.00407	0.00814	0.22000	0.02599	0.00520	0.01040	0.40435	0.02172	0.00434	0.00869	0.42537
24	0.00814	0.00407	0.00814	0.50600	0.01539	0.00641	0.01635	0.44068	0.01352	0.00516	0.01401	0.40454
25	0.01628	0.00814	0.01628	4.07000	0.00849	0.00626	0.01064	1.84578	0.0074	0.00578	0.00934	1.32730

Table 17. Continued

Aft fuselage												
Zone	Initial design				Linear design				Nonlinear design			
	0° ply	90° ply	+45° ply	Core	0° ply	90° ply	+45° ply	Core	0° ply	90° ply	+45° ply	Core
26	0.03256	0.00814	0.01628	0.88000	0.01604	0.00379	0.00875	0.84668	0.01908	0.00410	0.00893	0.76122
27	0.03256	0.00814	0.01628	0.88000	0.01507	0.00379	0.00797	0.75150	0.01617	0.00370	0.0074	0.71882
28	0.01628	0.00814	0.01628	0.88000	0.02037	0.00535	0.01124	0.47825	0.02215	0.00443	0.00886	0.48020
29	0.01628	0.00814	0.01628	0.88000	0.01373	0.00379	0.00797	0.55960	0.01268	0.0037	0.0074	0.56516
30	0.00814	0.00407	0.00814	0.88000	0.00758	0.00379	0.00810	0.78342	0.00916	0.0037	0.00949	0.81454
31	0.00814	0.00407	0.00814	0.88000	0.00758	0.00379	0.00797	0.44210	0.0074	0.0037	0.0074	0.51738
32	0.00814	0.00407	0.00814	0.88000	0.00797	0.00398	0.00797	0.52192	0.0074	0.00427	0.0074	0.52059
33	0.00814	0.00407	0.00814	0.88000	0.00797	0.00398	0.00797	0.43405	0.0074	0.0037	0.0074	0.52645
34	0.04884	0.01221	0.02442	1.10000	0.01672	0.00379	0.00797	1.02606	0.01710	0.0037	0.0074	1.07256
35	0.04884	0.01221	0.02442	1.10000	0.02260	0.00452	0.00904	0.87126	0.01953	0.00391	0.00781	0.96947
36	0.02442	0.00814	0.01628	1.10000	0.01687	0.00437	0.01124	0.67146	0.01866	0.00438	0.01038	0.66205
37	0.01628	0.00814	0.01628	1.10000	0.01900	0.00535	0.01124	0.49613	0.02329	0.00574	0.01206	0.48006
38	0.02442	0.00814	0.01628	0.88000	0.00797	0.00398	0.00797	0.65561	0.00903	0.00577	0.00965	0.83931
39	0.01628	0.00814	0.01628	0.88000	0.0074	0.0037	0.0074	0.2	0.00794	0.00397	0.00794	0.23742

Inboard wing upper surface												
Zone	Initial design				Linear design				Nonlinear design			
	0° ply	90° ply	+45° ply	Core	0° ply	90° ply	+45° ply	Core	0° ply	90° ply	+45° ply	Core
40	0.02849	0.08954	0.07326	1.14400	0.08931	0.05276	0.09008	1.04193	0.1	0.07641	0.1	0.71270
42	0.01221	0.06512	0.02442	1.01200	0.01663	0.04990	0.04515	0.66484	0.01540	0.03413	0.03247	0.64175
45	0.02035	0.08954	0.0407	0.96800	0.01405	0.05093	0.02840	0.63269	0.01063	0.05181	0.02081	0.78335
46	0.00407	0.00814	0.00814	1.12200	0.01618	0.00885	0.01415	0.64631	0.02121	0.00998	0.02049	0.58346
47	0.00407	0.00814	0.00814	1.12200	0.01618	0.00839	0.01106	0.53089	0.01286	0.0074	0.00862	0.54000
50	0.00407	0.00814	0.00814	0.92400	0.00422	0.01266	0.01266	0.42621	0.00370	0.00990	0.01006	0.49369
52	0.00407	0.00814	0.00814	0.72600	0.00379	0.00758	0.00795	0.41619	0.0037	0.0074	0.0074	0.42553

Table 17. Concluded

Inboard wing lower surface												
Zone	Initial design				Linear design				Nonlinear design			
	0° ply	90° ply	+45° ply	Core	0° ply	90° ply	+45° ply	Core	0° ply	90° ply	+45° ply	Core
41	0.02849	0.06512	0.06512	0.77000	0.08278	0.05246	0.06376	0.64965	0.09500	0.06975	0.05492	0.63064
43	0.02035	0.06512	0.03256	0.96800	0.01810	0.05240	0.04995	0.54699	0.01238	0.03584	0.03592	0.38495
44	0.02035	0.06512	0.03256	0.96800	0.01165	0.04990	0.02613	0.52031	0.01508	0.03588	0.01975	0.49677
48	0.01221	0.01628	0.01628	1.25400	0.03217	0.01243	0.01541	0.45798	0.03351	0.01800	0.02233	0.39625
49	0.00407	0.00814	0.00814	0.90200	0.01626	0.01388	0.02261	0.46366	0.02240	0.01912	0.03114	0.46946
51	0.01628	0.01628	0.01628	1.43000	0.01411	0.01321	0.00911	0.47219	0.01388	0.01567	0.00985	0.50458
53	0.00407	0.00814	0.00814	1.18800	0.00566	0.00758	0.00758	0.57808	0.00539	0.0074	0.0074	0.46295

Outboard wing upper surface												
Zone	Initial design				Linear design				Nonlinear design			
	0° ply	90° ply	+45° ply	Core	0° ply	90° ply	+45° ply	Core	0° ply	90° ply	+45° ply	Core
54	0.02035	0.09768	0.0407	0.94600	0.01790	0.08250	0.03929	0.74903	0.02592	0.1	0.05071	0.62574
55	0.02035	0.08954	0.0407	0.99000	0.01399	0.06993	0.02797	0.78578	0.02026	0.09634	0.03887	0.65117
56	0.01628	0.05698	0.03256	0.90200	0.01388	0.05015	0.03333	0.84112	0.02010	0.06985	0.04367	0.58671
57	0.01221	0.03256	0.03256	0.66000	0.01877	0.06431	0.03455	0.64702	0.02014	0.05649	0.02554	0.60560

Outboard wing lower surface												
Zone	Initial design				Linear design				Nonlinear design			
	0° ply	90° ply	+45° ply	Core	0° ply	90° ply	+45° ply	Core	0° ply	90° ply	+45° ply	Core
58	0.01628	0.07326	0.03256	0.59400	0.01156	0.05702	0.02349	0.62126	0.01674	0.08259	0.03402	0.58133
59	0.01628	0.06512	0.03256	0.81400	0.01045	0.04816	0.02197	0.64703	0.01513	0.06447	0.02653	0.51311
60	0.01221	0.04070	0.03256	0.48400	0.01265	0.05265	0.02770	0.48090	0.01739	0.07626	0.04012	0.44406
61	0.01221	0.03256	0.03256	0.35200	0.01877	0.06431	0.03187	0.26870	0.02460	0.07918	0.03459	0.2

Table 18. Design Variable Values for Canard Configuration (in)

Forward fuselage												
Zone	Initial design				Linear design				Nonlinear design			
	0° ply	90° ply	+45° ply	Core	0° ply	90° ply	+45° ply	Core	0° ply	90° ply	+45° ply	Core
1	0.00814	0.00407	0.00814	0.22000	0.01031	0.0037	0.0074	0.20273	0.00953	0.0037	0.0074	0.25711
2	0.00814	0.00407	0.00814	0.22000	0.03035	0.00607	0.01214	0.2	0.02184	0.00457	0.00965	0.2
3	0.00814	0.00407	0.00814	0.88000	0.03466	0.00747	0.01628	0.97214	0.02494	0.00624	0.01172	0.77309
4	0.00814	0.00407	0.00814	0.22000	0.03139	0.01001	0.01723	0.30690	0.03725	0.01074	0.02044	0.39562
5	0.00814	0.00407	0.00814	0.22000	0.01424	0.0037	0.00776	0.2	0.01132	0.0037	0.0074	0.2
6	0.00814	0.00407	0.00814	0.22000	0.01188	0.00490	0.01258	0.28249	0.00993	0.00410	0.01027	0.34604
7	0.00814	0.00407	0.00814	0.88000	0.01639	0.00671	0.01098	0.39869	0.01370	0.00757	0.00965	0.51857
8	0.00814	0.00407	0.00814	0.22000	0.02636	0.00527	0.01054	0.26100	0.02204	0.00451	0.00927	0.2
9	0.00814	0.00407	0.00814	0.88000	0.02707	0.00781	0.02160	0.97214	0.02906	0.00838	0.02318	0.99272
10	0.00814	0.00407	0.00814	0.88000	0.05178	0.01087	0.02301	0.87961	0.05844	0.01213	0.02535	0.94429

Mid fuselage												
Zone	Initial design				Linear design				Nonlinear design			
	0° ply	90° ply	+45° ply	Core	0° ply	90° ply	+45° ply	Core	0° ply	90° ply	+45° ply	Core
11	0.00814	0.00407	0.00814	0.22000	0.04382	0.00876	0.01753	0.41338	0.05199	0.01040	0.02079	0.51913
12	0.00814	0.00407	0.00814	1.10000	0.03619	0.00724	0.01448	0.68522	0.04294	0.00859	0.01717	0.80154
13	0.00814	0.00407	0.00814	0.22000	0.01237	0.00468	0.01196	0.22595	0.01328	0.00441	0.01321	0.27745
14	0.00814	0.00407	0.00814	0.88000	0.01812	0.00522	0.01434	0.58924	0.02150	0.00599	0.01619	0.57236
15	0.00814	0.00407	0.00814	0.44000	0.01875	0.01163	0.02279	0.59375	0.01648	0.01380	0.01640	0.70446
16	0.00814	0.00407	0.00814	0.66000	0.01637	0.00588	0.01669	0.47871	0.01609	0.00664	0.01704	0.48136
17	0.02442	0.00814	0.01628	0.66000	0.01888	0.00633	0.01891	0.46427	0.01359	0.00479	0.01360	0.49806
18	0.02442	0.00814	0.01628	0.44000	0.04269	0.00945	0.02090	0.66063	0.05064	0.01122	0.02479	0.78381
19	0.02442	0.00814	0.01628	0.52800	0.07337	0.01483	0.02940	0.40992	0.06666	0.01457	0.03223	0.50034
20	0.04884	0.01221	0.02442	0.88000	0.07202	0.01440	0.02881	0.65077	0.05781	0.01156	0.02313	0.51752
21	0.06512	0.01221	0.02442	1.10000	0.03181	0.00959	0.02438	0.50689	0.02406	0.00725	0.01844	0.64273
22	0.00814	0.00407	0.00814	1.10000	0.04457	0.00891	0.01783	0.73697	0.04785	0.00866	0.01647	0.53028
23	0.00814	0.00407	0.00814	0.22000	0.03471	0.00696	0.01398	0.34390	0.04118	0.00838	0.01712	0.47115
24	0.00814	0.00407	0.00814	0.50600	0.01690	0.00819	0.01882	0.38708	0.01908	0.00942	0.02137	0.52449
25	0.01628	0.00814	0.01628	4.07000	0.01399	0.00699	0.01574	1.34963	0.01007	0.00503	0.01132	1.02092

Table 18. Continued

Aft fuselage												
Zone	Initial design				Linear design				Nonlinear design			
	0° ply	90° ply	+45° ply	Core	0° ply	90° ply	+45° ply	Core	0° ply	90° ply	+45° ply	Core
26	0.03256	0.00814	0.01628	0.88000	0.03311	0.00693	0.01462	0.47753	0.02383	0.00499	0.01052	0.57301
27	0.03256	0.00814	0.01628	0.88000	0.02793	0.00559	0.01117	0.44295	0.02009	0.00402	0.00804	0.44051
28	0.01628	0.00814	0.01628	0.88000	0.02723	0.00545	0.01089	0.37533	0.01959	0.00392	0.00784	0.31621
29	0.01628	0.00814	0.01628	0.88000	0.01625	0.00469	0.01089	0.29225	0.01169	0.0037	0.00784	0.25304
30	0.00814	0.00407	0.00814	0.88000	0.00819	0.0037	0.00843	0.59536	0.0074	0.0037	0.0074	0.71243
31	0.00814	0.00407	0.00814	0.88000	0.0074	0.0037	0.0074	0.38250	0.0074	0.0037	0.0074	0.42311
32	0.00814	0.00407	0.00814	0.88000	0.0074	0.0037	0.0074	0.45596	0.0074	0.0037	0.0074	0.49796
33	0.00814	0.00407	0.00814	0.88000	0.00903	0.0037	0.0074	0.37405	0.0074	0.0037	0.0074	0.40217
34	0.04884	0.01221	0.02442	1.10000	0.03255	0.00651	0.01302	0.70030	0.02462	0.00492	0.00985	0.84840
35	0.04884	0.01221	0.02442	1.10000	0.03026	0.00605	0.01210	0.70565	0.02289	0.00458	0.00915	0.84640
36	0.02442	0.00814	0.01628	1.10000	0.02834	0.00567	0.01134	0.60248	0.02039	0.00408	0.00816	0.63653
37	0.01628	0.00814	0.01628	1.10000	0.02723	0.00545	0.01089	0.39849	0.01987	0.00412	0.00824	0.48841
38	0.02442	0.00814	0.01628	0.88000	0.01406	0.0037	0.00892	0.25154	0.01012	0.0037	0.0074	0.23321
39	0.01628	0.00814	0.01628	0.88000	0.0074	0.0037	0.0074	0.23905	0.0074	0.0037	0.0074	0.23221

Inboard wing upper surface												
Zone	Initial design				Linear design				Nonlinear design			
	0° ply	90° ply	+45° ply	Core	0° ply	90° ply	+45° ply	Core	0° ply	90° ply	+45° ply	Core
40	0.02849	0.08954	0.07326	1.14400	0.05801	0.06934	0.08147	0.76500	0.05924	0.08007	0.07851	0.55045
42	0.01221	0.06512	0.02442	1.01200	0.01624	0.04330	0.04251	0.46489	0.01432	0.04097	0.03927	0.53676
45	0.02035	0.08954	0.0407	0.96800	0.00785	0.03882	0.01556	0.81046	0.00594	0.02944	0.01179	0.95336
46	0.00407	0.00814	0.00814	1.12200	0.01735	0.00758	0.00971	0.67668	0.01685	0.0074	0.00992	0.69025
47	0.00407	0.00814	0.00814	1.12200	0.01351	0.00758	0.00777	0.59139	0.01271	0.0074	0.0074	0.70166
50	0.00407	0.00814	0.00814	0.92400	0.00473	0.01066	0.01154	0.45101	0.00533	0.00806	0.00830	0.51709
52	0.00407	0.00814	0.00814	0.72600	0.00370	0.0074	0.0074	0.41316	0.00439	0.0074	0.00827	0.43035

Table 18. Concluded

Inboard wing lower surface												
Zone	Initial design				Linear design				Nonlinear design			
	0° ply	90° ply	+45° ply	Core	0° ply	90° ply	+45° ply	Core	0° ply	90° ply	+45° ply	Core
41	0.02849	0.06512	0.06512	0.77000	0.07127	0.04768	0.07529	0.62933	0.07277	0.05587	0.05523	0.47605
43	0.02035	0.06512	0.03256	0.96800	0.02032	0.04579	0.03777	0.45632	0.01537	0.03464	0.03041	0.34518
44	0.02035	0.06512	0.03256	0.96800	0.01362	0.03512	0.03156	0.39041	0.01047	0.02612	0.02388	0.47228
48	0.01221	0.01628	0.01628	1.25400	0.03064	0.01815	0.01627	0.43716	0.02977	0.01763	0.01930	0.41003
49	0.00407	0.00814	0.00814	0.90200	0.02709	0.01510	0.01941	0.45514	0.02503	0.01467	0.01794	0.47395
51	0.01628	0.01628	0.01628	1.43000	0.01399	0.01399	0.01266	0.58030	0.01170	0.01058	0.00911	0.51343
53	0.00407	0.00814	0.00814	1.18800	0.00621	0.00994	0.00994	0.72017	0.00737	0.01179	0.01179	0.85445

Outboard wing upper surface												
Zone	Initial design				Linear design				Nonlinear design			
	0° ply	90° ply	+45° ply	Core	0° ply	90° ply	+45° ply	Core	0° ply	90° ply	+45° ply	Core
54	0.02035	0.09768	0.0407	0.94600	0.01714	0.08252	0.03586	0.72272	0.01923	0.09610	0.03850	0.71866
55	0.02035	0.08954	0.0407	0.99000	0.01498	0.07254	0.03114	0.70767	0.01708	0.08540	0.03416	0.70455
56	0.01628	0.05698	0.03256	0.90200	0.01299	0.05186	0.03252	0.63397	0.01513	0.06637	0.03491	0.66183
57	0.01221	0.03256	0.03256	0.66000	0.01049	0.03780	0.02673	0.51381	0.01072	0.03860	0.02870	0.65326

Outboard wing lower surface												
Zone	Initial design				Linear design				Nonlinear design			
	0° ply	90° ply	+45° ply	Core	0° ply	90° ply	+45° ply	Core	0° ply	90° ply	+45° ply	Core
58	0.01628	0.07326	0.03256	0.59400	0.01286	0.05601	0.02479	0.50409	0.01381	0.06525	0.02635	0.50965
59	0.01628	0.06512	0.03256	0.81400	0.01399	0.04929	0.02435	0.47824	0.01293	0.05925	0.02614	0.47786
60	0.01221	0.04070	0.03256	0.48400	0.01123	0.03368	0.03368	0.34519	0.01280	0.04288	0.03616	0.36794
61	0.01221	0.03256	0.03256	0.35200	0.01103	0.03298	0.03091	0.26476	0.01127	0.03517	0.03156	0.29579

Table 19. Design Variable Upper and Lower Bounds (in)

Design variable	Fuselage		Wing	
	Lower bound	Upper bound	Lower bound	Upper bound
0° ply	0.0074	0.1	0.0037	0.1
90° ply	0.0037	0.1	0.0074	0.1
+45° ply	0.0074	0.1	0.0074	0.1
Core	0.2	5.0	0.2	5.0

Table 20. Initial Violated Flutter Constraints

Aft-Tail configuration			Three Surface configuration			Canard configuration		
Mach number	Mass case	Damping, %	Mach number	Mass case	Damping, %	Mach number	Mass case	Damping, %
1.05*, 1.2, 1.5, 2.0, 2.6	1	0	0.8, 1.2, 1.5	1	0	1.2, 1.5	1	0
1.05*, 1.2, 1.5, 2.0, 2.6	2	0	0.8, 1.2, 1.5, 2.0	2	0	1.2, 1.5, 2.0	2	0
1.05*, 1.2, 1.5	3	0	0.8, 1.2	3	0	1.2	3	0
1.05*, 1.2, 1.5	4	0	0.8, 1.2	4	0	1.2	4	0
1.05*, 1.2, 1.5	5	0	1.2	5	0	0.8	1	3
1.05*, 1.2, 1.5, 2.0	1	3	0.8	1	3			
1.05*	3	3						

\*For first two optimization cycles, flutter was also evaluated at  $M = 1.05$ .

Table 21. Active Flutter Constraints

Aft-Tail configuration								
Initial design			Linear design			Nonlinear design		
Mach number	Mass case	Damping, %	Mach number	Mass case	Damping, %	Mach number	Mass case	Damping, %
2.0	3	0	1.2, 1.5	5	0	1.2, 1.5	5	0
2.0	4	0	0.95	3	3	1.2	4	3
			0.95, 1.2, 2.0	4	3			

Three-Surface Configuration								
Initial design			Linear design			Nonlinear design		
Mach number	Mass case	Percent damping	Mach number	Mass case	Damping, %	Mach number	Mass case	Damping, %
0.65	4	0	2.0	4	0			
2.0	1	0	1.2, 1.5	5	0			
0.8	4	3	0.95	4	3			
0.8	5	3						

Canard Configuration								
Initial design			Linear design			Nonlinear design		
Mach number	Mass case	Percent damping	Mach number	Mass case	Damping, %	Mach number	Mass case	Damping, %
2.0	1	0	1.2, 1.5	5	0	1.2	5	0
			0.95	3	3			
			0.95	4	3			

\*For first two optimization cycles, flutter was also evaluated at  $M = 1.05$ .

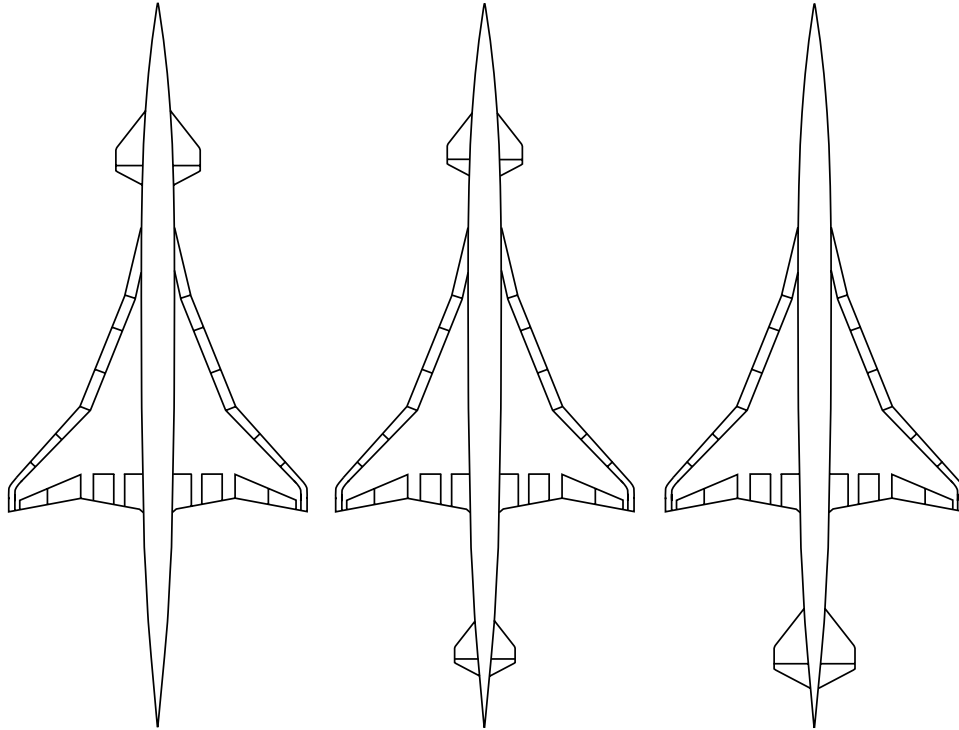


Figure 1. Planform views of three LCAP configurations.

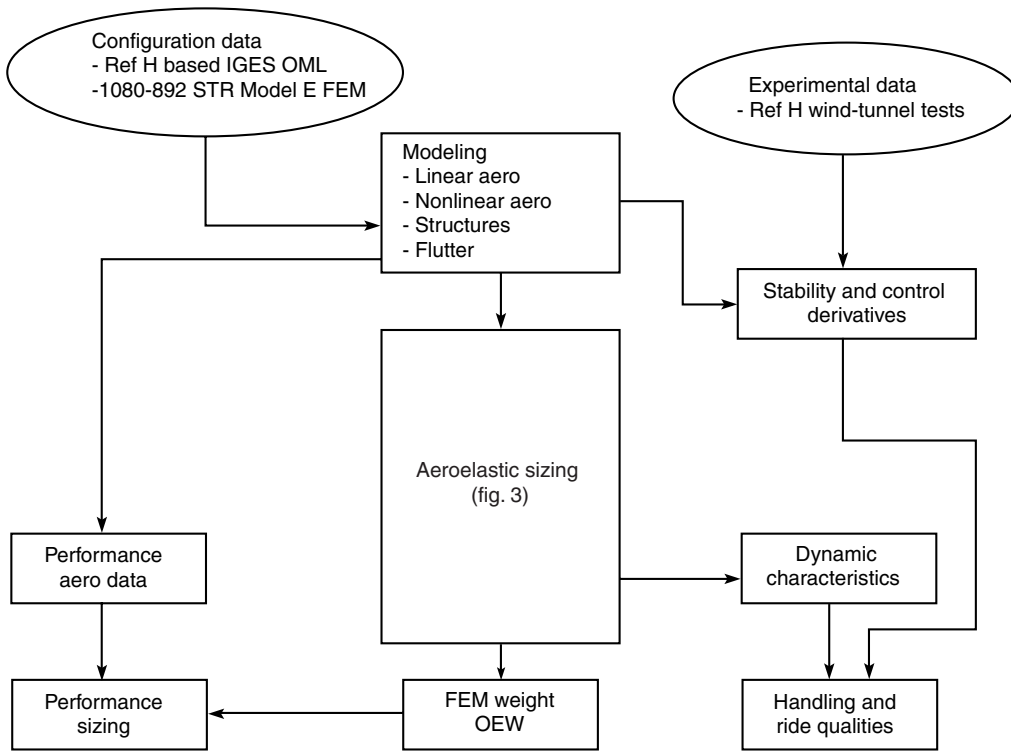
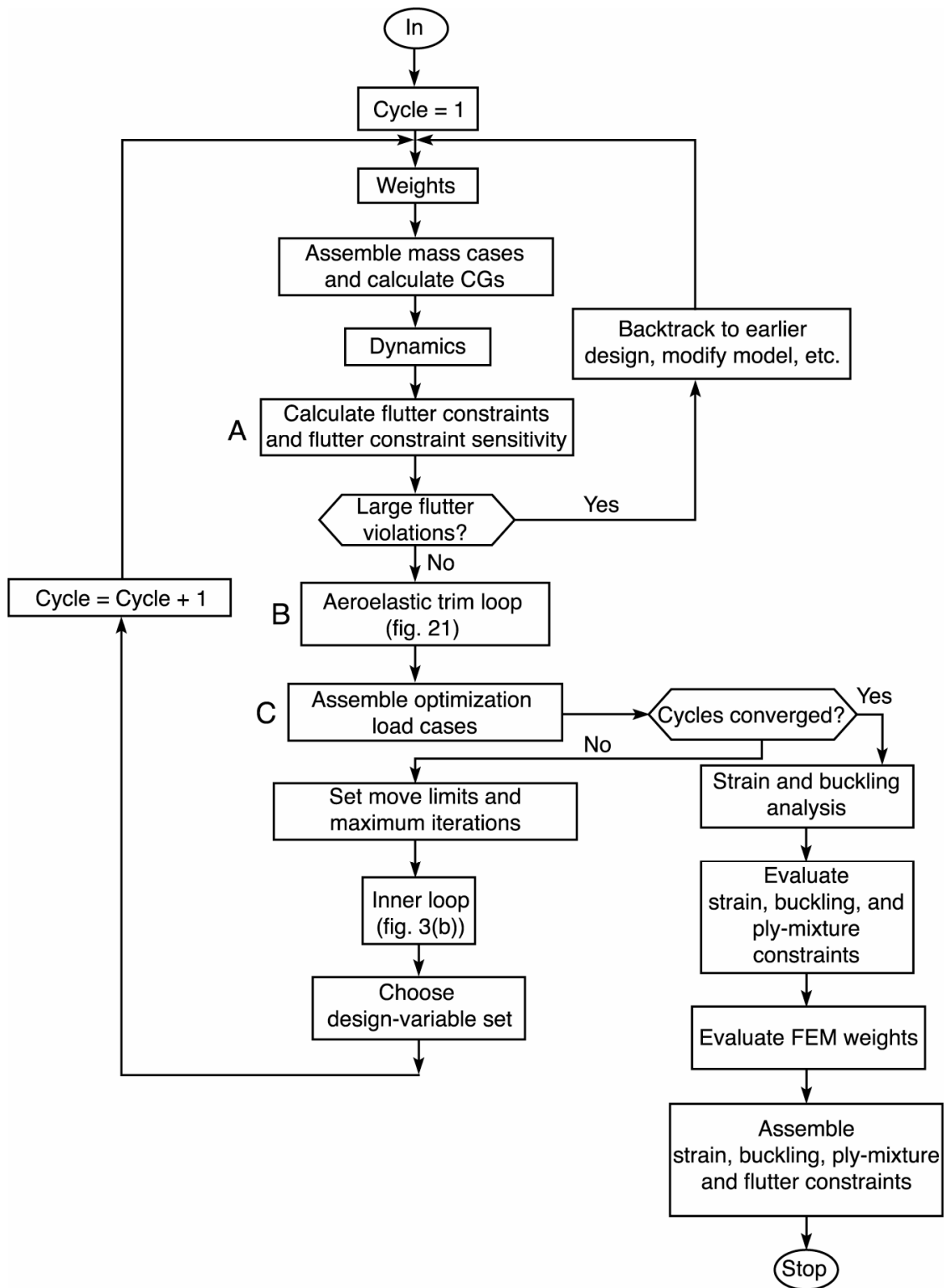
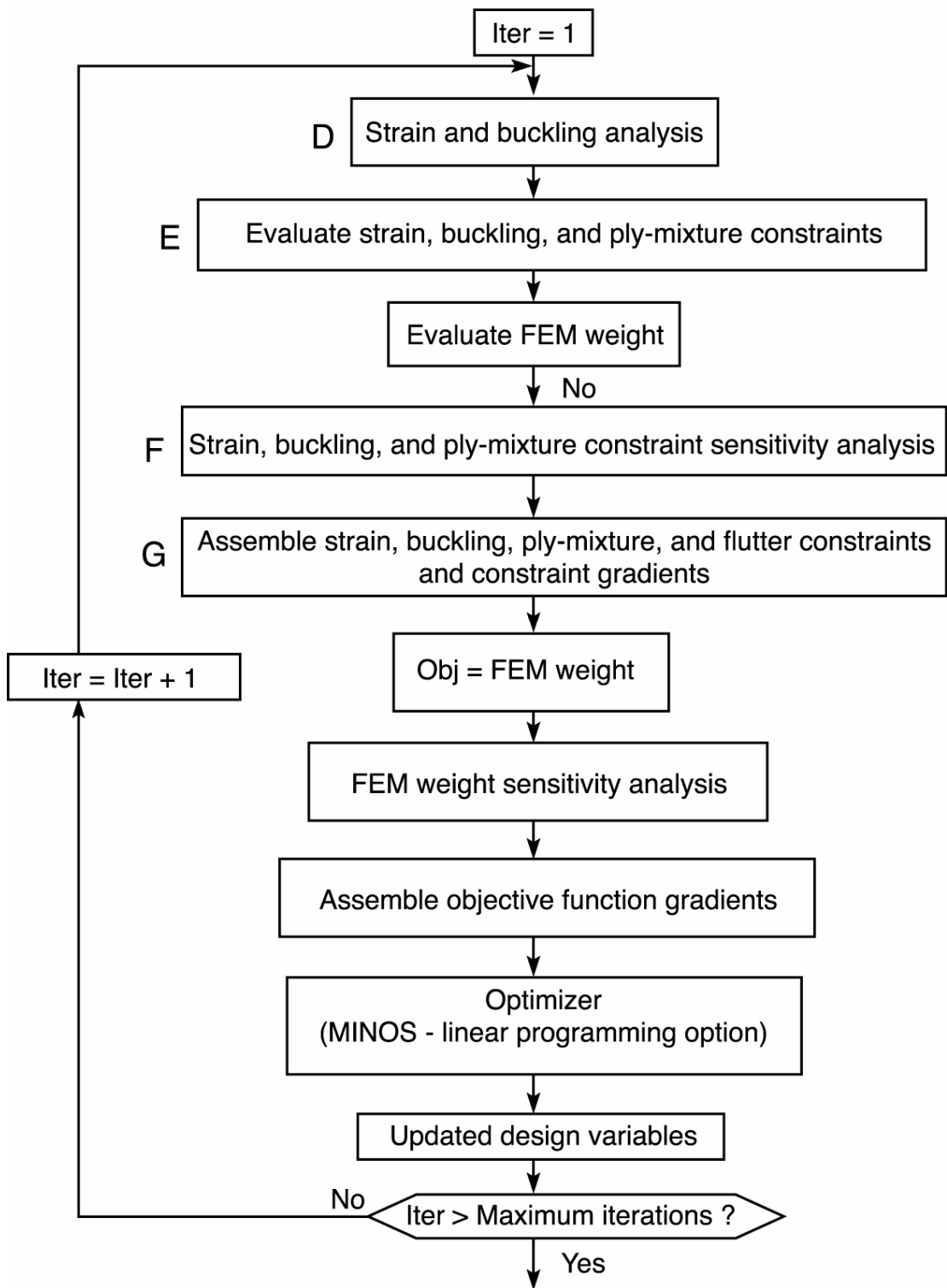


Figure 2. Overall LCAP process.



(a) Outer loop.

Figure 3. LCAP Aeroelastic sizing.



(b) Inner loop.

Figure 3. Concluded.

Boeing Commercial Airplane Group  
P.O. Box 3707  
Seattle, WA 98124 2207

December 23, 1992  
B-Y87B-JW-037

Stephen J. Scotti  
National Aeronautics and Space Administration  
Langely Research Center  
MS 396  
Hampton, VA 23681-0001

Subject: Transmittal of the Boeing HSCT 1080-892STR Finite Element Model

**BOEING**

Dear Stephen,

The Boeing Company is loaning you a structural finite element model of the Boeing High Speed Civil Transport in accordance with our earlier understanding. The model is of the 1080-892STR model "E" configuration that has undergone one cycle of sizing for loads and flutter. The model is being sent to you under the provisions of the loan agreement dated November 20, 1992 (Boeing Loan Control Number I22931).

The model data are written as 104 files on the enclosed magnetic tape that is in the UNIX TAR format that you have requested. The files are outputs from the ELFINI program in a form that can be adapted to any other finite element program. The model data consist of nodal and element definitions, four boundary conditions, five mass cases and eight unit load cases.

Also enclosed is documentation describing the element definition data contained in the files. This will assist you in translating the EFLINI elements into equivalent elements in another program. The detailed description of all the information being sent is included in the attachment. If you have any question regarding the model or the data please contact, Steve Sergev at (206) 965-5202 or Kumar Bhatia at (206) 965-5092.

Sincerely

**Original signed by:**

---

Jiri Wertheimer

Enclosure

Figure 4. Transmittal letter that accompanied Boeing-developed finite-element model of high-speed civil transport.

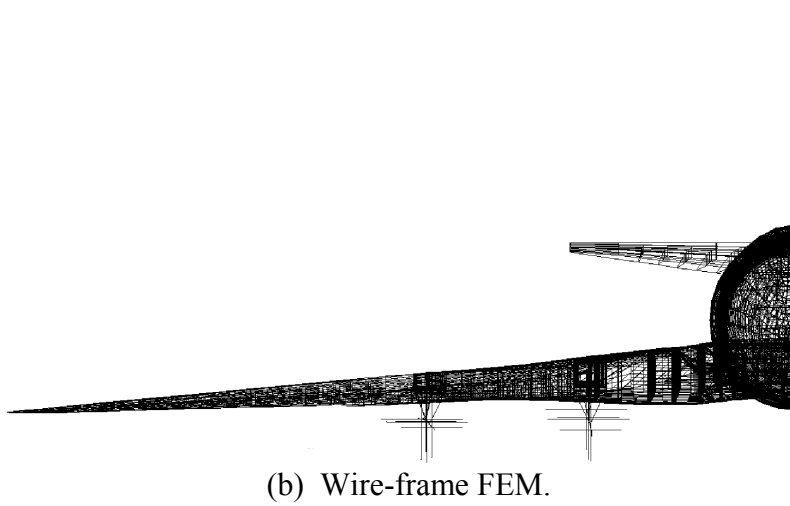
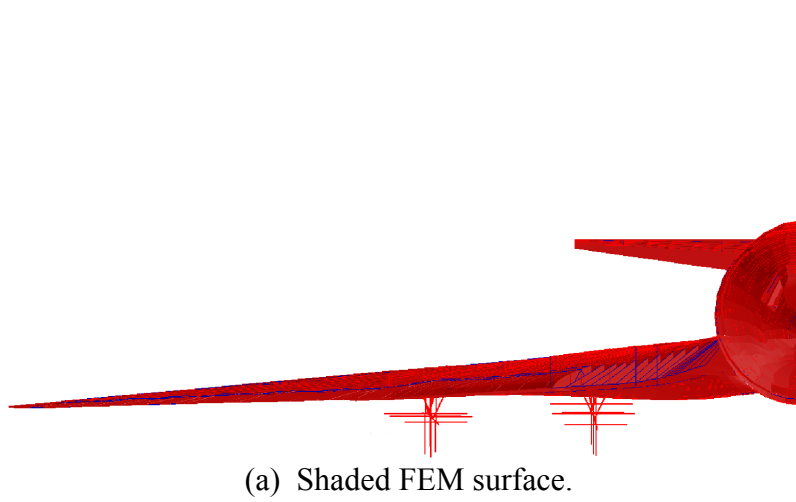
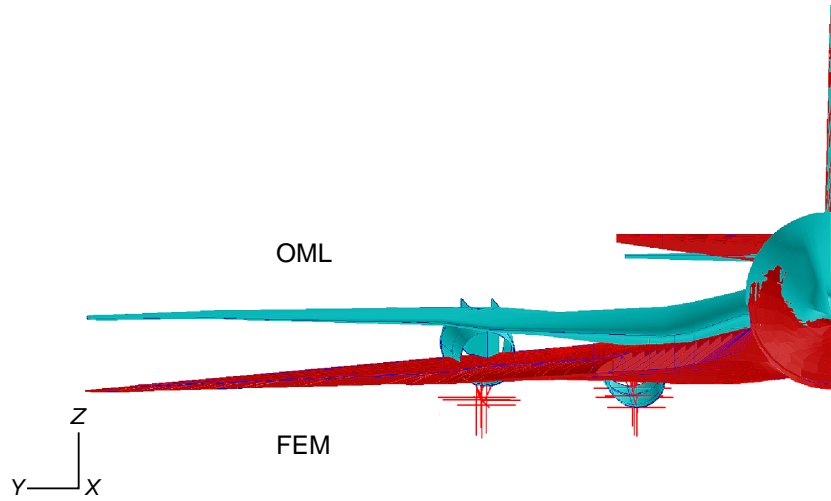


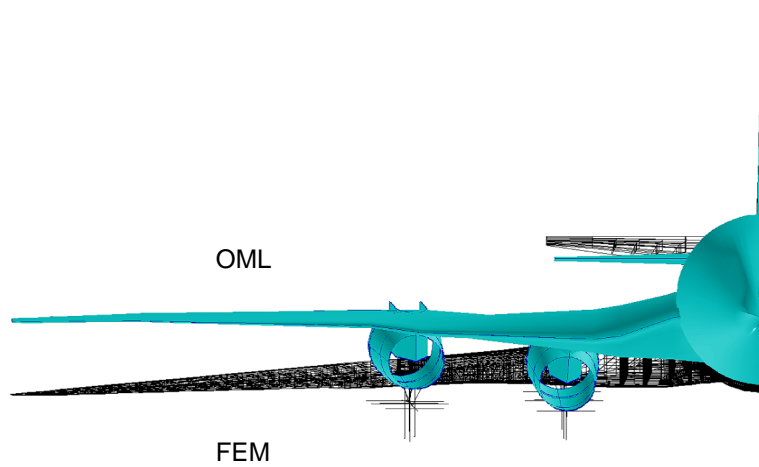
Figure 5. Finite-element model (FEM) for Aft-Tail configuration.



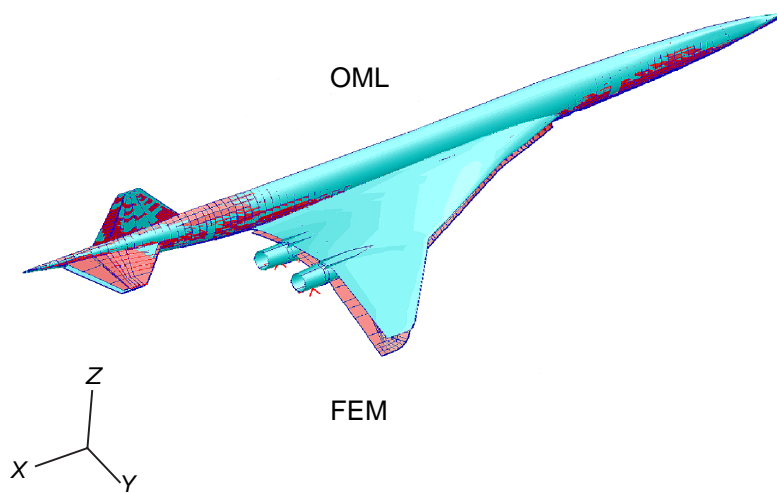
Figure 6. Outer mold line (OML) from IGES file for Aft-Tail configuration (basis for aerodynamic models).



(a) Front view of OML and FEM shaded surfaces superimposed.

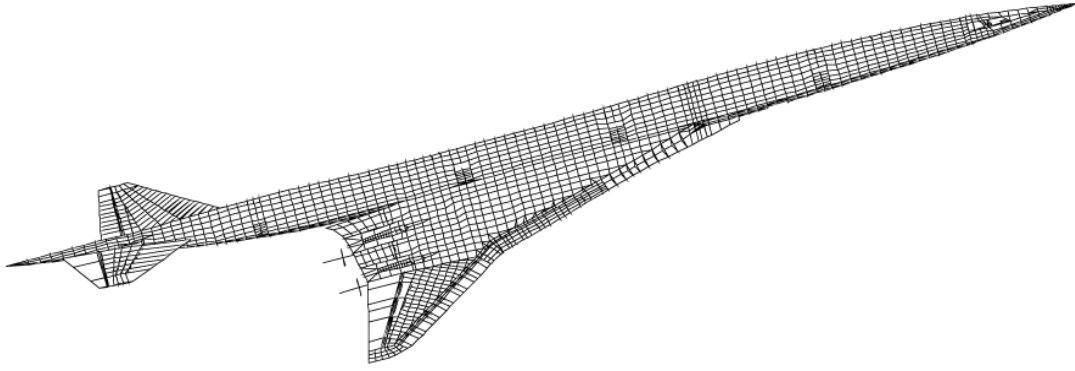


(b) Front view of OML shaded surface superimposed on wire-frame FEM.

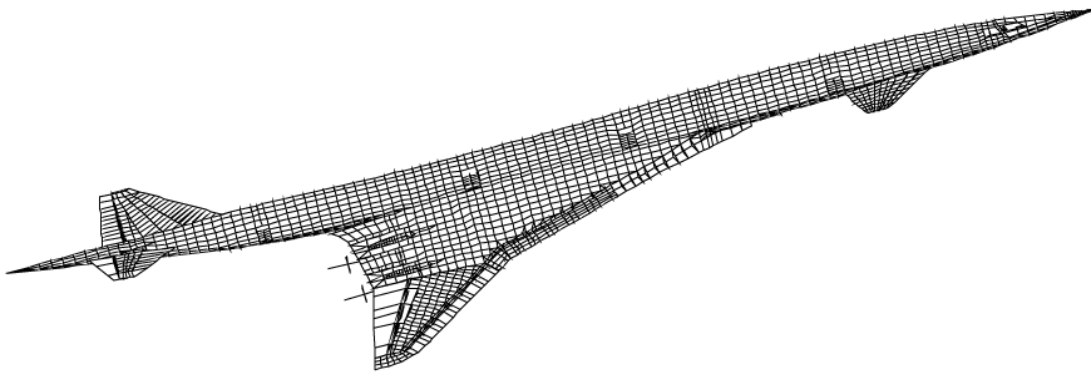


(c) OML and FEM shaded surfaces models superimposed.

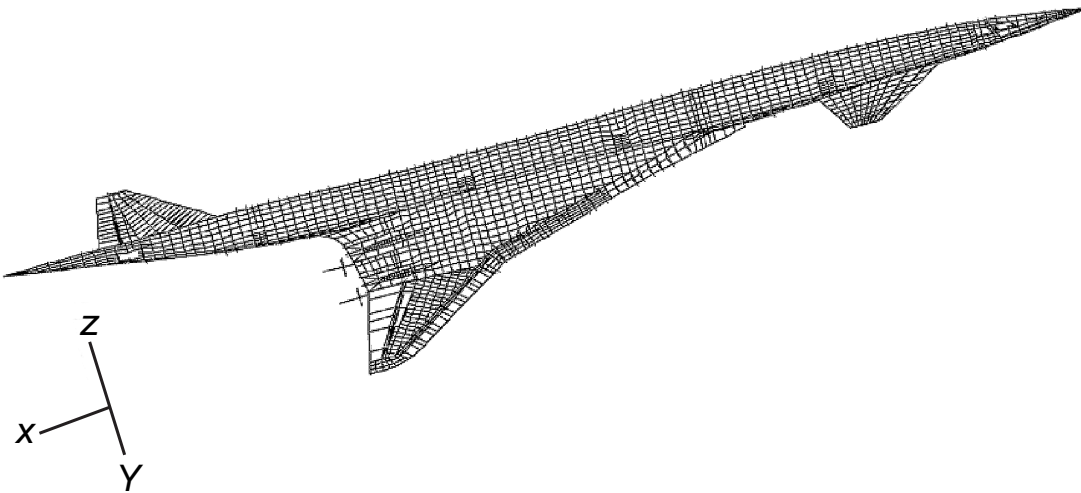
Figure 7. OML and FEM superimposed – Aft-Tail Configuration.



(a) Aft-Tail configuration.



(b) Three-Surface configuration.



(c) Canard configuration.

Figure 8. Finite element models.

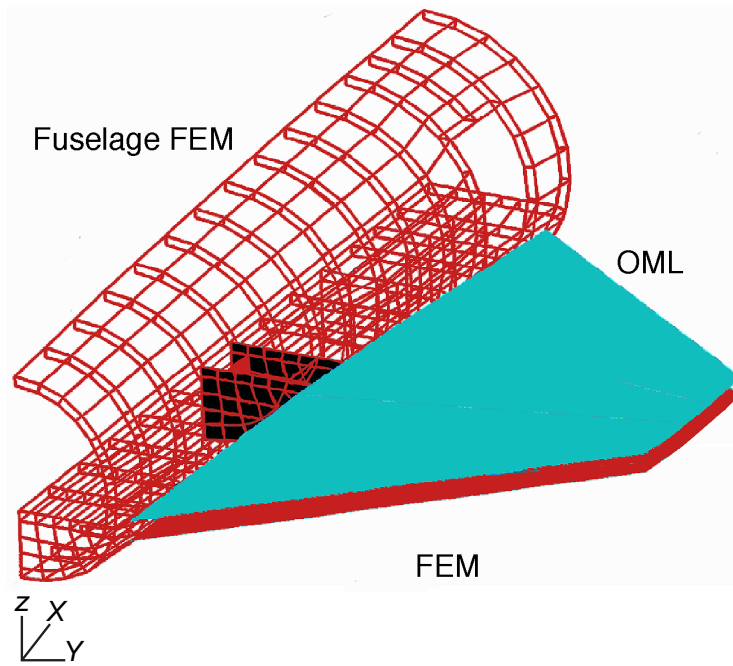


Figure 9. Canard OML model superimposed on the shaded FEM surface of canard and canard support structure for Canard configuration.

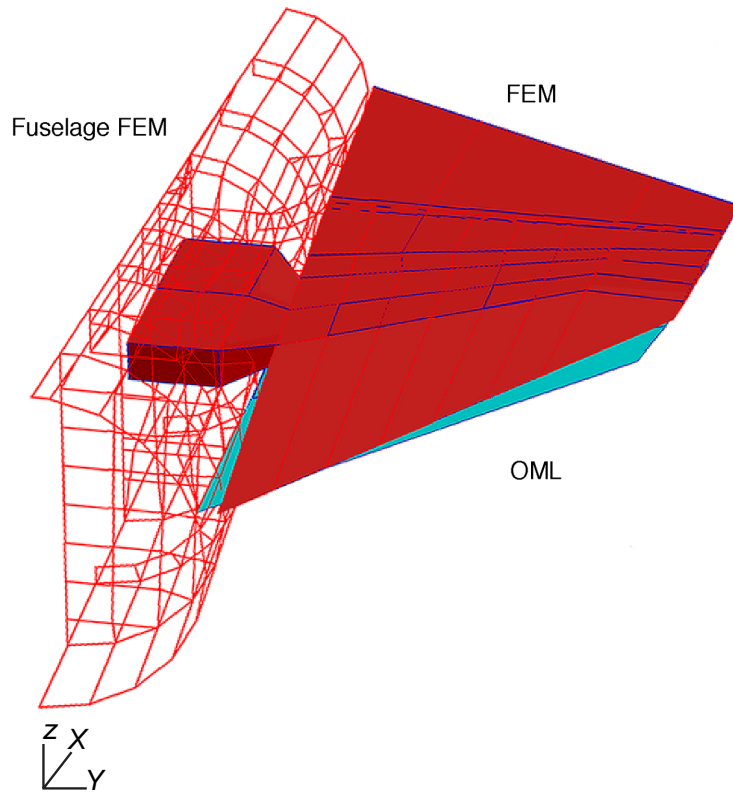


Figure 10. Shaded FEM surface of horizontal tail and support structure superimposed on horizontal tail OML for Three-Surface configuration.

Meshes used in resizing	
Mesh #	Location
1	Inboard wing
2	Outboard wing
3	Forward fuselage
4	Mid fuselage
5	Aft fuselage

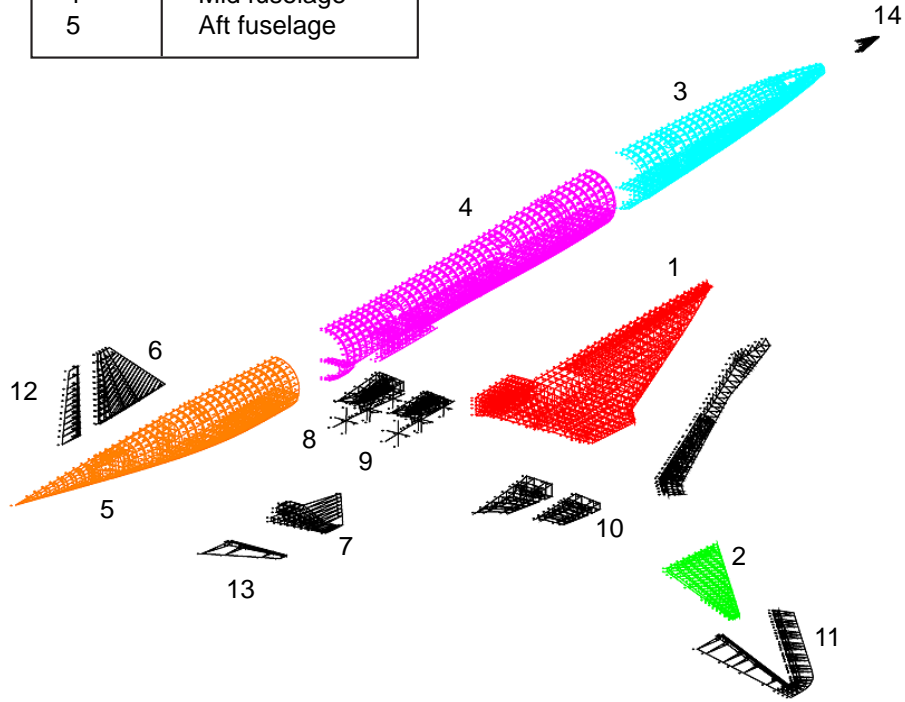


Figure 11. Weights model mesh.

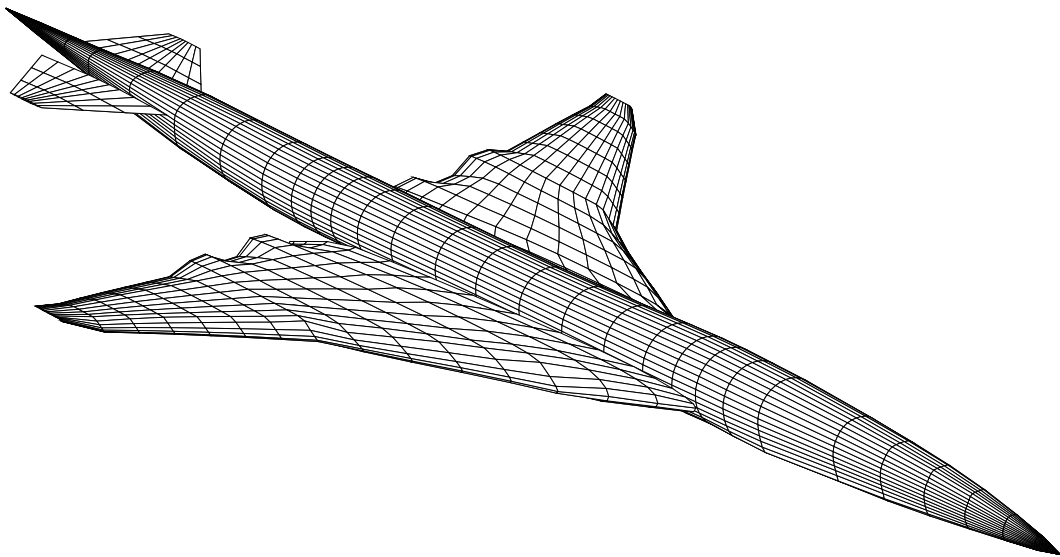


Figure 12. USSAERO grid for LX26 load condition for Aft-Tail configuration.

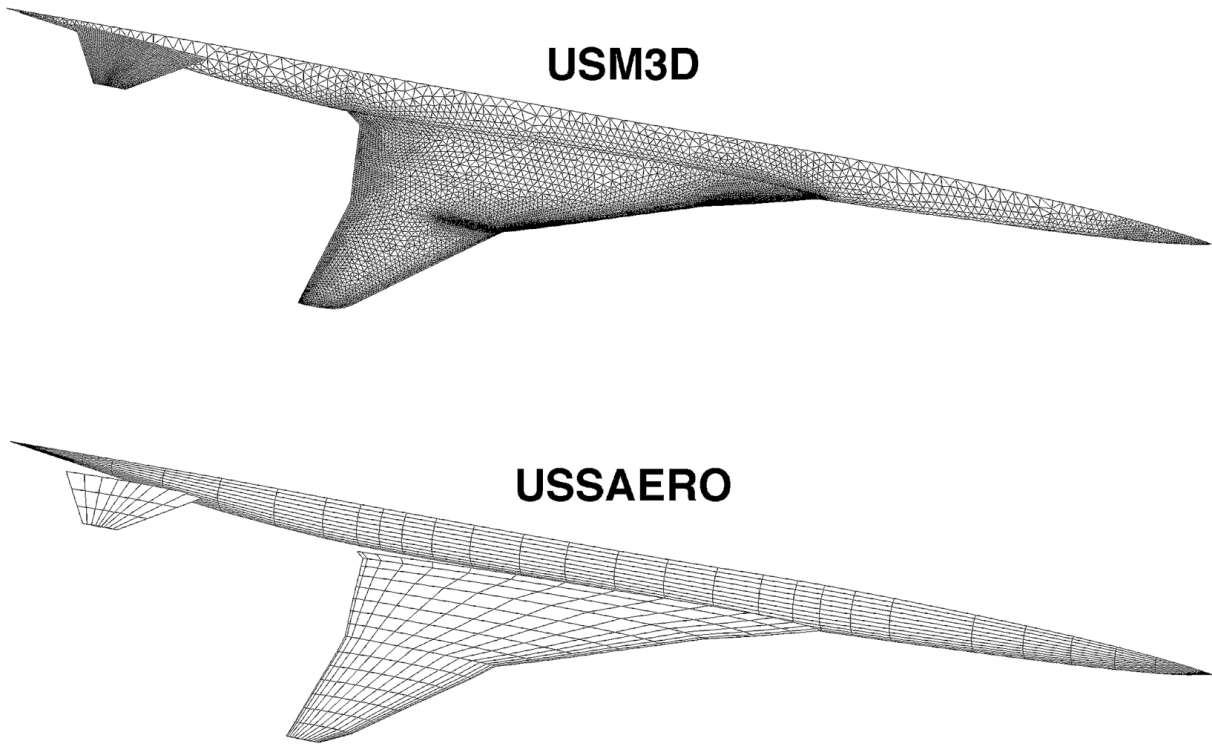


Figure 13. Surface grid distribution used in USM3D and USSAERO analyses for Aft-Tail configuration.

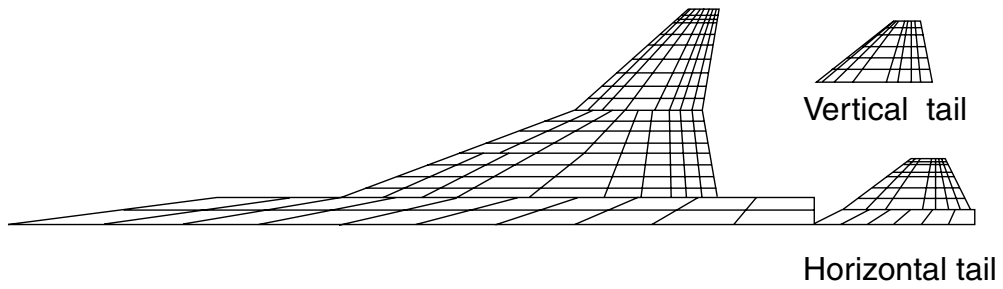
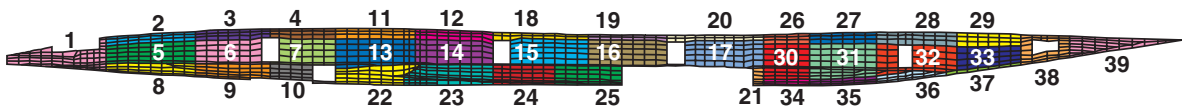
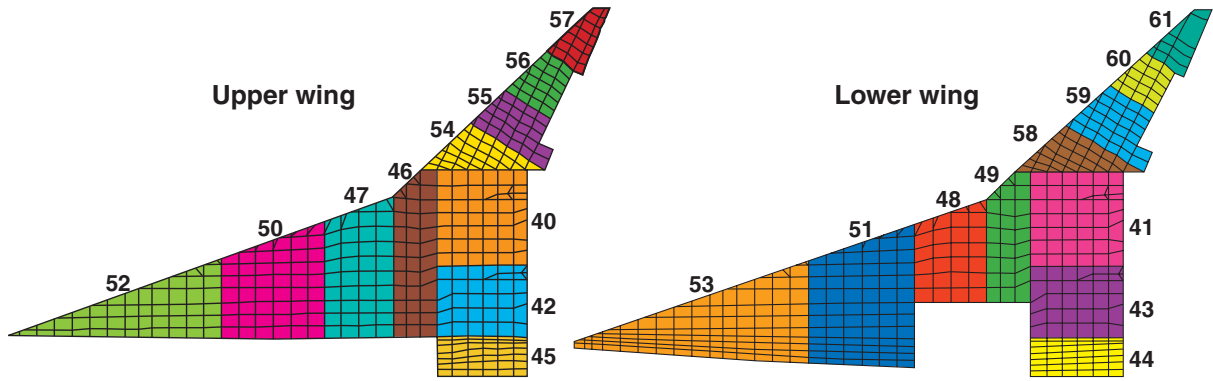
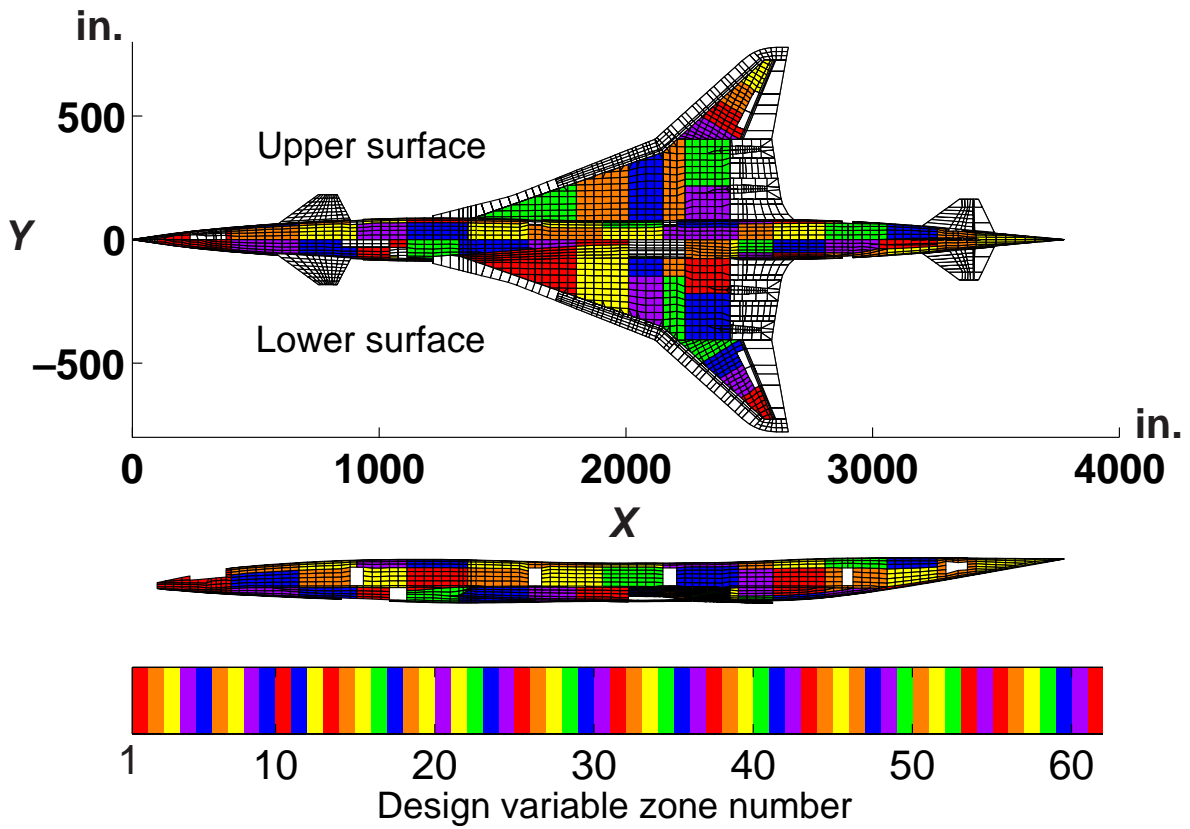


Figure 14. Box layout for flutter calculations.



(a) Exploded view on Aft-Tail configuration.



(b) Assembled view on the Three-Surface configuration.

Figure 15. Design variable zones used for all three configurations.

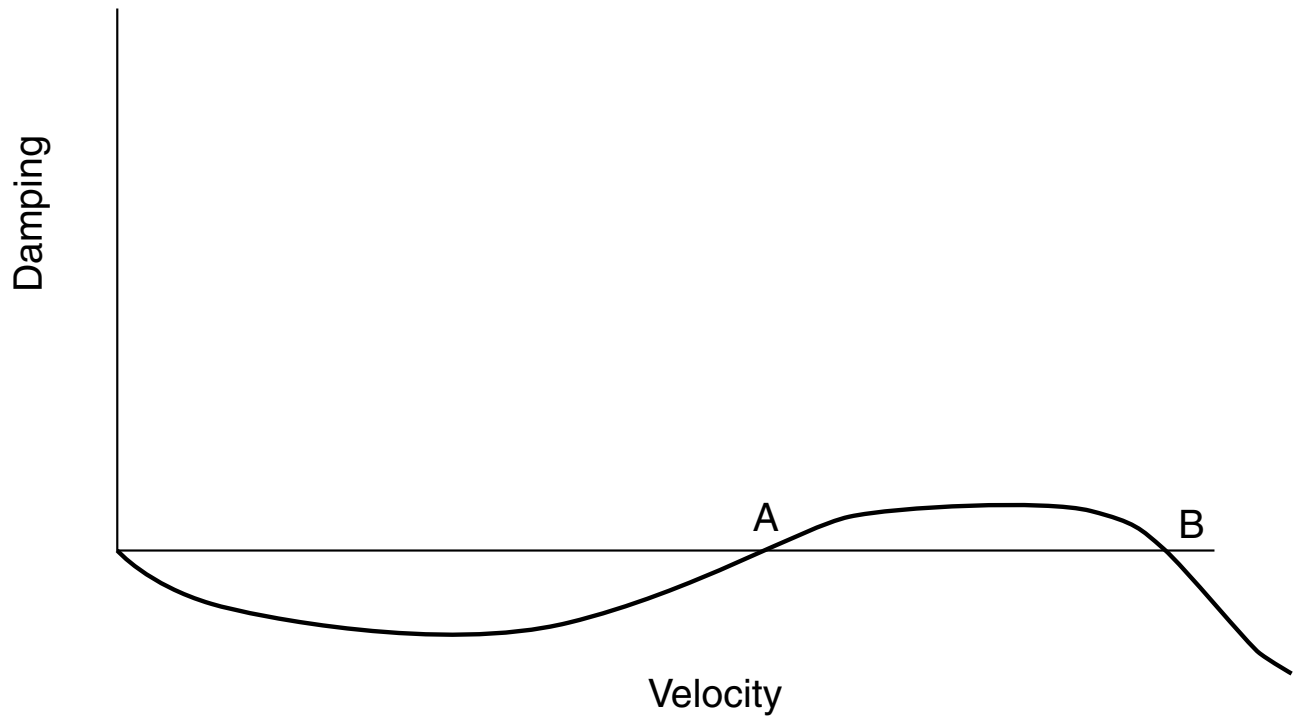
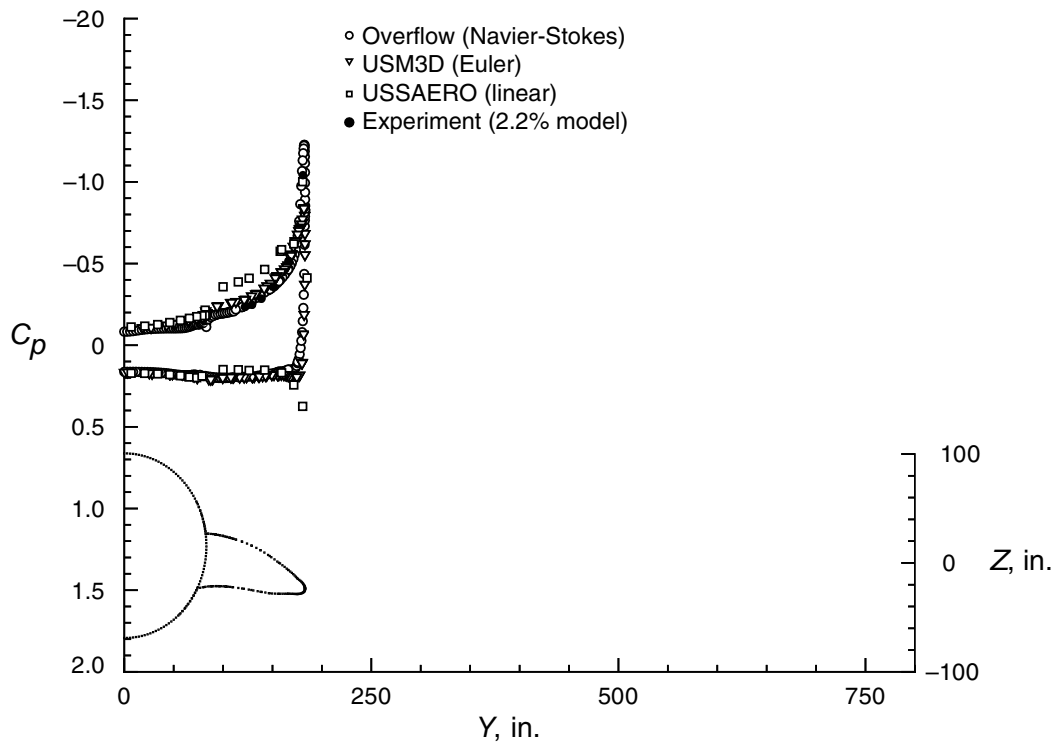
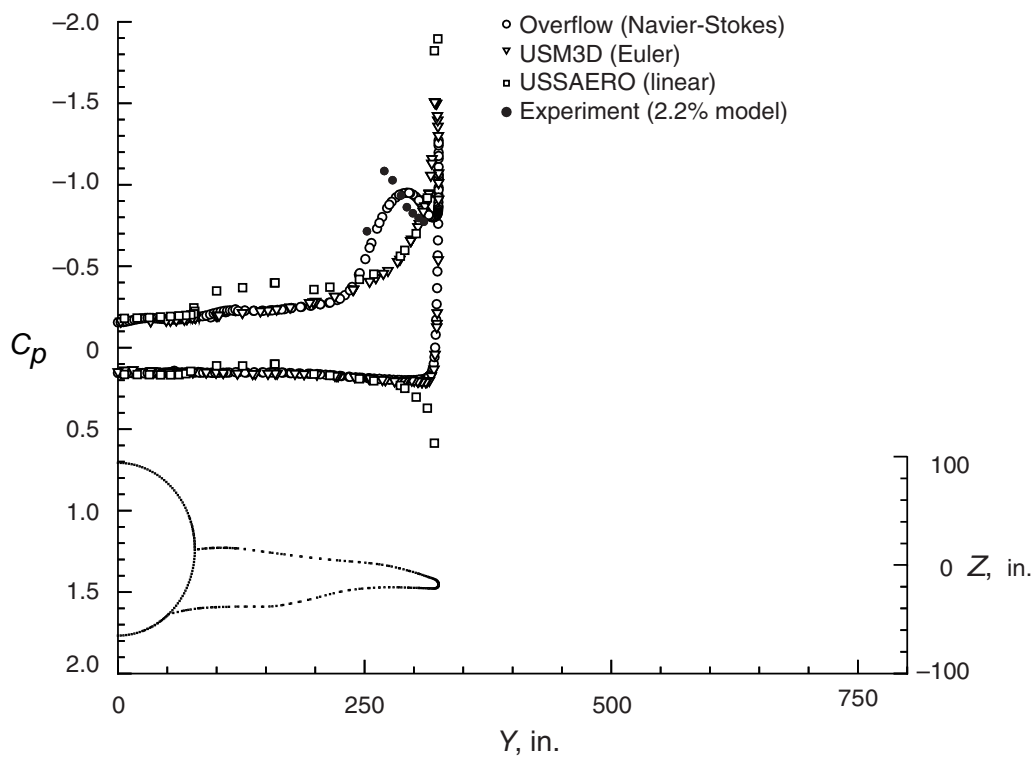


Figure 16. Sketch of hump mode

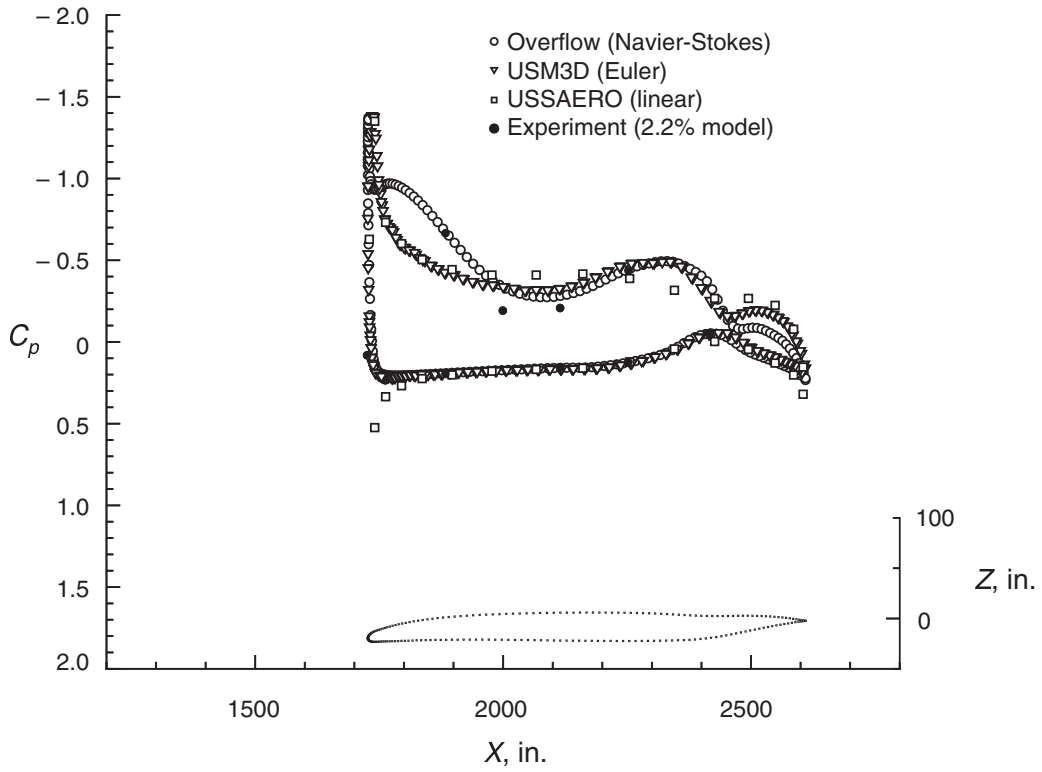


(a)  $X = 1550$  section cut.

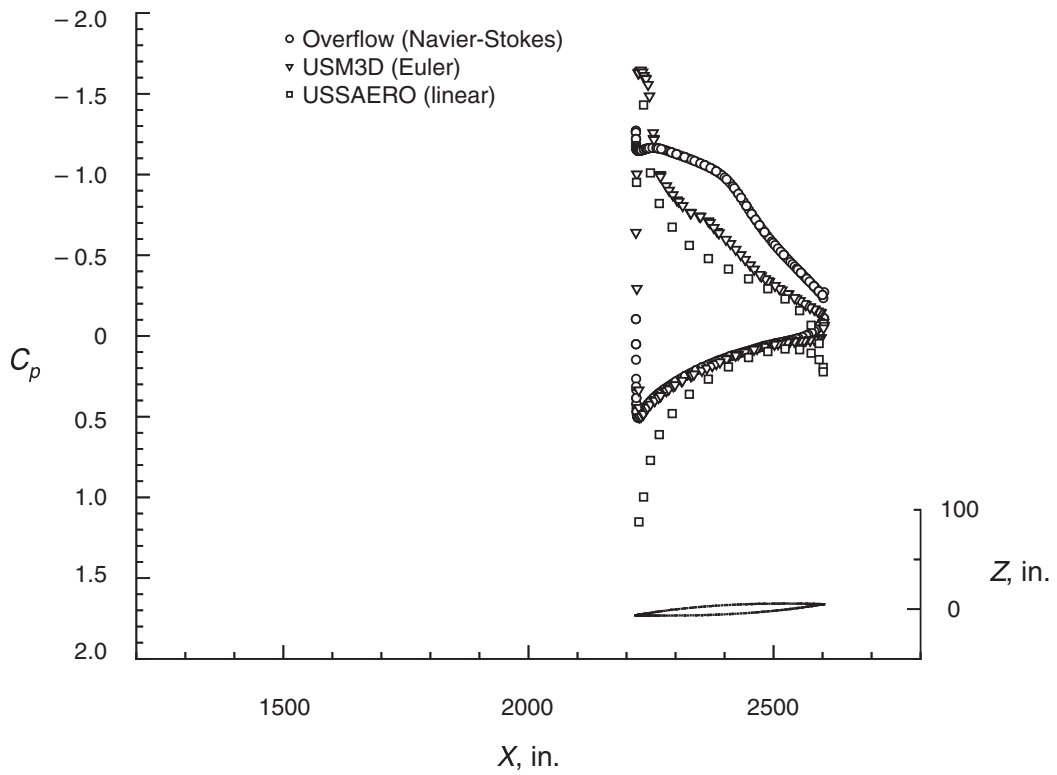


(b)  $X = 1910$  section cut.

Figure 17. Wing pressure distribution comparison at  $\alpha = 10.2^\circ$  and  $M = 0.9$  for Aft-Tail configuration.

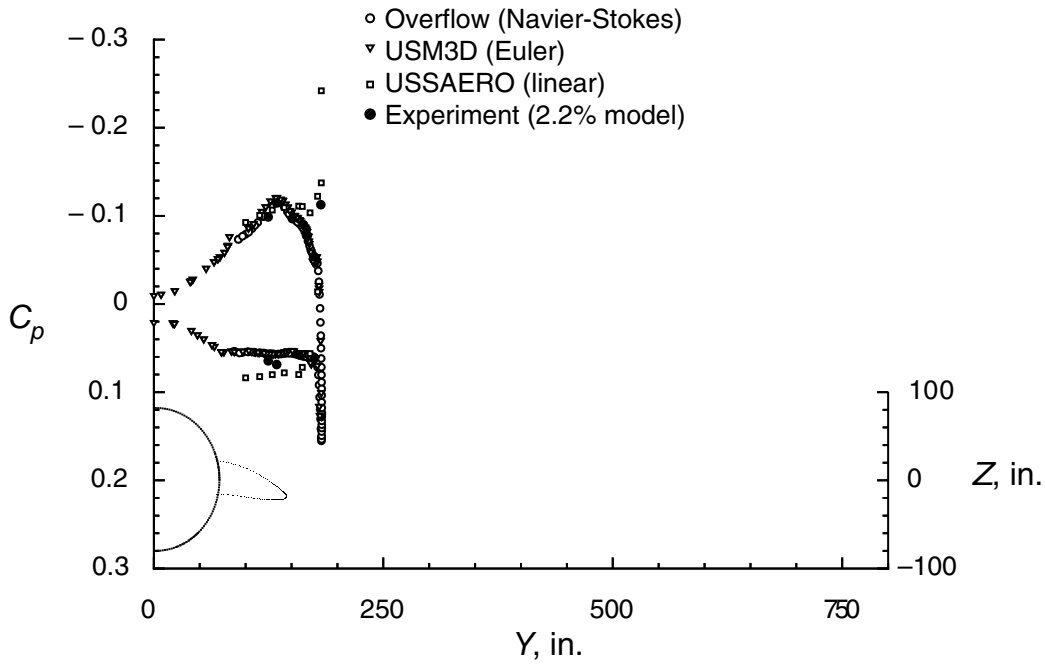


(c)  $Y = 253$  section cut.

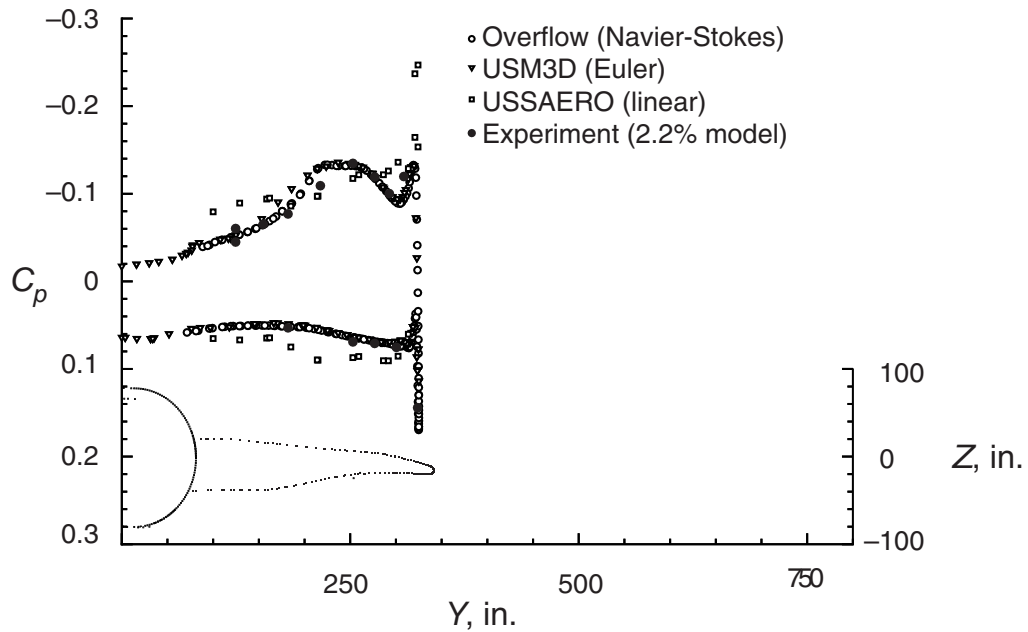


(d)  $Y = 500$  section cut.

Figure 17. Concluded.

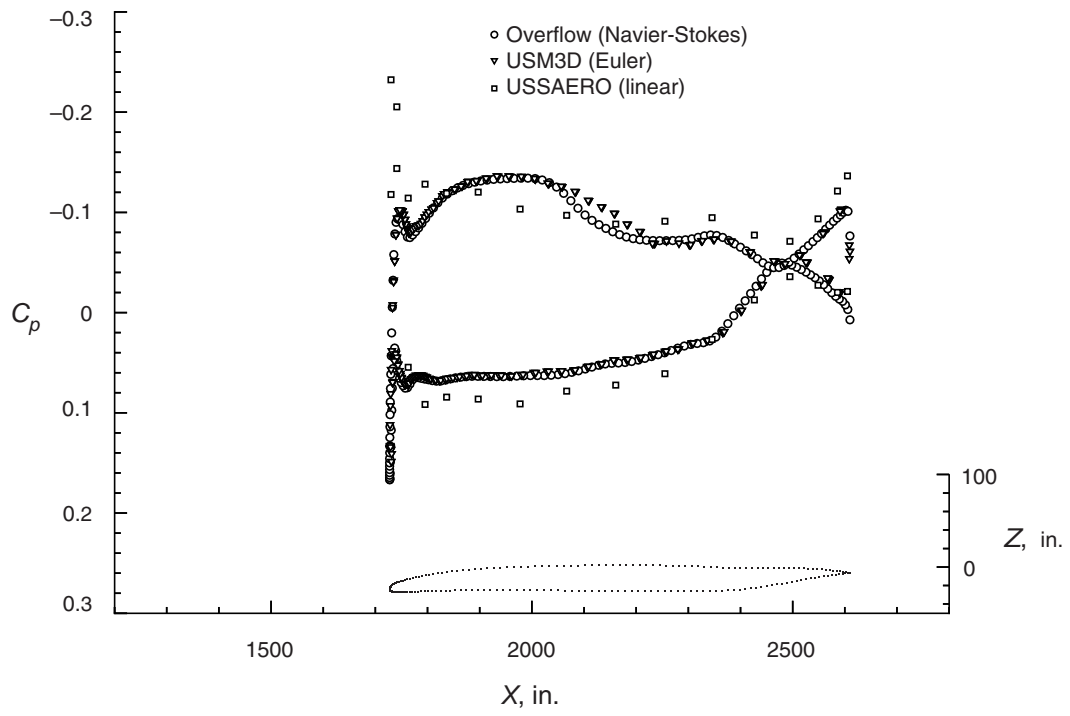


(a)  $X = 1550$  section cut.

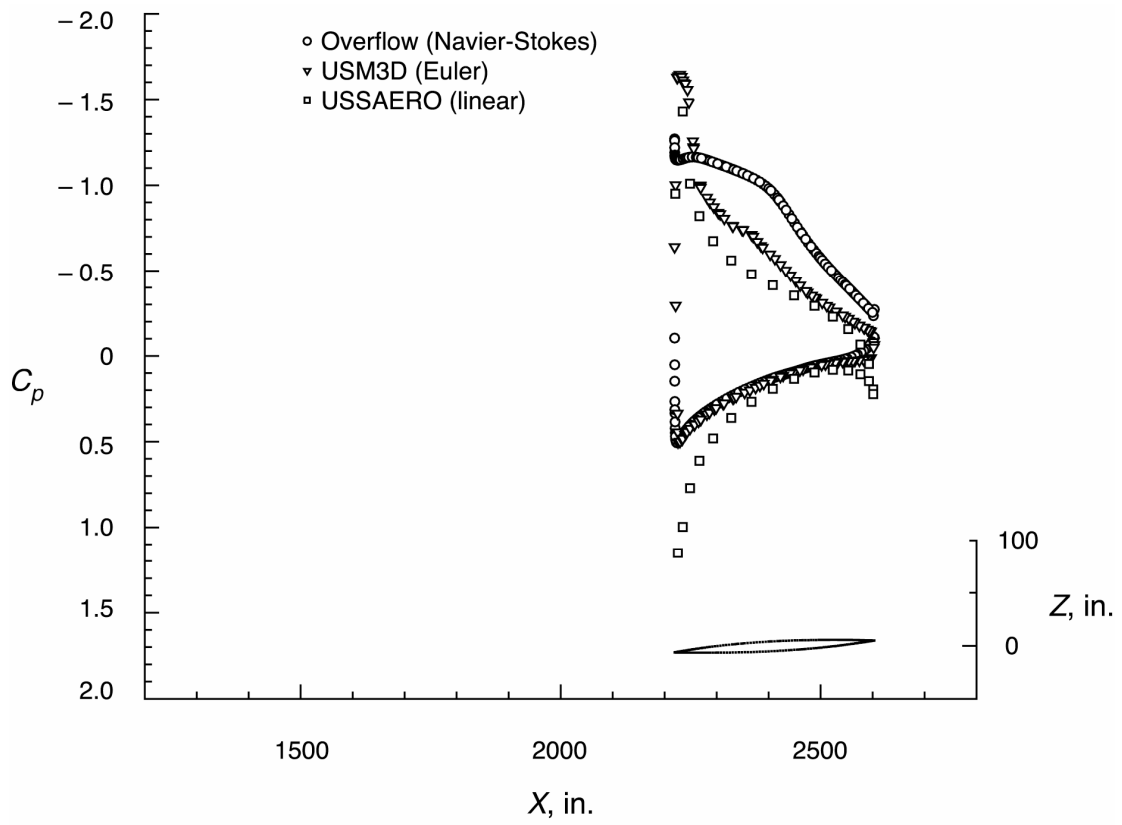


(b)  $X = 1910$  section cut.

Figure 18. Wing pressure distribution comparison at  $\alpha = 4.62^\circ$  and  $M = 2.4$  for Aft-Tail configuration.



(c)  $Y = 253$  section cut.



(d)  $Y = 500$  section cut.

Figure 18. Concluded.

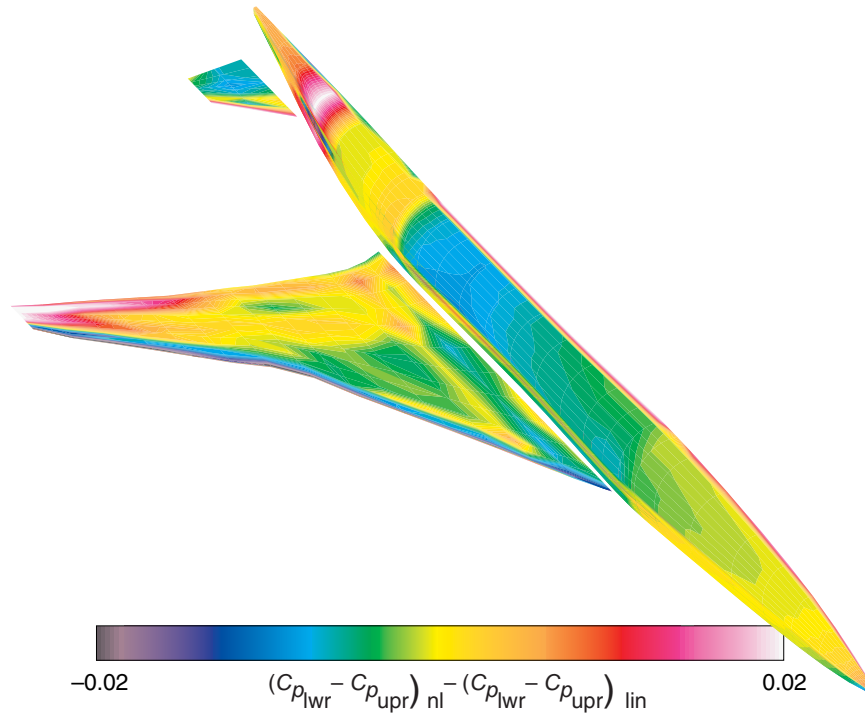


Figure 19. Distribution of nondimensional nonlinear corrections for load case LX43; rigid: Aft-Tail configuration.

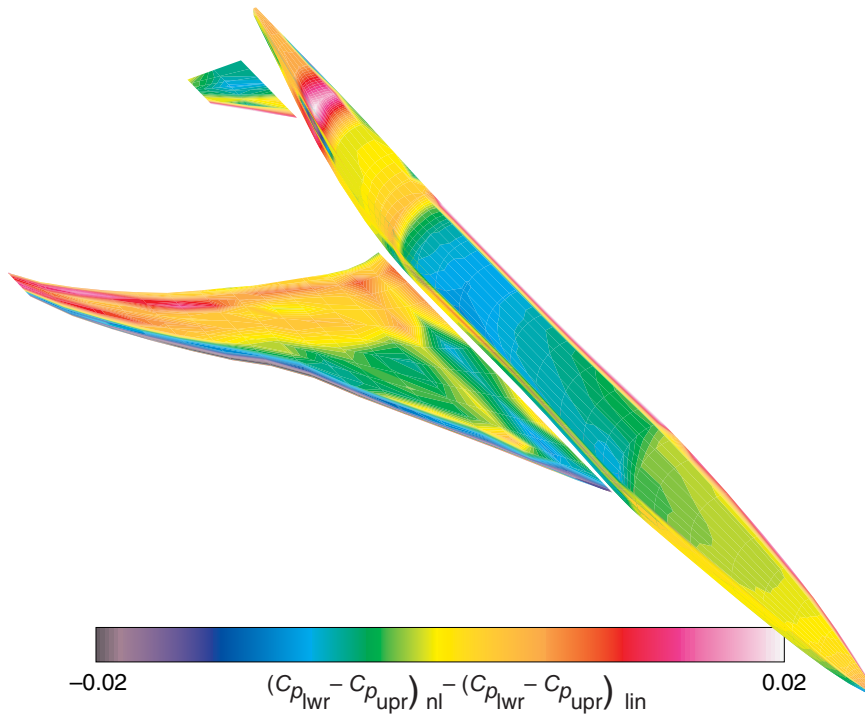


Figure 20. Distribution of nondimensional nonlinear corrections for load case LX43, with aeroelastic deformation: Aft-Tail configuration.

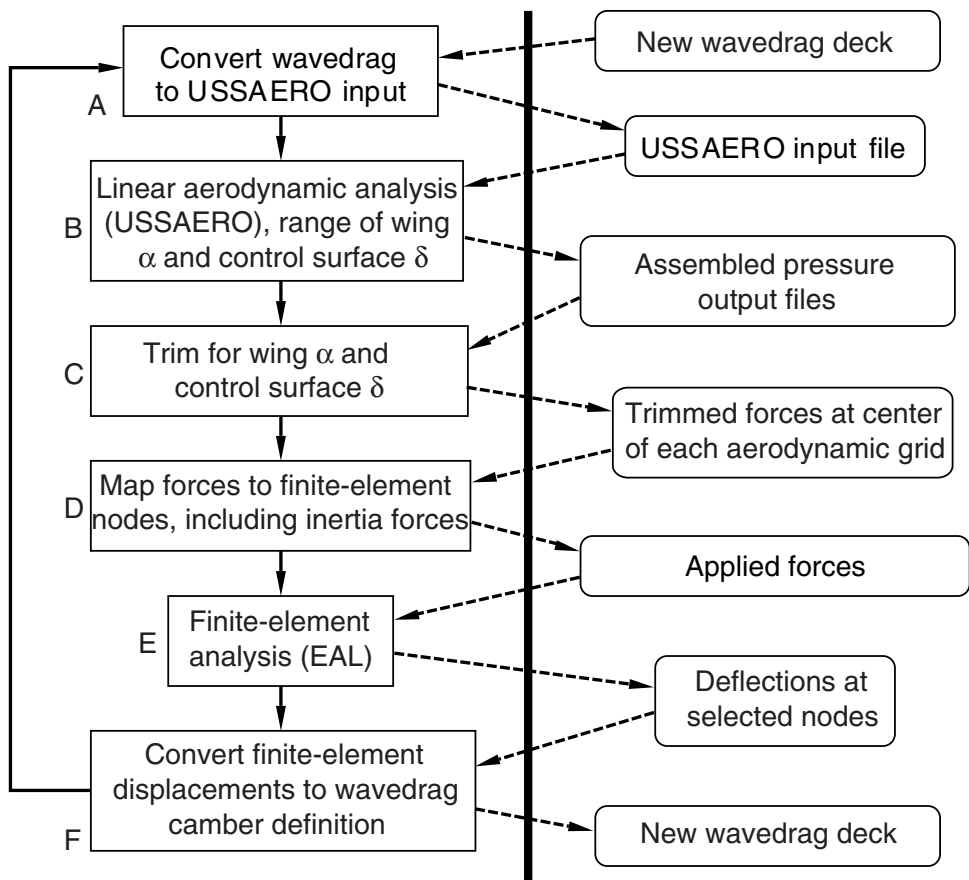


Figure 21. Trim loop process.

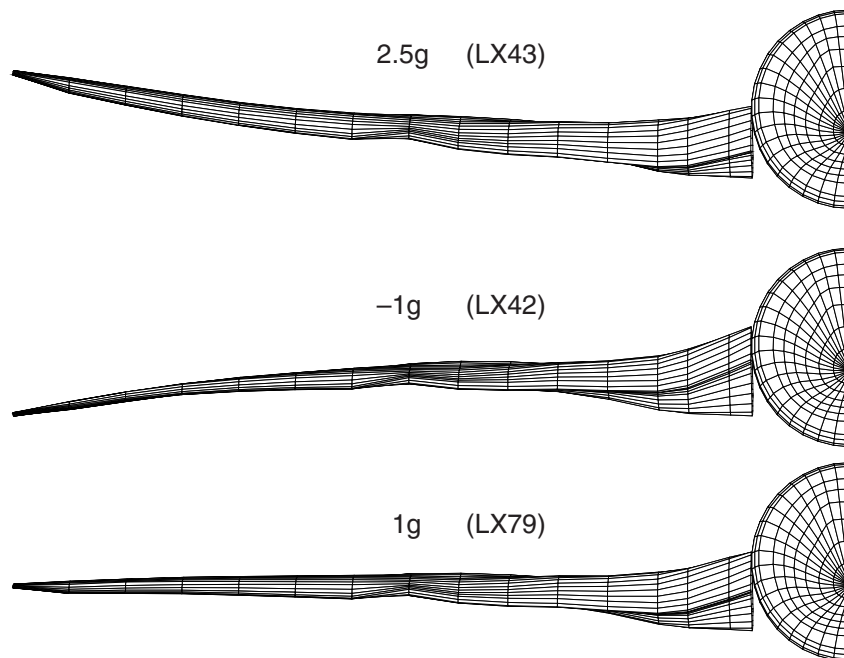


Figure 22. Wing deflections in wavedrag definition for  $M = 0.95$ ; Aft-Tail configuration.

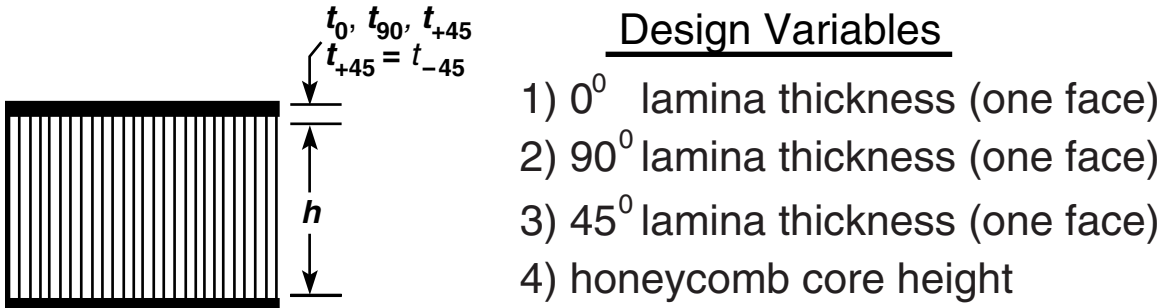


Figure 23. Sketch of composite honeycomb sandwich panel, showing design variables.

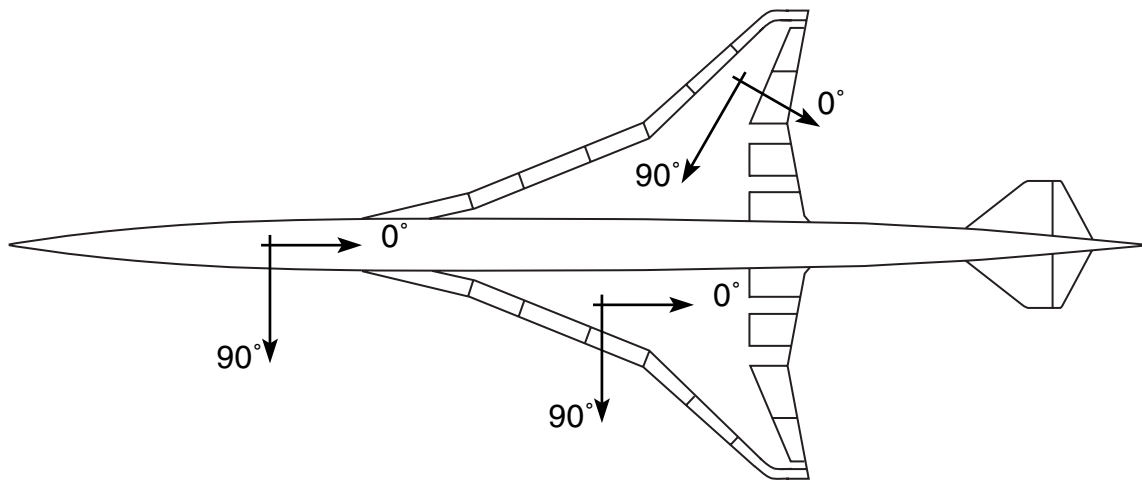


Figure 24. Sketch of composite ply orientation.

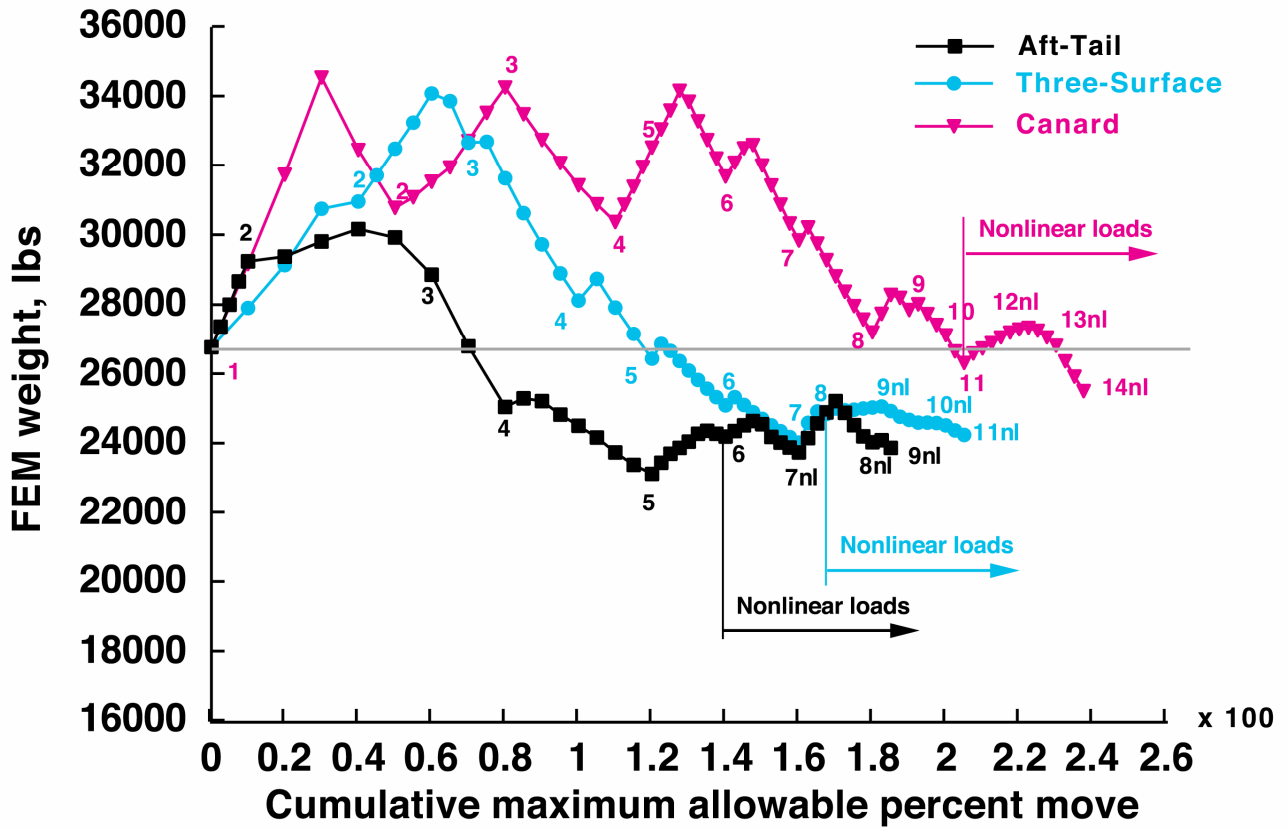


Figure 25. History of resized FEM weight for full models.

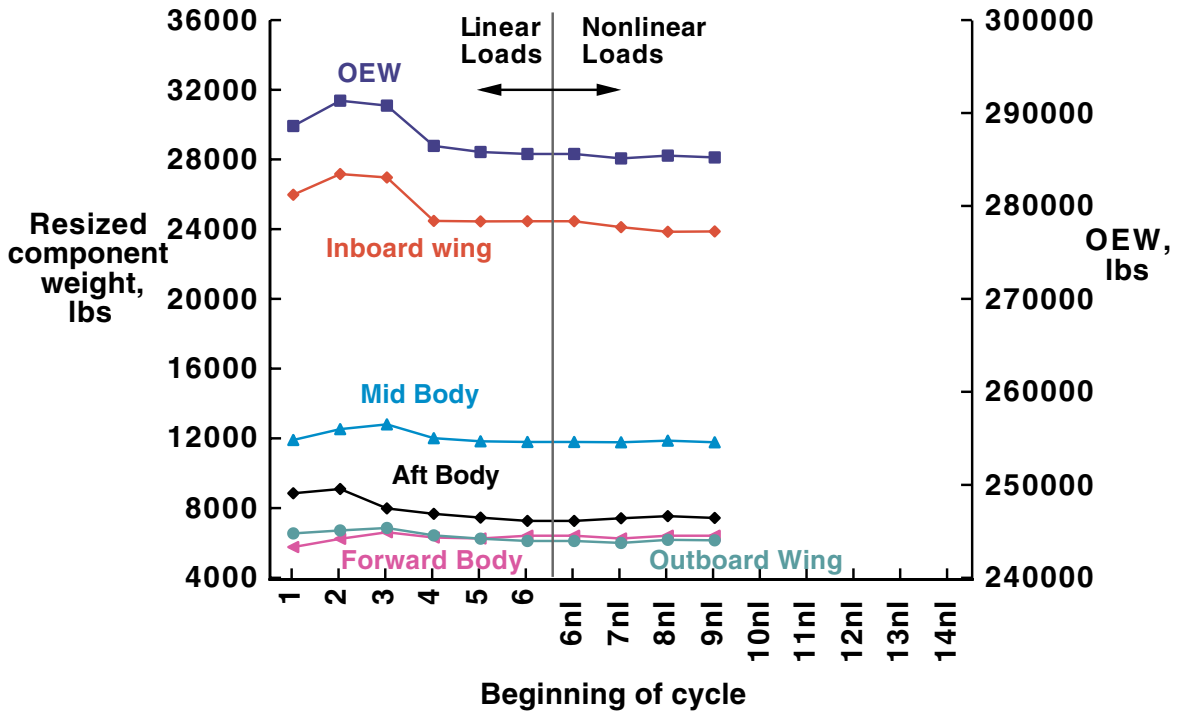


Figure 26. History of total (OEW) and resized component weights obtained from AM/FM; full model; Aft-Tail configuration.

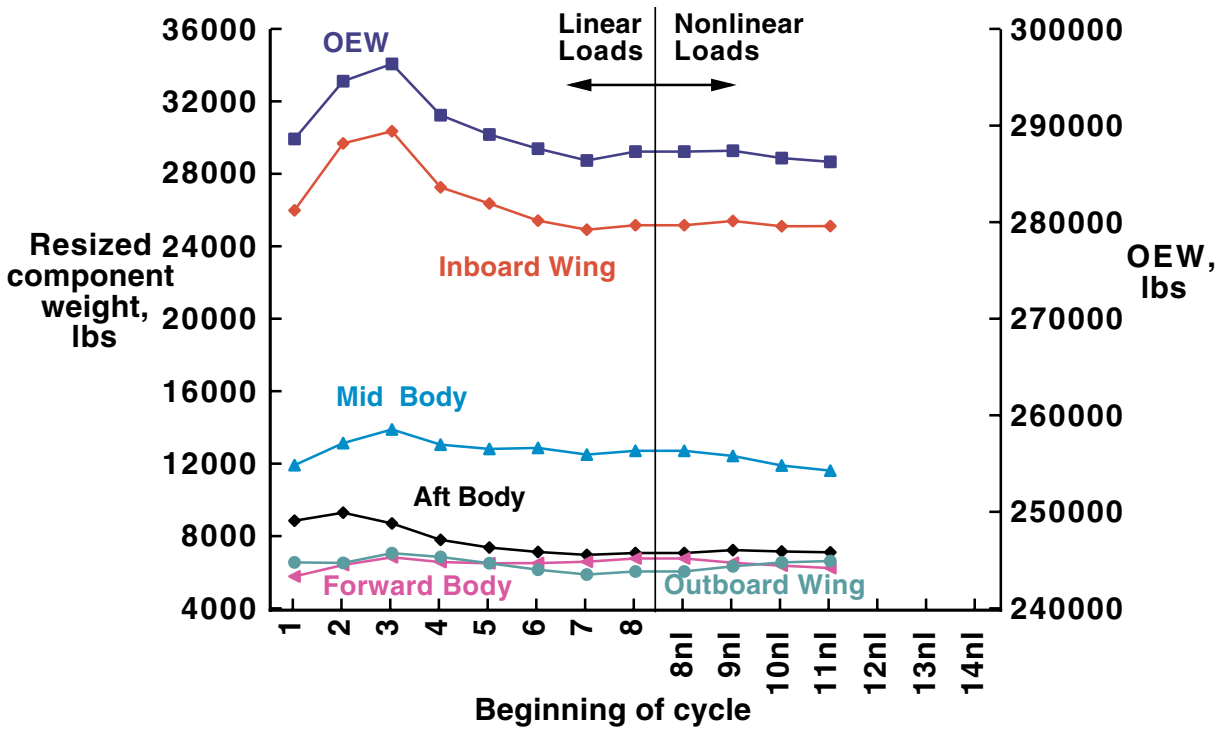


Figure 27. History of total (OEW) and resized component weights obtained from AM/FM; full model; Three-Surface configuration.

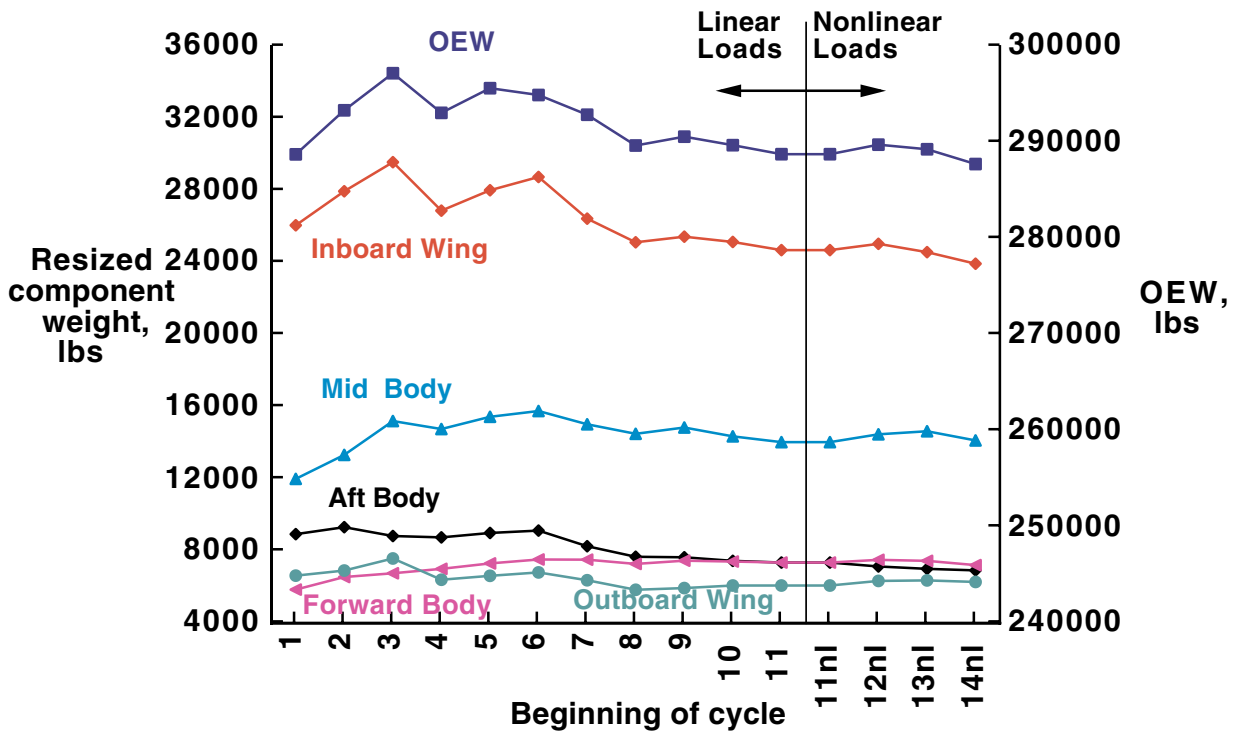


Figure 28. History of total (OEW) and resized component weights obtained from AM/FM; full model; Canard configuration.

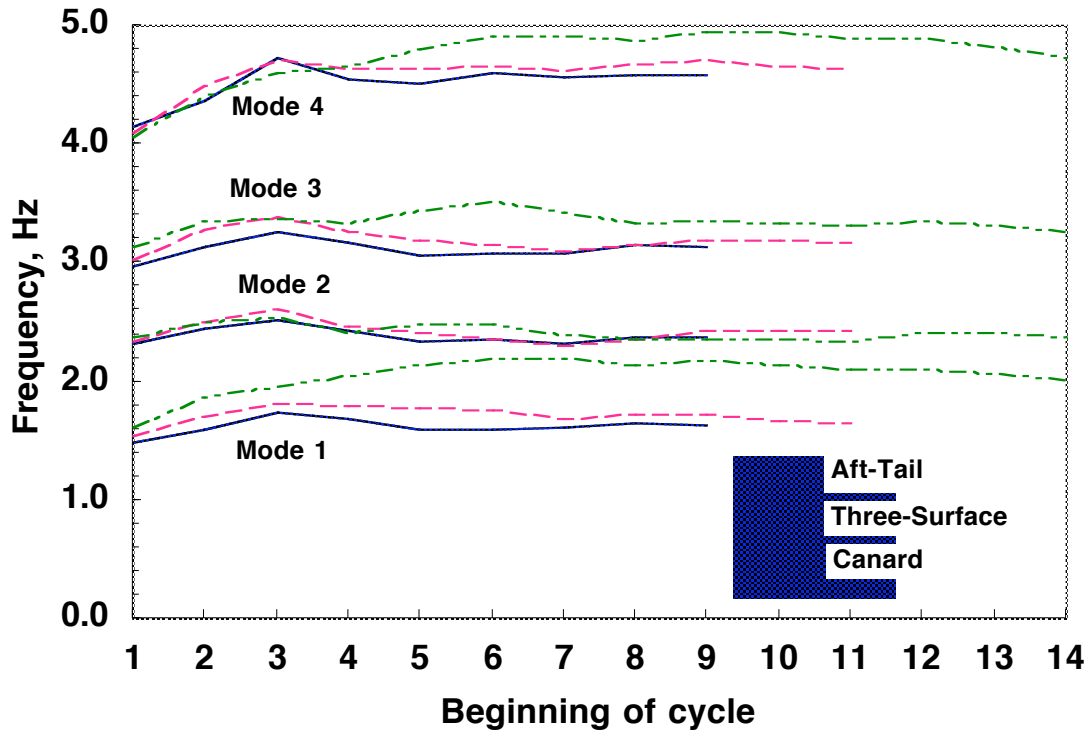


Figure 29. Comparison of frequencies for first four vibration modes for all configurations for mass case 1.

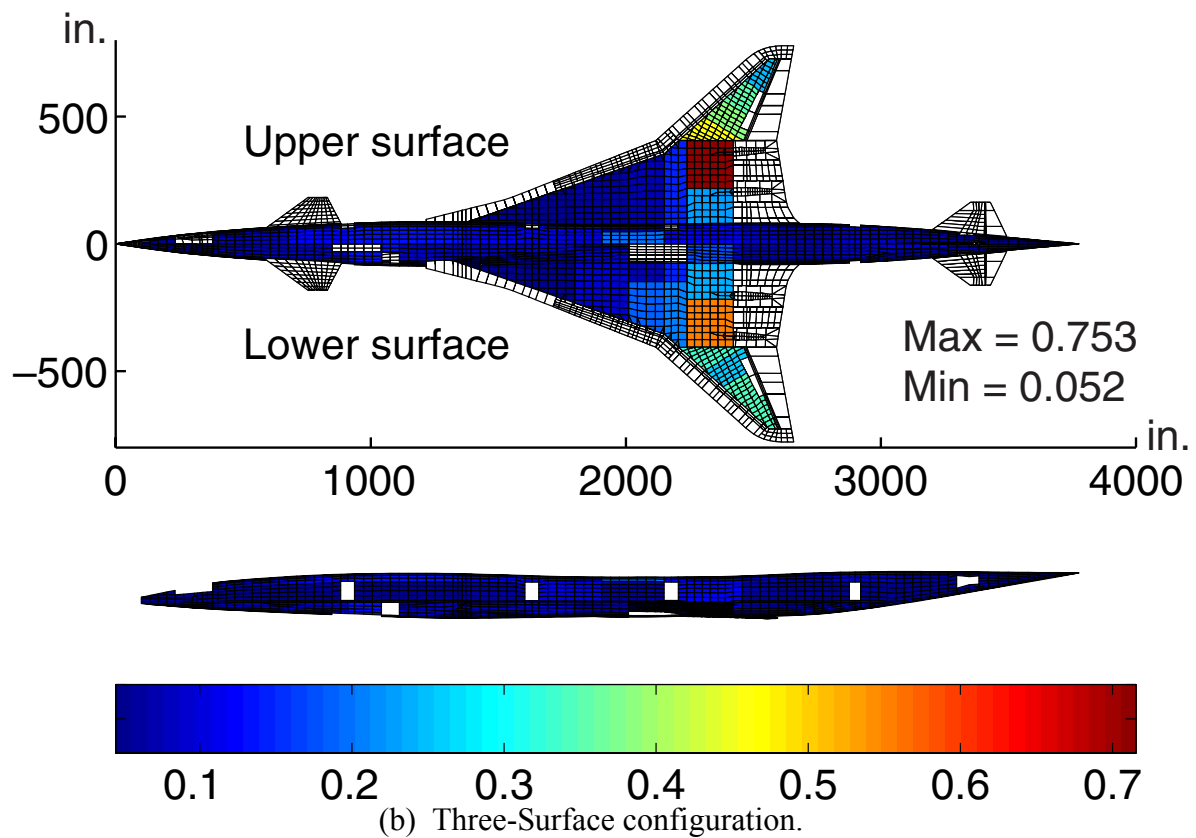
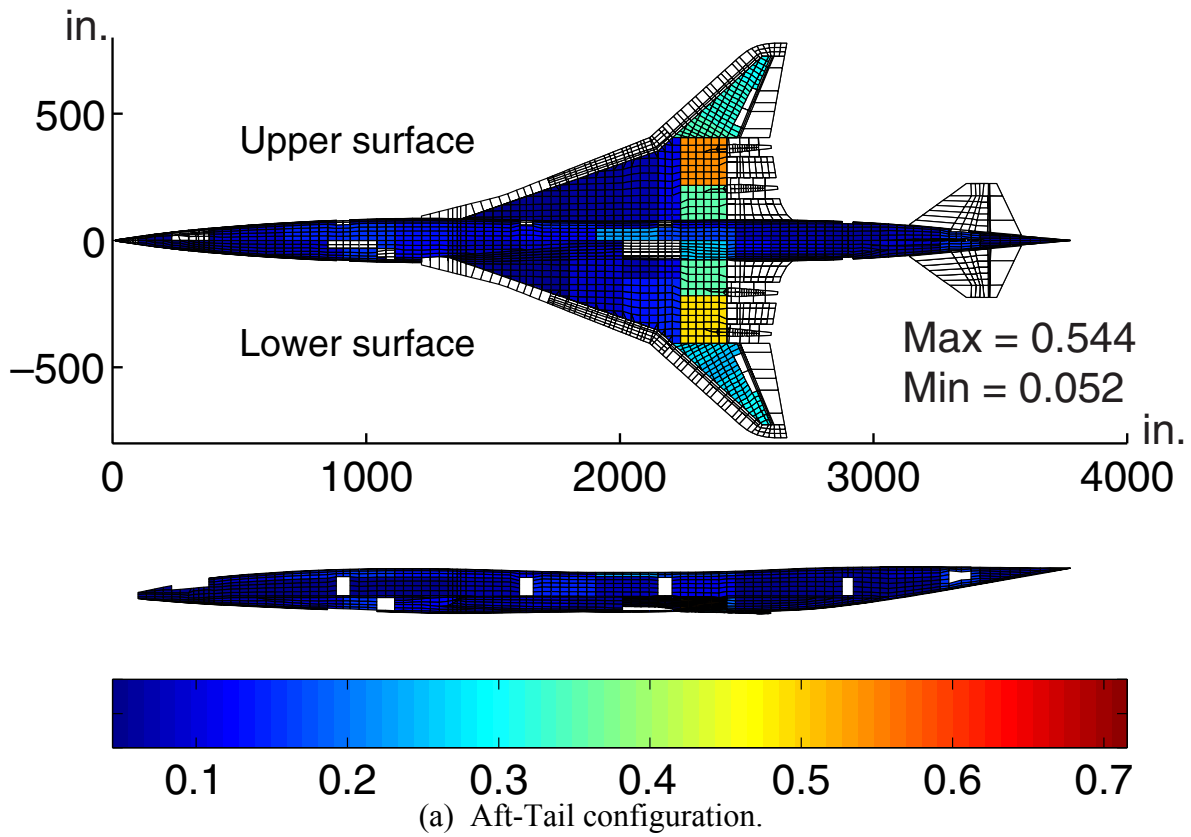
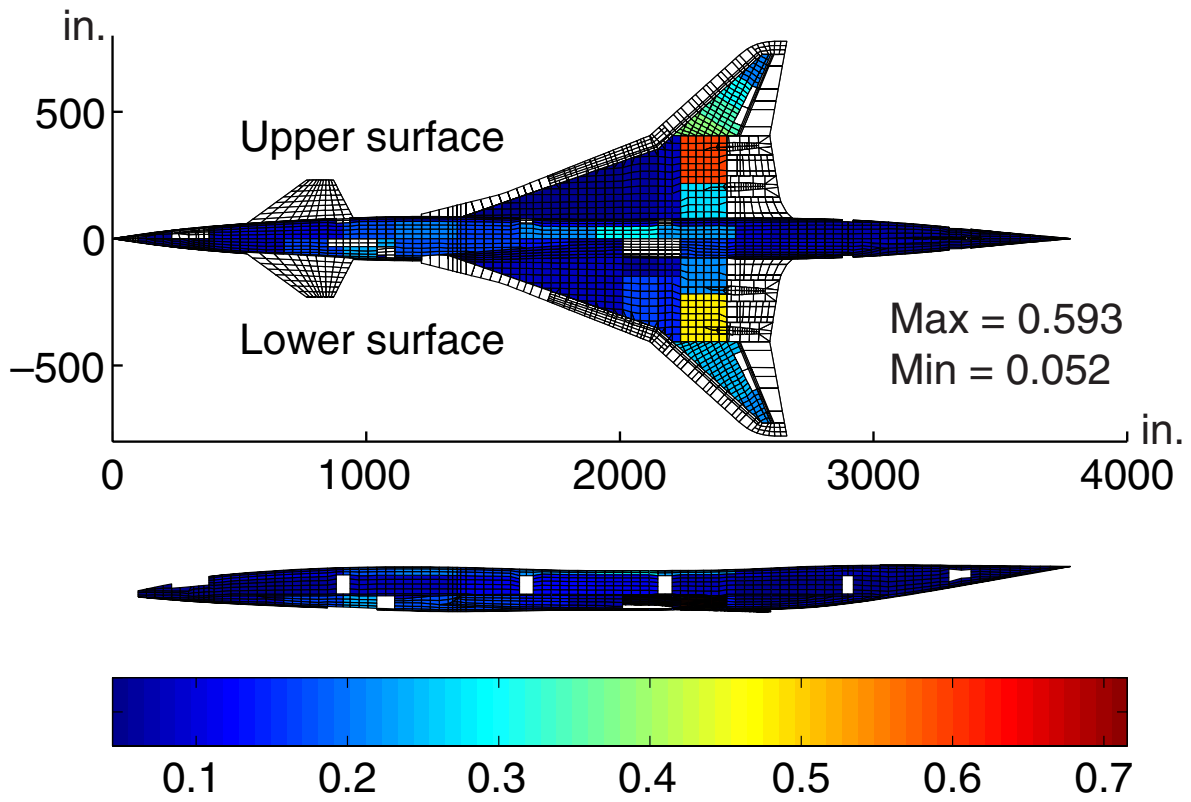


Figure 30. Total ply thickness of two face sheets for nonlinear designs for all configurations (in).



(c) Canard configuration.  
Figure 30. Concluded.

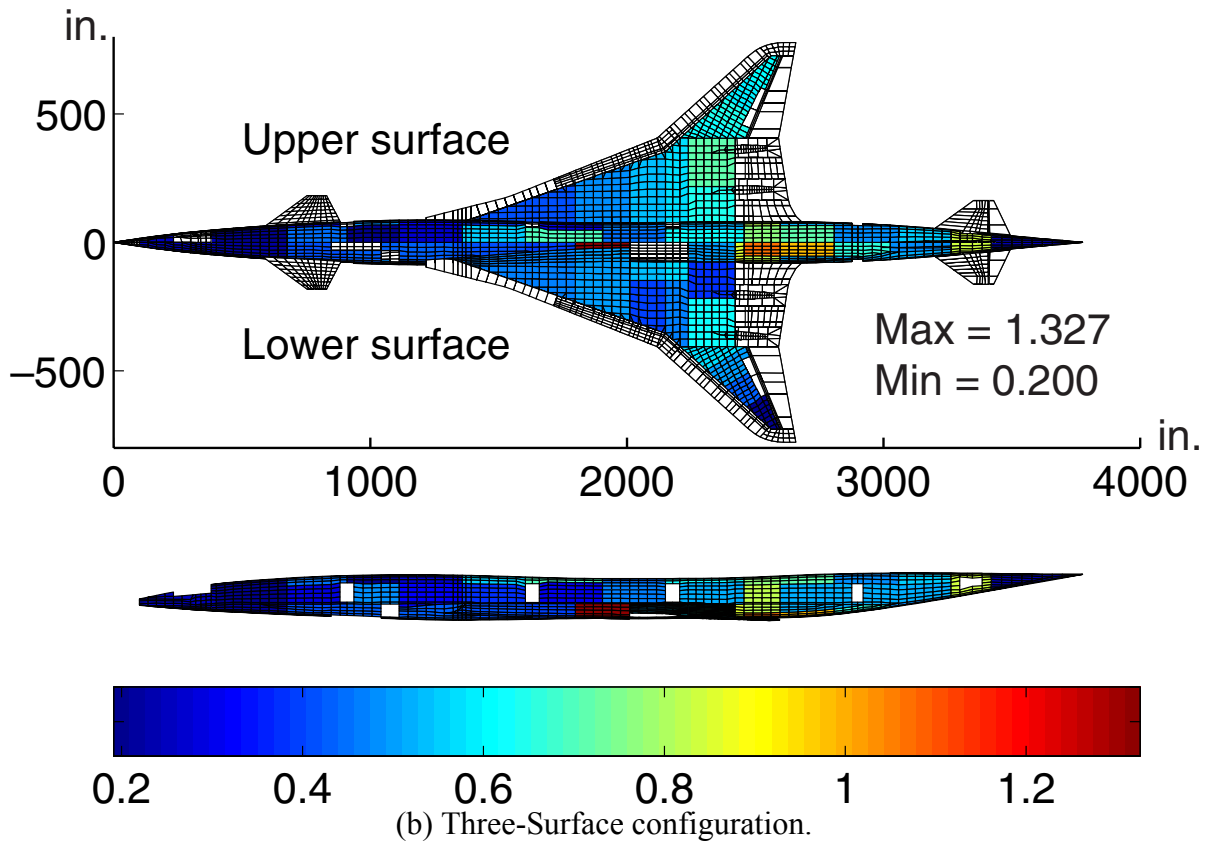
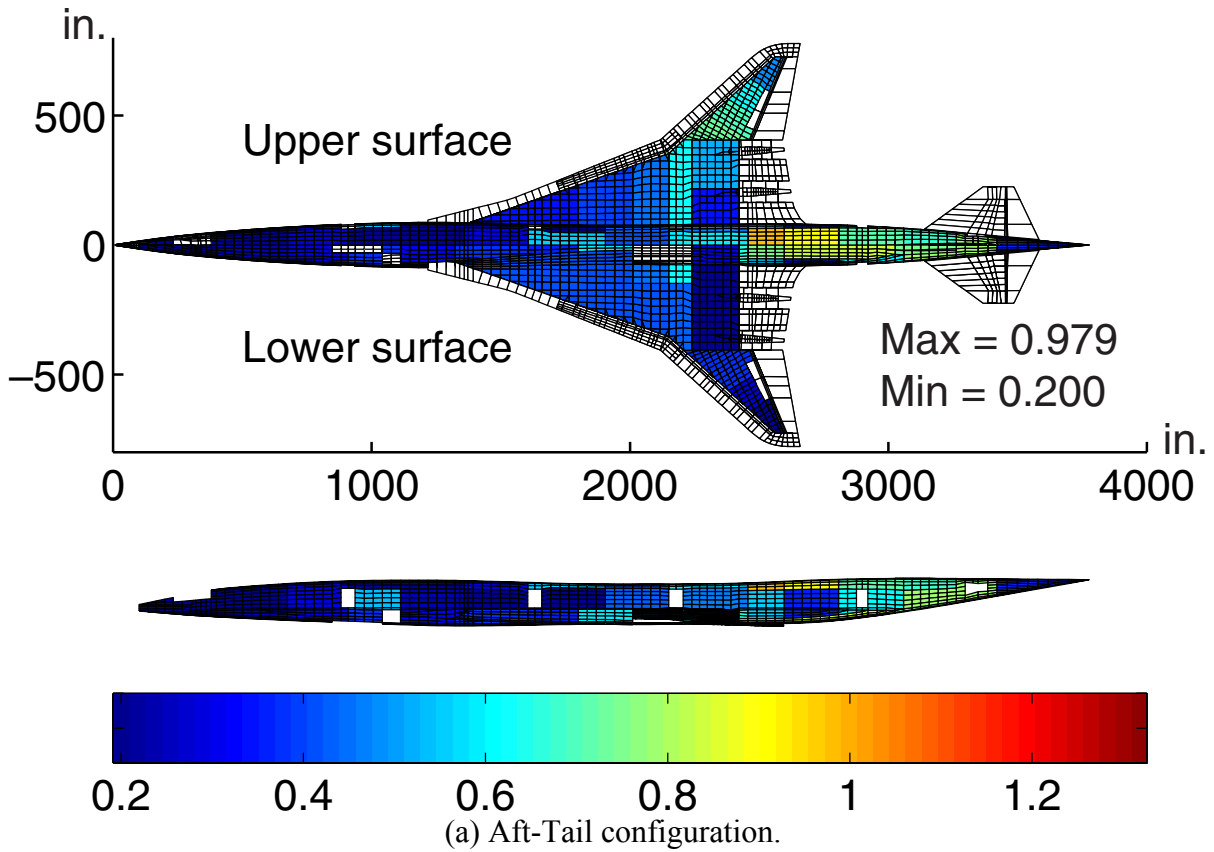
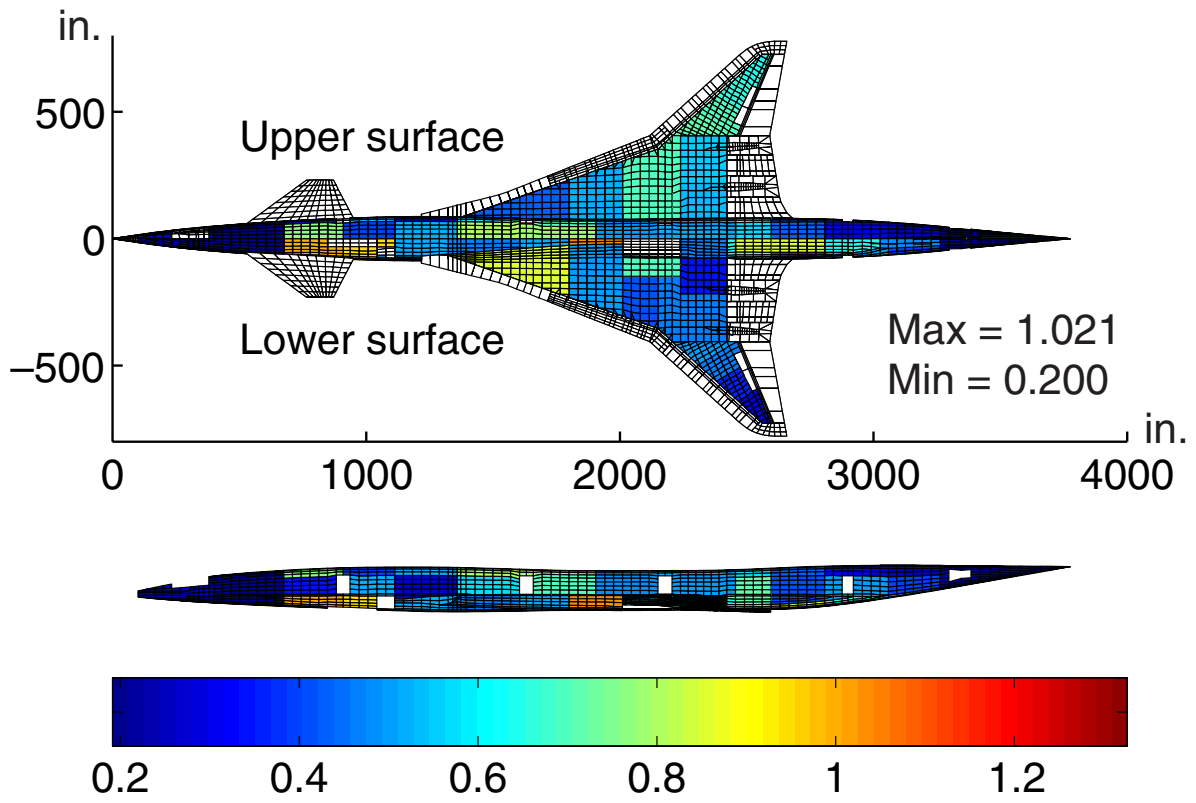


Figure 31. Total core thickness for nonlinear designs for all configurations (in).



(c) Canard configuration.  
Figure 31. Concluded.

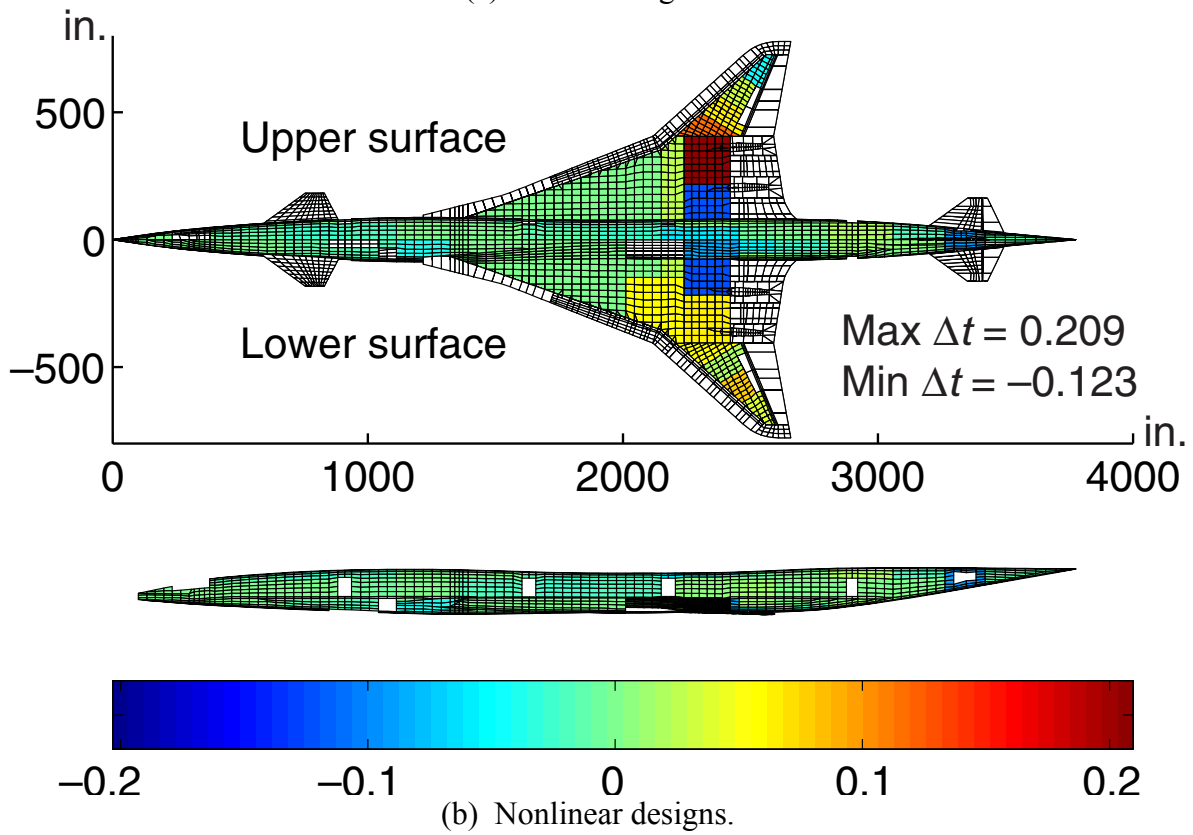
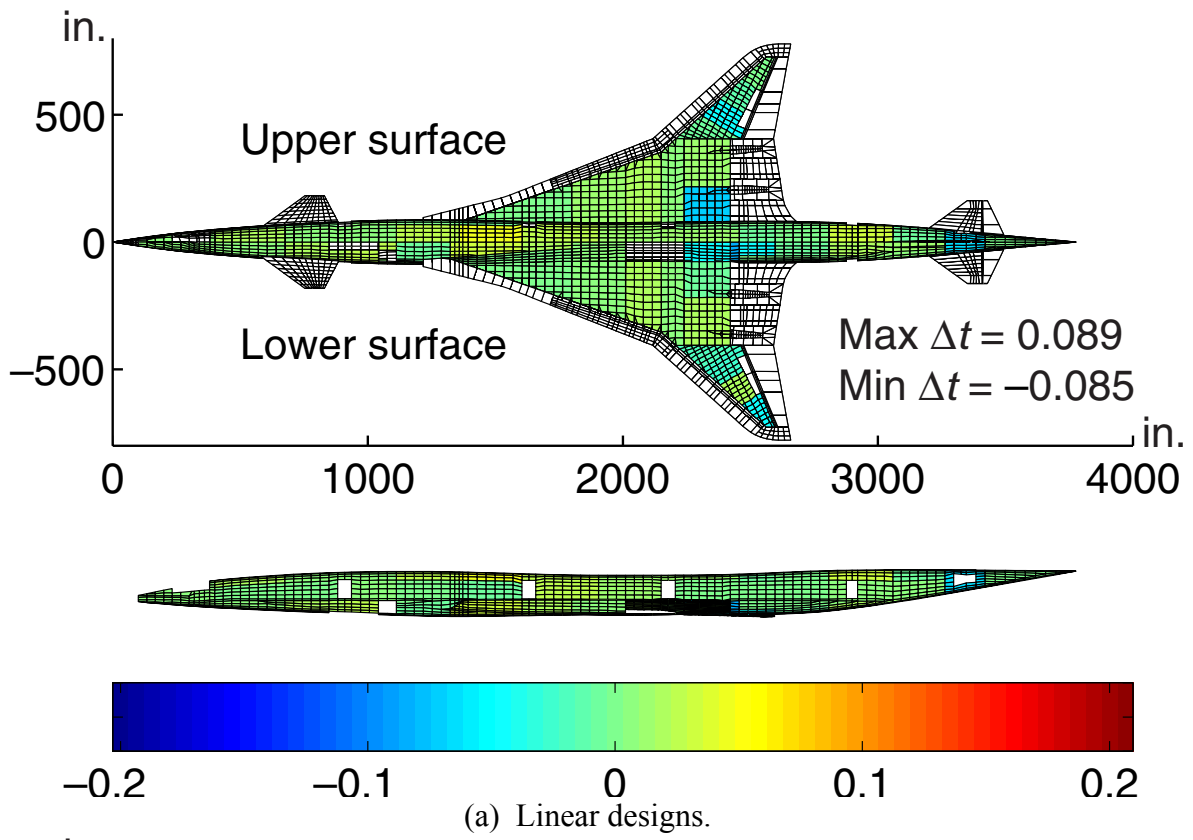


Figure 32. Difference in total ply thickness of two face sheets;  
Three-Surface configuration minus Aft-Tail configuration (in).

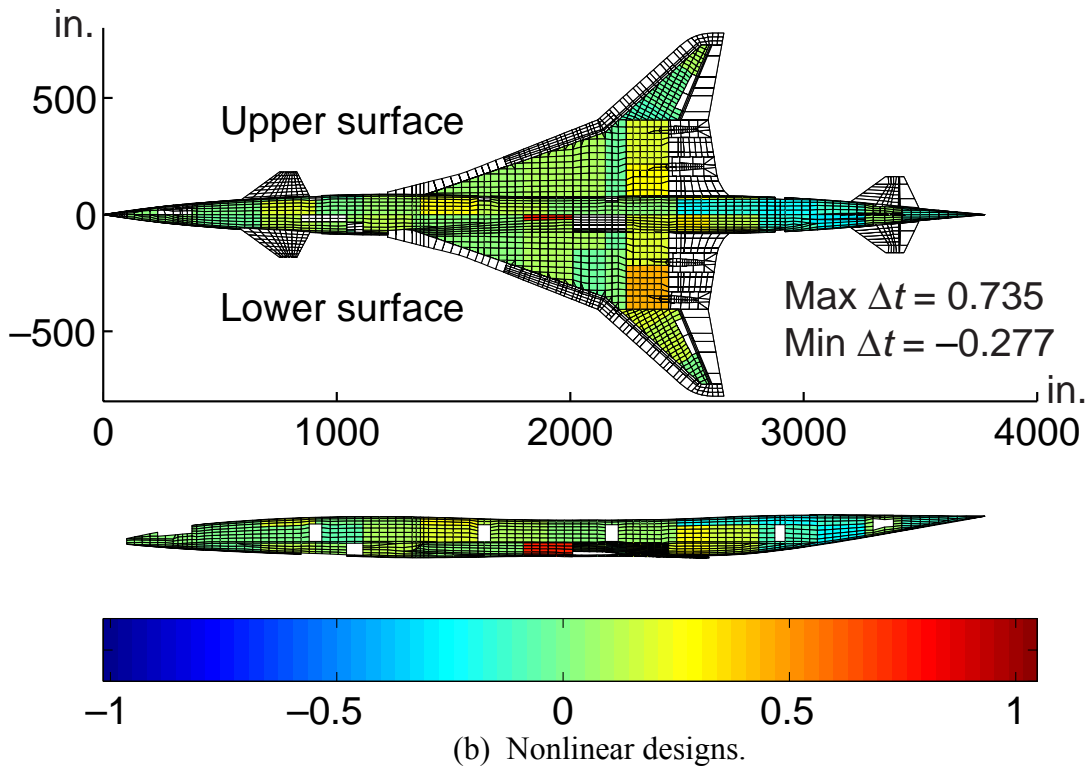
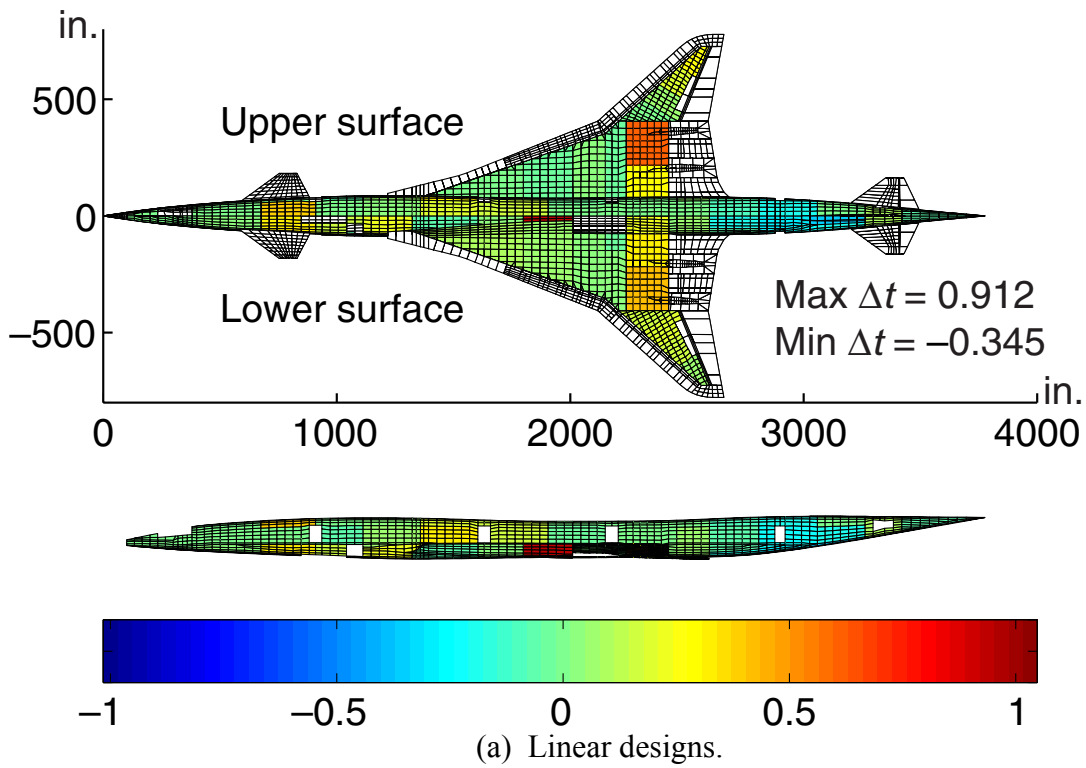


Figure 33. Difference in total core thickness;  
Three-Surface configuration minus Aft-Tail configuration (in).

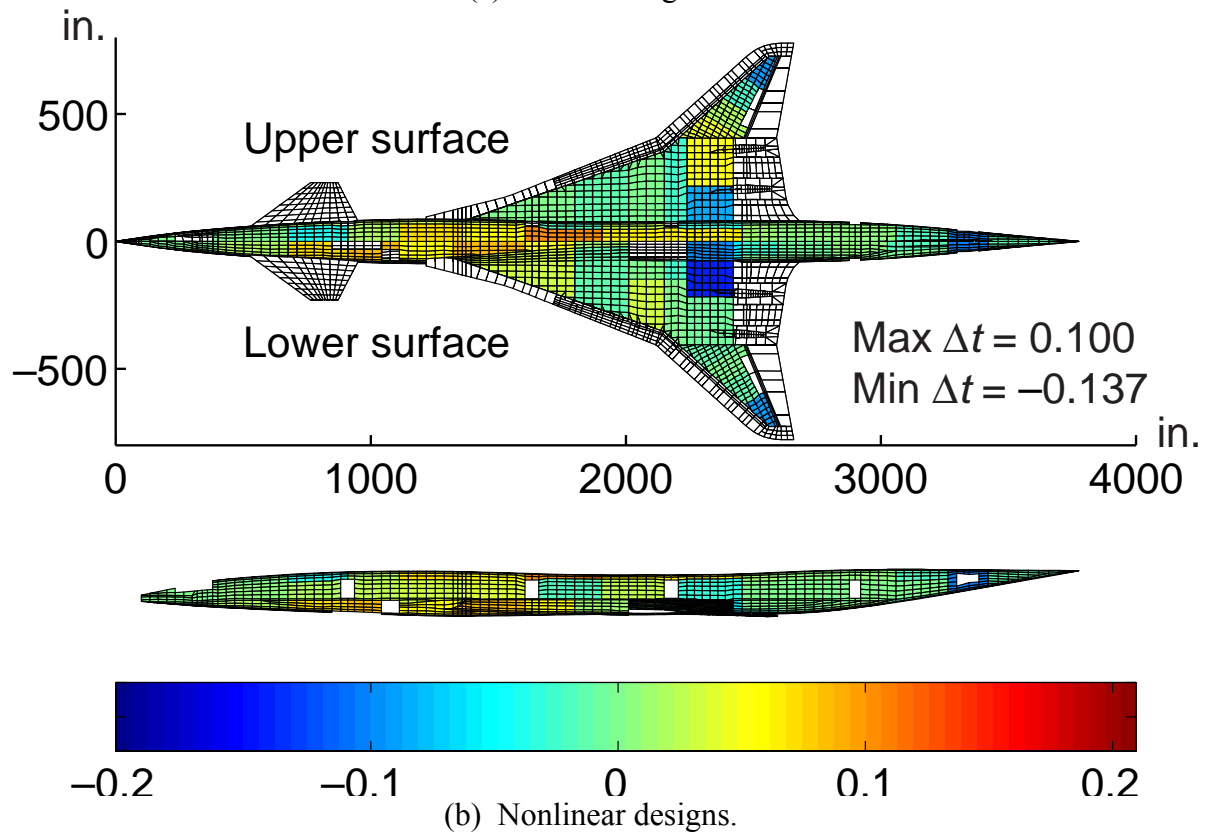
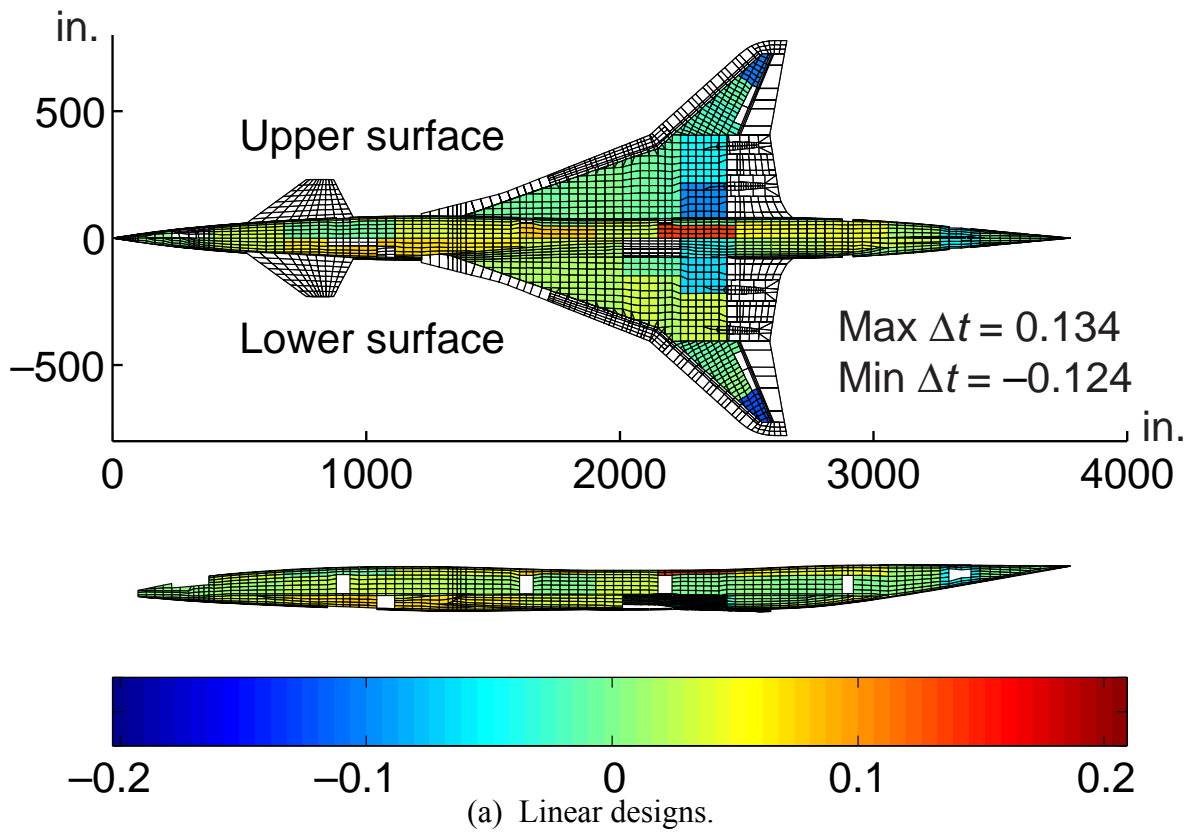
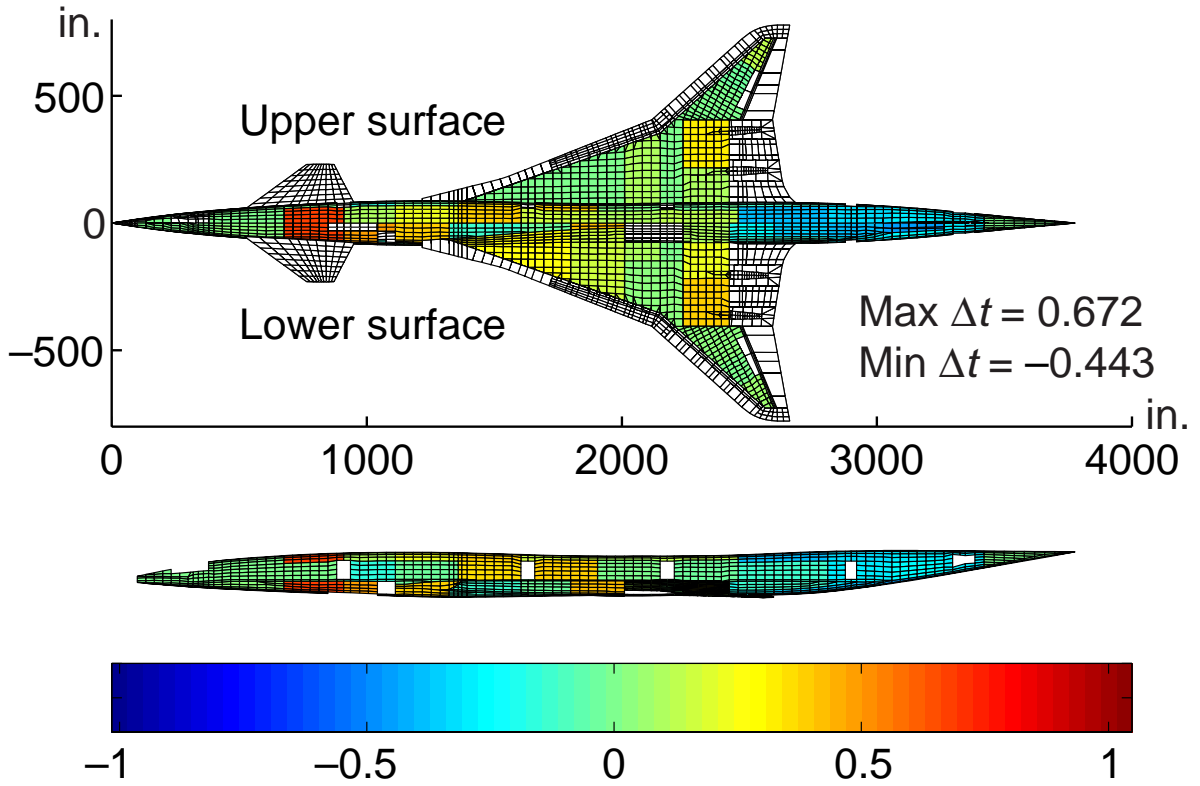
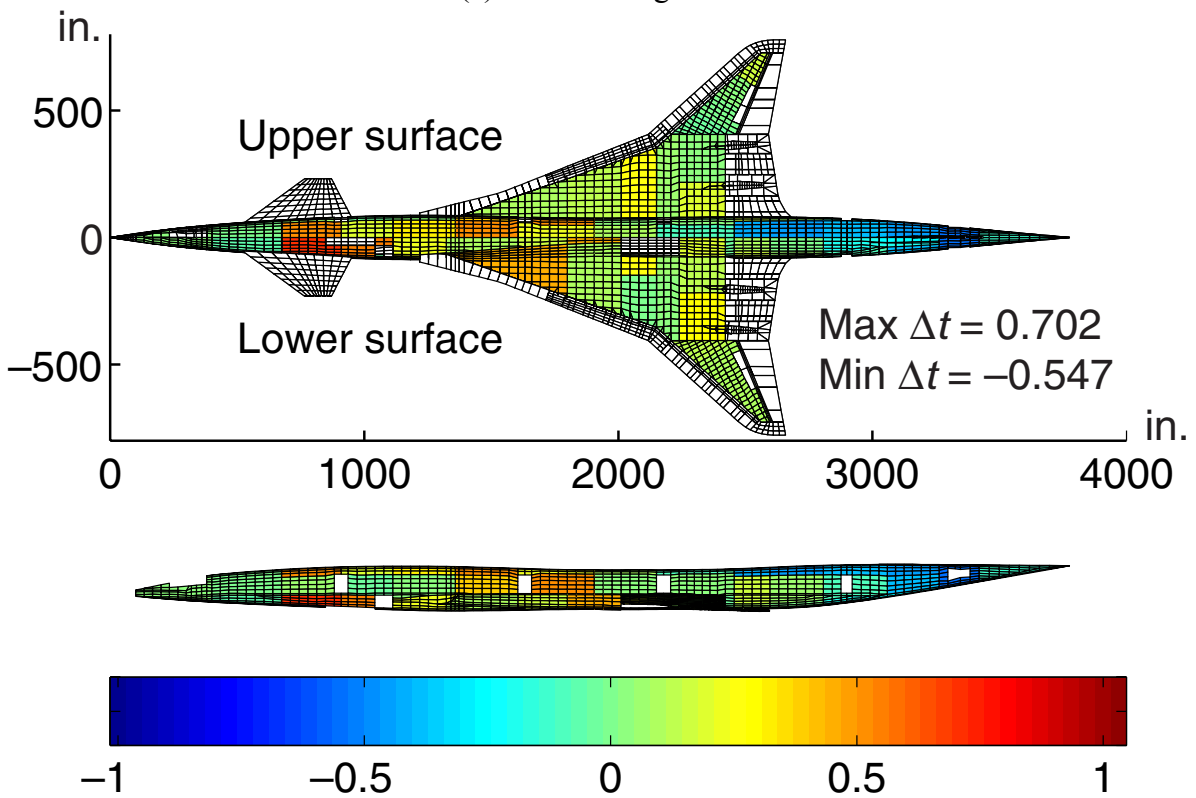


Figure 34. Difference in total ply thickness of two face sheets;  
Canard configuration minus Aft-Tail configuration (in).

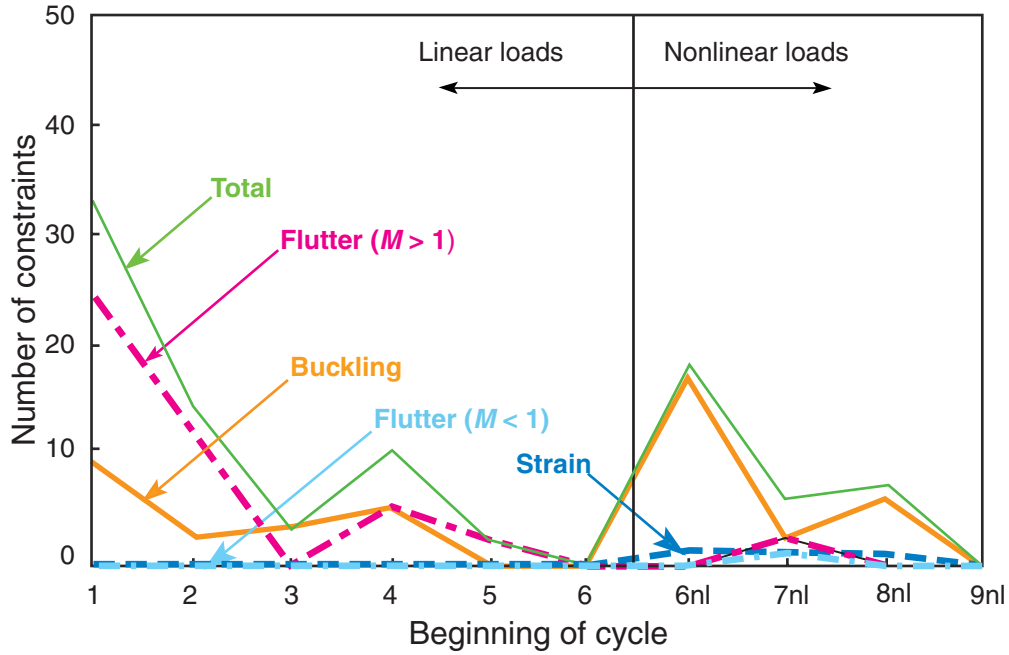


(a) Linear designs.

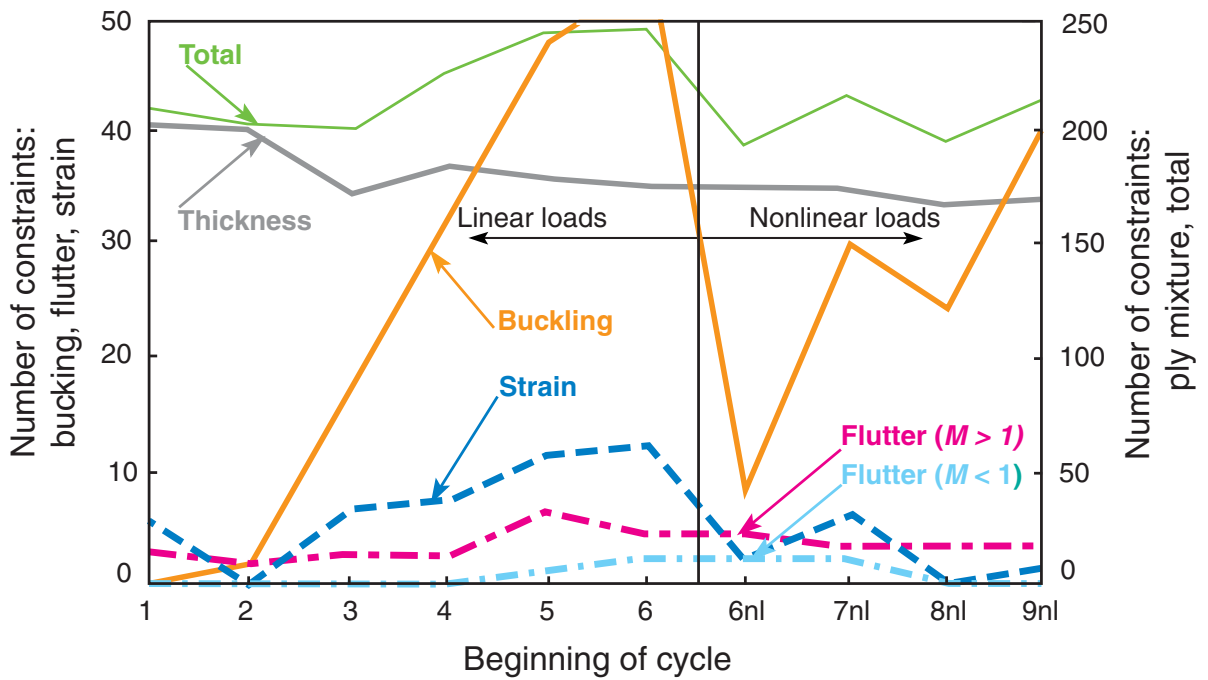


(b) Nonlinear designs.

Figure 35. Difference in total core thickness;  
Canard configuration minus Aft-Tail configuration (in).

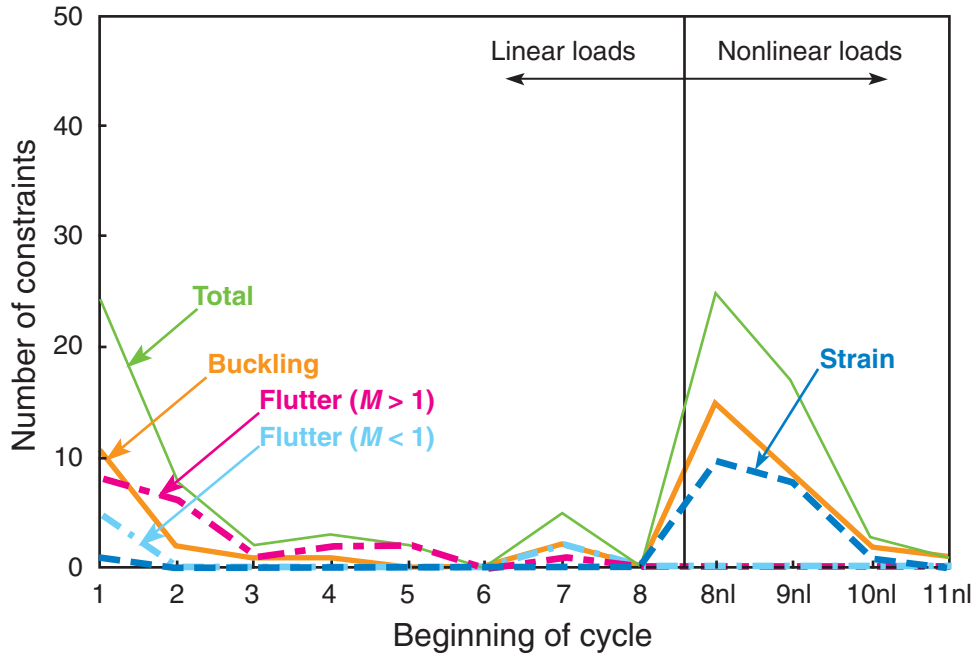


(a) Violated constraints.

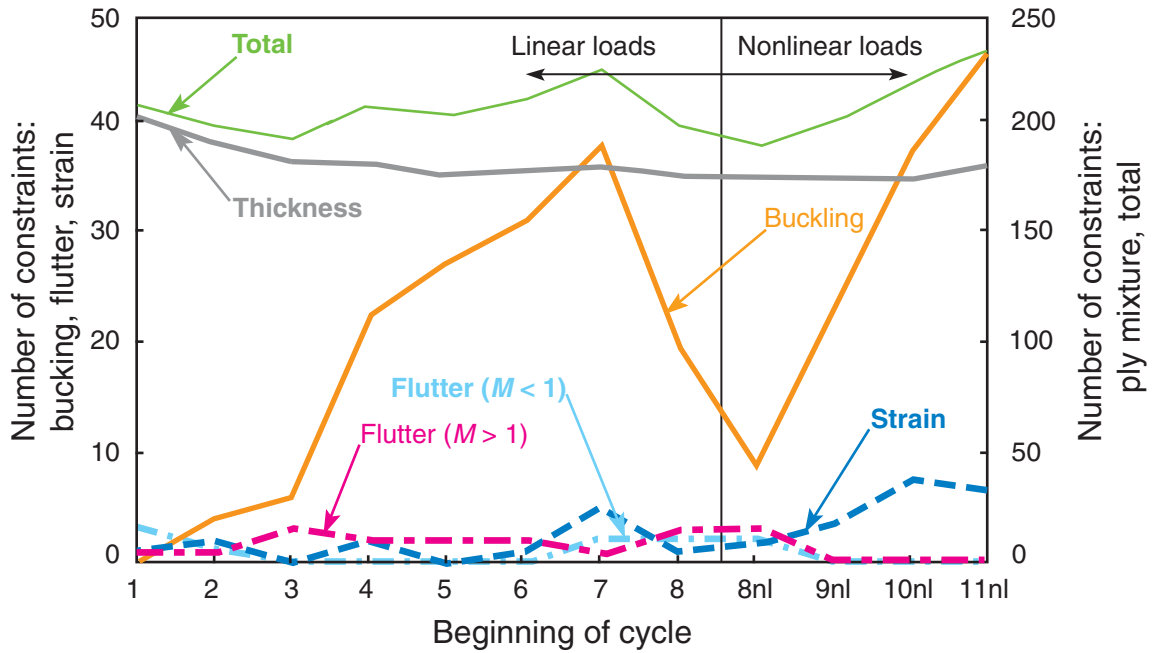


(b) Active constraints.

Figure 36. History of violated and active constraints for Aft-Tail configuration.

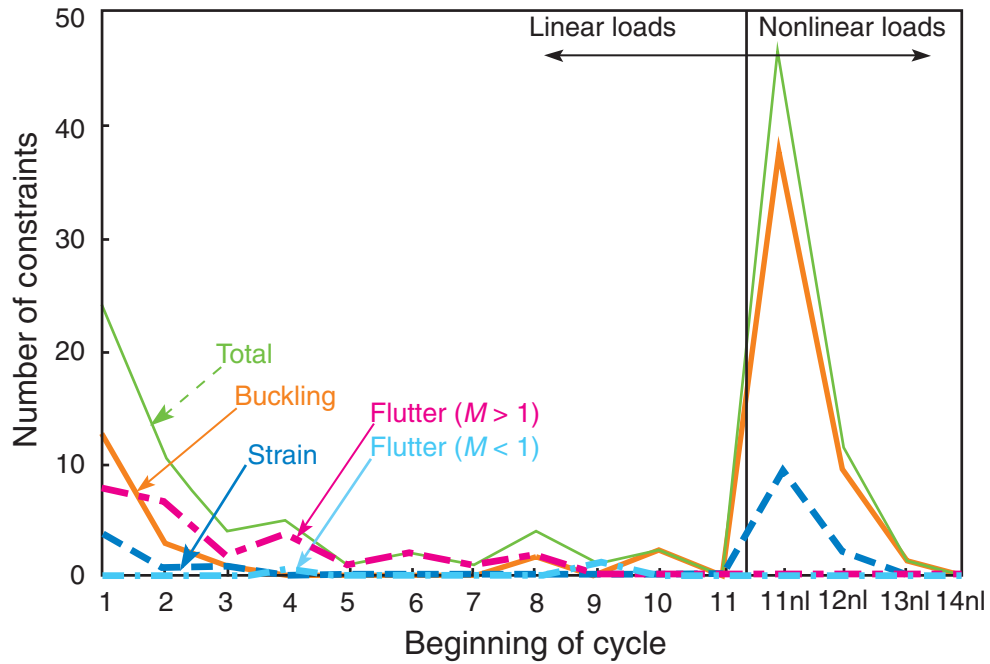


(a) Violated constraints.

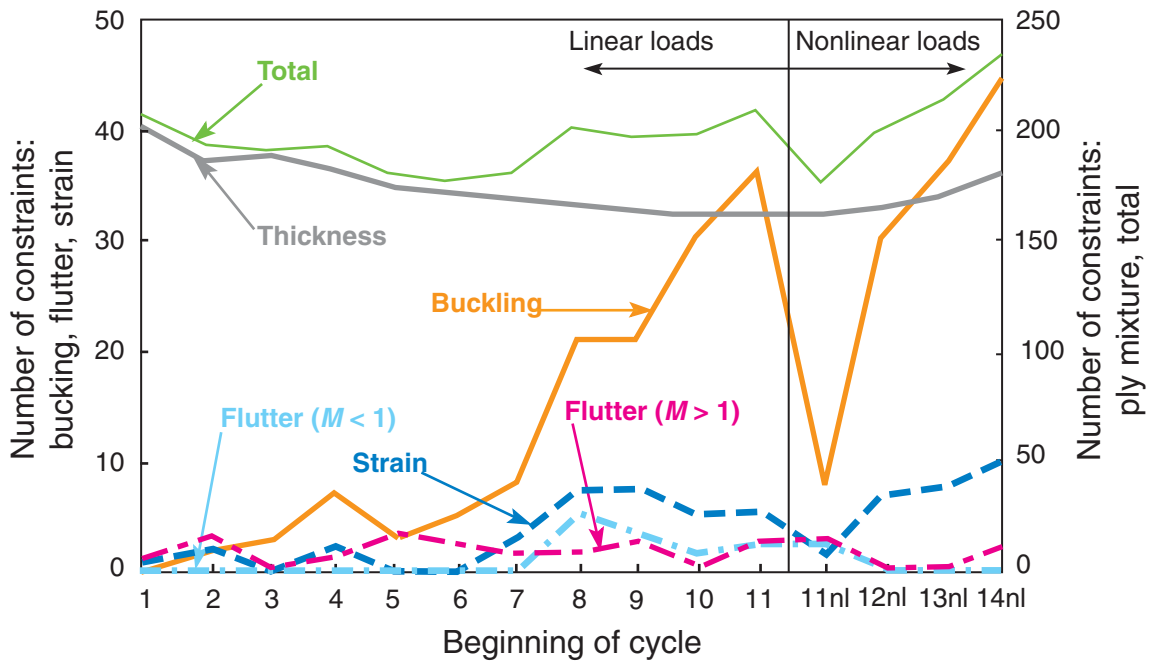


(b) Active constraints.

Figure 37. History of violated and active constraints for Three-Surface configuration.

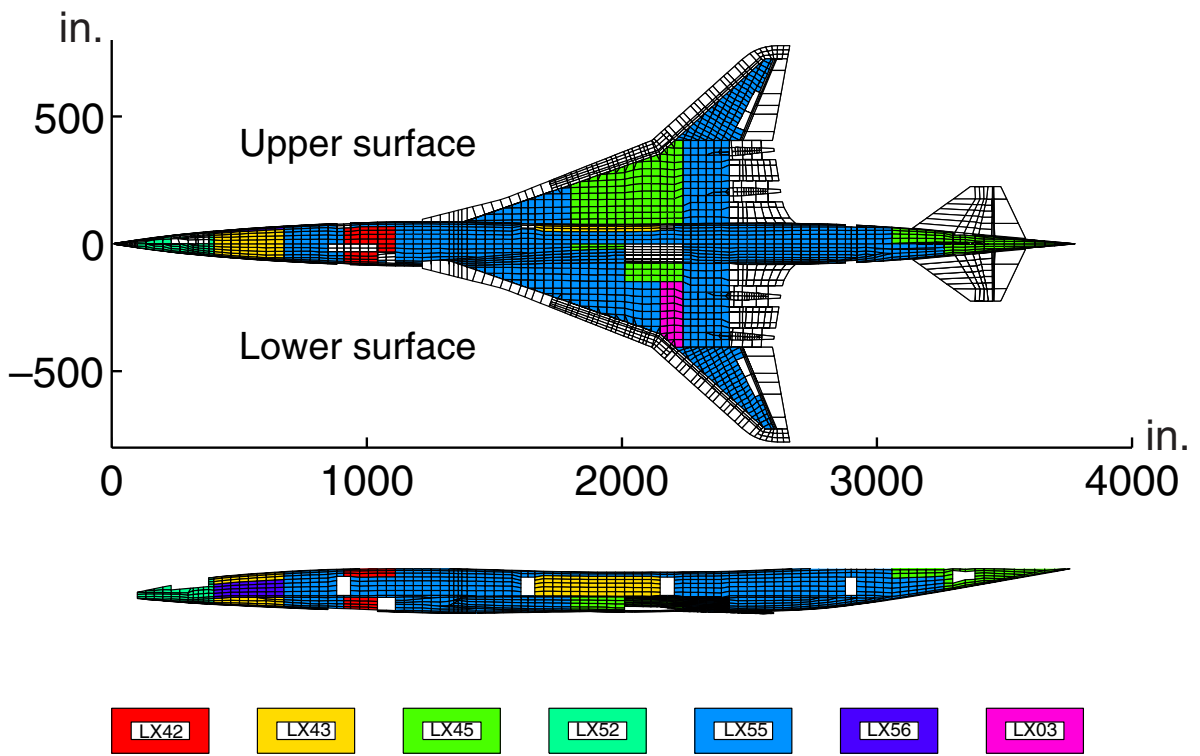
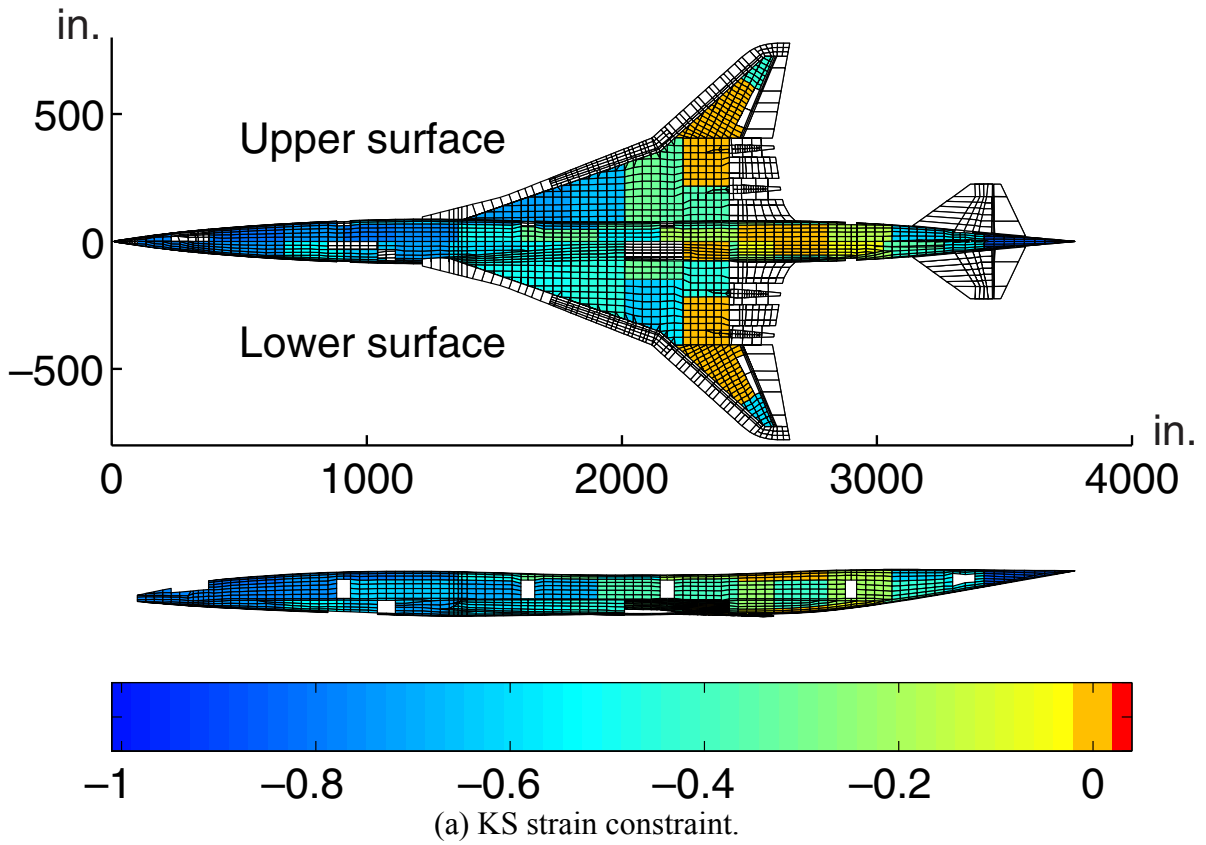


(a) Violated constraints.



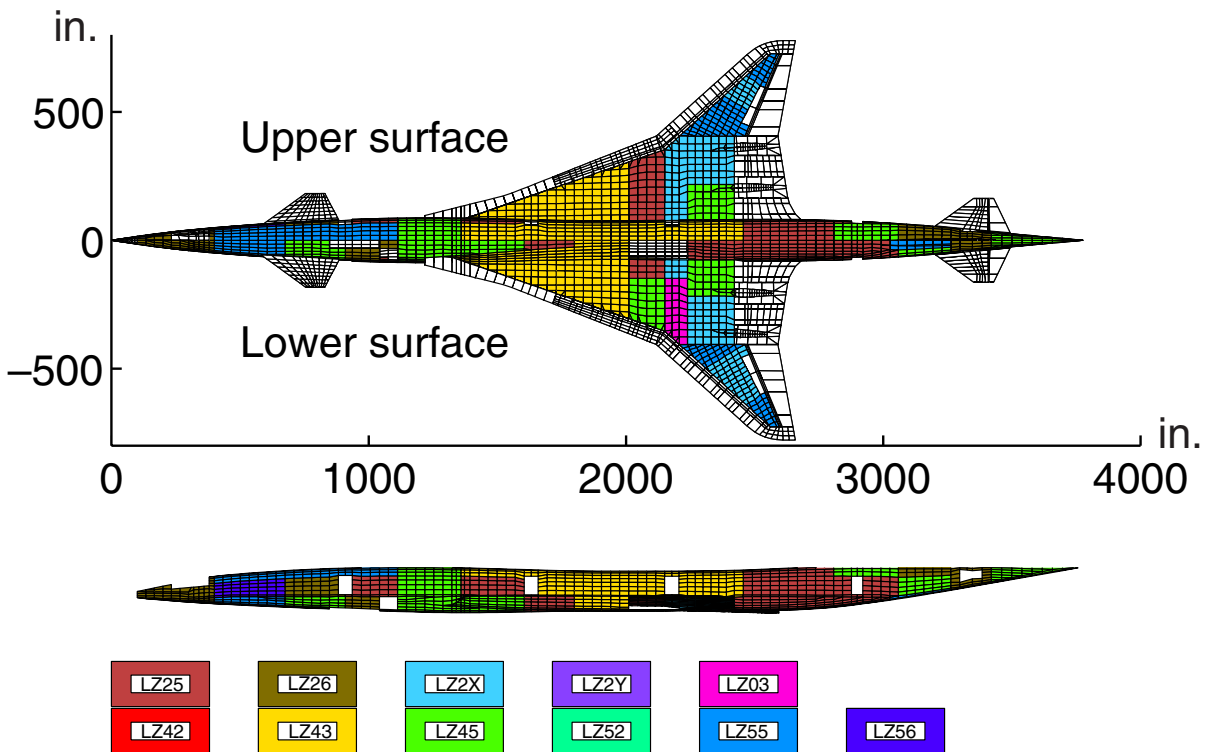
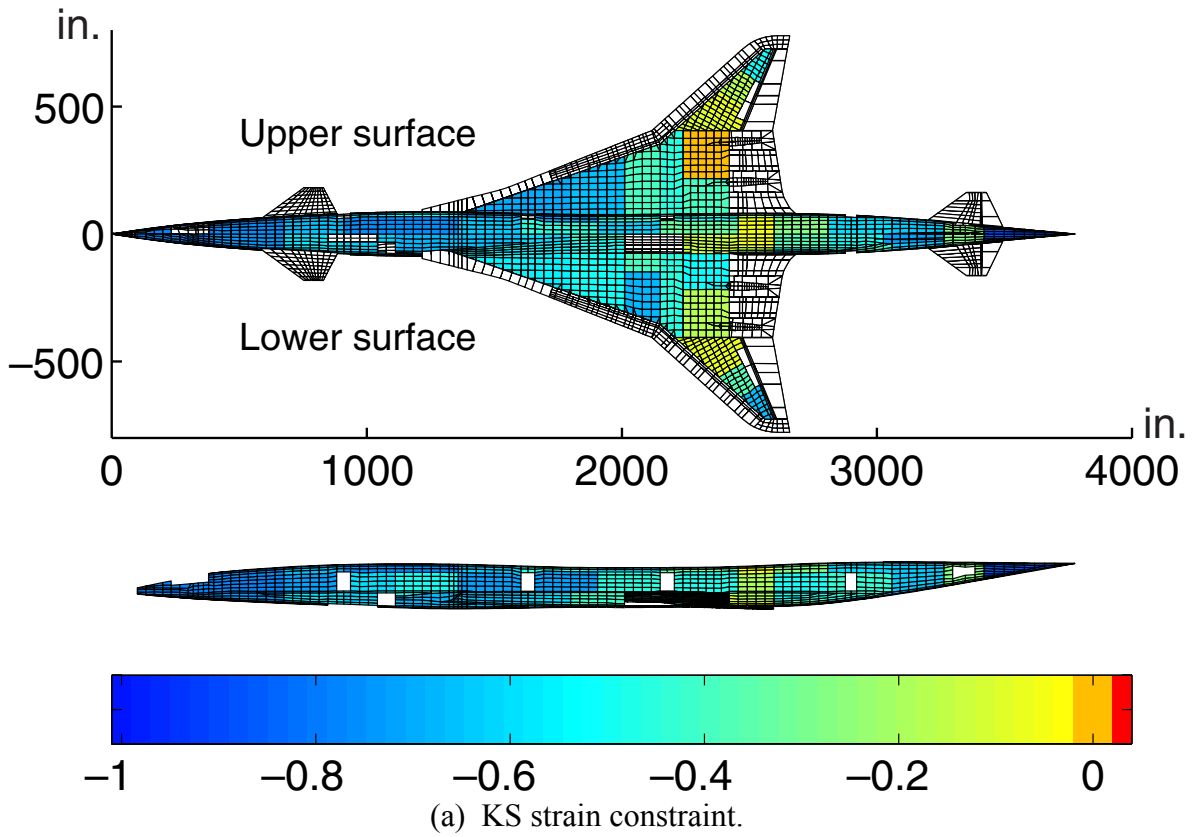
(b) Active constraints.

Figure 38. History of violated and active constraints for Canard configuration.



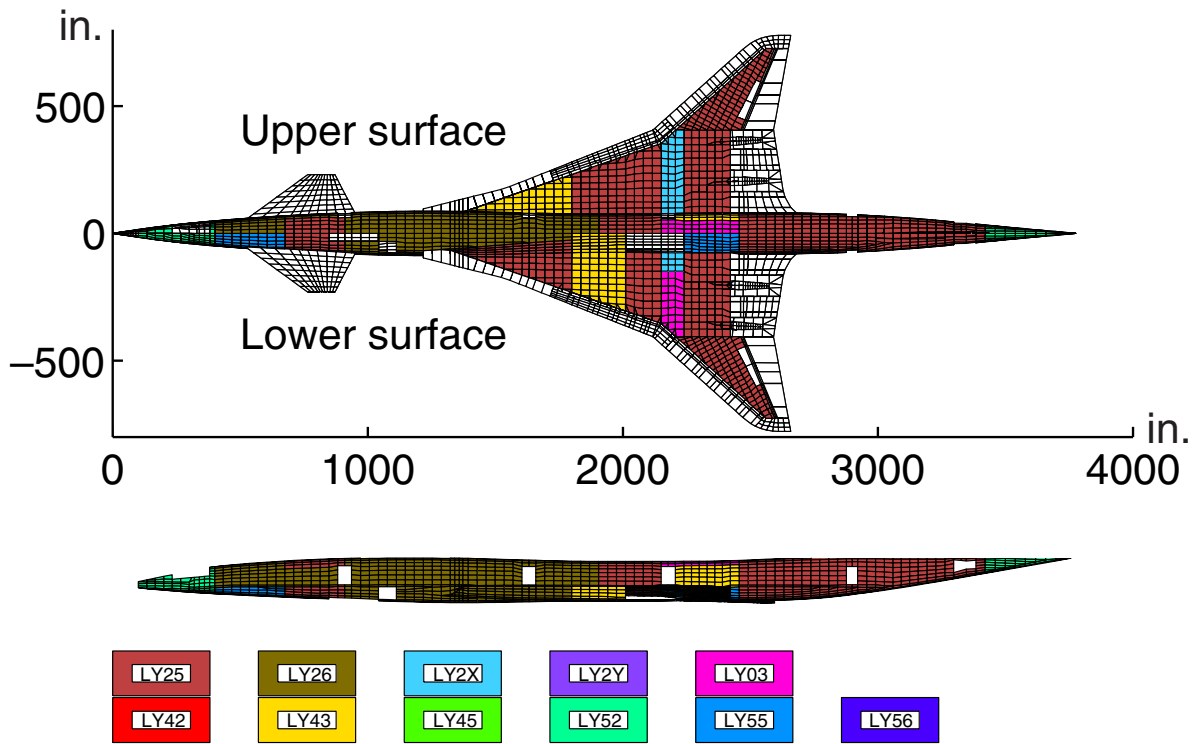
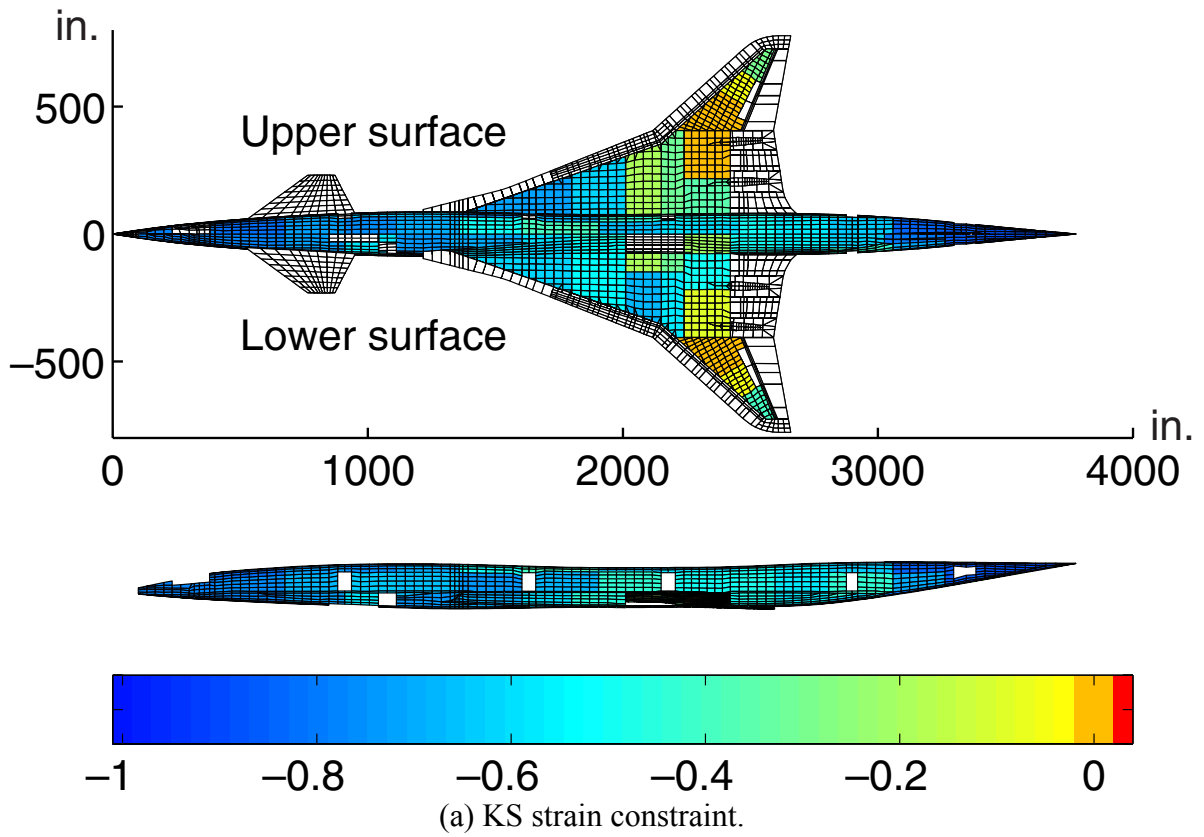
(b) Load case associated with maximum KS strain function.

Figure 39. Strain constraint information for linear design of Aft-Tail configuration.



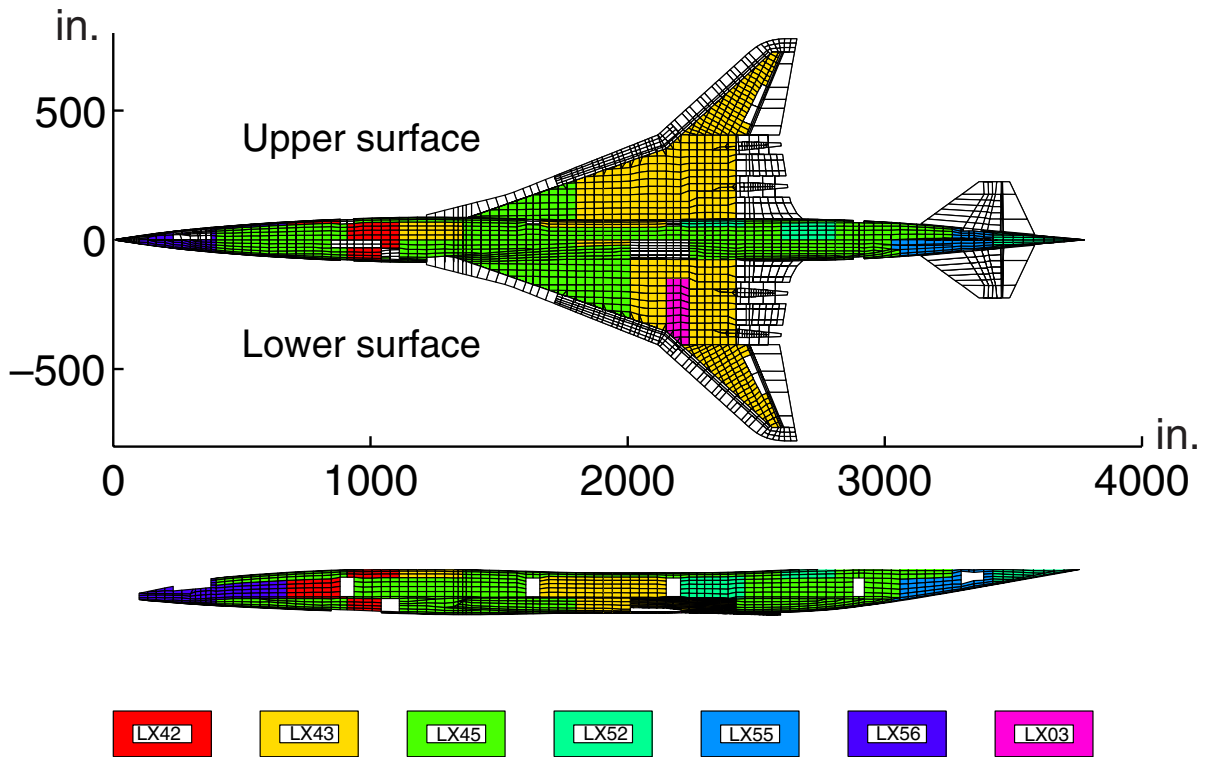
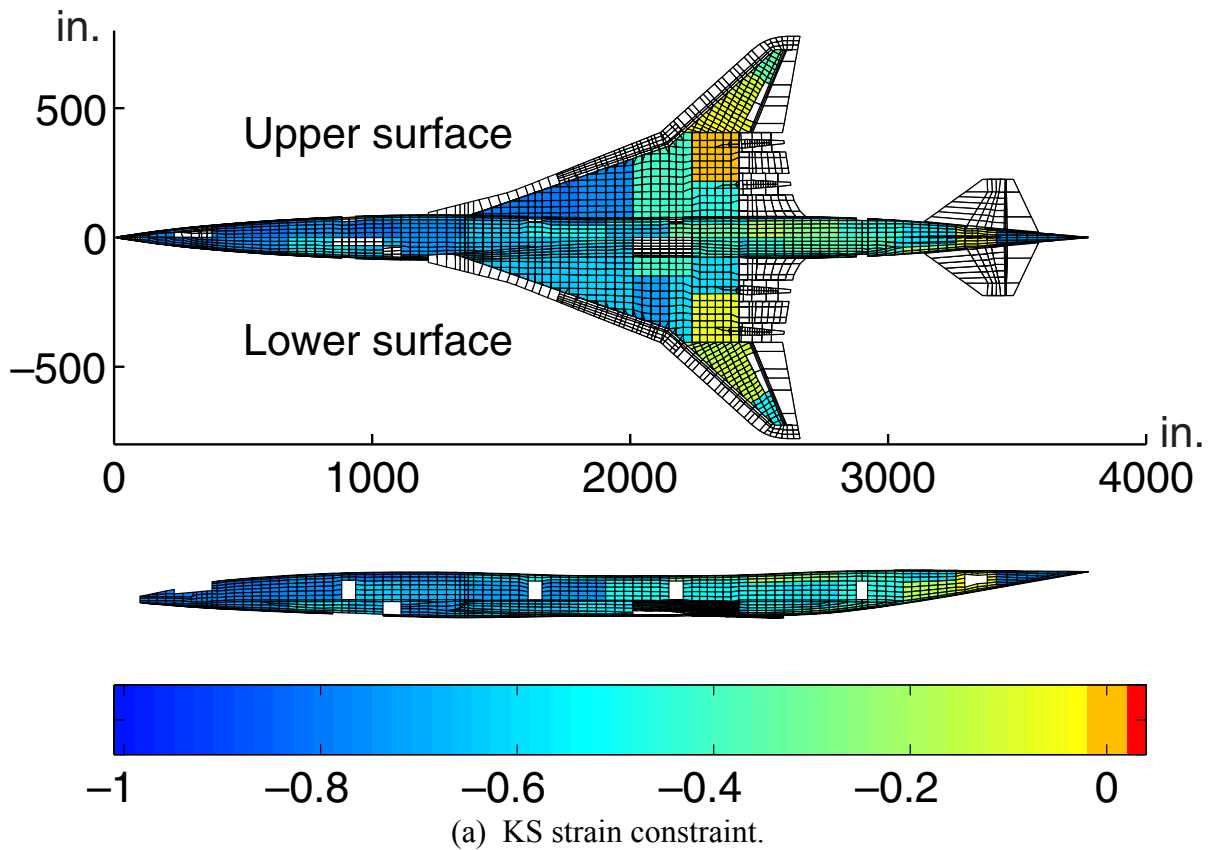
(b) Load case associated with maximum KS strain function.

Figure 40. Strain constraint information for linear design of Three-Surface configuration.



(b) Load case associated with maximum KS strain function.

Figure 41. Strain constraint information for linear design of Canard configuration.



(b) Load case associated with maximum KS strain function.

Figure 42. Strain constraint information for nonlinear design of Aft-Tail configuration.

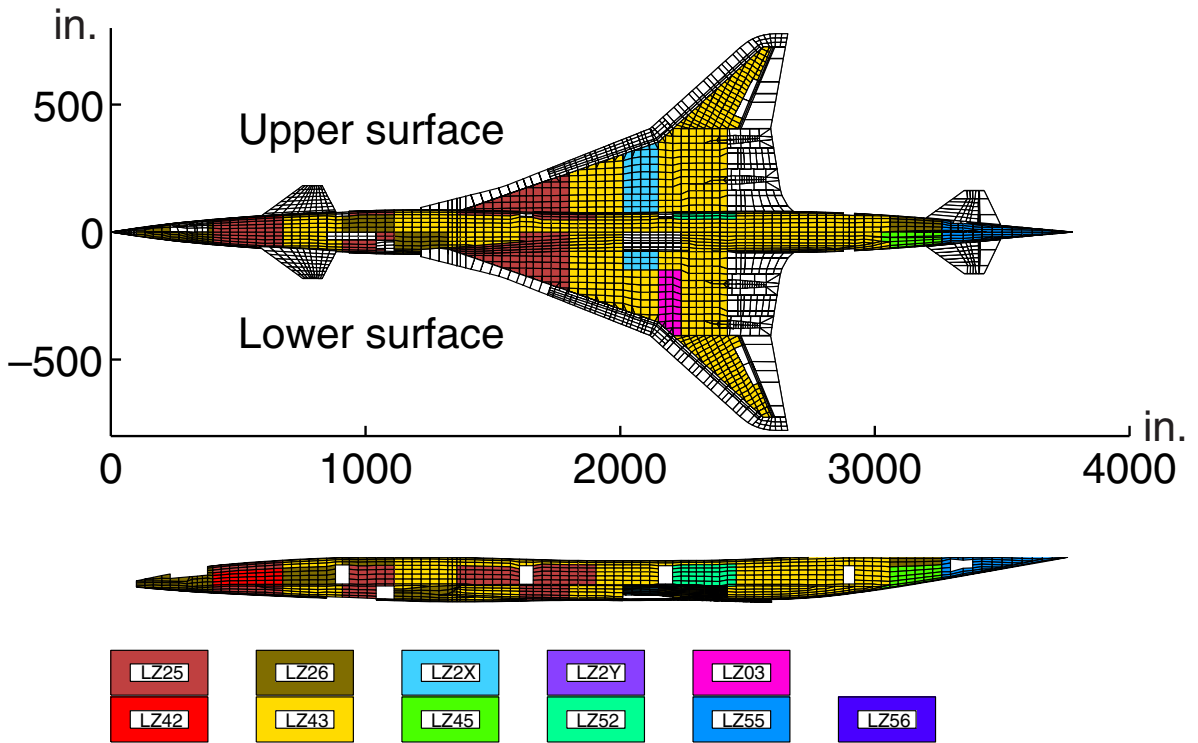
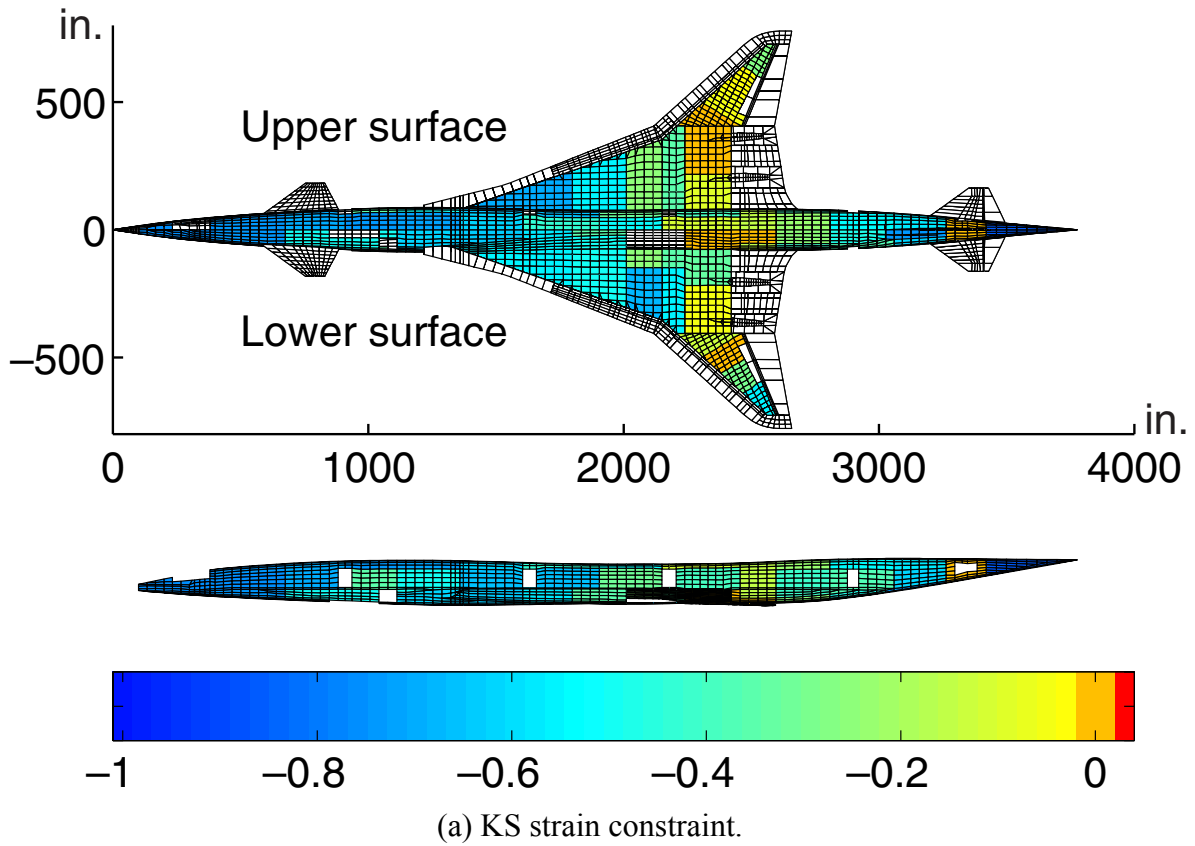
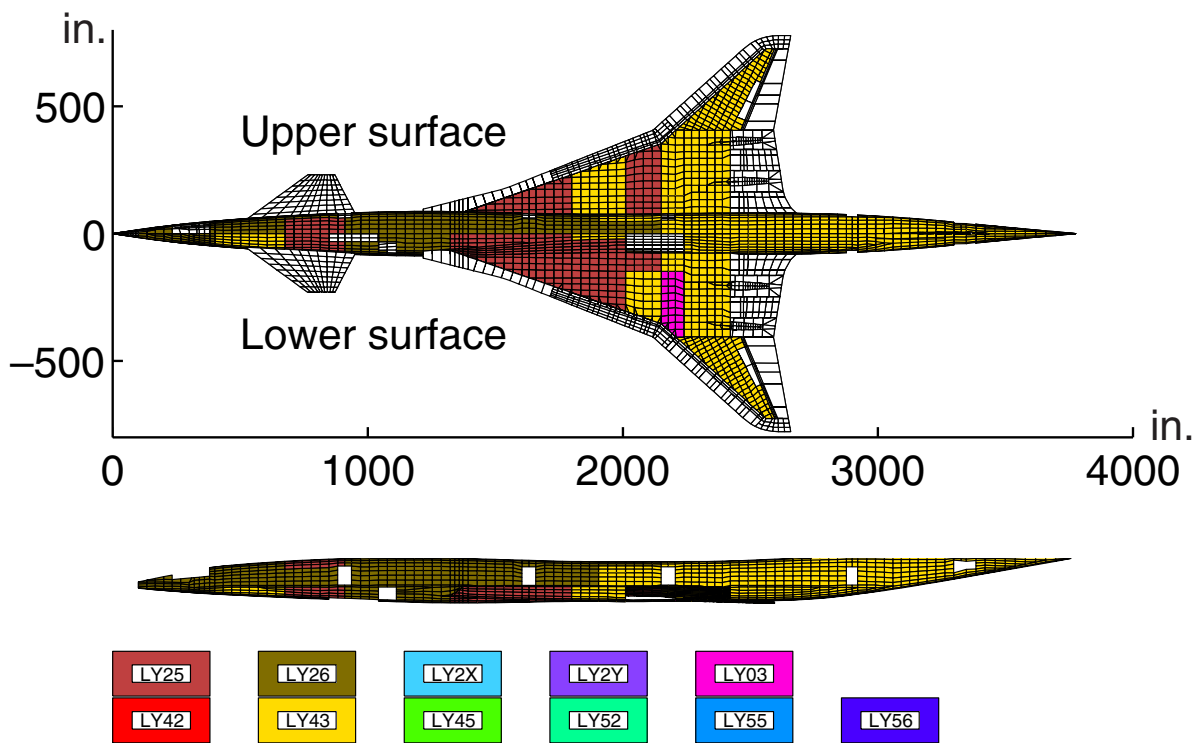
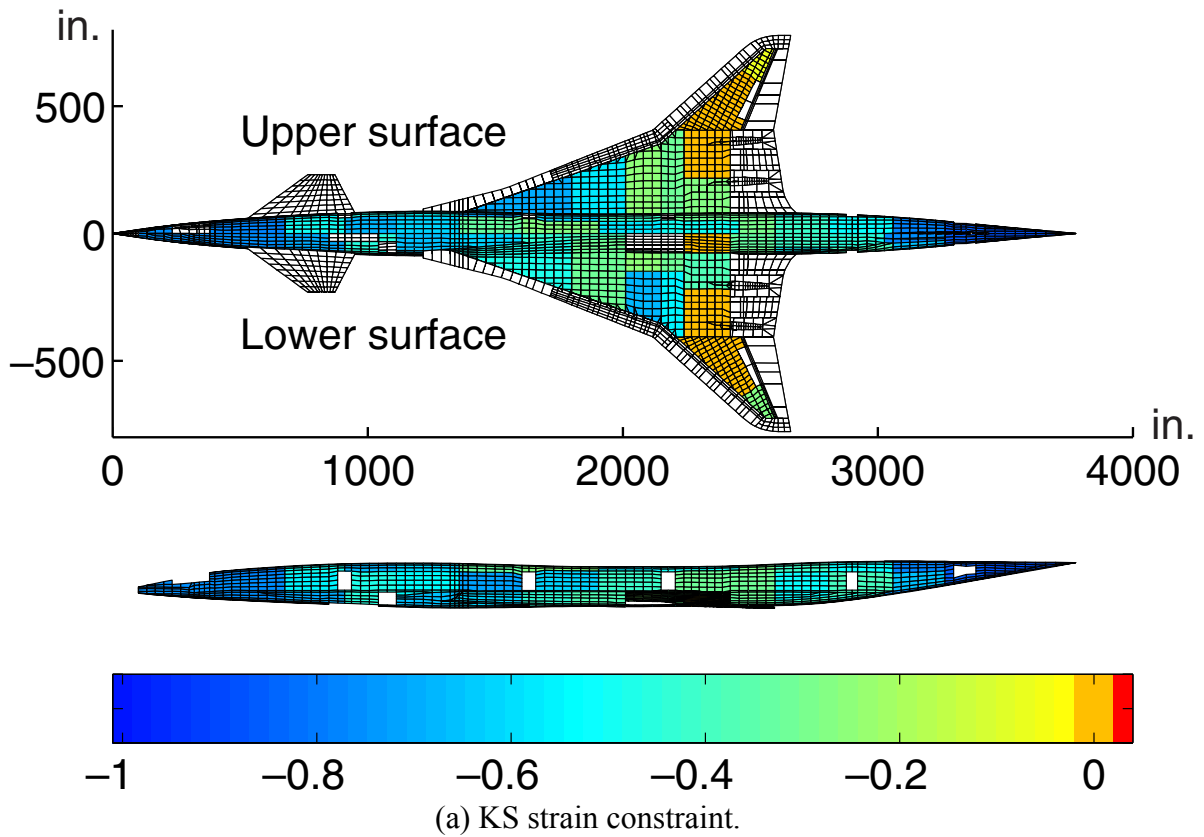
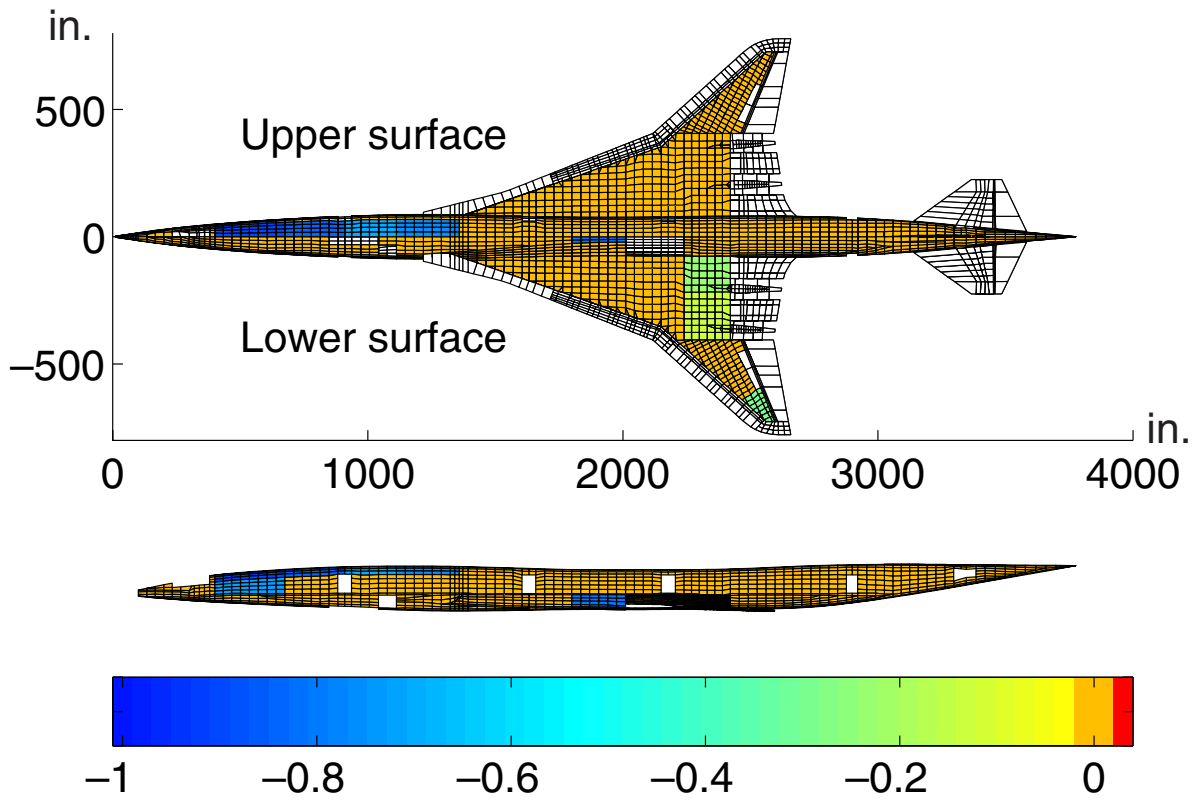


Figure 43. Strain constraint information for nonlinear design of Three-Surface configuration.

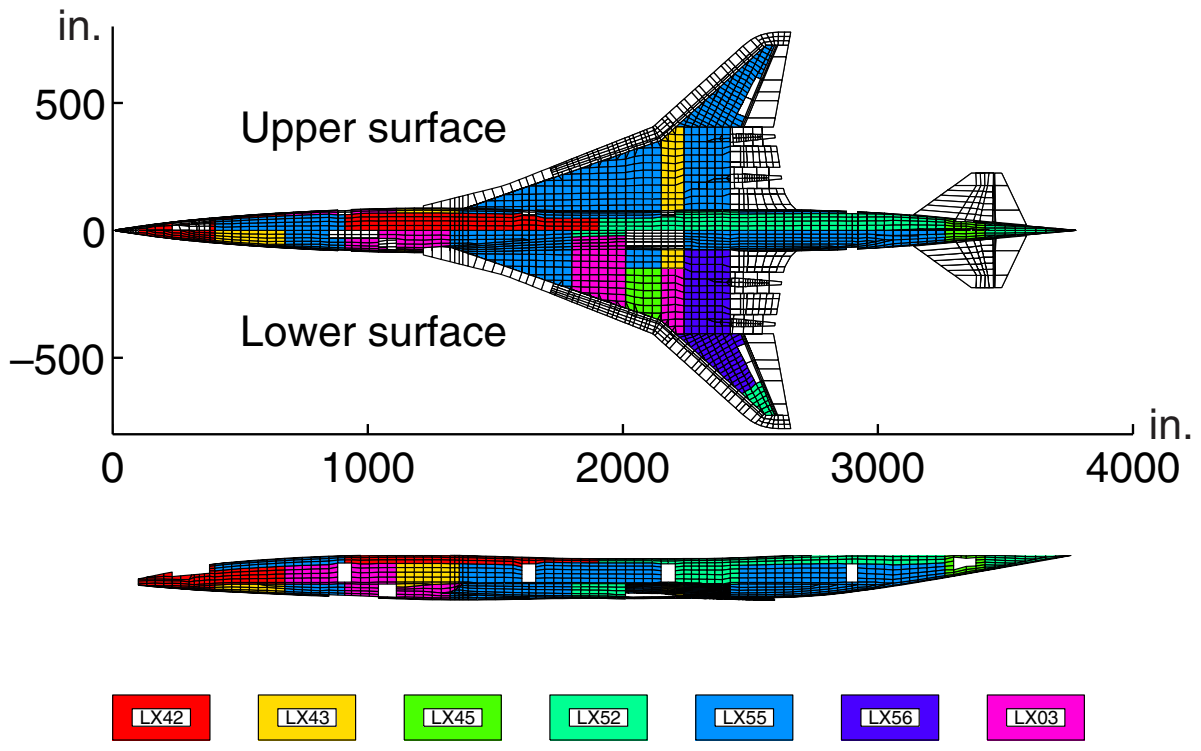


(b) Load case associated with maximum KS strain function.

Figure 44. Strain constraint information for nonlinear design of Canard configuration.



(a) KS buckling constraint.



(b) Load case associated with maximum KS buckling function.

Figure 45. Buckling constraint information for linear design of Aft-Tail configuration.

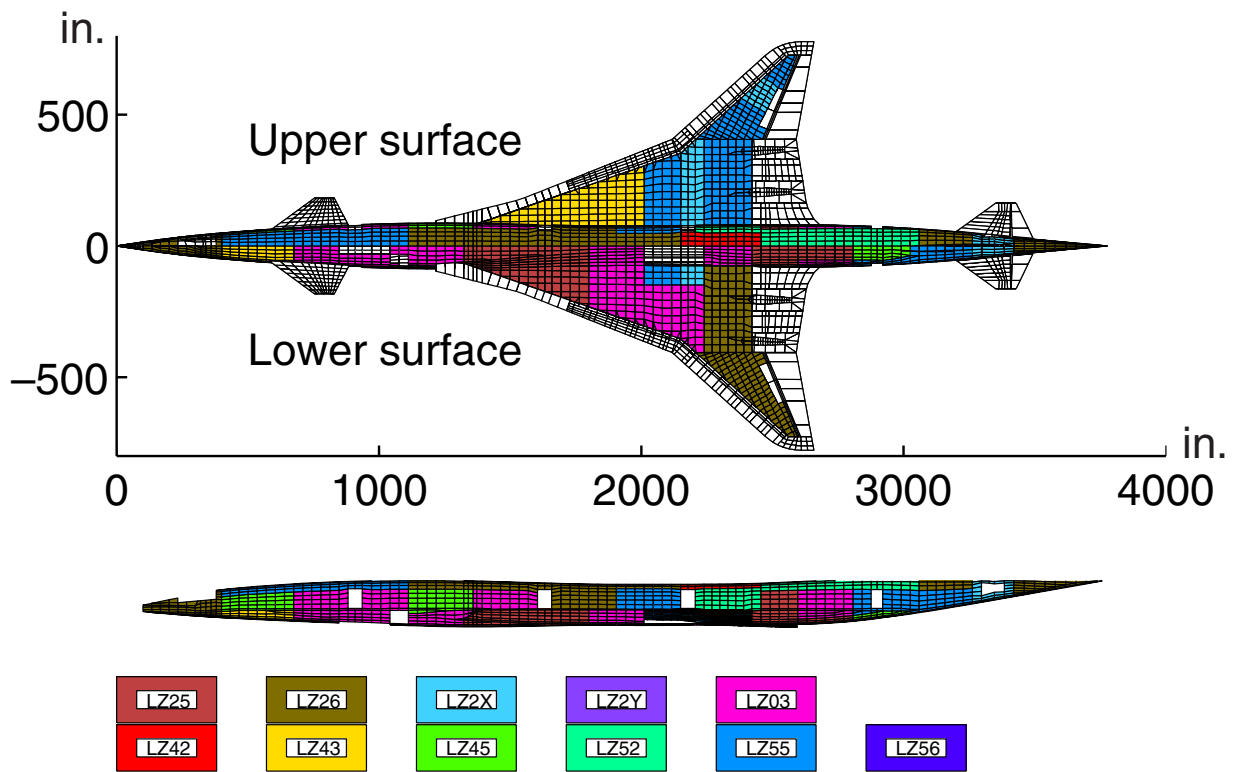
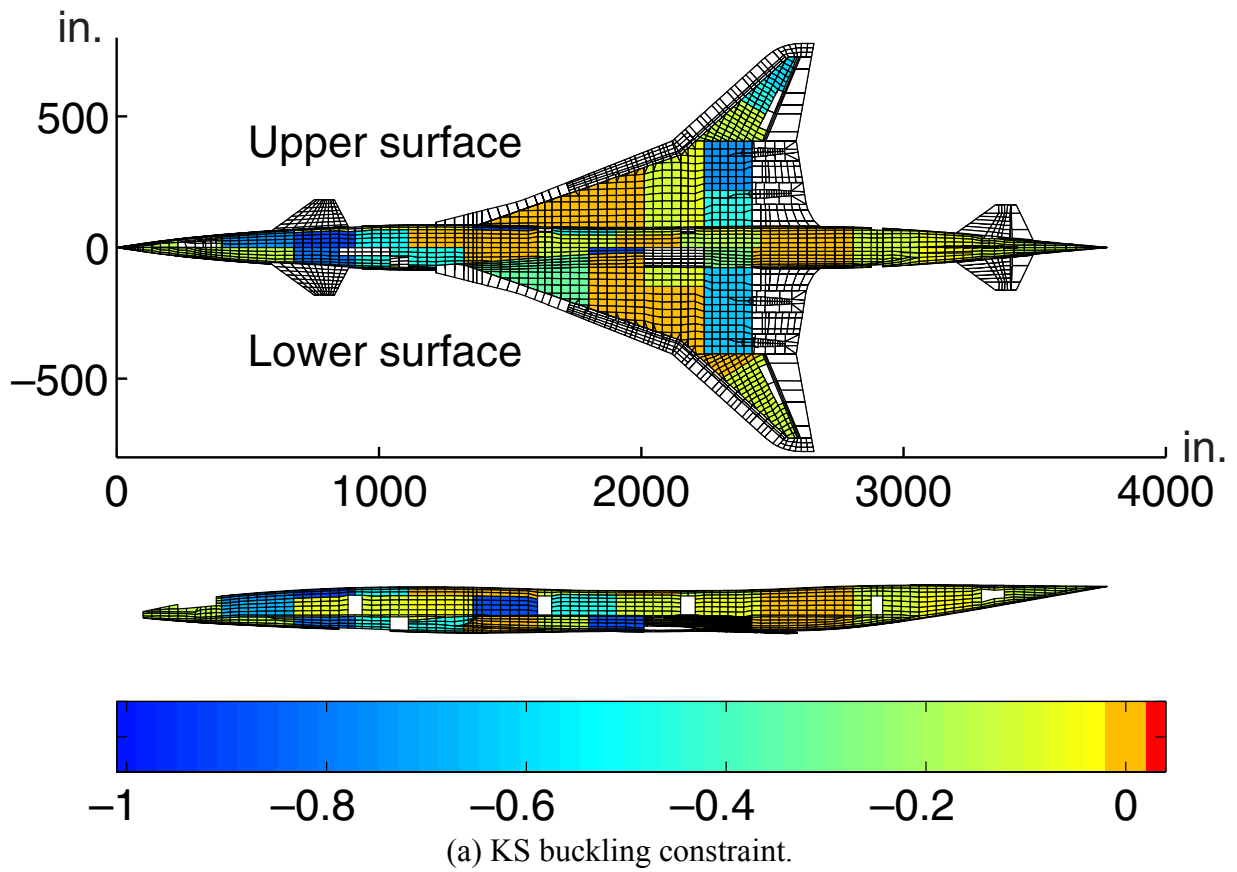
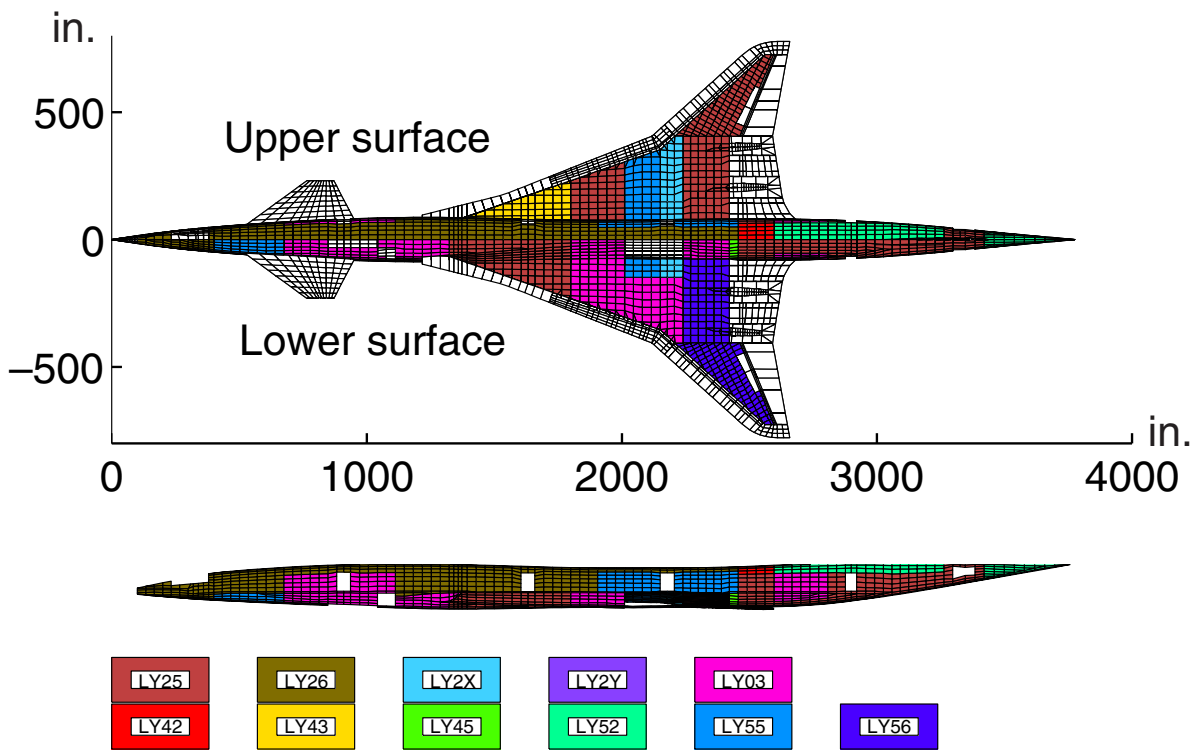
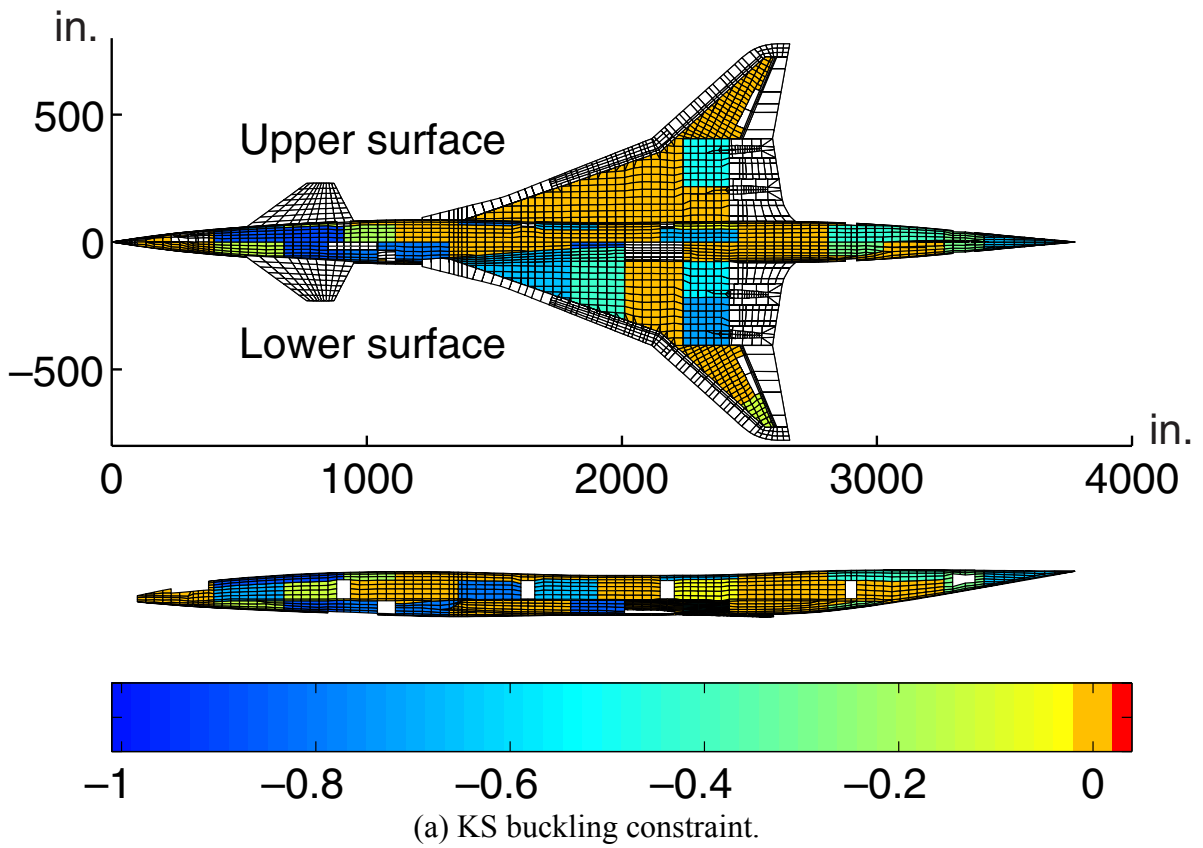
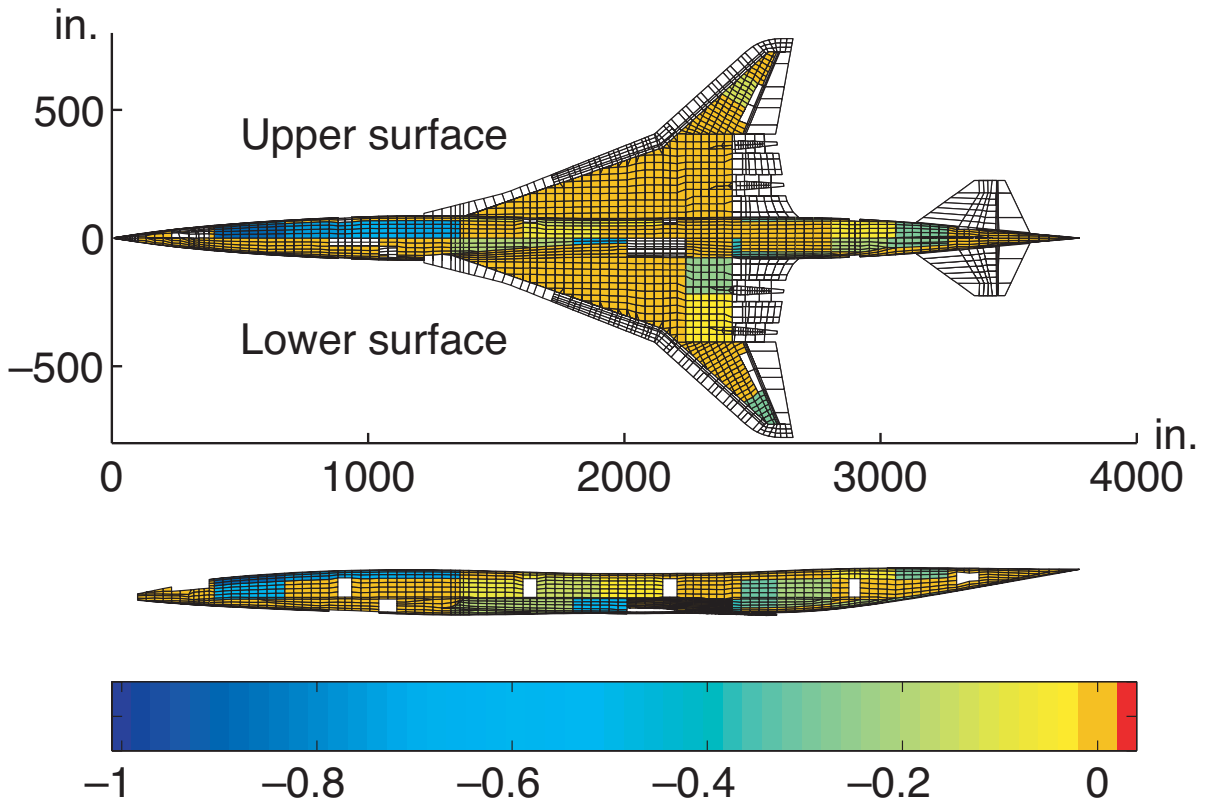


Figure 46. Buckling constraint information for linear design of Three-Surface configuration.

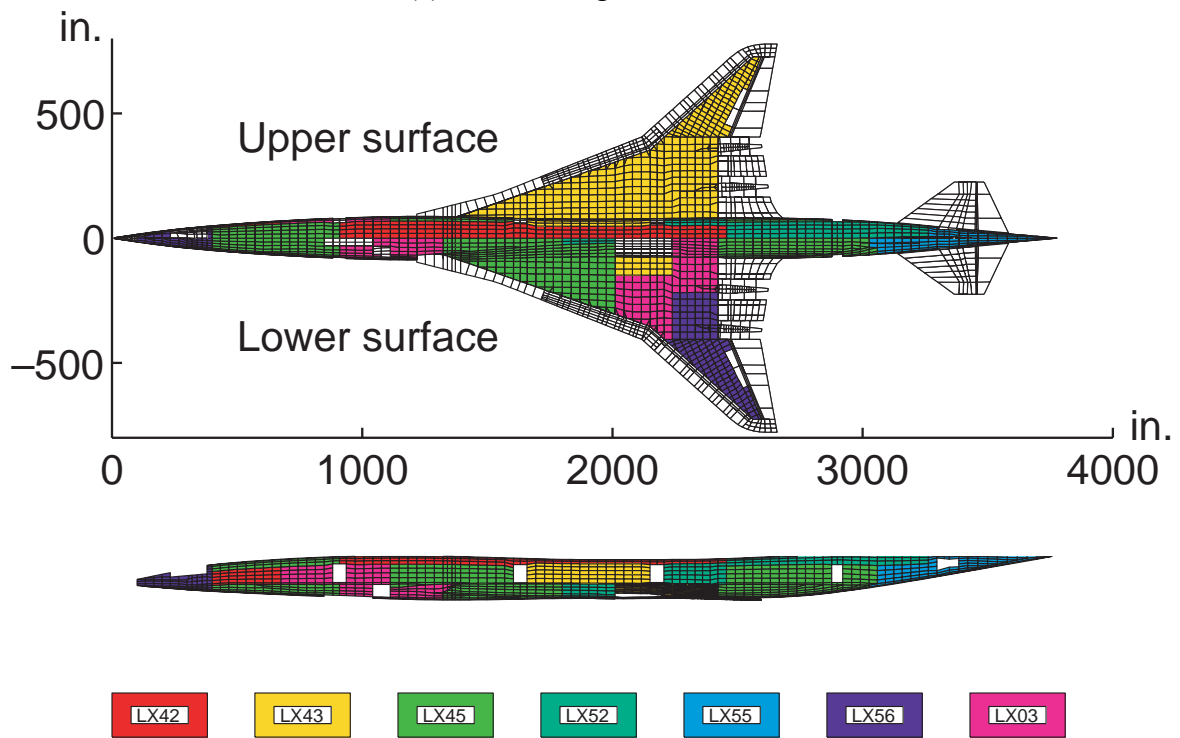


(b) Load case associated with maximum KS buckling function.

Figure 47. Buckling constraint information for linear design of Canard configuration.

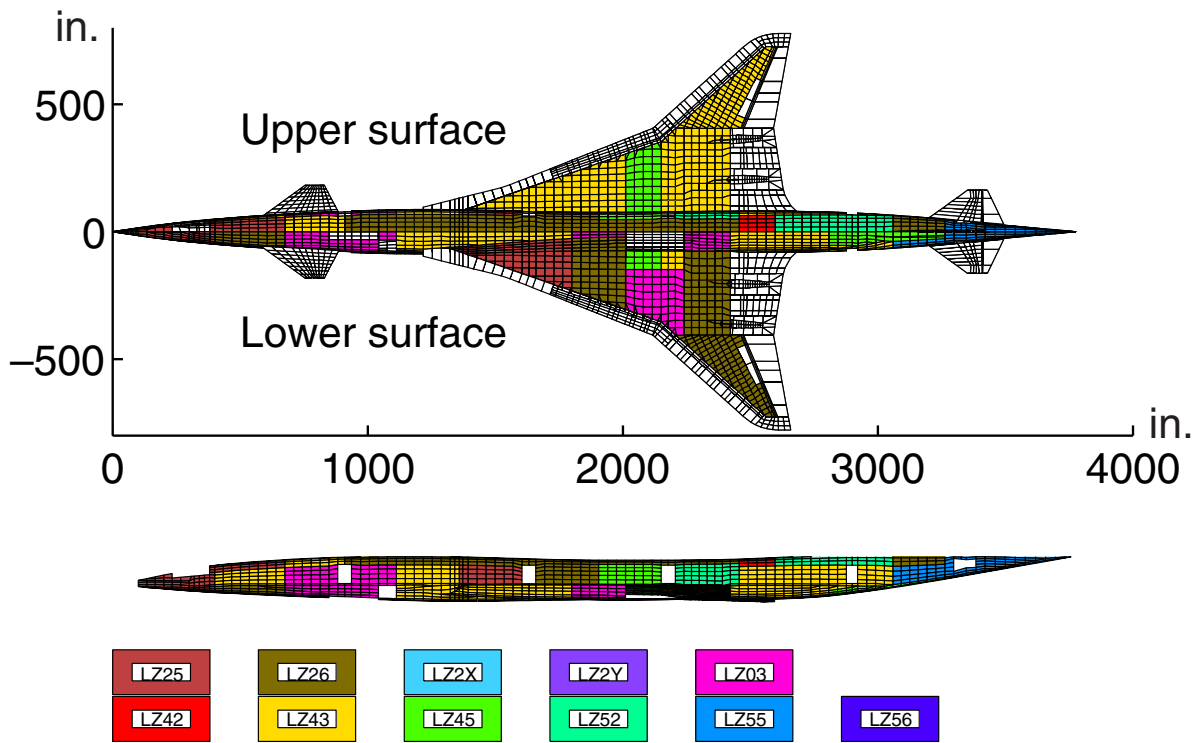
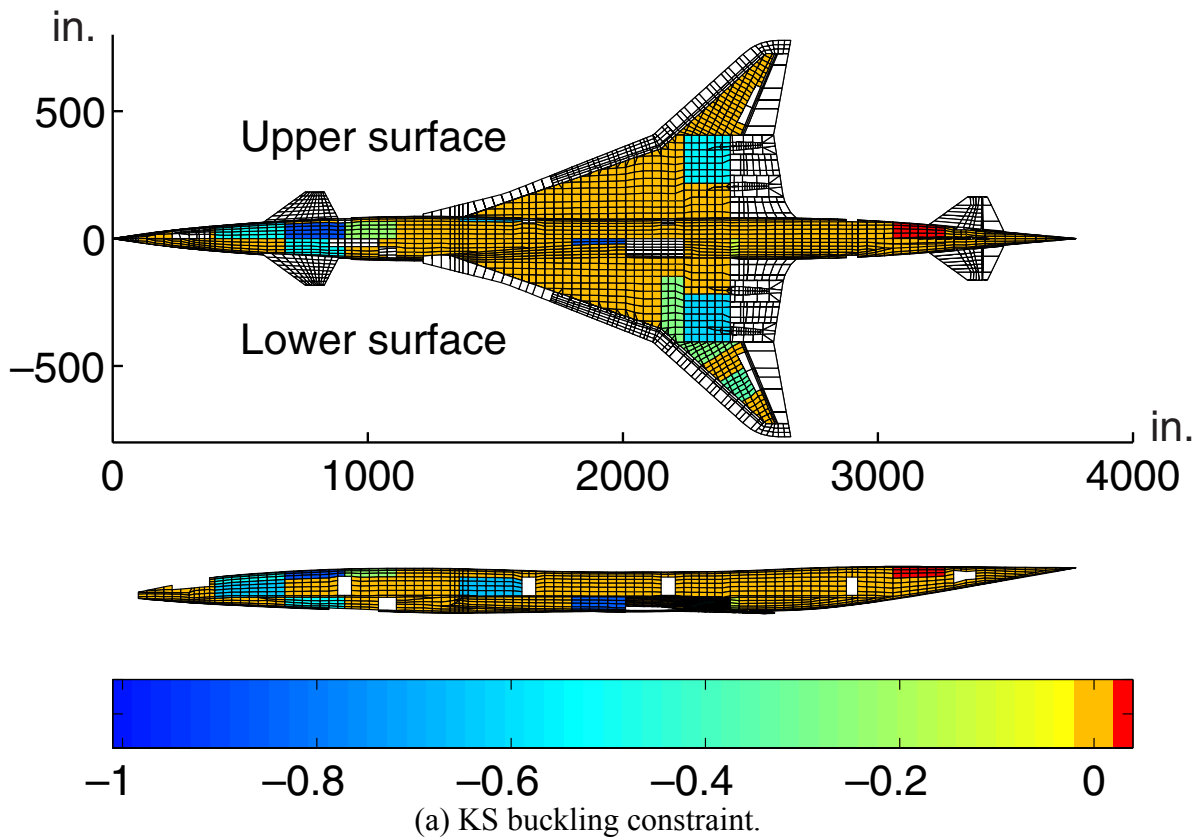


(a) KS buckling constraint.



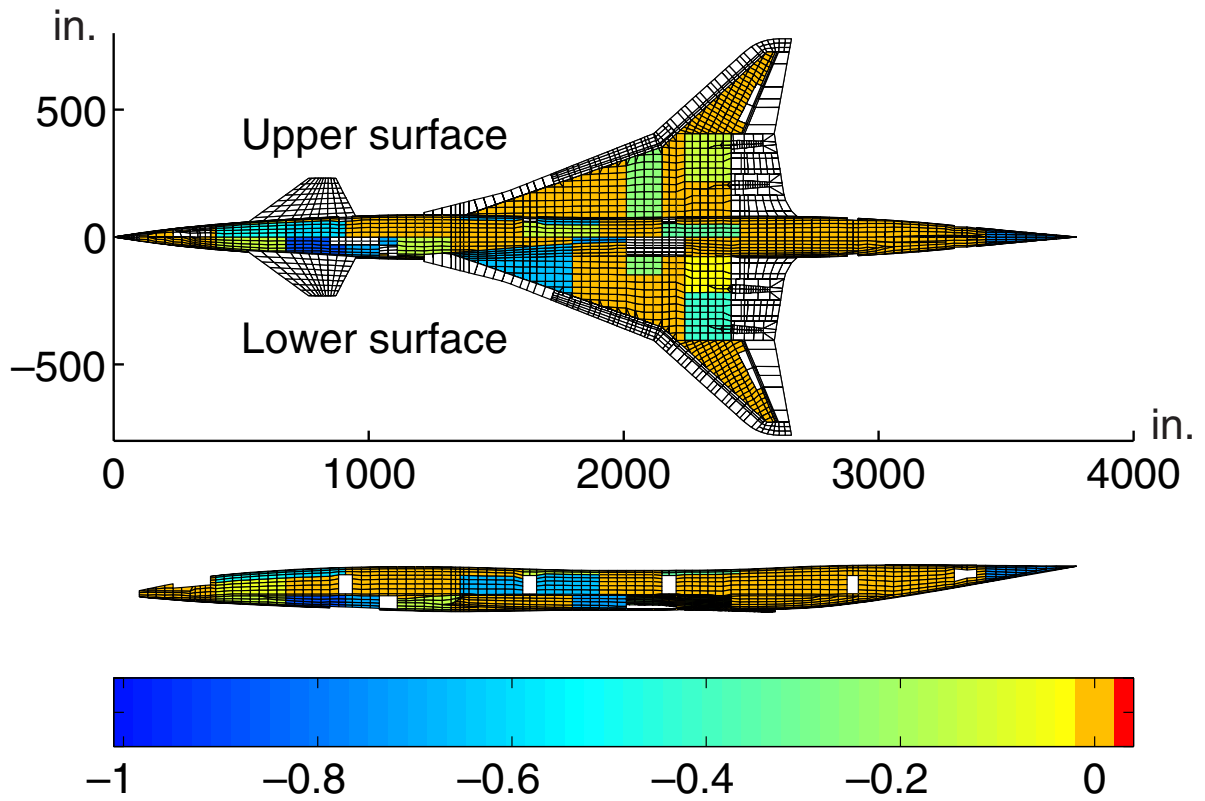
(b) Load case associated with maximum KS buckling function.

Figure 48. Buckling constraint information for nonlinear design of Aft-Tail configuration.

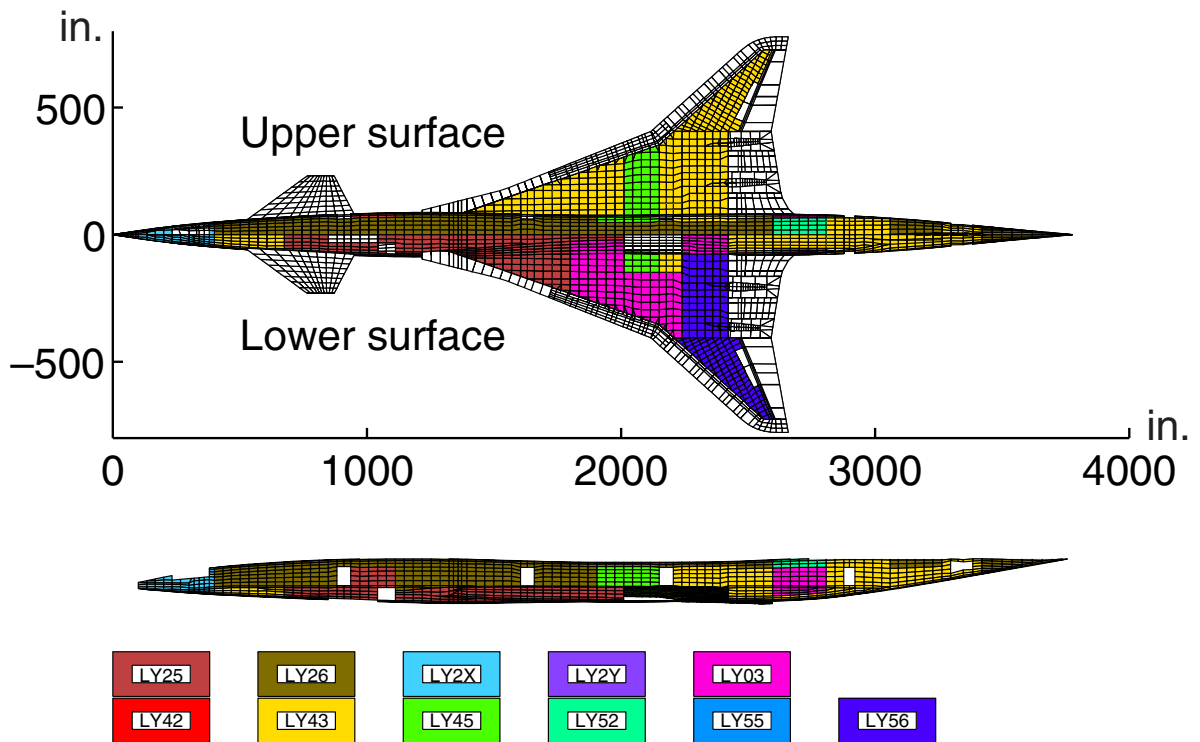


(b) Load case associated with maximum KS buckling function.

Figure 49. Buckling constraint information for nonlinear design of Three-Surface configuration.



(a) KS buckling constraint.



(b) Load case associated with maximum KS buckling function.

Figure 50. Buckling constraint information for nonlinear design of Canard configuration.

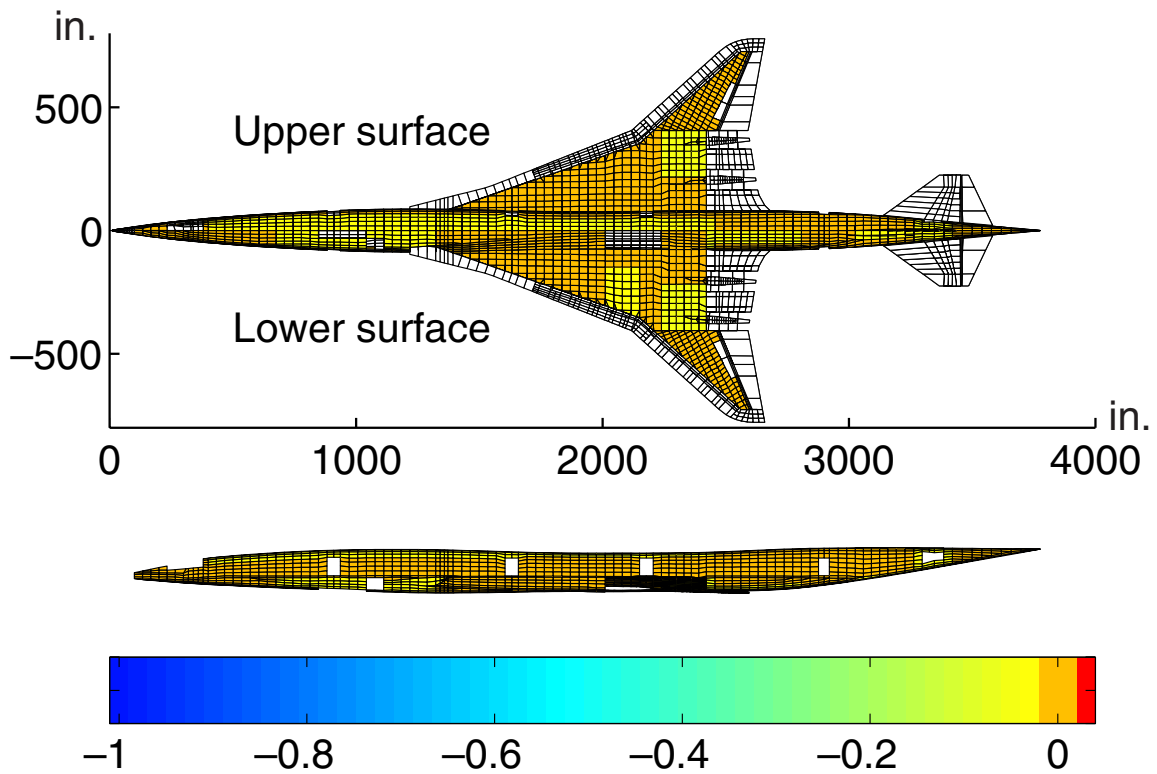


Figure 51. Zero-degree ply mixture constraint defined by equation (12) for nonlinear design of Aft-Tail configuration.

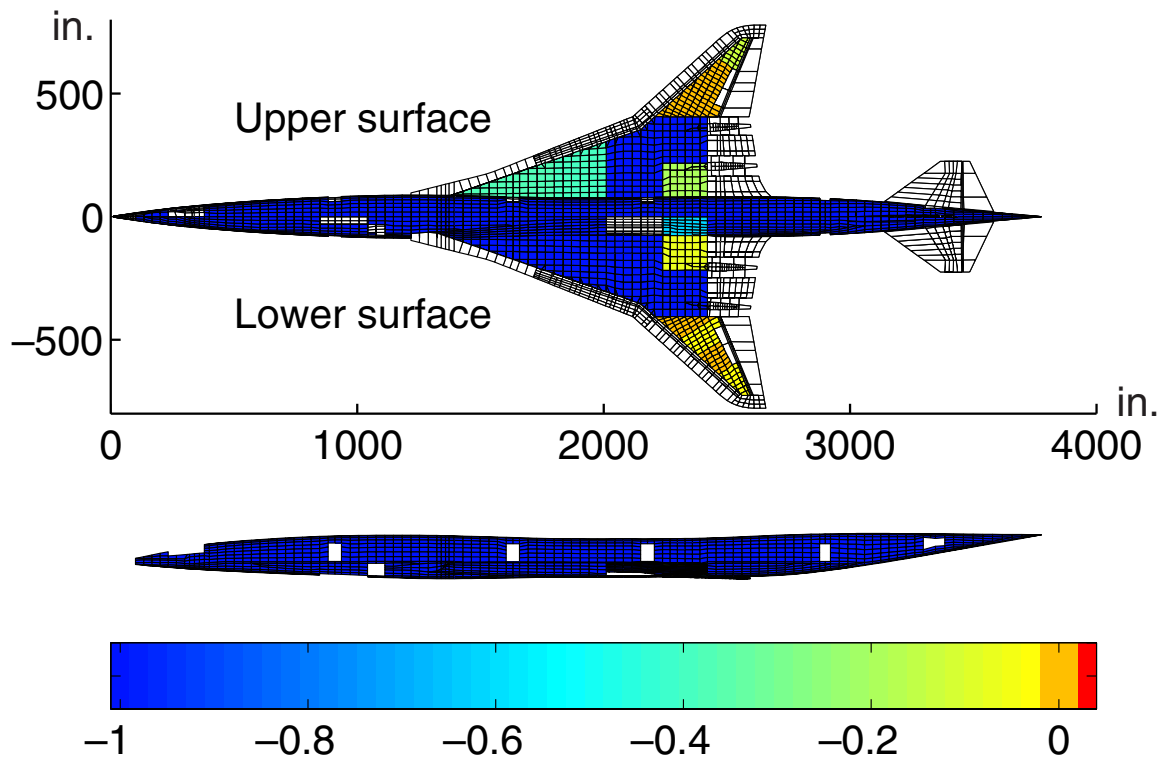
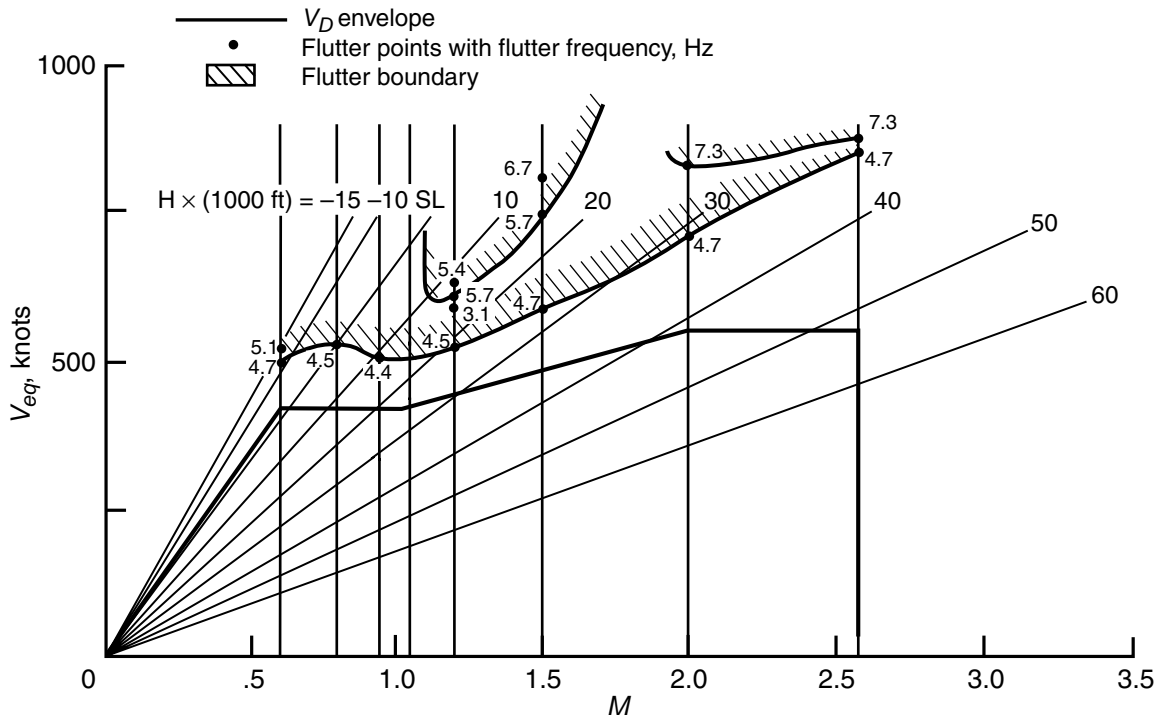
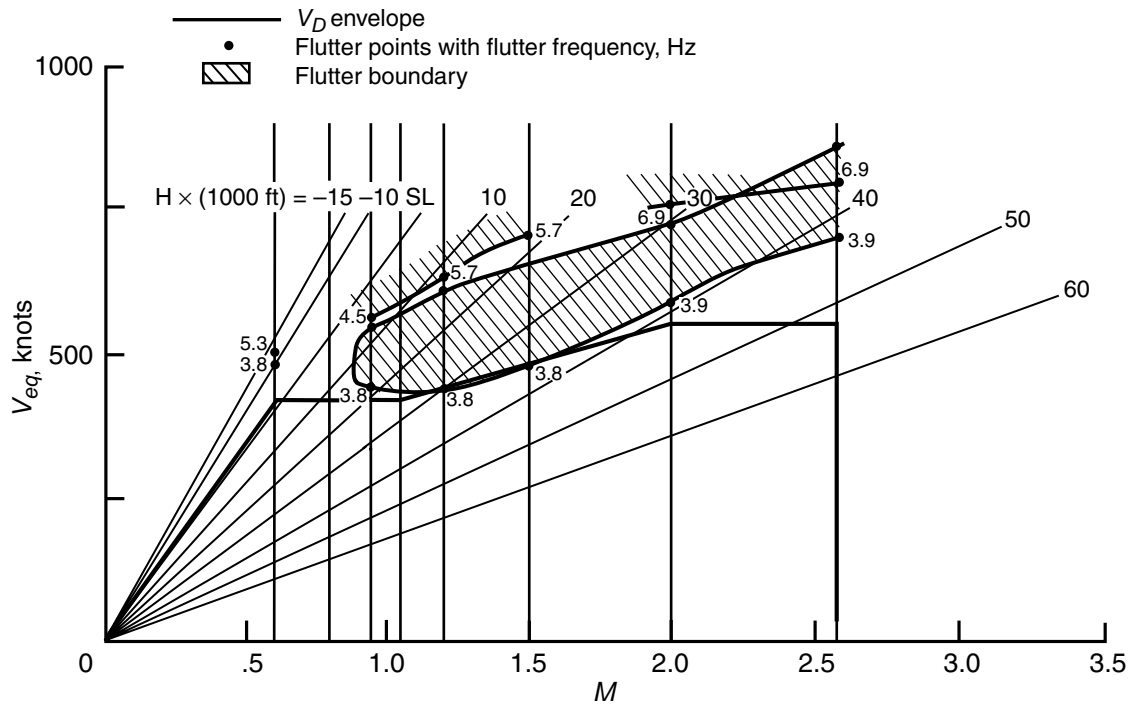


Figure 52. Zero-degree ply mixture constraint defined by equation (17) for nonlinear design of Aft-Tail configuration.



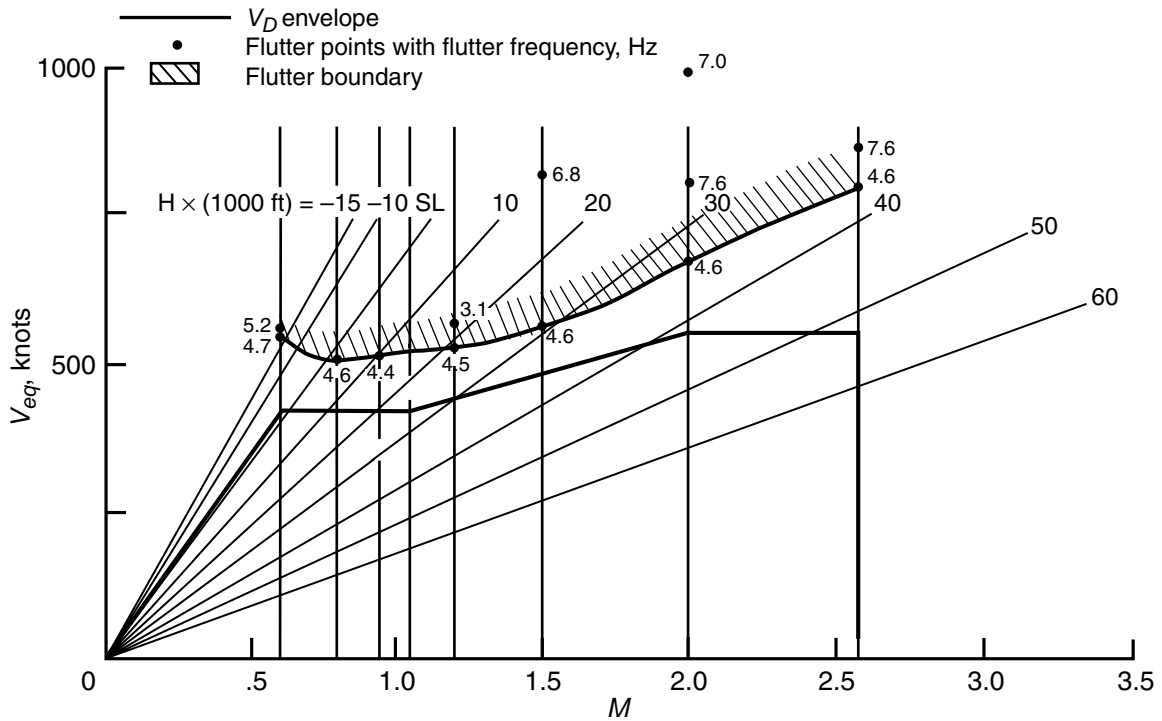


(a) Mass case 1, zero damping.

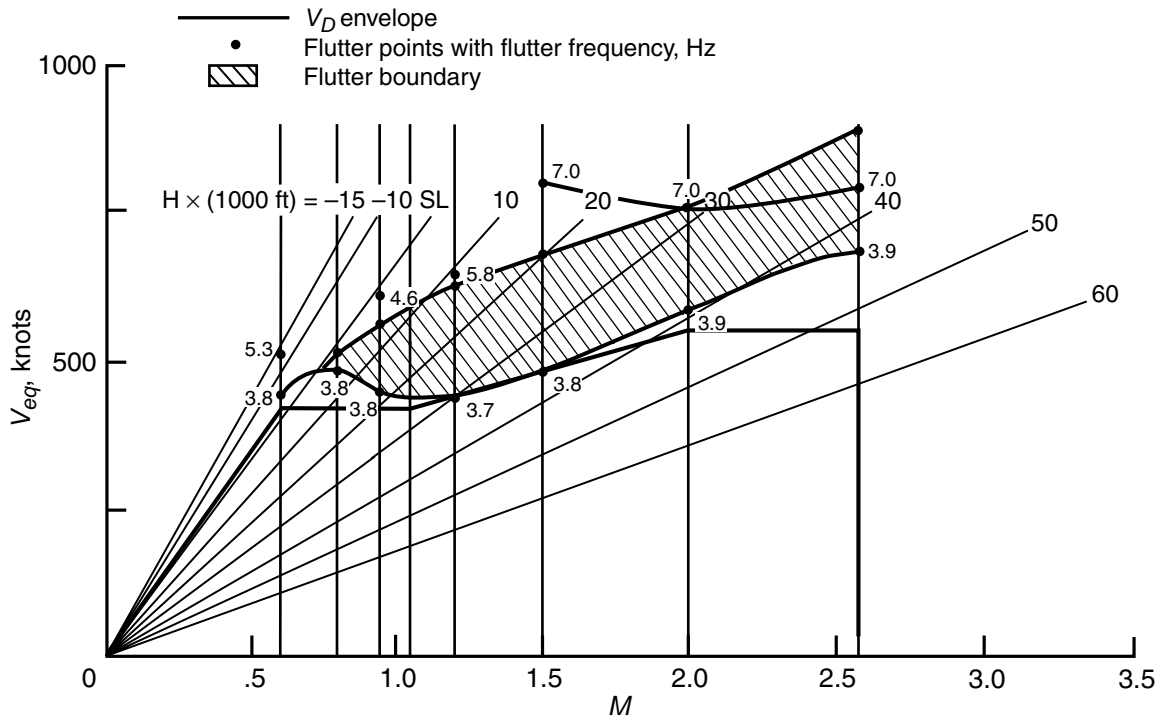


(b) Mass case 5, zero damping.

Figure 54. Flutter results for linear design of Aft-Tail configuration.

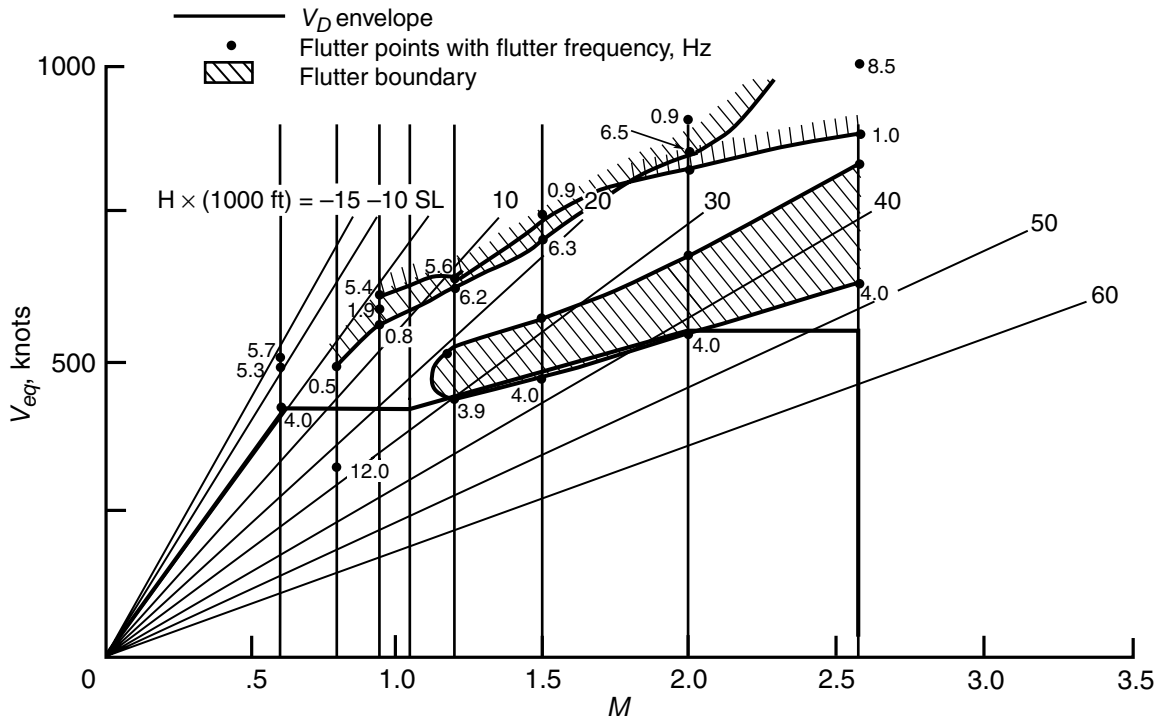


(a) Mass case 1, zero damping.

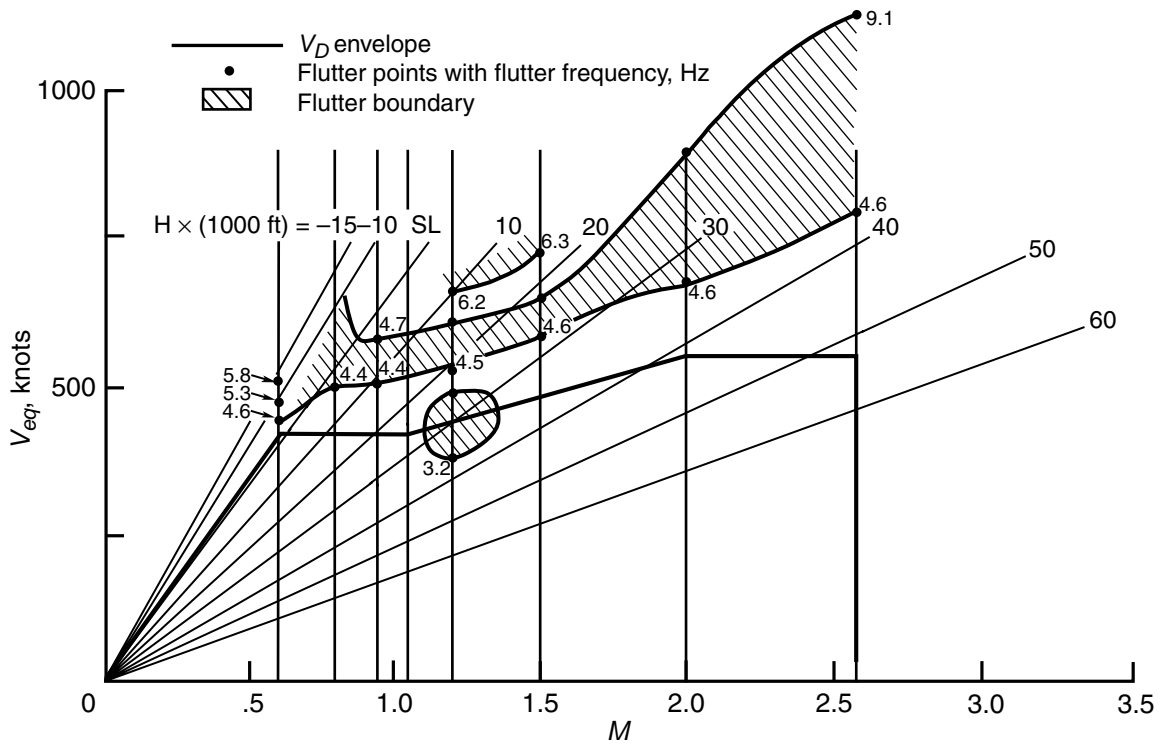


(b) Mass case 5, zero damping.

Figure 55. Flutter results for nonlinear design of Aft-Tail configuration.

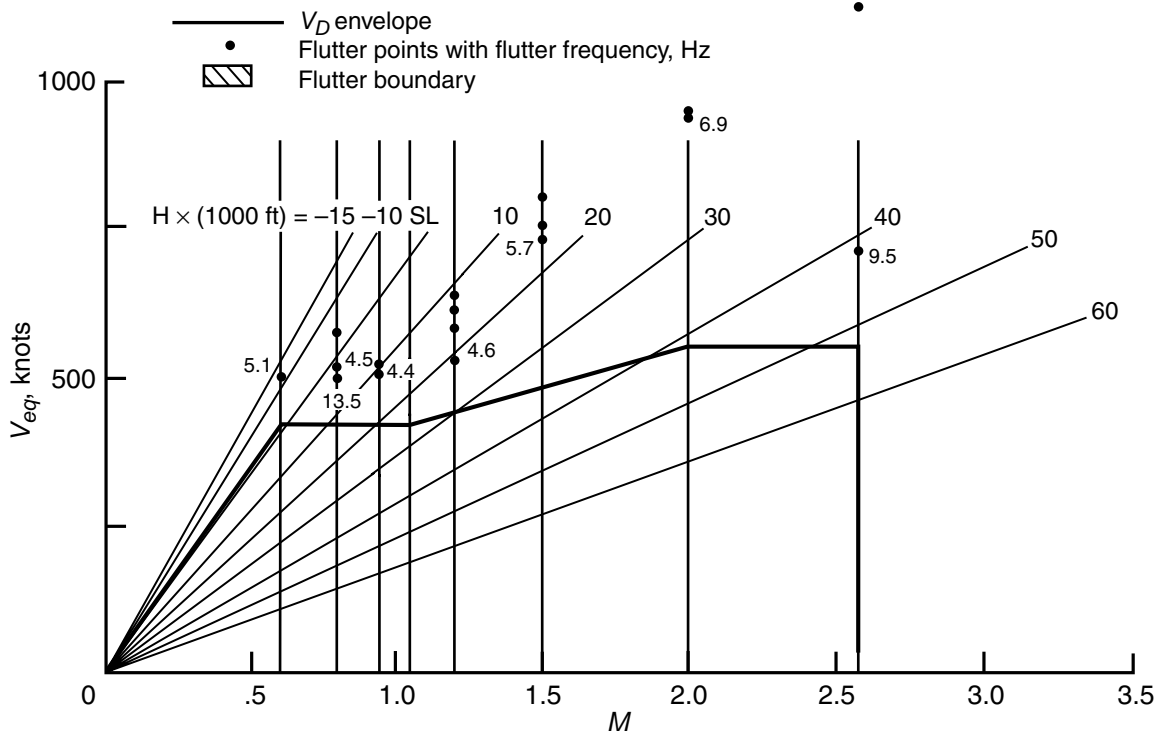


(a) Mass case 1, zero damping.

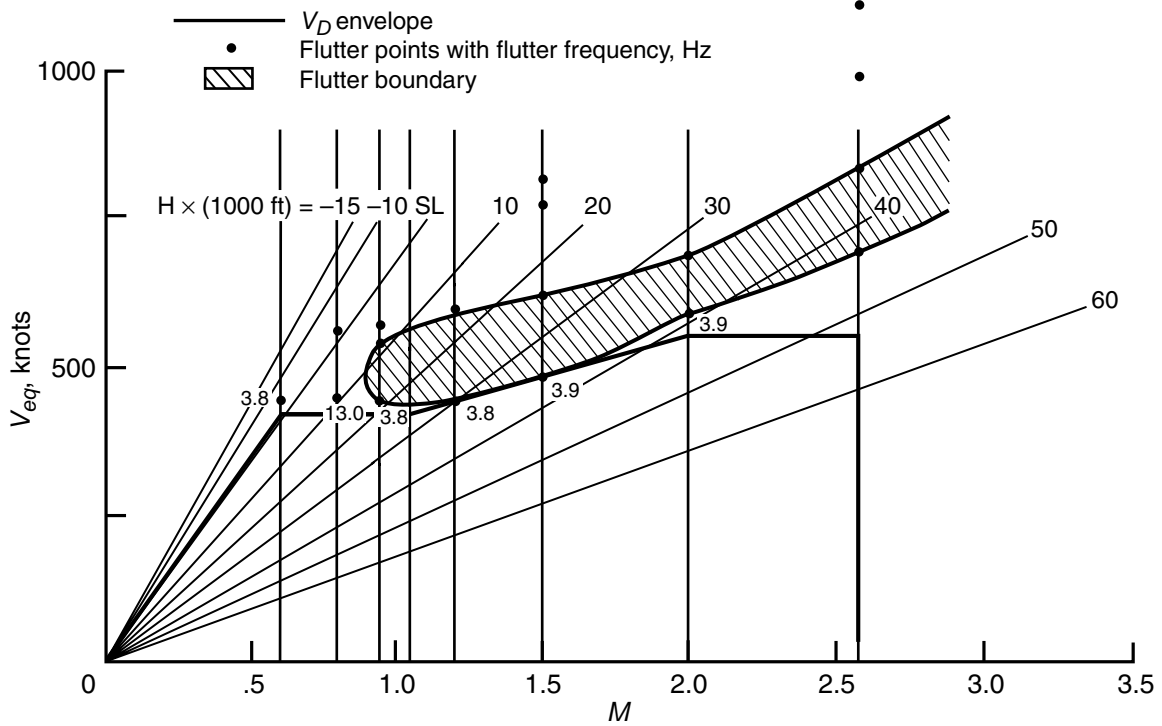


(b) Mass case 5, zero damping.

Figure 56. Flutter results for initial design of Three-Surface configuration.

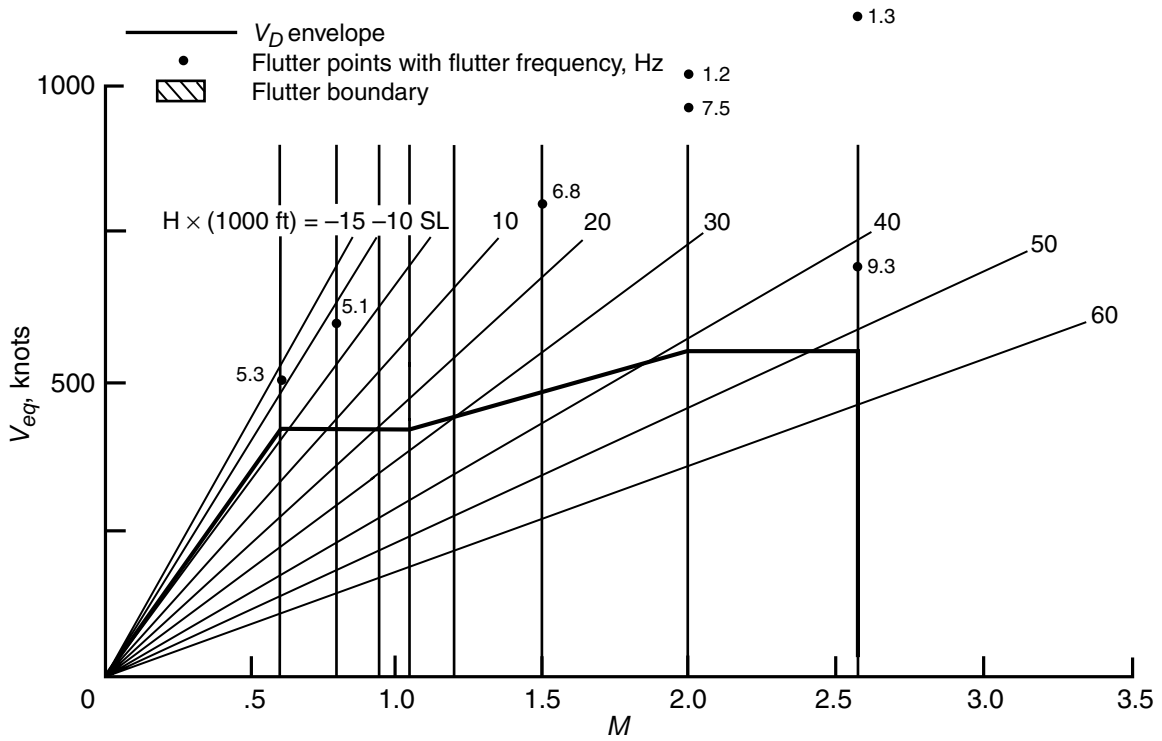


(a) Mass case 1, zero damping; no flutter boundary drawn.

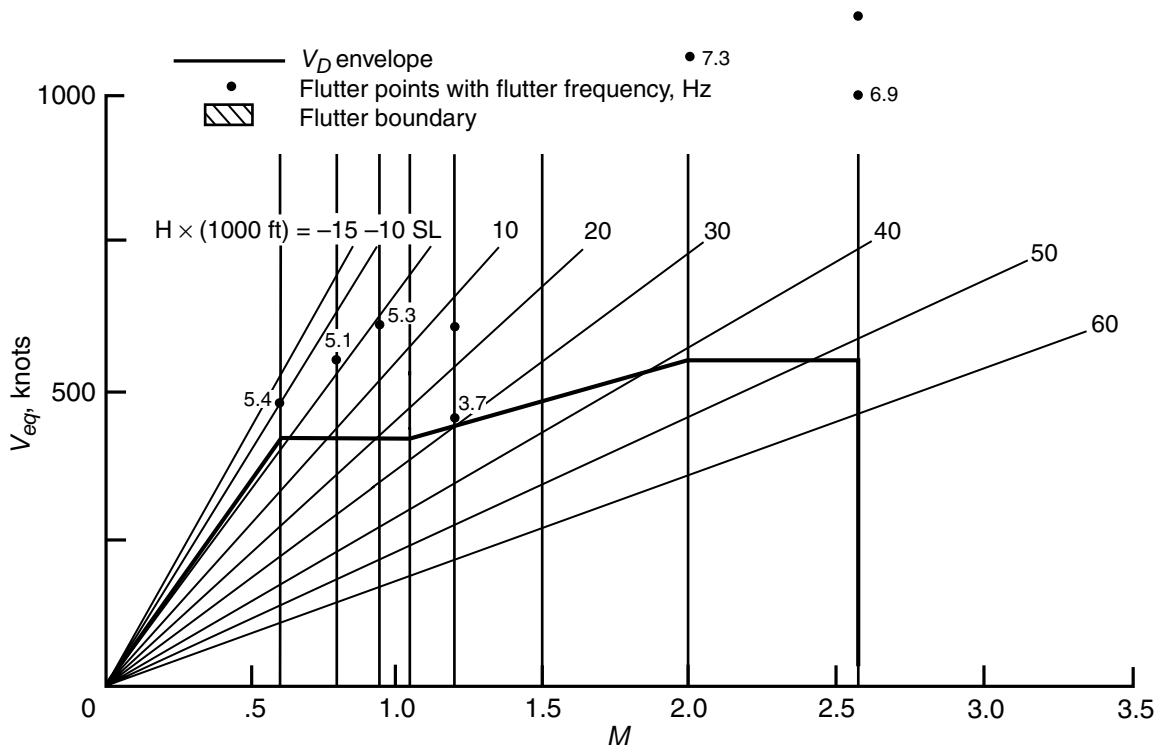


(b) Mass case 5, zero damping.

Figure 57. Flutter results for linear design of Three-Surface configuration.

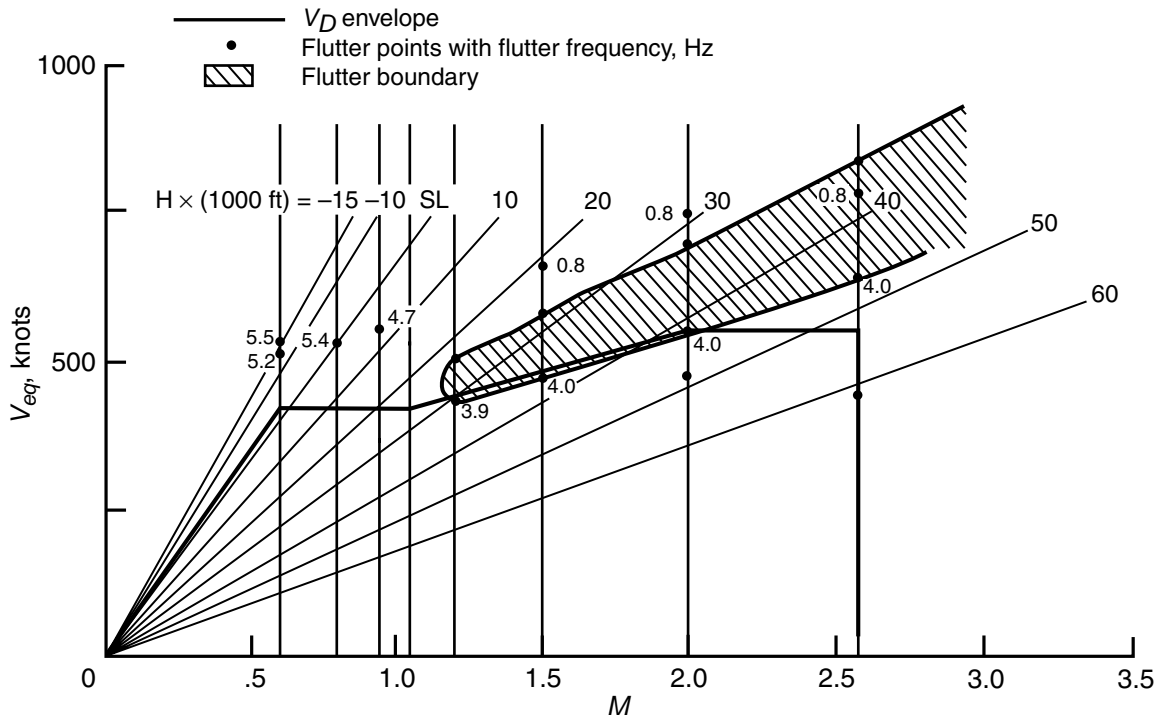


(a) Mass case 1, zero damping.

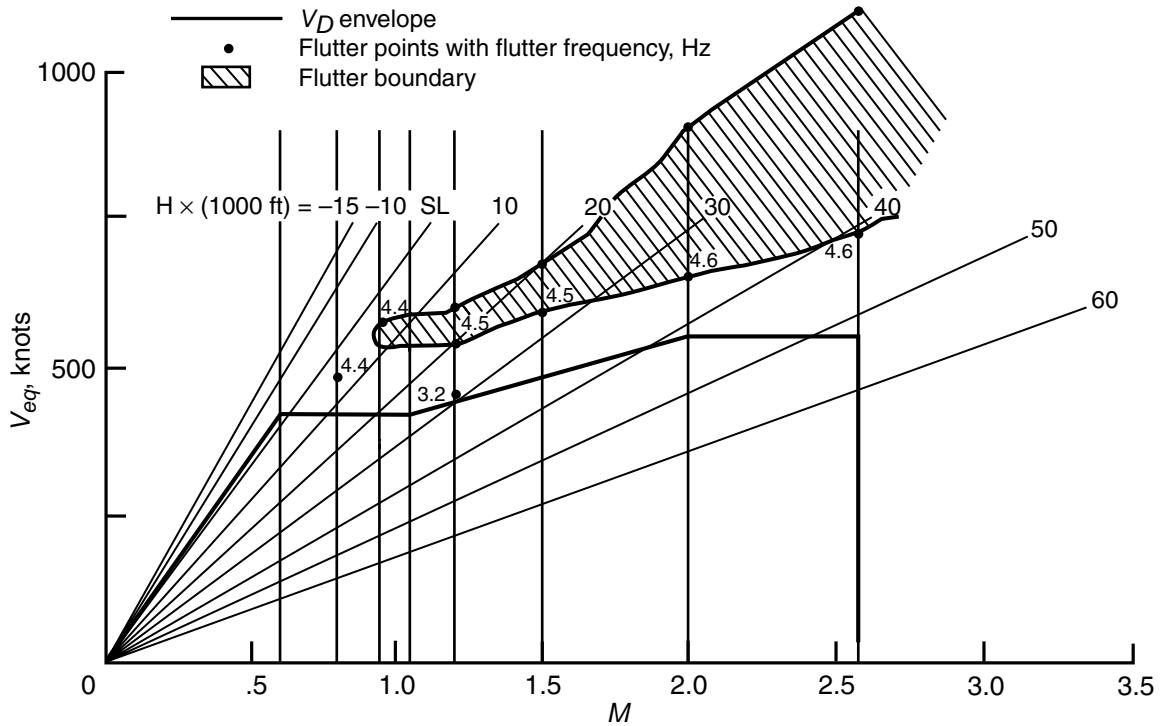


(b) Mass case 5, zero damping.

Figure 58. Flutter results for nonlinear design of Three-Surface configuration; no flutter boundary drawn.

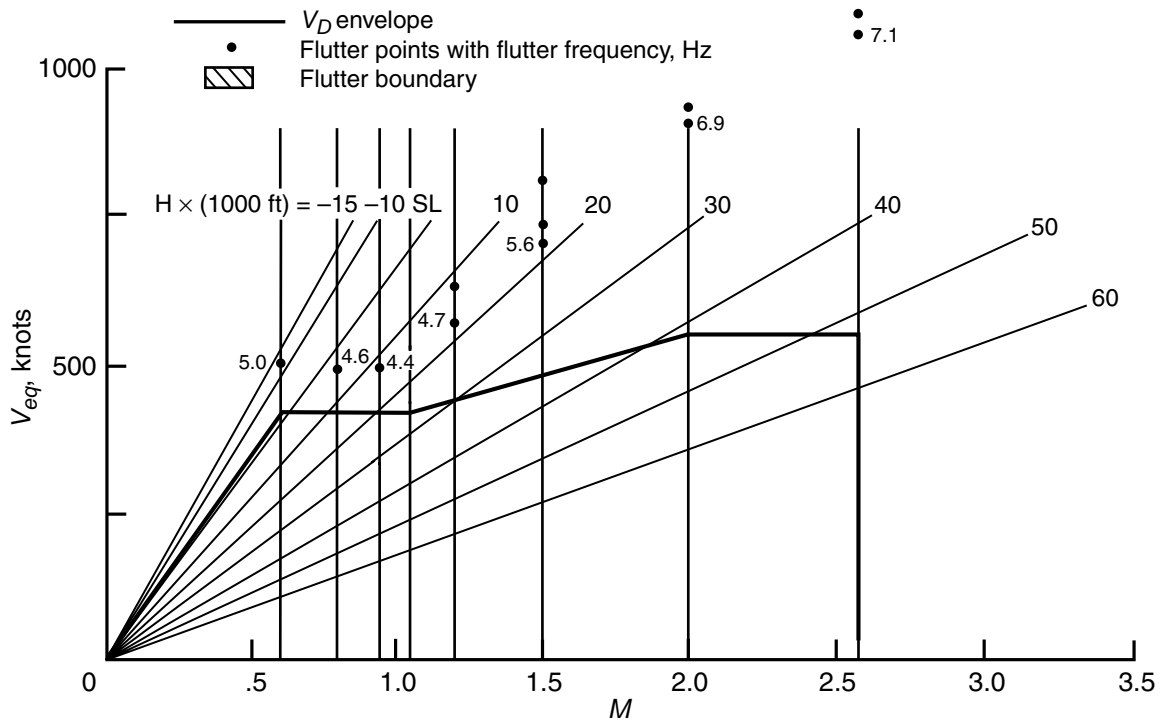


(a) Mass case 1, zero damping.

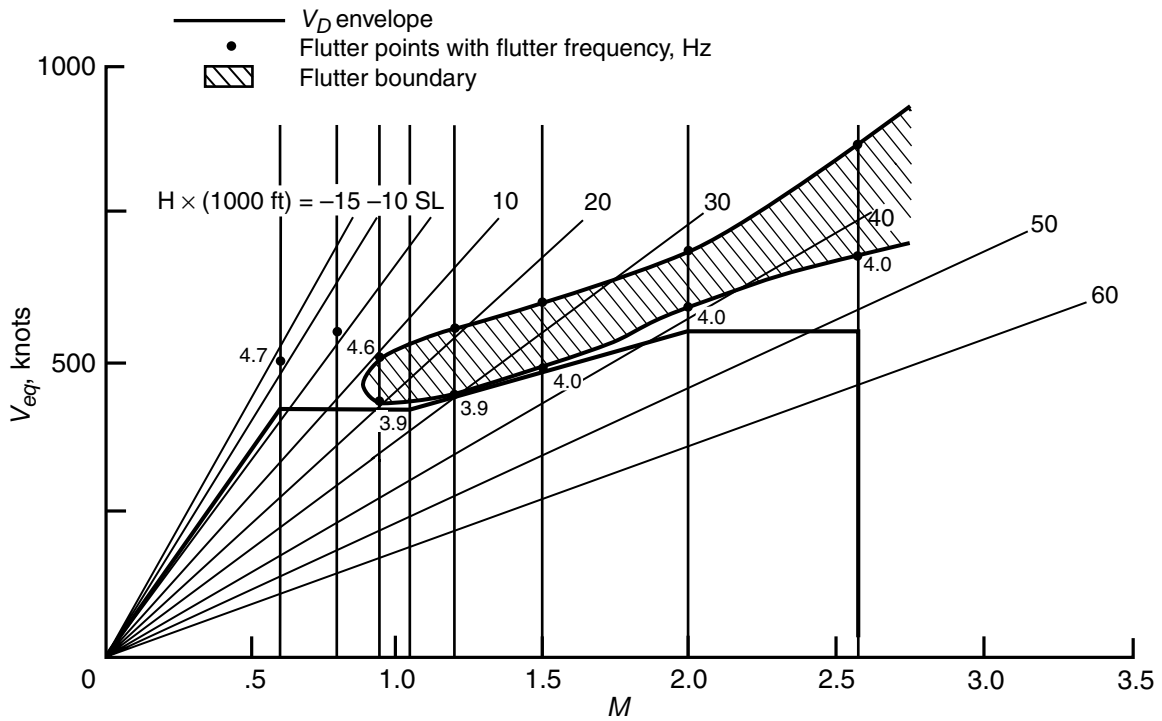


(b) Mass case 5, zero damping.

Figure 59. Flutter results for initial design of Canard configuration.

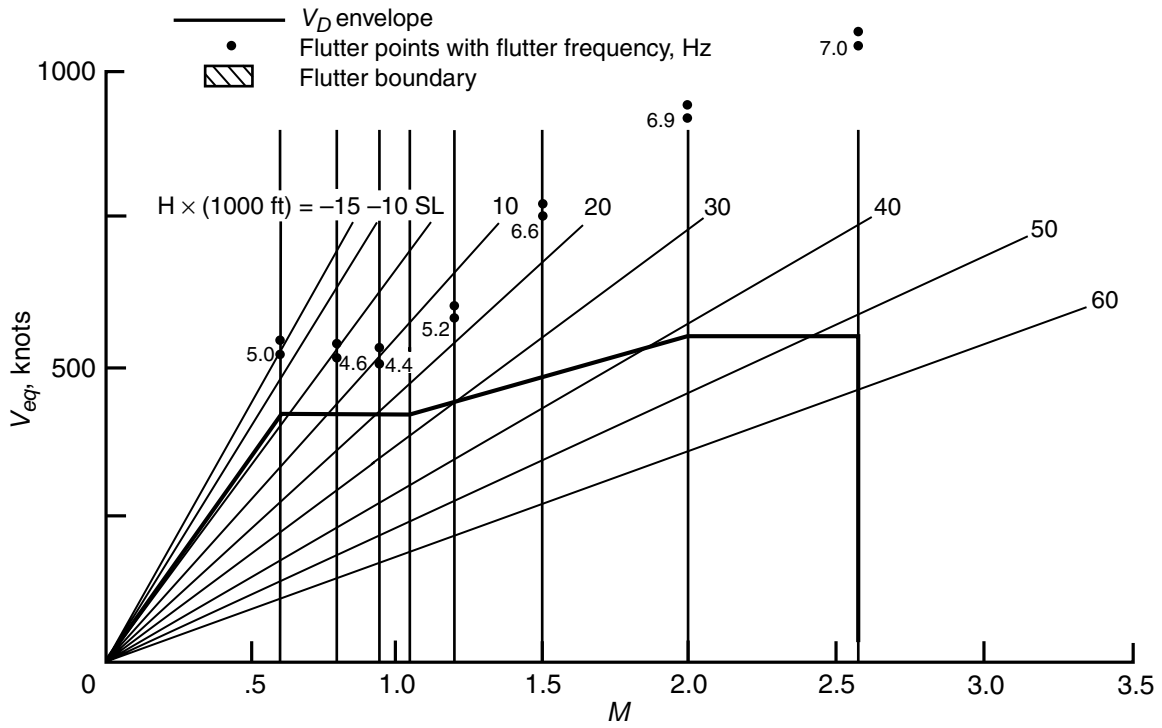


(a) Mass case 1, zero damping; no flutter boundary drawn.

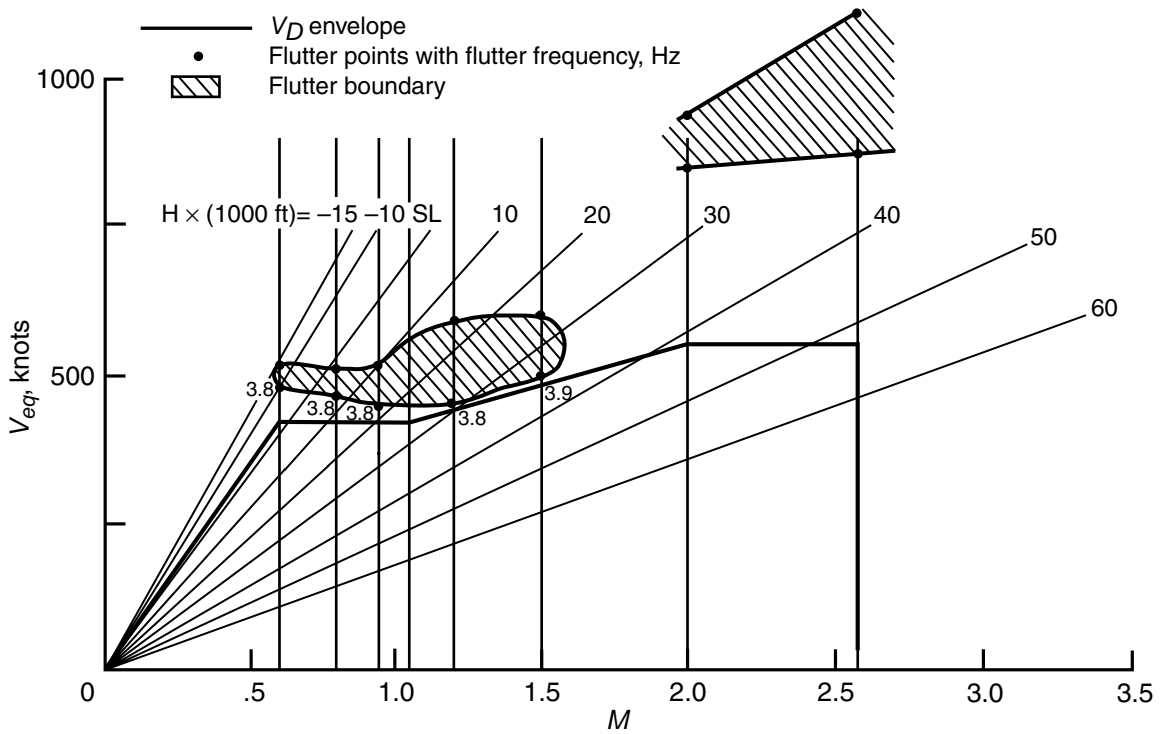


(b) Mass case 5, zero damping.

Figure 60. Flutter results for linear design of Canard configuration.



(a) Mass case 1, zero damping; no flutter boundary drawn.



(b) Mass case 5, zero damping.

Figure 61. Flutter results for nonlinear design of Canard configuration.

**REPORT DOCUMENTATION PAGE**

*Form Approved  
OMB No. 0704-0188*

The public reporting burden for this collection of information is estimated to average 1 hour per response, including the time for reviewing instructions, searching existing data sources, gathering and maintaining the data needed, and completing and reviewing the collection of information. Send comments regarding this burden estimate or any other aspect of this collection of information, including suggestions for reducing this burden, to Department of Defense, Washington Headquarters Services, Directorate for Information Operations and Reports (0704-0188), 1215 Jefferson Davis Highway, Suite 1204, Arlington, VA 22202-4302. Respondents should be aware that notwithstanding any other provision of law, no person shall be subject to any penalty for failing to comply with a collection of information if it does not display a currently valid OMB control number.  
**PLEASE DO NOT RETURN YOUR FORM TO THE ABOVE ADDRESS.**

<b>1. REPORT DATE (DD-MM-YYYY)</b> 01-07-2005		<b>2. REPORT TYPE</b> Technical Publication		<b>3. DATES COVERED (From - To)</b>	
<b>4. TITLE AND SUBTITLE</b> Aeroelastic Sizing for High-Speed Research (HSR) Longitudinal Control Alternatives Project (LCAP)				<b>5a. CONTRACT NUMBER</b>	
				<b>5b. GRANT NUMBER</b>	
				<b>5c. PROGRAM ELEMENT NUMBER</b>	
<b>6. AUTHOR(S)</b> Walsh, Joanne L.; Dunn, H. J.; Stroud, W. Jefferson; Barthelemy, J.-F.; Weston, Robert P.; Martin, Carl J.; and Bennett, Robert M.				<b>5d. PROJECT NUMBER</b>	
				<b>5e. TASK NUMBER</b>	
				<b>5f. WORK UNIT NUMBER</b> 537-09-20-02	
<b>7. PERFORMING ORGANIZATION NAME(S) AND ADDRESS(ES)</b> NASA Langley Research Center Hampton, VA 23681-2199				<b>8. PERFORMING ORGANIZATION REPORT NUMBER</b>  L-19079	
<b>9. SPONSORING/MONITORING AGENCY NAME(S) AND ADDRESS(ES)</b> National Aeronautics and Space Administration Washington, DC 20546-0001				<b>10. SPONSOR/MONITOR'S ACRONYM(S)</b>  NASA	
				<b>11. SPONSOR/MONITOR'S REPORT NUMBER(S)</b>  NASA/TP-2005-213533	
<b>12. DISTRIBUTION/AVAILABILITY STATEMENT</b> Unclassified - Unlimited Subject Category 05 Availability: NASA CASI (301) 621-0390					
<b>13. SUPPLEMENTARY NOTES</b> An electronic version can be found at <a href="http://ntrs.nasa.gov">http://ntrs.nasa.gov</a> CD-ROM supplement of report (NASA/TP-2005-213533/SUPPL) is available from NASA CASI.					
<b>14. ABSTRACT</b> The Longitudinal Control Alternatives Project (LCAP) compared three high-speed civil transport configurations to determine potential advantages of the three associated longitudinal control concepts. The three aircraft configurations included a conventional configuration with a layout having a horizontal aft tail, a configuration with a forward canard in addition to a horizontal aft tail, and a configuration with only a forward canard. The three configurations were aeroelastically sized and were compared on the basis of operational empty weight (OEW) and longitudinal control characteristics. The sized structure consisted of composite honeycomb sandwich panels on both the wing and the fuselage. Design variables were the core depth of the sandwich and the thicknesses of the composite material which made up the face sheets of the sandwich. Each configuration was sized for minimum structural weight under linear and nonlinear aeroelastic loads subject to strain, buckling, ply-mixture, and subsonic and supersonic flutter constraints. This report describes the methods that were used and the results that were generated for the aeroelastic sizing of the three configurations.					
<b>15. SUBJECT TERMS</b> High Speed Civil Transport; Multidisciplinary Optimization; Aft Tail Configuration; Canard Configuration; Three Surface Configuration					
<b>16. SECURITY CLASSIFICATION OF:</b>			<b>17. LIMITATION OF ABSTRACT</b>	<b>18. NUMBER OF PAGES</b>	<b>19a. NAME OF RESPONSIBLE PERSON</b>
<b>a. REPORT</b>	<b>b. ABSTRACT</b>	<b>c. THIS PAGE</b>			STI Help Desk (email: <a href="mailto:help@sti.nasa.gov">help@sti.nasa.gov</a> )
U	U	U	UU	118	<b>19b. TELEPHONE NUMBER (Include area code)</b> (301) 621-0390